DOCTOR OF PHILOSOPHY

Studies on Effects of Optical Feedback Based Micro-Ring Resonator on the Integrated 40 GHz Opto-Electronic Oscillator

Roy, Ugra Mohan

Award date:
2016

Awarding institution:
Coventry University
M S Ramaiah University of Applied Sciences

Studies on Effects of Optical Feedback Based Micro-Ring Resonator on the Integrated 40 GHz Opto-Electronic Oscillator

By

Ugra Mohan Roy

Ph.D

December 2016

Studies on Effects of Optical Feedback Based Micro-Ring Resonator on the Integrated 40 GHz Opto-Electronic Oscillator

By

Ugra Mohan Roy

December 2016

A thesis submitted in partial fulfilment of the University's requirements for the Degree of Doctor of Philosophy

CERTIFICATE

This is to certify that the Doctoral Dissertation titled "Studies on Effects of Optical Feedback Based Micro-Ring Resonator on the Integrated 40 GHz Opto-Electronic Oscillator" is a bonafide record of the work carried out by Mr. Ugra Mohan Roy in partial fulfilment of requirements for the award of Doctor of Philosophy Degree of Coventry University

December- 2016

Dr. Govind R. Kadambi
Director of Studies
M. S. Ramaiah School of Advanced Studies, Bangalore

Dr. Omid Razmkhah
Supervisor
Coventry University, U.K.

ACKNOWLEDGEMENT

I, the author sincerely thank the Almighty for providing enough courage and patience to accomplish this research work. I sincerely acknowledge and thank my guide Prof. Govind R. Kadambi, Pro-Vice Chancellor, M. S. Ramaiah University of Applied Sciences, for his valuable guidance throughout my research work. His friendly support and continuous encouragement with valuable suggestion and minute details have helped me to accomplish this thesis. It would have been very difficult to complete this thesis without his useful and valuable guidance. I sincerely acknowledge the effort of Dr. Yuri Vershinin, Coventry University, for his valuable guidance. I wholeheartedly acknowledge the effort of Dr. Omid Razmkhah, Coventry University, for his valuable technical guidance during the dissertation drafting phase of my research work. I sincerely thank Dr. S. Malathi, Associate professor MSRUAS for her help, support and discussion during photonics simualtion and thesis writing. I would also like to thank Dr.T. Srinivas, Associate Professor, IISC, for having permitted me to work at the Photonics Lab of Indian Institute of Science, Bangalore. I thank Dr. B. R. Karthikeyen for his support during the entire period of my research work. I also sincerely thank Dr. Peter White, Coventry University, UK and Dr. M.D. Deshpande, Professor, MSRUAS for their continuous technological feedback throughout the progress report panel review. I would also like to thank Prof. S. R. Shankapal, Vice-Chancellor, MSRUAS for his moral support and friendly suggestions. I heartily extend my thanks to all my colleagues who directly or indirectly helped me in the accomplishment of this task. I thank my entire colleague who were available for the long discussions regarding technical details. I personally appreciate them for their long technical discussions and the help they extended. Special thanks are due to my entire family especially to my parents Shri Rama Kant Roy and Shrimati Ambika Devi, wife-Archana Roy, daughter-Aastha Roy, brother-Shri Madan Mohan Roy and sister-Shrimati Sheela Mishra, for their patience and continuous support during the entire period of my research work. I also extend my thanks to one and all who directly or indirectly helped me in this endeavor and whose name I might have unintentionally left out.

ABSTRACT

This thesis presents the design and simulation of 40 GHz Integrated Opto-Electronic Oscillator (IOEO) with high spectral purity, minimum phase noise, high quality factor as well as better thermal and frequency stability. Simulation studies of the designed IOEO have been carried out using a novel Linear Time Invariant (LTI) architecture having all optical components in the feedback path which is contrary to the conventional IOEO. The long optical fiber present in the conventional IOEO has been replaced by an Integrated Optical Microring Resonator (IOMR). The proposed IOMR replaces the few km long fiber cable making the IOEO compact. The designed IOEO exhibits a minimum phase noise of -245 $dBcHz^{-1}$ at 100 kHz offset compared to phase noise of -160 $dBcHz^{-1}$ of conventional design. The computation of the phase noise of the designed IOEO has been carried out using variance method. The proposed design of IOEO also eliminates the fiber loss thereby improving the Quality (Q) factor of the IOEO. The simulation study on the effect of IOMR on the Q factor of the IOEO reveals the loaded quality factor of 1000. Through simulation studies invoking Sellmeier model, the thermal stability of the designed IOEO is found to be $\pm$ 0.325 $ppmK^{-1}$ over a temperature range of 150-300 K. Frequency stability analysis of the designed IOEO has been studied analytically using two port network theory. Effect of Butt-coupling coefficient on the stability is also explored.

This thesis presents a novel analytical model for the straight and curved waveguides of IOMR, invoking the Coupled Mode Theory (CMT). The potential utility of derived mathematical expressions has been illustrated in the calculation of quality factor, coupling length and gap between straight and curved waveguides of the ring resonator. The significance of Butt-coupling coefficient in the CMT has been explored and its effects on resonance and output power of IOMR have been analyzed for a novel resonance condition. The analysis of the effects of gap between straight and curved waveguides on the output power of IOEO facilitates additional insight into the underlying principles and its phase noise. The phase noise contribution of IOMR in the IOEO is found to be extremely small and is insignificant. The fabrication tolerance of the designed IOMR has been computed using derived analytical model to support the feasibility of manufacturing the IOEO.

The simulation model of proposed IOEO has been utilized for design and simulation of an optical beam steering system. The simulation study directed towards Wavelength Division Multiplexing (WDM) substantiates the utility and relevance of IOEO as modulator and modulation frequency generator simultaneously. This thesis also presents design and simulation studies on an IOEO based novel architecture for label-free optical Bio-sensor. The proposed IOEO based label free sensor eliminates the laborious labeling procedure and its associated cumbersome effects. The proposed Bio-sensor exhibits a bulk refractive index sensitivity of -140 $MHzRIU^{-1}$.

CONTENTS

LIST OF TABLES

LIST OF FIGURES

NOMENCLATURE

c	-	Velocity of light in free space
e	-	electronic charge
e^x	-	Exponential of x
f	-	Frequency (Hz) (MHz) (GHz)
j	-	Imaginary component of the complex term
x	-	x coordinate
y	-	y coordinate
z	-	z coordinate
S	-	Gap between modulating signal $v(t)$ electrode and ground electrode
mm	-	Millimeter
W	-	Watts
Wcm^{-1}	-	Watts per centimeter
Wm^{-1}	-	Watts per meter
$W3$	-	Width of the strip waveguide
G	-	Gap between laser input and the electrode
$W1$	-	Width of the electrode
T_{buffer}	-	Thickness of the buffer layer
E_1 and E_2	-	The electric field input at the two arms of MZIM
V_B	-	DC bias voltage
γ	-	Intensity insertion loss
L	-	Circumference of the ring
ρ	-	Attenuation (propagation)loss
l	-	Coupling length
I_d	-	Average primary dark current
$< I^2amp >$		Mean square noise current
$F(M_1)$	-	Noise factor related to random nature of an avalanche process
Δf	-	Effective noise bandwidth
K	-	Boltzmann constant

R_L	-	Load resistance
M_1	-	Multiplicative factor
Z_{in}	-	Input impedance
Z_0	-	Characteristic impedance
λ	-	Wavelength
ll	-	Length of the microstrip line
d	-	Gap between straight and curved waveguide of IOMR
k_{ab}	-	Coupling coefficient between straight and curved waveguides
m	-	Mode number
n	-	Effective refractive index
R	-	Ring radius of IOMR
α	-	Total amplitude attenuation coefficient
K_2	-	Normalized coupling coefficient between of the IOMR
a	-	Attenuation factor
n_r	-	Effective refractive index
r	-	Transmission factor
α_{BEND}	-	Bend loss coefficient (radiation loss) of bend wave guide
β	-	z directed propagation constant
k_{xs}	-	x directed decay constant representing the evanescent field
n_{effp}	-	Effective index outside the strip waveguide
λ_0	-	Free space wavelength
h	-	Plancks constant
h_2	-	Sum of the height of lower cladding and the core
h_1	-	Height of the lower clad
$h_2 - h_1$	-	Height of the core
Δl	-	Incremental coupling length
k_1	-	vector that is nearly parallel to the z axis
ω	-	Angular frequency
t	-	Instantaneous time
V_p	-	phase velocity
k_{12} and k_{21}	-	coupling coefficients between the straight waveguides and the ring waveguide
c_{12} and c_{21}	-	Butt-coupling coefficient between strip waveguides I and II respectively
E_1 and H_1	-	Electric and magnetic fields
ω	-	Angular Frequency

ε	-	Free Space Permittivity
u_z	-	Unit vector in the direction of propagation
λ_R	-	Resonance shift
M	-	M-factor
A	-	Gain of Amplifier
ϕ	-	Phase
A_0	-	Amplitude
f_0	-	Frequency
$B(jf)$	-	Feedback transfer function
dB_cHz^{-1}	-	decibels relative to the carrier per hertz at a certain frequency offset
f_m	-	Offset frequency
σ_ϕ^2	-	Unit variance of the random phase noise process
$\sigma_\phi^2(t)$	-	Total variance
σ_ϕ	-	Standard deviation
X	-	Output signal sample of the LNA
μ	-	Mean of the output signal sample
N_{sample}	-	Total number of output signal sample
$L(f_m)$	-	Phase noise in units of dB_cHz^{-1}
V_1	-	Voltage across port 1
I_1	-	Current into port 1
V_2	-	Voltage across port 2
I_2	-	Current into port 2
0.55°	-	Denoting 0.55 Degrees
E	-	E field of EM wave or E Plane
H	-	H field of EM wave or H Plane
D_0	-	Wavelength dispersion
L_0	-	Length of the Single Mode Fiber
$\Delta\lambda_{opt}$	-	Wavelength spacing
$\Delta\phi$	-	Phase difference between antenna elements
f_{RF}	-	Modulating frequency
$d3$	-	Antenna Spacing
$\triangle t$	-	Time delay
θ	-	Beam steering angle of the antenna elements
n_{eff}	-	effective refractive index

λ_0	-	Resonant wavelength
$\triangle f_0$	-	Frequency shift of the IOMR
n_g	-	Group index
$MHzRIU^{-1}$	-	Mega Hertz per refractive index unit
$ppmK^{-1}$	-	Parts per million per Kelvin
kHz	-	KiloHertz
$K1$	-	Rollet's stability criteria
Y_{11}	-	Y-Parameters
Y_{12}	-	Y-Parameters
Y_{21}	-	Y-Parameters
Y_{22}	-	Y-Parameters
S_{11}	-	S-Parameters
S_{12}	-	S-Parameters
S_{21}	-	S-Parameters
S_{22}	-	S-Parameters
A_{11}	-	ABCD-Parameters
B_{12}	-	ABCD-Parameters
C_{21}	-	ABCD-Parameters
D_{22}	-	ABCD-Parameters
pF	-	Pico Farad
T	-	Temperature in Kelvin
S_i	-	Strengths of the resonance features in the material at wavelength λ_i

LIST OF ABBREVIATIONS

ASE	-	Amplified Spontaneous Noise
BPM	-	Beam Propagation Method
AMZI	-	Asymmetric Mach-Zenhder Interferometer
CMT	-	Coupled Mode Theory
CMOS	-	Complementary Metal Oxide semiconductor
dB	-	Decibel
nH	-	Nano Henry
mm	-	Millimeter
km	-	Kilometer
μm	-	Micrometer
mW	-	MilliWatt
nm	-	Nanometer
AW^{-1}	-	Ampere per Watt
Gbs^{-1}	-	Giga byte per second
GHz	-	Giga Hertz
MHz	-	Mega Hertz
BPF	-	Band Pass Filter
DSF	-	Dispersion Shifted Fiber
DWDM	-	Dense Wavelength Division Multiplexer
DM-AFL	-	Duel-Mode Amplifier Feedback Laser
EDFA	-	Erbium Doped Fiber Amplifier
EAM	-	Electro Absorption Modulator
FP	-	Fabry perot
FP-LD	-	Febry perot- Laseer Diode
FSR	-	Free Spectral Range
FDTD	-	Finite Difference Time Domain
FWHM	-	Full Width Half Maximum
GEO	-	Geostationary Orbit

HW	-	Half width
IOMR	-	Integrated Optical Micro Ring Resonator
IOEO	-	Integrated Opto-Electronic Oscillator
ITU-T	-	International Telecommunication Union for Telemetry
LEO	-	Low Earth Orbit
LTI	-	Linear Time Invariant
LNA	-	Low Noise Amplifier
LC	-	Liquid Crystal
MZIM	-	Mach-Zenhder Intensity Modulator
MMF	-	Multi Mode Fiber
MPF	-	Microwave Photonic Filter
OM	-	Optical Modulator
OEO	-	Opto-Electronic Oscillator
OF	-	Optical Fiber
PD	-	Photo Detector
PIN	-	P-type-Intrinsic-N type
PWRR	-	Photonic Wire Microring Resonator
PSD	-	Power Spectral Density
Q	-	Quality Factor
RFO	-	Radio Frequency Oscillator
RI	-	Refractive Index
RF	-	Radio Frequency
SMF	-	Single Mode Fiber
SNR	-	Signal To Noise Ratio
SOI	-	Silicon On Insulator
SW1	-	Switch 1
SiON	-	Silicon Oxynitride
VSAT	-	Very Small Aperture Terminal
VCSEL	-	Vertical Cavity Surface Emitting Laser
WDM	-	Wavelength Division Multiplexing
WGM	-	Whispering Gallery Mode
WGMR	-	Whispering Gallery Mode Resonator

CHAPTER 1

INTRODUCTION TO THE OSCILLATOR

1.1 Introduction to the Oscillator

Optical or photonics communication is known for the high speed, extremely broad bandwidth and secured communication. Developments in the area of light sources and detectors along with low transmission loss in fiber brought a phenomenal growth in the fiber optic domain. Photonics communication is a novel branch of engineering or physics which has fulfilled the dream of very fast internet, data and voice communication. In the evolving global technological advancements and requirements, perceiving the absence of optical communication is now virtually beyond imagination. The optical communication is the field in which photons facilitate the analog or digital communication. Any operating frequency is inherently associated with bandwidth, which is medium dependent and the corresponding wavelength has its own photon. The energy of a photon is described by $E = hf$, where h is Planck's constant and f is frequency. The concept of photon has been used in the optical communication. Einstein (Einstein, 1905) has discussed light in his photoelectric effect theory as discrete wave packets known as 'photons' . The growth of optical communication has occurred over a period of time and could be categorized as per the generation I, II, III, IV and V. In the first generation 0.8 μm Multi Mode Fiber (MMF) has been used. In the second generation 1.3 μm Single Mode Fiber (SMF) was in use (Keiser, 2013). In the third generation 1.5 μm Dispersion Shifted Fiber (DSF) has been widely used.

The coherent technology has been the prime focus of the fourth generation and fifth generation of optical communication. It has lead to the development of Erbium Doped Fiber Amplifier (EDFA), Wavelength Division Multiplexing (WDM), Optical Modulator (OM), Multiplexer and De-multiplexer devices. With the advent of these devices, the applications such as Bio-sensing (He, 2012) and (Sun and Fan, 2011) and optical beam steering (Ohuchi et al., 2007) using optical system have attracted increased emphasis and thrust. The linear optical effects such as attenuation, dispersion and Polarization Mode Dispersion

(PMD) have been the focus of recent study of many researchers. The non-linear effects such as Kerr effect, Four wave mixing and Raman scattering (Keiser, 2013) still pose many challenging issues both at device as well as system level of optical system.

The block diagram of an optical communication system is shown in Figure 1.1 consisting of a transmitter and receiver connected through re-generator and optical amplifier. The need of optical to electrical and electrical to optical conversion is also felt in the present scenario. But the futuristic typical optical communication system is supposed to be based on an all optical components. One such example is the Photonics Field Gate Programmable Array (P-FPGA). The oscillator is the integral part of the optical transmitter and receiver as shown

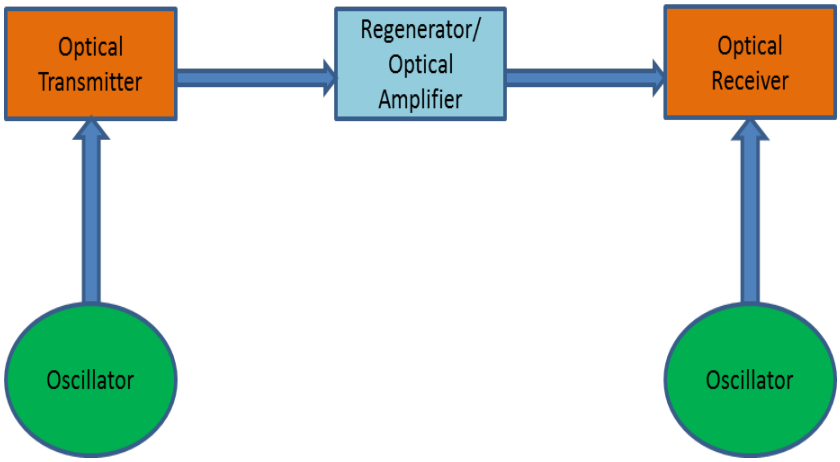

Figure 1.1: Block diagram of an optical communication system

in Figure 1.1. The oscillator which is known for the generation of the sinusoidal frequency is a critical device. The oscillators are used in communication system at various stages or levels. In the modern engineering discipline, oscillators are used for the generation of low to high sinusoidal frequency required for the transmitter and receiver section of the communication system.

Communication industry has seen the usage of large number of electronics oscillators named Hartley oscillator, Colpit oscillator and phase shift oscillator (Millman and Halkias, 1972). Any desired information could be transmitted using the generated sinusoidal and periodic waves of oscillators. Many communication systems have been using the oscillators. A few exemplary examples include radar, signal processing, sensors, metrology and radio astronomy. In an all optical communication applications, very high spectral purity is required and it is dependent on the loss in photonic device of the feedback path. The power dissipation in the optical feedback path decides the Q-factor of the device. Q-factor is a

very significant performance parameter for advanced communications such as radar and data transmission systems.

The Piezoelectric quartz resonators ranging from (10 Hz to 100 MHz), having high Q-factors such as 10^7 at 1 MHz (Jauch, n.d.), is suitable for use in RF systems. But as the frequency increases, the sharpness of resonance response degrades leading to the deterioration of the spectral purity. Therefore the quartz oscillators find its usage in microwave and millimeter-wavelength applications. While using a quartz oscillator in the frequency multiplication process, the noise of the oscillator also gets multiplied. This leads to the degradation of the system performance.

Another significant parameter of measure of the oscillator is the phase noise (Ham, Andress, and Ricketts, 2004) and (McNeill, 1997). The analysis of the phase noise requires fundamental interpretation of the phase and the noise (Edson, 1960). The analysis of the characteristics of the optical wave inside the optical waveguides and optical devices is mandatory. Phase is one of the important parameter to interpret the optical wave. The angular frequency is another parameter and is generally given as Equation (1.1).

$$\omega = 2\pi f \tag{1.1}$$

Where,

f is the center frequency.

Propagation of an optical wave can be represented by Equation (1.2)

$$E = E_0 exp[j(K_0 z + \omega t)] \tag{1.2}$$

Where, E is the electric intensity of the optical wave, E_0 is the maximum electric intensity of the optical wave, K_0 is the wave number, t is the time, and z is the propagation direction of the optical wave. Using the Euler's Formula, and considering the real part of Equation (1.2), the electric field intensity of an optical wave is represented as

$$E = E_0[Cos(K_0 z + \omega t)] \tag{1.3}$$

By considering an additional phase shift of ($\pi/2$ radians or 90^0) in Equation (1.2), its real part can also be written as $E = E_0 Sin(K_0 z + \omega t)$, which can also describe the electric field intensity of an optical wave (Sadiku, 2009).

$$\varphi = K_0 z + \omega t \tag{1.4}$$

The term $K_0 z$ describes the progress of the wave in the z-direction. K_0 is a propagation constant.

The wave number K_0 is given by

$$K_0 = \frac{2\pi}{\lambda} \tag{1.5}$$

The phase change over a distance z is ϕ and is given by

$$\varphi = K_0 z \tag{1.6}$$

Because of the periodic phenomenon in nature (Maleki et al., 2015), oscillators play a fundamental role in state of the art technology. In theoretical physics, oscillators are one of the basics to explore various concepts covering field theory, linear and non-linear dynamics. In modern communication systems, oscillators have been the source for generation of signals. The performance metrics of oscillators such as amplitude, frequency and phase get affected, either by the properties of its internal components or by interaction with the environment, in which the oscillator resides. The study of the oscillator's noise has been the fundamental to understanding of all other phenomena, in which the model of an oscillator has been invoked in optimization of the performance of systems requiring an oscillator.

Instability of the oscillator (Sauvage, 1977) is one of the major challenges for the satisfactory performance of optical communication systems. Phase noise of oscillator limits the Signal-to-Noise Ratio (SNR) in optical communication systems such as microwave relay systems, including satellite and deep-space links.

A random fluctuation in the waveform of an oscillator referred to as noise can be decomposed into amplitude noise and phase noise. In most of the optical communications, the phase noise has been a limiting factor. The phase noise has been proved to be a bottleneck especially at high frequencies. The design and development of oscillator with a stable output and low phase noise has always been a dream for the engineering community. The electronic oscillators such as Wein bridge oscillator are suitable for an operating range of 1 Hz to 1 MHz and phase shift oscillators are suitable for the 1 MHz to 10 MHz. The Colpits and Hartley oscillators (Millman and Halkias, 1972) are suitable for the range of 10 MHz to 100 MHz. Crystal oscillator can generate signals of frequencies up to 1 GHz. But beyond that frequency, the drastic surge in power dissipation of the oscillator degrades the quality factor.

A circuit containing an active device with feedback elements must have the amplitude of feedback signal larger than the corresponding amplitude of the input signal for the sustenance of oscillation. In addition, both the feedback as well as the input signal should

be in-phase also. Quality factor or Q factor of an oscillator is a dimensionless quantity to determine nature of generated oscillations. Equivalently, the quality factor characterises the bandwidth of the oscillator relative to its center frequency (Rubiola, 2008). Higher value of Q indicates a lower rate of energy loss relative to the stored energy of the oscillator implying that the amplitude of oscillations decrease rather slowly. Oscillators with high Q oscillate over a smaller range of frequencies but are more stable.
In optics, Q factor of an optical resonant cavity is given by

$$Q = \frac{2\pi f_0 \varepsilon}{P} \tag{1.7}$$

Where, f_0 is the resonant frequency, P is the dissipated power and ε is the stored power in the cavity. The optical Q is equal to the ratio of the resonant frequency (f_r) to the bandwidth (Δf^{-1}) of the cavity resonance $(f_r \Delta f^{-1})$. It compares the frequency at which a system oscillates to the rate at which it dissipates its energy. The instantaneous frequency of the system varies randomly because of the variation in phase of the signal with respect to time. This leads to the change in the angular frequency of the system. In order to compute the phase noise of the oscillator, the power at $\Delta\omega$ having bandwidth of 1 Hz is calculated, then it is normalized by carrier power denoted as P_c. The carrier power is the power carried by the impulse at ω_0 (Rubiola, 2008).
The relative phase noise P_{noise} at $\Delta\omega$ can be expressed in $dB_c Hz^{-1}$ as Equation (1.8).

$$P_{noise} = 10log\frac{P_{1Hz(\Delta\omega)^{-1}}}{P_c} \tag{1.8}$$

Where, $P_{1Hz(\Delta\omega)^{-1}}$ is the normalized power at the frequency of $\Delta\omega$ having bandwidth of 1 Hz.

1.2 Motivation of the Research

Couple of decades of the last century have witnessed the tremendous growth and technological innovation of unimaginable proportion in a broad domain of communication comprising wireless, cellular satellite and radar technologies. The last decade of the 21st century continued to witness the earlier trend and the bandwidth requirement for the system applications continues show relentless increase with no sign of receding. In the context and perspective of enormity of the bandwidth requirement in system applications, the oscillators with conventional functional principle and architecture are unlikely to be an viable option for the realization of extremely wide bandwidth. Photonics is emerging as

an potential avenue to meet the system requirements of wider bandwidth with low loss and high reliability. But the realization of the all optical oscillator has been a challenging issue. Hence an another intermediate solution known as Opto-Electronic oscillator came into being. Research labs such as (OEwaves, n.d.) is striving to realize a compact opto electronic oscillator at higher frequencies of K_a-band ranges from 26 GHz to 40 GHz. In the recent past there has been a significant and sustained increase in demand of K_a-band usage. Further the 40 GHz is the high end frequency of the K_a-band and is very useful for the satellite communication, beam steering and Bio-sensors application. A source for generation of 40 GHz can also be used for the cancer therapy using beam steering technique.

The emergence of the design and development of the novice oscillator, known as Opto-Electronic Oscillator (OEO) can be attributed to the need and requirement of the generation of sinusoidal signal at extremely high frequency such as 40 GHz with high spectral purity. This novice device has been extensively explored in recent time and various novel architectures have been reported in the literature (Chembo et al., 2009), (OEwaves, n.d.), (P. S. Devgan, Urick, and Williams, 2012) and (P. Devgan, 2013). The spectral purity of signal generated by an oscillator is usually determined by the phase noise. The phase noise arises due to internal characteristics of the various components of the OEO. To overcome the draw back of an electronic and quartz oscillator, an Integrated Opto Electronic Oscillator (IOEO) has been proposed by Jet Propulsion Laboratory (Yao and Maleki, 1996b) that is based on the use of optical waveguides and resonators. In a conventional OEO, emitted light with laser as a source is modulated before being fed to the long optical Single Mode Fiber (SMF). The output of the SMF is an input to the photo diode. With the help of Low Noise Amplifier (LNA), the output of the photo diode is amplified and the amplified output is filtered through an electrical filter. The phase of the filtered out is tuned to satisfy Barkheusen criterion before it serves as a positive feedback signal to the optical modulator. The gain of the feedback loop helps to attain selfsustained oscillation when the gain of the oscillator higher than 1.

In spite of recent development of the OEO, still the realization of K_a-band particularly IOEO at 40 GHz is in the preliminary phase. The motivation to have miniaturized, stable and high performance oscillators is mainly driven by the recent advances in communication industries. In addition to that very high quality factor oscillators can be realized by using optical components. Hence the study of utility of optical components in the design of IOEO opens a new avenue for research.

1.3 Research Questions

Photonics device, such as IOEO, has been studied with respect to design and analysis, but none of the literature have studied IOEO having all optical feedback. In this thesis an integrated optical feedback ring resonator based IOEO as shown in Figure 1.2 has been analyzed and a bound on the resonant wavelength and Free Spectral Range (FSR), phase noise and quality factor is found.

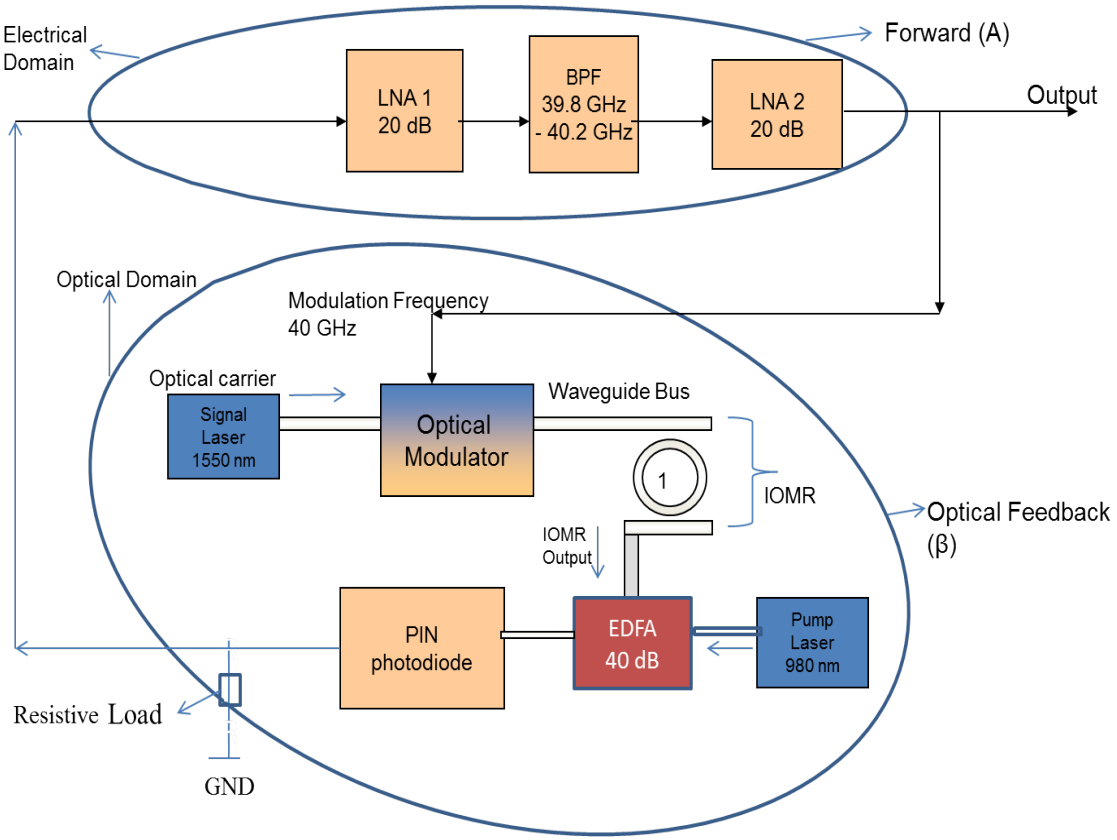

Figure 1.2: Schematic of IOEO with single IOMR

IOEO provides better phase noise, quality factor and stability of IOEO compared to their RF counterparts, but the cost makes them economically less attractive. However use of an optical feedback micro ring resonator instead of an optical fiber delay line, improves the performance.

The integration of an optical feedback micro ring resonator with OEO creates issues related to phase noise, quality factor and stability thereby offering immense potential for further studies. Also optical feedback influences the performance metrics like phase noise, quality factor and stability of the optical feedback micro-ring resonator based IOEO. In IOEO, an Integrated Optical Micro-Ring Resonator (IOMR) is one of the components and feedback provided by IOMR is significant. IOMR is the critical component which carries the optical data and thereafter it is converted into the electrical signal. The quality factor and the phase noise of the IOEO are significantly affected by the inclusion of optical feedback based micro-ring resonator in the IOEO. An IOMR consists of a ring waveguide coupled to two bus waveguides. Strip waveguide based IOMR is a compact device occupying few μm^2 footprint. The micro ring resonator is in miniaturized form and consumes insignificant power. The study of the feedback system provided by IOMR is very crucial. Study of effects of optical feedback based micro-ring resonator to improve the quality factor and phase noise of IOEO is worth considering.

The IOEO gets affected due to multiple noise sources along with non-white noise such as flicker noise. However, fluctuations associated with these noise sources may induce interesting stochastic features and that need immediate attention in future work. Better spectral and statistical fitting of the noise is an essential requirement for the determination of phase noise spectra. Hence the need to explore the various phase noise reductions method arises. The reduction of the phase noise through novel IOEO architecture is one of the potential area of research.

Coupled-mode equations are the result of a trial solution which consists of superposition of (uncoupled) modes and the variational expression. For the chosen uncoupled modes, the propagation constants and coupling coefficients are determined uniquely using developed coupled mode equations. Coupled optical waveguides could further be studied referring variational expression for the coupled mode equations. Researchers have discussed about the single optical micro-ring resonator and arrays. Micro-ring resonator is used in the development of basic integrated optical devices. The developed optical device could be used for various applications such as optical communications, optical signal processing and Bio-sensors.

An extensive survey of current literature on IOMR and their applications shows its academic and industrial status. A comparison of different types of optical filters, highlighting the advantages of ring resonator based filter is dealt in the literature (Okamoto, 2010). A detailed analysis of ring resonator properties has been carried out (Okamoto, 2010), such as Field Enhancement (FE), Free Spectral Range (FSR), Full Width Half Maximum (FWHM), Finesse and Quality factor (Q). The development of novel micro ring resonator structures having improved Free Spectral Range (FSR), Full Width Half Maximum (FWHM) and Quality factor (Q) is required for the development of application such as IOEO. The IOMR can also be used for filtering and multiplexing applications. Apart from structural development of IOMR, thorough studies on the straight-curve waveguide coupler and curve-curve waveguide coupler are required to be addressed for future advancement of the IOEO technology.

In the design of IOEO using IOMR, effect of ring curvature and non-linearity of cladding should be considered. The change of ring curvature leads to change in the propagation length, which in turn changes FSR, FWHM, Finesse and Quality factor of the IOMR (Okamoto, 2010) and (Maleki et al., 2015). Hence, optimization of the IOMR needs to be carried out based on the application such as IOEO, optical beam steering and optical Bio-sensor. The effects of non-linearity of the straight bus waveguide and ring waveguide of the IOMR also need to be analysed. Optimization of the non-linear parameters should be carried out to significantly enhance coupling between the straight bus waveguide and ring waveguide of the IOMR.

Following are the summary of the potential research questions in the field of OEO:

- Is it possible to realize IOEO having all optical components in the feedback path?
- How do the performance metrics such as phase noise, quality factor and stability of the IOEO get affected while integrating all optical feedback micro-ring resonator in the feedback path of IOEO?
- Whether the all optical feedback based IOEO exhibits improved quality factor and phase noise?
- Is it possible to develop an analytical formulation to determine the phase noise of IOEO and the contribution of IOMR to the phase noise in the IOEO?

- Is it possible to arrive at an architecture of IOEO that can reduce the phase noise in the IOEO? Does it require single loop architecture, dual loop architecture or multiple-loop architecture?
- Is it possible to suggest a simplistic mathematical model of the CMT of the integrated micro-ring resonator?
- Is it possible to explore various mathematical models for the IOMR using two port network theory and analyse the effect of these models on the FSR, FWHM and the quality factor of the IOEO?
- Can the potential advantages of the proposed all optical feedback based IOEO be demonstrated for commercial applications such as Bio-sensors and Beam steering?

1.4 Objectives of the Research

To answer the entire research questions stated above, following objectives have been framed and research has been carried out on these objectives.

- To carry out the literature review on micro-ring resonator, optical micro-ring resonator, oscillator and IOEO.
- To analyse the effects of optical feedback based micro-ring resonator on the quality factor of Opto-Electronic Oscillator by avoiding the problem of less energy storage time
- To investigate the effects of optical feedback based micro-ring resonator on the phase noise of Integrated Opto-Electronic oscillator
- To analyse the effect of phase noise on a simulated IOEO and emphasize on the noise reduction methods to achieve a better spectral and statistical fitting of the phase noise
- To arrive at an improved architecture of IOEO using all optical feedback based micro-ring resonator

Hence an integrated optical feedback based OEO can be investigated. This could possibly provide better performance as compared to existing oscillators. In this thesis an integrated optical feedback ring resonator based IOEO has been proposed and a bound on the resonant

wavelength and Free Spectral Range (FSR), phase noise and quality factor is analysed. This thesis also investigates the influence of size of the bend radius on the FSR, the measurement range and trade off between the range and sensitivity. Therefore the proposed research title **Study on Effects of Optical Feedback Based Micro-Ring Resonator on the Integrated Opto-Electronic Oscillator** is justified.

1.5 Organization and Outline of the Thesis

A brief discussion regarding the organization of the chapters of the thesis is as follows. This thesis has been organized into seven chapters. A succinct description and summary of each chapter have also been provided:

Chapter 1- Introduction to the Oscillator

This chapter is an introduction to the scope, theme and emphasis of the research objectives and the organization of the proposed thesis. Optical communication has witnessed tremendous growth in recent times. The high bandwidth and speed requirement have been the reasons for such phenomenal development. The backbone of the speed of the all optical networks is the signal source. The oscillators are known to produce stable and spectral pure signal for the required processing. In this chapter optical communication and their components are reviewed. The evolution and need of the oscillators along with the fundamental parameters of the oscillator are also emphasized.

Chapter 2 -A Review of the Principles of Opto-Electronic Oscillator and its Components

Literature review is a continual process with no uniquely defined process of begin and end. But it is very much required for the authentication of the research work carried out. The formulation and progress of a research work depends on the appropriate level of literature review. In this chapter, a discussion on realization of Opto-Electronic oscillator using optical micro ring resonator has been carried out. Two significant parameters of an Opto-Electronic oscillator namely the phase noise and quality factor have also been explored and discussed. Various models of the IOMR have also been addressed. The CMT for the IOMR has also been reviewed. This chapter presents the application of two port network concept for the analysis of stability of IOEO. Thermal stability and the utility of IOEO in applications such as optical beam steering and Bio-sensor have also been reviewed in this chapter.

Chapter 3 - The Design of an Integrated Opto-Electronic Oscillator (IOEO)

In this chapter, a novel Linear Time Invariant (LTI) architecture of IOEO has been proposed and analysed. The proposed architecture for IOEO reduces the size of the oscillator and thereby facilitating its integration on a single chip. The effect of compactness on the quality factor, thermal stability factor and phase noise of the proposed IOEO has also been discussed in this chapter. Technical description of all the sub components of the functional block of IOEO has been presented with requisite and pertinent details. The chapter also highlights the fundamental principle of the proposed architecture of IOEO. The analytical formulation of the proposed IOEO is also presented.

Chapter 4- The Analysis of an Integrated Optical Micro-Ring Resonator (IOMR)

This chapter presents the analysis of Optical Micro-ring Resonator. The effective refractive index and their corresponding strip waveguide dimension and mode profile have been discussed in detail. The coupling coefficient, coupling length and their dependence on the power transmission at the output port of optical ring resonator have been studied. Fabrication tolerance of the designed optical ring resonator has also been analysed. CMT for two straight optical waveguides has been analysed. The analysis of straight and curved optical waveguides by considering the Butt-coupling coefficient has been carried out. An analytical approach for the analysis of the IOMR has been suggested. Finally the effect of the Butt-coupling coefficient on the phase noise of the designed IOMR is also analysed.

Chapter 5 - The Analysis of an Integrated Opto-Electronic Oscillator

In this chapter, an analytical formulation to analyse the performance metrics of IOEO such as phase noise, thermal stability and stability with variation in design input parameters such as refractive index and offset frequency has been presented. The relative advantage of array of IOMR over single IOMR pertaining to the output power of IOEO has also been discussed in this chapter. The contribution of IOMR to the phase noise of IOEO has been addressed. The ABCD parameters have been explored to compute the contribution of the IOMR to the phase noise of the designed IOEO. Two port network theory for IOMR has been presented invoking ABCD parameters. Pollock and Okomoto models for SOI based IOMR have been used in the two port modeling of IOMR. Thermal as well as frequency stability analysis of the designed IOEO have been carried out in this chapter. The utility of two port network theory in the computation of ABCD parameters of the constituent subsystems of IOEO has been presented. The effect of Butt-coupling coefficient on the ABCD parameters of IOMR has also been discussed in this chapter.

Chapter 6 - The IOEO based Beam steering and Bio-sensor

This chapter discusses the analysis of the application of developed 40 GHz IOEO

in optical beam steering application. An architecture for the transmit beam steering has been discussed. Utility of the designed IOEO in the generation of the steered beam has been discussed. Analysis on the development of the optical sensor based on the proposed architecture of the 40 GHz IOEO has also been presented. The significance of the optical micro ring resonator as a sensing element has been emphasized in this chapter.

Chapter 7 - Conclusions and Future Recommendation

A chapter on conclusions is a succinct form of reflection on the achievement, accomplishment, significance and suggestion of the thesis. In this chapter all the quantitative as well as qualitative outcome of the analysis and studies carried out as a part of this thesis have been discussed with adequate details and reasonable rationale.

1.6 Summary

Oscillators have been used in the optical communication systems extensively. In evolving modern communication system, performance metrics such as speed, spectral purity, life cycle of the system and stability are significant. Hence there is need and requirement of the IOEO, that have all the above stated desirable features. These requirements demand further research work in the analysis of the quality factor, frequency stability and phase noise of the oscillator. The feasibility analysis requirement motivates the fabrication tolerance analysis. Efficient dissemination of knowledge warrants and demands effective organization and structured presentation of the research details. Therefore a detailed outline of the thesis has been discussed in this chapter. In the next chapter, literature related to the design and development of IOEO has been discussed.

CHAPTER 2

A REVIEW OF THE PRINCIPLES OF OPTO-ELECTRONIC OSCILLATOR AND ITS COMPONENTS

2.1 Introduction

In this chapter, literature review has been carried out on the design and development of IOEO. The study of OEO is extended by exploring the utility of optical micro-ring resonator in the realization of OEO. The phase noise and quality factor of the OEO have also been explored and discussed. Various models of the IOMR have also been discussed. The CMT for the IOMR has also been reviewed from the Integrated OEO design point of view. The discussion on two port network and the stability of the IOEO using two port network theory are also presented. Thermal stability of the IOEO is also studied and discussed in this chapter. Applications such as optical beam steering and Bio-sensor using IOEO have also been reviewed. The discussion and interpretation of the literature have been carried out to justify the need of the research work. The tasks of linking the research focus of this thesis with the existing literature have been carried out and are discussed at length.

2.2 Integrated Opto-Electronic Oscillator

The IOEO is the emerging topic in the ever evolving research domain of oscillators (Yao and Maleki, 1995), (Yao, 1997), (Yao, et al., 1998) and (Yao and Maleki, 2000). It is featured with a capability to generate a signal of very high frequency with high spectral purity. The IOEO consists of various building blocks such as Laser, Optical Modulator (OM), Micro-Ring Resonator, Erbium Doped Fiber Amplifier (EDFA), P-type-Intrinsic-N-type (PIN) Photo Diode (PD), Low Noise Amplifier (LNA), and Band Pass Filter (BPF). The IOEO has been known for the generation of high frequency signal with more stability, high quality factor and low phase noise. Noise plays significant role in the performance of any device. The IOEO which is an optical device has many active components such

as an Amplifier, Optical Modulator, EDFA and PIN PD. Therefore the non-linearity of these devices should be studied to achieve better functional performance of the IOEO. In this chapter the existing architecture of IOEO has been reviewed for a detailed analysis. Various performance parameters such as finesse, field or power output, coupling co-efficient, transmission co-efficient, quality factor and phase noise have been analysed. Figure (2.1) represents a schematic block diagram of an existing OEO (Chembo et al., 2009). The OEO comprises of the following components: laser source (optical carrier), Optical Modulator (OM), Optical Fiber (OF), Photo Diode (PD), Low noise amplifier (LNA) and Band Pass Filter (BPF). The IOEO (Chembo et al., 2009), shown in Figure 2.1 has been analysed

Figure 2.1: Block diagram of an Opto-Electronic oscillator (Chembo et al., 2009)

for the design and development of the OEO. The IOEO (D. Gunn et al., 2007) shown in the Figure 2.2 is the outcome of such an analysis. The IOEO of Figure 2.2 comprises the following components: Laser Source (Optical Carrier), Optical Modulator, Optical ring resonator, Photo diode, Low noise amplifier and Filter. In the IOEO design proposed by D. Gunn, long optical fiber has been replaced by an optical ring which is basically a wavelength filter (D. Gunn et al., 2007). Even though the optical ring resonator is an established concept presently, still the realization of the optical ring resonator poses many challenges especially at the micro dimension. At the same time lack of theoretical exploration of the CMT of the optical ring resonator has also been observed in the literature.

The IOEO (D. Gunn et al., 2007) which uses micro resonator in the optical section has already been proposed as shown in Figure 2.2. In the last decade, IOEO has been shown

Figure 2.2: Block diagram of an Integrated OEO (D. Gunn et al., 2007)

to have applications in both the RF and digital system. Its utility is expected to continue in future also. The IOEO shown in Figure 2.2 having a single loop comprising of laser (light input source), OM, an IOMR, Photo Diode (PD), Low noise amplifier (LNA), RF filter and RF splitter. The output of the RF filter is fed to the optical modulator through RF splitter. The laser output gets modulated with RF filter output. The modulated output is fed to the IOMR, which is frequency selective device and resonates at a particular frequency. The output of the IOMR is fed to the photodiode where the optical signal gets converted to the electrical signal (D. Gunn et al., 2007). The electrical signal controls the functionality of the optical modulator to provide the oscillation. The IOEO is widely known for its high performance in phase noise and quality factor. The initial design of IOEO has been improved over a period of time to satisfy the requirements of the upcoming applications. The IOEO has been explored from many aspects such as phase noise, quality factor, frequency stability and thermal stability. Comparative assessment of the advantages and disadvantages of various components such as electrical band pass filter, electrical amplifier, optical modulator, photo diode, with or without EDFA and IOMR have been potential topic of research interest.

2.2.0.1 IOEO Design with Electrical Filters

Unwanted side modes of the electrical band pass filter has been the limitation of the design of an IOEO and its removal has been a challenge. Because of the closeness of the side modes of the IOEO, the electrical band pass filter is not able to suppress it. The phase noise produced at the output of the band pass filter is one of the challenging issues in the IOEO. The propagation of non-oscillating side modes through the band pass filter contributes to the phase noise. Also the tunable band pass filter at the operating frequency of IOEO is not easily available and as consequence, it is not possible to generate wide range of radio frequency using IOEO. Investigation on the oscillator to generate signal without an electrical band pass filter stage has been reported. The Stimulated Brillouin Scattering (SBS) process to generate 10 GHz signal without band pass filter has been reported (Yao, 1997).

The IOEO, without electrical band pass filter (Ozdur et al., 2010) has been reported in the literature. Use of optical filter such as Fabry-Perot filter has been discussed. The use of photonic microwave filter (X. Liu et al., 2012) in the design of IOEO is also discussed. The tunable OEO has also been studied (Yang et al., 2012), and the underlying concept to generate range of frequencies has been reported. The injection locking of a Fabry-Perot Laser Diode (FP-LD) has been reported (Pan and Yao, 2010) and it can generate specified frequency without electrical band pass filter. The FP-LD architecture strengthens the gain of any one mode, while the other modes are suppressed. This scheme provides tunable IOEO over a frequency range covering 6 to 10 GHz (Pan and Yao, 2010). Temperature is one of the crucial parameters to achieve the tunability of the FP-LD.

2.2.0.2 IOEO Design with Optical Modulator

Another significant building block of an IOEO is the optical modulator. There are various types of optical modulators such as intensity modulator, phase modulator and polarization modulator (Sakamoto, Kawanishi, and Izutsu, 2006). Frequency of the IOEO determines the pulse rate whereas jitter of the optical pulses maps to the phase noise of the RF signal. A low phase noise (-140 $dBcHz^{-1}$ at an offset frequency of 10 kHz) has been reported (Yu, Salik, and Maleki, 2005). The non-linear response of the IOEO due to the intensity modulator such as Electro-Absorption Modulator (EAM) has been reported (Lasri et al., 2003). But the generation of the optical pulses and the electrical sinusoidal signals from the same cavity have discussed (Lasri et al., 2003) in the literature. The optical pulse does

not require any separate cavity. The phase noise of EAM based IOEO has been found to be the same as that of IOEO based on intensity modulation (Yu, Salik, and Maleki, 2005). But, the generated pulse width gets restricted due to the non-linear response of EAM.
Multi-loop EAM based IOEO (P. Devgan, et al., 2003), capable of suppressing the non-oscillating modes has also been reported. The simultaneous multiple generation of sinusoidal frequencies has become possible due to EAM based IOEO. However the generation of multiple optical pulses from IOEO requires multiple laser sources at the specified wavelengths. At the same time the restriction on the width of the pulse due to non-linear response of the EAM makes it unusable for the applications, where size is a priority.
In the IOEO design, Mach-Zenhder Intensity Modulator (MZIM) or an EAM has been used, especially for the intensity modulation. Apart from MZIM and EAM, phase modulator has also been popular modulator. In a phase modulation, the phase of the optical carrier gets modified rather than its amplitude. Unlike MZIM intensity modulator, the advantage of Phase Modulation (PM) is that, it does not require a DC bias control. But photo diode does not respond to phase changes in the optical carrier and hence the phase modulation must be converted to intensity modulation before photo detection. The Asymmetric Mach-Zehnder Interferometer (AMZI) can be used to convert the phase modulated signal to an intensity modulated signal. Inclusion of AMZI and phase modulator together compounds the non-linearity issues and size of the IOEO.
Polarization modulator is an another modulator used in the design of an IOEO. The role of the polarization modulator lies in modifying polarization state of the optical carrier. Polarization modulator can be used in the generation of high frequency, higher than 40 GHz with insertion loss smaller than a traditional MZM. A generation of 20 GHz signal (Pan and Yao, 2009) through a polarisation based IOEO with a single optical cavity has been reported.

2.2.0.3 IOEO Design with RF Amplifiers

RF amplifiers have been extensively used for the generation of low phase noise sinusoidal frequency. Presently, the loss in the optical fiber is very low. The optical modulator converts electrical signal to optical one whereas the reverse holds for photo diode. Both these conversions lead to the losses in the IOEO. The optical modulator modulates optical carrier with electrical signal, whereas the photo diode converts optical signal into electrical

signal. Both these conversions lead to the losses in the IOEO output. To compensate such losses without introducing external noise, the RF amplifiers especially Low Noise Amplifiers (LNAs) have been used. But, it adds an additional phase noise to the IOEO. Extensive research has been carried to reduce the phase noise of the LNA used in IOEOs. The wideband operation of an IOEO, gets limited due to disadvantages of LNA. But the wide band operation is achievable by using photonic gain. RF gain of all-photonic IOEO is determined by both the power handing capacity of photo diode and the efficiency of MZIM. The half wave voltage of MZIM defines its efficiency. These parameters are set, when the individual device is manufactured and cannot be altered by the user. The highest all-photonic RF gain occurs, when the DC bias of the MZIM is set to quadrature (P. S. Devgan, et al., 2007).

The second harmonic of the RF signal generated in the photonic gain based IOEO, can be eliminated using the electrical band pass filter. When compared to a RF amplifier based IOEO, an all-photonic IOEO with an electrical bandpass filter shows a reduction in phase noise. The phase noise spectrum of the IOEO with photonic gain shows that, the noise is no longer dominated by the flicker phase noise in the range of offset frequency covering 100 Hz to 1 kHz. The overall phase noise spectrum of the all-photonic IOEO, has been found to be lower than that of the electronic RF amplifier based IOEO.

Devices with higher frequency bandwidth such as polymer based modulator (Chang et al., 2002) and an EAM have been used in the generation of 39 GHz and 40 GHz (Shin et al., 2006) sinusiodal frequency. In such IOEOs, components such as optical modulator, band pass filter, photo diode, and LNA operate in the 40 GHz band. The phase noise of EAM based IOEO operating at 40 GHz is -100 $dBcHz^{-1}$ at an offset frequency of 10 kHz, when compared to a phase noise -70 $dBcHz^{-1}$ of conventional IOEO. However, it is pertinent to state that EAM based IOEO requires an additional laser source as well as zero dispersion fiber. But, the 40 GHz EAM based IOEO, utilizes two lasers and the relevant zero dispersion fiber in the dual loop cavity. The zero dispersion fiber is mandatory for the IOEO to oscillate. Other example of IOEO for the generation of sinusoidal frequency up to 52.8 GHz is also reported (Sakamoto, Kawanishi, and Izutsu, 2007) in the literature. Apart from the higher frequency components, these architectures also use mode locked laser (Van et al., 2008) for the generation of high frequency such as 52.8 GHz.

2.2.0.4 IOEO Design with Frequency Multiplication and Other Techniques

Frequency multiplication technique, has also been used to generate sinusoidal signals (Shin and Kumar, 2007a) and (Shin and Kumar, 2007b) using the IOEO. In frequency multiplication technique, the operating frequencies for the master and slave IOEOs are different. The slave IOEO with 10 GHz and master IOEO at 40 GHz have been reported (Zhou and Blasche, 2005) in the literature. A stable 40 GHz signal has been realized when the output of the master IOEO is fed to the slave IOEO. But this, frequency multiplication technique again increases the bulkiness of the IOEO.

The OEO has been demonstrated in 1996, by the researchers of the NASA Jet Propulsion Laboratory (Yao and Maleki, 1996b) and (Yao and Maleki, 1996a). Recently, IOEO having optical fiber has been reported for the telecommunication systems (Chembo et al., 2009). The phase noise of -163 $dBcHz^{-1}$ at an offset frequency of 10 kHz from a 10 GHz carrier has been reported. In the telecommunication system, frequency is adjusted for the chosen application with the appropriate settings of band pass filter. But optical fibers are bulky because of their extremely long length (several km) and are associated with the difficulties with temperature control. However, with a 4 km optical fiber delay line in IOEO, a 10 GHz oscillator prototype exhibiting phase noise lower than -140 $dBcHz^{-1}$ at an offset frequency of 10 kHz is reported (Chembo et al., 2009). Recently a major breakthrough in the design of IOEO (OEwaves, n.d.) has been reported. In this IOEO, optical fiber delay line has been replaced by a Whispering Gallery Mode (WGM) optical mini-resonator. Optical signal can propagate by total internal reflection by WGM inside the crystal resonator. Therefore achieving equivalent delay line by replacing the long fiber with an optical mini-disk resonators of diameters of a few mm has become a reality.

A wideband tunable OEO (Xie et al., 2013) based on a phase modulator and a tunable optical filter has been proposed and simulated. The fiber has been used as the delay line for the generation of the RF microwave signal (Chembo et al., 2009). It claims to have the desired low phase noise of -163 $dBcHz^{-1}$ at an offset frequency of 10 kHz for the 10 GHz optical carrier. The Leesons model has been used for the phase noise analysis of the oscillators (Sauvage, 1977). Various ultra low phase noise (Salik, Yu, and Maleki, 2007) and low cost of the OEO has been reported (Binh, 2008) and (Lee, Kim, and Choi, 2008) in the literature. The conversion of the light (Yao and Maleki, 1996a) into the spectral pure microwave has been achieved. Various OEO and ultra-low phase noise dual loop OEO with single and dual loop have been developed. In the OEO, the laser is the primary source

of optical carrier. Currently tunable lasers are available for the use. The stabilisation of the laser source is required for the stability of an Opto-Electronic oscillator (Merrer, Llopis, and Cibiel, 2008).
Recently a tunable OEO (Lu et al., 2015) ranging from 32 GHz to 41 GHz has been reported. The OEO has single sideband phase noise below -97 $dBcHz^{-1}$ at an offset frequency of 10 kHz. Using the self-injection locking, a Duel-Mode Amplifier Feedback Laser (DM-AFL) acting as a tunable Microwave Photonic Filter (MPF) has been realized. The presented review of literature justifies the need and requirement of the design of a miniaturized IOEO with minimum phase noise and high quality factor.

2.2.0.5 Proposed IOEO

In the next chapter, an IOEO design has been proposed having all the electrical components in the active path and all optical components in the feedback path. The proposed IOEO has been designed as Linear Time Invariant (LTI) system. The IOEO has been designed for the generation of 40 GHz sinusoidal frequency, having many advantages such as minimum phase noise, high quality factor and miniaturized size. The analysis of the effect of the CMT on the performance of the IOEO has also been carried out. The designed IOEO has been found to be suitable for the application such as an optical RF phase shifter for transmit beam steering and Bio-sensor applications.

2.2.1 Phase Noise of Oscillators

Phase noise determines the frequency fluctuation of an oscillator. In an IOEO, Single Side Band Power Spectral Density (PSD) is a measure of its phase noise. The phase noise is generally specified at a frequency which is offset from the carrier. The PSD is normalized to the power of the RF signal and has units of $dBcHz^{-1}$. Often, the phase noise is quoted as a single value measured at a frequency offset from the carrier.
The IOEO is dominated by various sources of noise at different frequencies of offsets. In the offset frequencies covering the range 1 Hz to 10 Hz, environmental fluctuations contribute significantly to the phase noise. The variation in the ambient temperature and vibrations induced by the acoustic sources lead to environmental fluctuations. In the frequency offset covering 10 Hz to 1 kHz, phase noise is attributed to the flicker noise. White phase noise is a major contributor to the offset frequency range spanning 1 kHz to 30 kHz. The phase noise has a flat noise response from 30 kHz and higher frequency offsets.

The higher non-oscillating side modes of the IOEO are attributed to the offset frequencies of 30 kHz and higher. Timing jitter is mostly used to determine the quality of the clock signal in the applications where timing of digital signals is involved. From the measured phase noise spectrum, the total noise can be derived.

The phase noise has been one of the major performance factors for the evaluation of an oscillator using Opto-Electronic techniques (Romisch et al., 2000). The outcome of the experiments (Ji, Yao, and Maleki, 1999) is the authentication of the ultra noise performance of the Compact-Opto Electronic Oscillator (C-OEO). The compact Opto-Electronic oscillator (C-OEO) is a millimeter wave oscillator (OEwaves, n.d.) at 10 GHz having phase noise of -140 $dBcHz^{-1}$ at 10 kHz offset from the carrier. The model exhibits thermal stability of $\pm$1ppm. The size of the device is 4.5 inch x 5.9 inch x 0.94 inch. Design of the C-OEO can be scaled to higher frequencies with same phase noise performance. The C-OEO supports low phase noise, low spurious content, compact size, frequency scalability, Electro Magnetic Interference (EMI) tolerant and high stability. A 39 GHz OEO (Chang et al., 2002) has been reported. The broadband polymer based electro-optical modulator has been used in the generation of 39 GHz frequency. At the same time other optical modulator such as electro-absorption modulator has also been used for the generation of the 40 GHz optical pulse (Chou, Chiu,and Bowers, 2002). Various Erbium doped fiber amplifier based IOEOs (E. Salik et al., 2004) have been explored and the architecture for IOEO have been reported.

Optical networks (Fukuchi, 2001) require low phase noise signals. OEO having very low phase noise have been reported using Poseidon oscillator (Jiang et al., 2002). Poseidon oscillators are microwave oscillator (Rubiola, 2008) which differ from quartz oscillators in that the f^{-1} frequency noise is governed by the amplifier's f^{-1} phase noise through the Leeson effect. The volume of energy confinement is significantly larger in microwave resonators than in quartz resonators. The Poseidon DRO-10.4-FR and Poseidon Shoebox are the examples of such oscillator. The Poseidon DRO-10.4-FR is based on a dielectric resonator, whereas the Poseidon Shoebox makes use of a sapphire whispering-gallery (WG) resonator and a bridge noise-degeneration amplifier. Operating frequency range only around 10 GHz as well as the cost are the major limitations of Poseidon oscillators. However, the possibility of designing the OEO (Yao, Davis, and Maleki, 2000) with reduced cost, tunable frequency and similar phase noise performance is reported. An IOEO which can provide low phase noise at 34.6 GHz RF signals without the need for an electrical RF filter is also reported (Savchenkov et al., 2010) in the literature.

The analysis of various architectures of the OEO system and their phase noise can be found extensively in the literature. Leeson (Leeson, 1966) presented the simple model for noise spectrum of feedback oscillator. The Leeson model for phase noise is described by the Equation (2.1)

$$S_\phi(\omega_m) = S_{\Delta\theta}[1 + (\frac{\omega_0}{2Q\omega_m})^2] \tag{2.1}$$

Where, $S_\phi(\omega_m)$ is the power spectral density at the output of oscillator, $S_{\Delta\theta}$ is the power spectral density at the input of the oscillator, ω_0 is the carrier frequency, Q is the quality factor of the oscillator and ω_m is the offset frequency. The Leeson model discusses the additive noise (thermal and shot noise) and the parametric noise such as f^{-1} of the device. The Leesons model is the most significant contribution, which presents the mathematical analysis of the phase poise in any oscillator (Sauvage, 1977). Further research on IOEO has been extended to the application such as microwave signal generation. The phase noise spectra in an opto electronic microwave oscillators (Chembo et al., 2009) has been successfully determined. The OEO has been demonstrated with the optical fiber as the delay line. The frequency generation upto the 10 GHz has been shown successfully. The lowest phase noise reported is -163 dB_cHz^{-1} at an offset frequency of 10 kHz.

The generation of signal waveform of 10 GHz (Chembo et al., 2009) is reported to be useful in light wave telecommunications and radar applications. The main advantage of reported OEO is its low phase noise (-160 $dBradHz^{-1}$ at 10 kHz offset). Even though some preliminary investigations on the phase noise in IOEOs have been reported, but still it is not fully resolved. The rigorous theoretical analysis is required for further improvements of phase noise of the IOEOs. Because of lack of time domain model, stochastic analysis cannot be used to perform the phase noise study of IOEO. Since IOEO is a delay line oscillator, a few analysis has been reported which explains the effect of phase noise on time-delay induced limit-cycles (Chembo et al., 2009).

Presently optical signal processing has found to be significantly useful in telecommunication applications (Dorren et al., 2005). An OEO is one of the components which is used to generate the required microwave signal (Lasri et al., 2003). Phase noise analysis is the most significant requirement of the OEO. Various phase noise reduction methods (Chenakin, 2009) have been reported that are applicable to microwave as well as to IOEO. The basic mathematical models provided by the Leeson's model are widely studied. The phase noise and jitter with color noise sources (Demir, 2002) has emphasized in the literature. The phase noise contributions of the Distributed Feedback Laser (DFB) to the

OEO (Volyanskiy et al., 2010) have also been explored and reported.
The literature justifies the need of an IOEO with minimum phase noise and high quality factor. The design of compact-IOEO with minimum phase noise and high quality factor has not been addressed in the literature. The contribution of the IOMR in the phase noise of the IOEO has also not been addressed. Hence in the proposed thesis, a novel IOEO with all optical components in the feedback path has been designed. The phase noise of the IOEO has been computed using variance method. The contribution of the IOMR in the phase noise of the IOEO is also analysed.

2.2.2 Quality Factor of an IOEO

Quality factor is the measure of the rate of power dissipation of an oscillator. The higher the quality factor, the slower is the dissipation rate of the oscillator. The quality factor in the phase shifter, crystal oscillators and Opto-Electronic oscillators has been an important design issues. Generally to realize the highest quality factor (Q) for the IOEO, the maximization of the SMF in the existing design has been attempted. But due to the long SMF, decrease in spacing between the cavity modes occurs. This in turn leads to difficulty in suppressing the side modes (Lasri et al., 2003). Many IOEO architectures have been proposed and demonstrated using multi-loop IOEO to suppress the side modes (Banky, Horvath, and Berceli, 2006). The shortcomings of the multi-loop OEO, a dual cavity OEO (Zhou and Blasche, 2005) and (Zhou et al., 2008) have been addressed.
A passive micro-ring resonator coupled semiconductor laser structure (B. Liu, Shakouri, and Bowers, 2001) is proposed in the literature. The high quality factor micro-ring resonator with strong mode selection filter has been discussed. The improvement in the side-mode suppression ratio, the line width and the frequency chirp have been reported as compared to distributed feedback and distributed Bragg reflector lasers.
In this thesis, an architecture for the IOEO has been designed with a quality factor of 1000 under loaded condition. The designed IOEO has IOMR, which generally exhibits very high quality factor. But the generation of the 40 GHz with very high quality factor appears to have not been addressed in the open literature.

2.3 Integrated Optical Micro-Ring Resonator

In this section, utility of IOMR in recent times has been discussed. Many applications such as satellites or computer chips require miniaturised IOEO. One such attempt, where the

study of the noise properties of an IOEO with fiber ring resonators (Saleh et al., 2012) is reported in the literature. The size of the IOEO can be minimized using a smaller delay line such as IOMR. The size can be further minimised by using electrical RF filter. An atomic vapor cell (Kitching, Knappe, and Hollberg, 2002) has been reported to be used as one of the components of IOEO (Strekalov et al., 2003). This atomic vapor cell is responsible for the selection of the required operating frequency. Another example is using WGM resonator (A. Matsko et al., 2003). In this IOEO, WGM resonator replaces fiber delay line and electrical band pass filter. The usage of WGM resonator allows its integration with other components of the IOEO. The usage of the WGM resonator also ensures not only the high quality factor but also the reduction in the overall size of the IOEO. These types of OEOs have possible utility in applications where both the size and the precise clock are critical parameters to synchronize the Global Positioning System (GPS) signals. One such example is in satellite communications.

An OEO has been reported having optical resonator filter operating at selected modulation sideband (Maleki et al., 2015). Recently generation of a microwave signal with a frequency-tuning from 2.4 to 10.765 GHz (Li, Chen, and Zhang, 2015) is reported in the literature. A tunable OEO, through adjusting the wavelength of the pump laser is realized and the investigation on single-side band phase noise of the generated microwave is also discussed.

2.3.1 Models of an Integrated Optical Micro-Ring Resonator

The IOMR has been studied extensively in the literature. The device has been proved to be useful in many applications such as Mux, Demux and Filter. Most of the researchers (Okamoto, 2010) have explored the IOMR through its transfer function. The transfer function basically relates the input and output power of the IOMR and the transfer function involves various parameters of the IOMR. The IOMR has also been found its utility in optical communication. The photonic signal processing techniques using the IOMR have been discussed (Binh, 2008) in the literature. The transfer function of IOMR (Okamoto, 2010) has the assumption that drop in optical power at the output port of the IOMR is independent of the gap between straight and curved waveguides of the IOMR, provided gap is within the periphery of the coupling region. Researchers (Hunsperger, Yariv, and Lee, 1977) have proved that using coupling technique considering Butt-coupling coefficients in the optical integrated circuits (Davidson et al., 1999), the high spectral purity of the microwave oscillation can be achieved. Hence an architecture for multi-loop OEO which

uses the photonic filters (Yao and Maleki, 2000) has been presented for generation of signal at microwave frequency range.

2.3.1.1 Okamoto and Pollock Model of IOMR

In the proposed thesis two major models of the IOMR have been explored in detail. First model is the Okamoto model (Okamoto, 2010) and other being Pollock model (Pollock and Lipson, 2003). The Okamoto model is described by transfer function given by

$$T(\phi) = (1-\gamma)\frac{x_1^2(1-y_1)^2}{(1-x_1^2y_1^2)+4x_1^2y_1^2sin^2(\frac{\phi}{2})} \tag{2.2}$$

Where, the parameters x_1, y_1, and ϕ are defined by Equations (2.3), (2.4) and (2.5) respectively.

$$x_1 = (1-\gamma)^{\frac{1}{2}}exp(\frac{-\rho L}{2}) \tag{2.3}$$

$$y_1 = cos(kl) \tag{2.4}$$

$$\phi = \beta L \tag{2.5}$$

Where, γ is intensity insertion loss, L is the circumference of the ring, ρ is intensity attenuation coefficient, β is the wave number, l is the coupling length and k is the coupling coefficient.

Whereas, the Pollock model (Pollock and Lipson, 2003) is described by the outgoing waves S_{-1}, S_{-2}, S_{-3}, and S_{-4}. The S_{-1}, S_{-2}, S_{-3}, and S_{-4} are given by Equations 2.6, 2.7, 2.8, and 2.9 respectively.

$$S_{-1} = e^{-j\beta L}\frac{k_1k_2}{\frac{1}{\tau_e}+\frac{1}{\tau_f}+\frac{1}{\tau_0}}S_{+1} \tag{2.6}$$

$$S_{-2} = e^{-j\beta L}(1-\frac{k_1k_2}{\frac{1}{\tau_e}+\frac{1}{\tau_f}+\frac{1}{\tau_0}})S_{+1} \tag{2.7}$$

$$S_{-3} = e^{-j\beta L}\frac{k_1k_2}{\frac{1}{\tau_e}+\frac{1}{\tau_f}+\frac{1}{\tau_0}}S_{+1} \tag{2.8}$$

$$S_{-4} = e^{-j\beta L} \frac{k_1 k_2}{\frac{1}{\tau_e} + \frac{1}{\tau_f} + \frac{1}{\tau_0}} S_{+1} \tag{2.9}$$

Where, L is the Ring circumference, k_1 and k_2 are the coupling coefficients in the forward direction; $\frac{1}{\tau_0}$ is the decay rate due to the propagation loss ; $\frac{1}{\tau_e}$ and $\frac{1}{\tau_f}$ are the decay rates due to the coupling to the bus waveguide and the resonator respectively.

The reasons for selecting these models are as follows: the Okamoto model describes the best coupling length and coupling coefficient for the maximum transfer of the power between the two waveguides. On the other hand the Pollock model describes the power transfer by considering the gap between the two waveguides. The Pollock model also takes into consideration the effect of the waveguide dimension on the coupling of the optical power. In the existing literature the utilization of these two models has not been addressed in the analysis of IOEO.

2.3.2 Coupled Mode Theory

The CMT describes the crosstalk in the optical domain. It explains the transfer of the optical power from one waveguide to another through air medium. Since in the design of the optical ring resonator, air gap exists between straight and the curved waveguides, the optical ring can be best described with the use of CMT. Hermann A. Haus and Weiping Huang (H. A. Haus and Huang, 1991a) have a pioneering contribution in the development of the CMT for the photonic coupler. The CMT for the fiber has been dealt (Snyder, 1972) in the literature. Application of CMT to the waveguide has also been discussed (H. A. Haus and Huang, 1991a) in the literature.

The formulation of CMT (Y. Liu, Chang, and Craig, 2005) is still widely referred in the design of IOMR as well as for guided wave optics. The use of the CMT in the modelling of the optical micro- ring resonator is extensive. Therefore the influence of the coupling on the sensitivity of refractive index of the photonic wire ring resonator (Guo, Xu, and Lu, 2012) has been studied and has been further explored in the photonics domain. The investigation of the degenerated modes in the two parallel optical waveguides has become the basis of exploring the straight and curved type of the coupled structure (Marcuse, 1971).

Okamoto (Okamoto, 2010) has specified that the Coupled Mode Theory (CMT) of feedback based micro-ring resonator (Y. Liu, Chang, and Craig, 2005) has great potential for future

research. The literature shows the research carried out about passive micro-ring resonator and coupled lasers. The transfer function of the device has been simulated and improvement in the quality factor (Q) at the resonance frequency has been shown. although various novel IOEOs using single loop micro ring resonator have been reported in the literature (P. Devgan, 2013), but none of them provided the proof of the physics of the proposed IOEO. The principal features of CMT in particular as applied to passive structures, such as coupled resonators and coupled wave guides are the reality today.

Variational principle of β for the proof of the CMT paved way for the historical development of the coupled mode theory and it relevance to the modern optical waveguide (H. A. Haus and Huang, 1991a). Phase noise and timing jitter in oscillator using Leesons approach (Leeson, 1966) have been discussed in oscillators with coloured noise sources. Ultra low phase noise coupled Opto-Electronic oscillators have been reported but the portability and their need for the specific applications are not addressed.

The CMT was first developed by J. R. Pierce to analyse coupling of electron beam waves and waves on electromagnetic structures in electron-beam tubes (Pierce and Tien, 1954). Later, CMT was developed for the analysis of optical waveguides. CMT is approximate, with approximations that are not always self-evident. For this reason, it was worth looking for a formal theoretical framework from which CMT could emerge in an unequivocal way. In 1958, Haus showed that CMT is derivable from a variational expression for the propagation constant (H. Haus et al., 1987).

In this thesis, an analytical approach for the computation of the relation among the gap, coupling length and the coupling coefficients of the IOMR has been presented. The derived equations explore the power transfer of the IOMR. It helps in the analysis of the change in the FSR, FWHM and Quality factor of the IOMR. In the analysis, both the Okamoto and Pollock models have been considered.

2.3.2.1 Coupled Mode Theory for IOMR

The main aim of the CMT is to study the interaction of the power in the composite optical waveguides. CMT is basically the study of the super mode formed between the two power carrying media. When the two separate entities come in the close proximity of each other, then the transfer of power takes place. In case of optical system, the transfer of power between two closely spaced waveguides takes place through the optical modes existing in the optical wavguides. This transfer of power has been extensively studied in the literature

(H. Haus et al., 1987).

The CMT has been in use since the use of electron tubes, transmission line and microwave waveguide problems. In the beginning either wave equation or reciprocity relation has been used to explore the CMT for the various composite optical waveguides. Later the CMT has been re-derived by Hardy and Streifer (Hardy and Streifer, 1985) taking the radiation mode into consideration. Variational principle by Haus (H. A. Haus and Huang, 1991a) and the generalized Chuang theory have (Chang et al., 2002) also proved that the consideration of the radiation mode is a must for the accurate analysis of the CMT.

Various authors (Y. Liu, Chang, and Craig, 2005) have analysed the CMT and experimentally verified also. But the couple mode theories find its role in all the optical devices where the composite structures come into existence. CMT is applicable to various structures such as multiple waveguides, periodic waveguide, non parallel waveguide, non-linear waveguide and externally perturbed waveguide. In this section, study of the CMT as applied to the micro-ring resonator has been carried out in the design of OEO for the optical phase shifter for transmit beam forming application.

Maxwells equations are one of the most significant scientific development of the 19th Century. It can be applied from the Direct Current (DC) to any frequency (Pollock and Lipson, 2003). Maxwell's equations completely describe the electromagnetic field in time and space. The propagation of electromagnetic waves involves two velocities namely phase velocity and group velocity. For an electromagnetic wave whose direction of propagation is +ve z-axis.

$$e^{-j(k_1 z-\omega t)} = constant \tag{2.10}$$

where k_1 is propagation constant and is defined as the product of group velocity and phase velocity and is given as

$$k_1 = \frac{2\pi}{\lambda} \tag{2.11}$$

where, z is propagation direction, ω is the angular frequency and t is the instantaneous time. Equation (2.10) is satisfied, if $k_1 z - \omega t = constant$, Then z(t) must satisfy

$$z(t) = \frac{\omega t}{k_1} + constant \tag{2.12}$$

Differentiating Equation (2.12) with respect to time, the phase velocity V_p is represented as

$$V_p = \frac{dz}{dt} = \frac{\omega}{k_1} \tag{2.13}$$

The group velocity describes the speed of propagation of a pulse of light. The group velocity is defined as

$$V_g = \frac{\Delta\omega t}{\Delta k_1} \tag{2.14}$$

The waveguide is also characterized by the single or multimode operation. The number of modes supported by a waveguide is dependent on its geometry (width and thickness). If the refractive indices between the layers are adjusted, then the mode number also varies. The lowest order mode of a waveguide has a k_1 vector that is nearly parallel to the z axis.

$$\beta_{lowestorder} = k_1 n_f \tag{2.15}$$

The highest order mode has a wave vector at nearly the critical angle. The critical angle is defined as the angle of incidence that provides an angle of refraction of 90-degrees.

$$\beta_{highestorder} = k_1 n_f cos\theta_{critical} = k_1 n_s \tag{2.16}$$

The rest of the modes have eigenvalues for β that fall between these two extremes namely $beta_{lowestorder}$ and $beta_{highestorder}$.

Another technique known as Beam Propagation Method (BPM) is also used for the evaluation of the spatial structure of a mode as it propagates through a waveguide. The BPM does not account the interference occurring due to reflection of forward and backward waves. The reflection generally occurs if the waveguide has abrupt changes in refractive index. Since many optical devices depend on interference based on reflections to function, other techniques are needed to simulate such structures. The Finite Difference Time Domain (FDTD) technique is the powerful method for such simulations. Since FDTD is a numerical technique, the derived results of the simulation are exact, provided round-off error does not exist.

Mutual coupling between optical modes is essential in the design of integrated optic devices. The coupling techniques describe the scalar electromagnetic field of a perturbed waveguide in terms of a superposition of modes of the ideal waveguide. In each waveguide, there are two waves; one propagates in the forward direction and the other in the backward direction. Power transfer or coupling can occur if the evanescent field from one waveguide extends into the core of the neighbouring waveguide. The exponential decay of the guided mode in the cladding region is defined as evanescent field. The degree to which modes exchange power depends on the design of the optical waveguide coupler and the mode structure of the two waveguides.

Using the principles of superposition, one can describe amplitude distribution of a waveguide in terms of a superposition of ideal waveguide modes. By ideal, it means a waveguide with no perturbation. The amplitude of the mode gets changed when there is a perturbation of a waveguide. Derivation for the coupled mode equation for the two straight optical waveguides as shown in Figure 2.3 is as follows: Consider two weakly coupled loss less

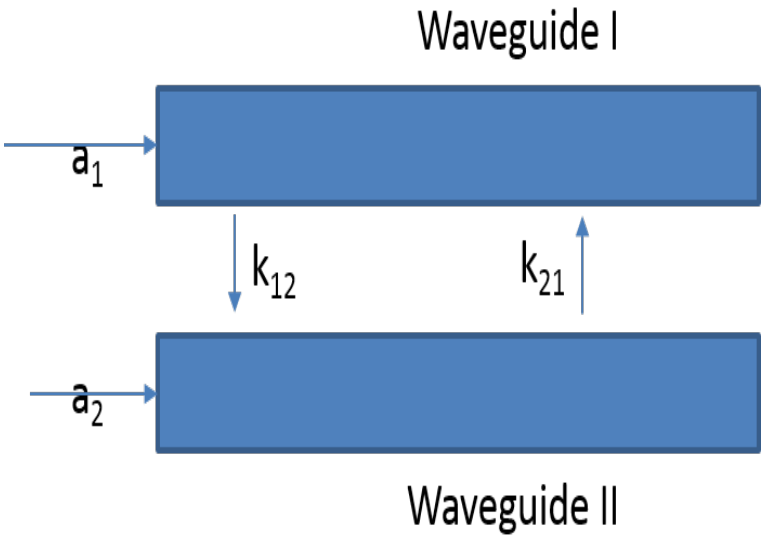

Figure 2.3: Two parallel straight waveguide

optical waveguides. The a_1 and a_2 are the initial electric field at ω_1 and ω_2 for the waveguide I and II respectively. Where, ω_1 and ω_2 are the angular frequency for the waveguides I and II respectively.

$$a_1 = e^{(j\omega_1 t)} \tag{2.17}$$

$$a_2 = e^{(j\omega_2 t)} \tag{2.18}$$

By differentiating the Equation (2.17) with respect to 't'

$$\frac{\delta a_1}{\delta t} = j\omega_1 e^{(j\omega_1 t)} = j\omega_1 a_1 \tag{2.19}$$

Likewise, by differentiating Equation (2.18)

$$\frac{\delta a_2}{\delta t} = j\omega_2 e^{(j\omega_2 t)} = j\omega_2 a_2 \tag{2.20}$$

When the two optical waveguides are coupled, their time dependence changes. When the coupling is weak, it has to be of the form (H. A. Haus and Huang, 1991a).

$$\frac{\delta a_1}{\delta t} = j\omega_1 a_1 + jk_{12}a_2 \tag{2.21}$$

$$\frac{\delta a_2}{\delta t} = j\omega_2 a_2 + jk_{21}a_1 \tag{2.22}$$

The k_{12} and k_{21} are the coupling coefficients between the straight waveguides and the ring waveguide. k_{12} represents the power coupling coefficient from waveguide I to waveguide II. Similarly k_{21} represents the power coupling from waveguide II to waveguide I.
The CMT of the two straight waveguides has been extended for the proposed IOMR which is used in the IOEO. The IOMR used in the IOEO is laterally coupled (fabricated on the same horizontal plane) architecture. The IOMR has two straight waveguides and one ring waveguide. The materials to be used for the manufacturing of the optical ring resonator are as follows:Silicon as the substrate (this is the substrate for both ring and the bus wave guides), $Si0_2$-Cladding layer for the bus wave guide and straight wave guide. Silica is the core for both the straight and curved wave guides.
The total length of the bus wave guide should be multiple of coupling length l. The width of the bus wave guide and ring wave guide is kept same as $W3$. The thickness of both the waveguides is also kept same. The coupling length of the curved waveguide is approximated as a parallel to the straight waveguide. The transfer function of the ring resonator is discussed (Okamoto, 2010) in the literature. The transfer function given by Equation (2.2) is studied and is being used for the better coupling of the power at the desired wavelength. This transfer function also holds for the proposed schematic of IOMR shown in Figure 4.1. Noise in the optical ring resonator introduces phase noise. IOMR is a wavelength selective device. The light inside the ring resonator undergoes multiple encircling. For simplicity, in the present study, it is assumed that light undergoes only a single encircling.

2.3.2.2 Analytical Study on the Butt-coupling Co-efficient for IOMR

Research on IOMR and its fabrication using Silicon-On-Insulator (SOI) techniques have gained significant attention since a few decades due to its wide range of applications. In laterally coupled IOMR shown in Figure 2.4, d is the gap between straight and curved waveguides, k is the coupling coefficient, l is the coupling length, and L is the total ring

circumference and R is inner radius of the ring. SOI technology is compatible with well-established Complementary Metal Oxide semiconductor (CMOS) fabrication techniques. Analysis of the IOMR employing analytic and experimental methods by taking into account the coupling effect has been topic of research interest for the past few years. The study of resonance condition and sensitivity of a Photonic Wire Micro-ring Resonator (PWRR) has been addressed by considering the coupling effect (Guo, Xu, and Lu, 2012).

An accurate expression for the coupling coefficient has been derived (Y. Liu, Chang, and Craig, 2005) and is found to be useful in the study of Butt-coupling coefficient. Butt-coupling coefficient (Guo, Xu, and Lu, 2012) is a phenomenon of the excitation of the optical mode in the adjacent waveguide. This mode excitation occurs when the second waveguide suddenly comes to close vicinity of the first waveguide. The coupled mode analysis (H. A. Haus and Huang, 1991a) through both in space and time domains has been studied through variational principle (H. A. Haus and Huang, 1991b). This helps in the analytic study of the Butt-coupling coefficient in the IOMR. Butt-coupling method is found to be a viable technique for coupling an injection laser to a thin film (Hunsperger, Yariv, and Lee, 1977).

The analysis of resonance condition of the SOI based IOMR is of significance for many applications like optical filter, sensors, and multiplexer since Butt-coupling coefficient leads to shift in resonance of IOMR. In most of the conventional analysis of the IOMR (Guo, Xu, and Lu, 2012), Butt coupling coefficient (c_{pq}),where p=1 and q=2 represent the waveguides I and II respectively as shown in Figure 2.4.

The field perturbation (χ_{pq}) is also neglected (Hunsperger, Yariv, and Lee, 1977) and they are assumed to be $c_{12} = c_{21} = 0$. However, both c_{pq} and c_{qp} cannot be ignored in analysing the effect of the mode coupling, if the distance between two optical waveguides is less than 200 nm. This is due to the excitation of the mode from one to another waveguide and their effects on the mode of the waveguide. In the analysis, reciprocity of the coupling coefficients, $k_{12} = k_{21}$ exists, since c_{12} is assumed to be zero. In this section the propagation constants are assumed to be different and the distance between optical waveguides is considered to be less than 200 nm. The Equations (2.23) and (2.25) have been used for the calculation of coupling co-efficient k_{12} and k_{21}.

$$\delta = (\frac{\beta_1 - \beta_2}{2}) \tag{2.23}$$

$$k_{12} = \dot{k_{21}} + 2\delta c_{12} \tag{2.24}$$

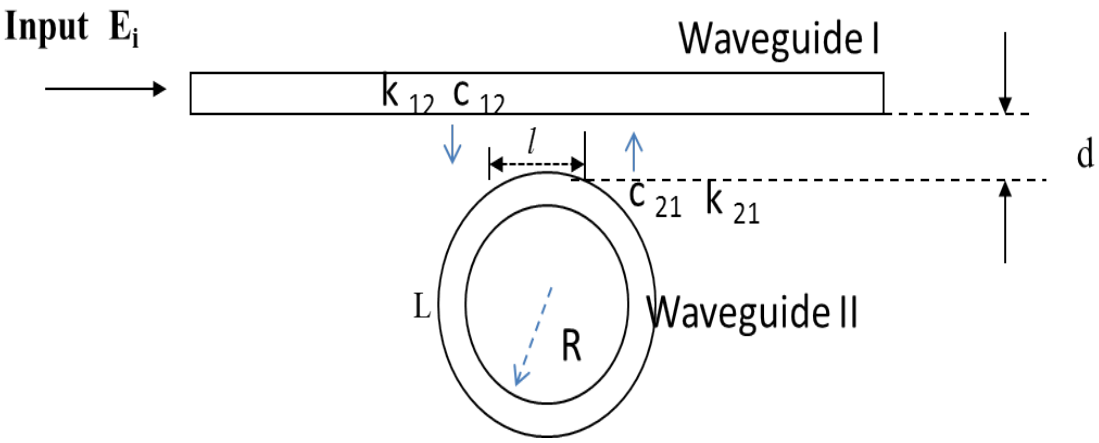

Figure 2.4: Straight and curved waveguide of an IOMR

Where, k_{12} and k_{21} are the coupling coefficients; β_1 and β_2 are the propagation constants of the two optical waveguides I and II; c_{12} and c_{21} are the Butt-coupling coefficients between waveguides I and II. The coupling coefficients (Guo, Xu, and Lu, 2012) of the straight and curved waveguides with relevant notations are given by Equations (2.25) and (2.27). The E_1 and H_1 are electric and magnetic fields of waveguide I and E_2 and H_2 are electric and magnetic fields of waveguide II. The E^* and H^* are the complex conjugate of the electric and magnetic fields respectively. ω is angular the angular frequency of operation and ε_0 is free space permittivity. u_z is the unit vector in the direction of propagation.

$$k_{12} = \frac{\omega\varepsilon_0 \int_{-\infty}^{+\infty}\int_{-\infty}^{+\infty}(N^2 - N_2^2)E_1^* E_2 \partial x \partial y}{\int_{-\infty}^{+\infty}\int_{-\infty}^{+\infty} u_z \cdot (E_1^* \times H_1 + E_1 \times H_1^*)\partial x \partial y} \tag{2.25}$$

$$k_{21} = \frac{\omega\varepsilon_0 \int_{-\infty}^{+\infty}\int_{-\infty}^{+\infty}(N^2 - N_1^2)E_2^* E_1 \partial x \partial y}{\int_{-\infty}^{+\infty}\int_{-\infty}^{+\infty} u_z \cdot (E_2^* \times H_2 + E_2 \times H_2^*)\partial x \partial y} \tag{2.26}$$

Butt-coupling coefficient is given by Equation (2.27):

$$c = c_{12} = \frac{\int_{-\infty}^{+\infty}\int_{-\infty}^{+\infty} u_z \cdot (E_1^* \times H_2 + E_2 \times H_1^*)\partial x \partial y}{\int_{-\infty}^{+\infty}\int_{-\infty}^{+\infty} u_z \cdot (E_1^* \times H_1 + E_1 \times H_1^*)\partial x \partial y} \tag{2.27}$$

When the distance between the straight and curved optical waveguides is less than 200 nm, the influence of the Butt-coupling on the performance of IOMR has been studied through simulation. Applications such as high frequency oscillator and Dense Wavelength Division Multiplexer (DWDM) need miniaturization of the components. Hence the miniaturization of IOMR is essential and significant for the development of such devices. It has also been

observed that, to achieve maximum power coupling and better performance of IOMR in terms of noise and the bandwidth, the Butt-coupling must be considered. In this thesis, a study on the resonance condition of optical IOMR is presented considering a gap of 15 nm between straight and curved waveguides.

2.4 Two Port Network

Two port network is widely used in the analysis of linear network. Two port network theory is used to derive various matrices or parameters such as ABCD, h, S, and Z (Laughton, and Say, 2013). These parameters are useful in the analysis of the performance characteristics of the circuits. Generally the analysis of an optical components as two port network has not been widely addressed in the literature. In this thesis, IOEO has been modelled in terms of two port network.

All the components of IOEO such as IOMR, EDFA, LNA, PD and OM have been considered to be a two port network. Since the linearity of the components is a mandatory condition to apply the two port network theory, the linearity has been ensured (Farago, 1961) for all the network components of IOEO. The two port network modelling of all the listed components of the IOEO is required for the computation of the phase noise of the designed IOEO. The computation of phase noise of IOEO and its components invoking the two port network theory appears to have not been addressed in the literature.

In this thesis, the computation of the phase noise of IOEO has been carried out applying the two port network theory. The modelling of the IOMR which is present in the feedback path of the designed IOEO uses both Okamoto and Pollock models and the phase noise contribution by the IOMR has been computed.

The study of phase noise of IOEO and IOMR through ABCD parameters for the optical components although is novel but poses many challenges such as two port modelling of devices (IOMR, OM, PD, LNA and BPF), Computation of the ABCD matrix of the IOEO and the utility of the Okamoto and Pollock model for the computation of the ABCD matrix for IOMR. The proposed thesis presents a detailed analytical procedure for the modelling of the optical components and the computation of the ABCD parameters. In addition, the thesis also presents the computation of phase noise of the IOEO and its components utilizing the computed ABCD parameters of the individual components and the IOEO itself.

2.5 Thermal Stability of an Integrated Opto-Electronic Oscillators

The oscillators generally have two type of stability issues; one is the long term stability and other being the short term stability (Pham et al., 2015). The long term stability is ensured through the analysis and testing of the effect of the temperature on the resonant frequency of the oscillators. Hence the temperature effects on the designed IOEO has been studied in this thesis to address the long term stability. Generally temperature variation has adverse effects on most of the electronic devices.

The OEO is also expected to experience similar nature of effects. Environmental temperature variation affects long-term stability of the OEO. Recently Vector Network Analyzer (VNA) has been utilized to estimate the frequency variation in oscillation at room temperature (Pham et al., 2015). The study reported correlation between frequency drift in oscillation of OEO and the phase measured in detail.

The Sellmiers model (Leviton and Frey, 2006) has been widely used for the stability analysis of the optical materials such as silicon and germanium. Sellmiers model relates the changes in refractive index as a function of wavelength and the temperature of the material. The temperature dependent Sellmeier model is represented as

$$n^2(\lambda, T) - 1 = \sum_{i=1}^{m} \frac{S_i \cdot (T)\lambda^2}{\lambda^2 - \lambda_i^2(T)} \tag{2.28}$$

Where,

n is the refractive index, T is the temperature in Kelvin, S_i are the strengths of the resonance features in the material at wavelength λ_i.

In the designed IOEO of this thesis, the Sellmeier model has been considered and the thermal stability of IOEO has been ensured. The IOMR is the main component which is responsible for the selection of the resonance frequency of IOEO. Hence the temperature effects on the performance characteristics of IOMR have been discussed through Sellmeir model.

2.6 Applications of an Integrated Opto-Electronic Oscillators

Modern high speed signal processing systems utilize integrated photonic devices and its principle. High speed signal processing constitutes technologies to address various applications. To name a few of these applications; radars, medical ultrasound imaging, digital systems for long haul communication network and on-chip interconnects in computers.

Photonics Signal Processing Techniques (PSPTs) are able to address (Okamoto, 2010) the need of higher frequency of operation (above 40 GHz). The PSPT also addresses low attenuation loss (less than 0.2 $dBkm^{-1}$). Various techniques to suppress EMI effects have also been addressed in PSPTs.

Precise timing has been one of the significant signal processing parameters. Application such as radars need low phase noise clock sources so that objects can be tracked efficiently. The optical network generally transmits a few Tbs^{-1} of data (P. Devgan, 2013). The optical network needs low phase noise for the precise clock signal and also for multiplexing of the data streams. Requirement of low phase noise is not limited to optical networks. The low phase noise signal is also used in the Analog to Digital Converter (ADC) for the sampling purpose and clock requirements. The application of IOEO can also cover both the clock recovery and conversion of data format (P. Devgan, 2013).

Since 1966, the IOEO has been used in various applications. The IOEO continues its prominence going beyond its initially perceived utilities. The IOEO continues to be investigated theoretically (Kouomou Chembo et al., 2007) to improve its performance.

The exploration of new applications, such as use in sensors (Duy et al., 2008) and determination of effective refractive index of SMF (Nguyen, Nakatani, and Journet, 2010) are just a few to highlight the recent trend. Finally IOEO continues to be investigated for its use in computer architectures (C. Gunn et al., 2007). Some of the existing and more recent trends in the design and development of IOEO are as follows: the major focus is on the design of an architecture of an IOEO using an optical micro-ring resonator and the utility of designed architecture for the applications such as optical phase shifter and Bio-sensors.

The IOEO is an optical device known for its low phase noise. The requirement for low phase noise oscillators covers applications in computers and on-chip optical interconnects. The photonic IOEO eliminates the bandwidth issues of the electrical interconnects. When the speed of execution of chips exceeds 1 GHz, the phase noise associated with the data clock signal becomes significant. Hence the realization of a photonic low phase noise IOEO becomes very important. Appropriate routing and processing is an avenue to satisfy the ever increasing requirement of bandwidth (P. Devgan, 2013) of the interconnects. The accurate signal processing of an optical data also helps in addressing the ever increasing bandwidth requirement. Hence the design and development of low phase noise IOEO is an important requirement for the optical network.

Presently one of the major research domains is the Photonics FPGA also known as P-FPGA. P-FPGA is seen as the future of the Very Large Scale Integration (VLSI) (Mal, Patel, and

Beyette, 2009). Optical ring resonator is proved to be a basic building block of the P-FPGA. Various analyses have been reported (Xu and Lipson, 2007) regarding the structure of basic optical logic gates using SOI based optical ring resonator. A few basic gates such as XOR and XNOR have been proved (Jalil et al., 2011) in the literature. The optical ring resonator has also been used in the application such as optical filters. Apart from Silicon-on-Insulator (SOI) based IOMR, other III-V group materials such as GaInAsP/InP have been used as substrate for fabrication (Rabus, 2002).

Up-conversion of the analog as well as digital baseband signal is required in communication applications. The up-conversion of the frequency (from 1.25 GHz to 20 GHz) has been reported using OEO (Shin and Kumar, 2007b). The up-converted signal can be transmitted to a distance upto 50 km without significant degradation of signal strength. (Shin and Kumar, 2012) present a simultaneous up-conversion of 161.25 Gbs^{-1} channels to a carrier of 20 GHz. The down-conversion is also possible using IOEO. The down conversion of 1 Gbs^{-1} signal from a 20 GHz carrier (Zhu et al., 2012) has also been reported in literature. The architecture of IOEO proposed in this thesis is suitable for the above referred applications because of the extremely wide bandwidth and low phase noise. Serial to parallel converters also use IOEO. The conversion of a 40 Gbs^{-1} into two 20 Gbs^{-1} optical data streams (Tsuchida, 2009) using polarization modulator with the benefits of constant intensity at the output was reported. Literature discussed in this section justifies the utility of the IOEO in various signal processing applications.

The IOEO has been utilized in various applications such as telecommunication and optical communication. The K_a-band (Miller, 2007), is the future of satellite communication and OEO has been found to be extremely significant in the generation of K_a-band signal.

2.6.1 An Optical Beam Steering

The optical beam steering application is becoming more popular. It is emerging as an area of research due to its high precision and small size and portability. The beam steering with a frequency of operation upto 40 GHz (Ohuchi et al., 2007) has been reported. Two architectures of optical beam steering are shown in Figures 2.5 and 2.6 have been proposed (Vidal et al., 2012). The optical beam steering stages consists of tunable laser source or multi-wavelength laser, Mach-Zenhder interference based optical modulator, RF (f_{RF}) signal source, optical phase shifter (switch) and the photo diode. The optical beam forming (Vidal et al., 2012) for 4 GHz to 8 GHz signals has been reported using tunable laser and

Figure 2.5: An optical beam former based on tunable laser (Vidal et al., 2012)

optical ring resonator based fast switch. The 40 GHz modulating signal has been used for

Figure 2.6: An optical beam former based on fast switch and dispersive fiber (Vidal et al., 2012)

the optical beam forming (Ohuchi et al., 2007), but it does not ensure the spectral purity of the source.

The need to generate optical beam forming architecture with the spectral pure 40 GHz with thermal and frequency stability leads to analysis of the proposed optical beam steering based on designed IOEO.

2.6.2 Bio-sensors

A successful Fiber Optic Sensor (FOS) provides unique and superior solution. It also should be economically feasible. FOS exhibits many features such as Electro Magnetic Interference (EMI) immunity, small size, and reliability. FOS represents a new generation of sensors having a great potential for new applications such as: Large composite and concrete structures, electrical power industry, medicine and chemical sensing. These advantages have made FOS very attractive for quality control during construction, health monitoring, impact monitoring of large composite or concrete structures. The majority of commercial sensors widely used in medicine are electrically active and hence are not appropriate for use in a number of medical applications. Particularly in applications involving the use of high radio frequency fields or ultrasound fields or laser radiation associated with hyperthermia treatment, there is a high probability of erroneous reading by the sensors. This can be attributed to local heating of the sensor head and the surrounding tumor due to the presence of metallic conductors and electromagnetic interference of currents and voltages in the metallic conductors. FOS can overcome these problems as it is virtually a dielectric. The Bio-sensor has been in use because of its compactness and high sensitivity. Bio-sensors find their application in many areas like clinical diagnosis, drug development and food quality control. Recently a fiber-optic temperature sensor has been proposed (Zhang, Chen, and Fu, 2015) with an OEO using part of the fiber as the sensing fiber. The refractive index of the fiber varies due to variation in temperature. This in turn leads to the variation in optical path length as well as the FSR of the OEO. Monitoring of the temperature variation is also possible using such OEO.

Fiber optics based Bio-sensors are bulky. Hence to reduce the size of Bio-sensors a WGM resonator has been proposed as label-free Bio-sensors (A. Matsko et al., 2003). Low-loss dielectrics are used in the manufacturing of Bio-sensors. The Bio-sensors show sharper resonances, high quality factor and miniaturized diameter size (in the range of a few tens of micrometers).

Another application of optical ring resonator is a sensor (Malathi et al., 2011) and therefore the designed IOEO can be used in development of a Bio-sensor. As shown in Figure 2.7 a microring resonator (Malathi et al., 2011) has been simulated as a bulk sensor. In this work the simulation and analytical analysis for bulk sensing of protein on Silicon-on-Insulator strip waveguide based microring resonator has been reported. The analysis has been carried at a ring radius of 5 μm and 20 μm with strip waveguide dimensions of $300nm \times 300nm$.

Figure 2.7: Ring resonator with adlayer (Malathi et al., 2011)

The gap of 200 nm and 300 nm are taken between the ring and the bus waveguide. The sensitivities of 32.5 $nmRIU^{-1}$ and 17.5 $nmRIU^{-1}$ (RIU-Refractive index unit) have been reported.

Recently a Label-free (Guider et al., 2015) Bio-sensor has also been reported. These sensors are able to differentiate minute variation in the refractive index of bulk solutions and hence exhibit high sensitivity. A Bio-sensor based on an intensity-interrogated planar waveguide double ring resonator is reported in (He, 2012) which uses a low-cost broadband light source combined with simple intensity measurements without requiring an external bulky and expensive tunable laser.

Rigorous research in the field of Biochemical sensors has been reported for healthcare, environmental monitoring, food industry and pharmaceuticals applications. To simulate these sensors, sensitive and high speed simulation tools are required. The ring resonator based Bio-sensor has a number of distinctive advantages such as high quality factor ranging from 10^4 to 10^8 (Sun and Fan, 2011). It also has small physical size, which provides the ring resonator comparatively good sensing performance and compact footprint. (Duy et al., 2008) have reported an IOEO based sensor with a fiber loop as a sensing element. Similar structures with microring resonator and microspheres have also been reported in (Quan and Guo, 2005), (H. Quan, et al., 2005) and (Schweinsberg et al., 2007).

The exploration of bio-sensors based on IOEO having all optical components in the feedback path has not been addressed in the literature. Hence a novel configuration of Bio-sensor based on designed IOEO having all optical components in the feedback path has been analysed in this thesis. The proposed IOEO has all-optical feedback, which provides

thermal and frequency stability and low phase noise suitable for Bio-sensing application.

2.7 Summary

In this chapter the existing architecture of IOEO has been reviewed for detailed analysis. Various performance parameters such as finesse, field or power output, coupling co-efficient, transmission co-efficient, quality factor and phase noise have been reviewed. Comparative assessment of the advantages and disadvantages of various components such as electrical band pass filter, electrical amplifier, optical modulator, photo diode, with or without EDFA and integrated optical micro-ring resonator have been discussed.

Use of optical filter such as Fabry-Perot filter in IOEO has been discussed highlighting its ability to suppress side modes of the IOEO. The relative comparison of various types of modulations such as phase, intensity and polarisation modulation has also been presented. The wideband operation of an IOEO is limited by the disadvantages of LNA. But the wide band operation of IOEO is achievable by using photonic gain.

The presented succinct review on performance of IOEO justifies the need and requirement of the design of a miniaturized IOEO with low phase noise and high quality factor. The importance of phase noise and the significance of Leeson's model have also been discussed in this chapter. The relevance of two port network model in the analysis of phase noise of IOEO and its components has also been discussed in this chapter.

A major breakthrough in the design of IOEO has been the replacement of optical fiber delay line by a WGM optical mini-resonator. Therefore the realization of an equivalent delay line by replacing the long fiber with an optical mini-disk resonators of diameters of a few mm has become a reality. The high quality factor micro-ring resonator with strong mode selection filter provides improvement in the side-mode suppression ratio, the line width and the frequency chirp.

An architecture for the IOEO with a quality factor of 1000 under loaded condition is possible with the IOMR in the feedback path of IOEO. The utility of Okamoto and Pollock models as well as the CMT in the performance analysis of IOMR has also been discussed in this chapter. The potential utility of IOEO in system applications such as optical beam steering and Bio-sensors has been reviewed with a discussion on the relevant existing architectures.

CHAPTER 3

THE DESIGN OF AN INTEGRATED OPTO-ELECTRONIC OSCILLATOR

3.1 Introduction to the Oscillators

Oscillators are used for the generation of the sinusoidal frequency and are extensively used in modern communication systems. In every communication system, the oscillator has its own relevance and significance. The evolution of design and development of the oscillator could be witnessed from the electronic era to the photonics era. The principles and performance of electronic oscillators of the primitive configurations such as Collpitts, Hartley and Crystal oscillator (Hajimiri and Lee, 1998) have been extensively analysed. Over the past several decades, these oscillators have proved their significance, reliability and utility in both commercial and non commercial system applications. As the operating frequency increases, the resulting complexities of the electronic oscillator tend to exhibit themselves in a multifold nature. For example in communication systems, particularly long haul communication systems where the phase noise is very critical, oscillators such as Collpitts, Crystal and Complementary Metal Oxide Semiconductor (CMOS) based oscillators do not ensure the necessary low phase noise and high quality factor. Hence the spectral purity has become one of the urgent requirements of the high frequency oscillator so that it could be used in communication systems. To deal with the challenges pertaining to performance parameters of oscillators operating at extremely high frequencies, over the past decade an evolving topic of intense and continued research has emerged under the broad purview of Opto-Electronics in general and OEO in particular.

In the Opto-Electronic domain both electronic and optical devices are utilized to produce a spectral pure sinusoidal frequency. A few of OEOs are also commercially available (OEwaves, n.d.). The need and requirement of the design and simulation of the novel OEO arise from its low phase and high quality factor requirement.

The need and requirement of OEO have raised several research questions such as high

quality factor, minimum phase noise and high thermal stability of an OEO leading to an extensive study and analysis of the OEO. In the success of the novel OEO, the parameters such as quality factor and phase noise are significant. The existing OEOs (Chembo et al., 2009) and (D. Gunn et al., 2007) have all electrical components in the feedback path effecting phase noise and quality factor of the OEO. Hence analysis of all optical components in the feedback path of the OEO becomes significant from the phase noise and quality factor perspective.

To analyse the effect of optical feedback on the performance of optical ring based OEO, a study involving the design and simulation of a novel architecture for IOEO as shown in Figure 3.2 has been undertaken with specific emphasis on the performance metrics such as quality factor and phase noise. A novel IOEO has been designed to study the effects of IOMR on the OEO. To analyse the effects of IOMR on the OEO, a novel IOEO is designed such that IOMR remains in the feedback path along with the other optical devices.

In this chapter, the design of low phase noise 40 GHz IOEO has been proposed to cover the applications such as optical beam steering and Bio-sensors. In the architecture of the designed IOEO, long optical fiber has been replaced by an IOMR. Use of IOMR miniaturized the IOEO. Use of IOMR also reduces the line loss which in turn increases the quality factor (Q) of the IOEO. In the designed architecture, an array of IOMR can also be used to increase the maximum power transmission in the feedback loop/feedback path. Various specification details have been discussed to facilitate a better appreciation of the novel features of proposed design of IOEO.

The designed IOEO is basically a device to generate a fixed 40 GHz signal. In the proposed architecture of IOEO, the initial excitation of the oscillator is through the random noise. It then receives feedback signal from the output of the forward path to the optical modulator in the feedback path. The output of optical modulator passes through array of ring resonators or a single IOMR and then it is amplified by Erbium Doped Fiber Amplifier (EDFA) (refer to Figure 3.14) and gets converted into electrical signal using photo diode.

The design architecture of IOEO can be viewed as a device with two stage configuration. The two stages are the forward path and the feedback path respectively (refer to Figure 3.2). The forward path comprises a first low noise amplifier; band pass filter configured with a center frequency corresponding to fixed operating frequency of IOEO and a second low noise amplifier. The feedback path comprises a signal laser source providing an optical source signal of 1550 nm; an intensity optical modulator; an IOMR configured to provide an optical feedback signal from the modulated optical signal; a pump laser provides a

reference optical signal to an EDFA and a PIN photo diode to convert the optical feedback signal to electrical signal which in turn is fed to the forward path after the initial excitation. The designed IOEO also uses an impedance matching circuit between feedback path and the forward path.

3.2 Design and Modelling of an IOEO

In this section, design and modelling of the IOEO has been discussed. The design and performance analysis of the OEO at radio, microwave and millimeter-wavelength frequencies have been addressed (Chembo et al., 2009) and (D. Gunn et al., 2007). The design of the proposed IOEO is the result of an extensive study of the existing OEO (Chembo et al., 2009).

None of the existing architectures of the IOEO discusses the generation of the 40 GHz with high spectral purity. The 40 GHz is the higher end frequency of the K_a-band and is in demand for the use in satellite and long haul communication. The multiple of 40 GHz could generate very high speed data rates for optical communication. The existing architecture shown in Figures 2.1 and 2.2 (Chembo et al., 2009) and (D. Gunn et al., 2007) have reported being partially analysed from the phase noise and the quality factor points of view.

The spectral purity of the signal in the IOEO depends on Q-factor of the system. The Q-factor of an IOEO depends on the performance of the optical storage system. An obvious consequence of using a large fiber is the generation of 'super modes' that appear in the phase noise spectrum. The super modes are combination of the two fundamental modes of the two different integrated optical waveguides.

For certain applications such as oscillators these super modes are undesirable. The multiple propagation of these super modes in the IOMR generates phase noise in the IOEO. These super modes can be suppressed using multiple loops of fiber, which together function as a narrow band filter. But multiple loops of fiber increases the size of the system drastically. Other than the optical fiber, high-Q optical cavity can be used to filter the undesired super modes.

Although Fabry-Perot cavities with high Q-factors are useful for achieving this, a more convenient choice is ultrahigh-Q Whispering Gallery Micro-Ring Resonator (WGMR) (Savchenkov et al., 2010). Whispering gallery travels along the circular gallery (Righini et al., 2011), where the whispering can be heard across the dome. Lord Rayleigh explained

this phenomenon for acoustic waves, which is applicable to EM wave travelling in a resonator. WGMR can be fabricated with size spanning a few hundred micrometres to a few millimeters using wide variety of optical materials. In particular, WGMR made from crystalline materials have Q-factors in excess of a billion, with the largest reaching 3×10^{11} (Savchenkov et al., 2010). Such high Q-provides narrow bandwidth which is sufficient to remove unwanted super mode noise in the spectrum of IOEO.

Recently, in photonics domain several commercialized systems have been demonstrated for a number of data processing and radar applications that require microwave and millimeter-wavelength oscillator. Such applications demand not only miniaturized size of an oscillator but also the optimum output power as compared to the existing devices.

Presently IOEO based on WGMR technology is the only available solution suitable for the above stated applications. In particular, IOEO having high-Q WGMR made from an electro-optic material provides high performance. An IOEO having high-Q WGMR produces 40 GHz output signal with higher spectral purity as compared to alternative approaches. The designed IOEO architecture finds its usage when high spectral purity is required with Q-factor upto 1000. These devices have already found applications in Wavelength Division Multiplexing (WDM) based optical beam steering (Burla et al., 2008) and optical Bio-sensing (Malathi et al., 2011). In the present research work, various existing Opto-Electronic architectures have been explored. To overcome the deficiencies of the IOEO, a novel IOEO architecture has been proposed, designed and simulated. The designed IOEO is based on the generalized delay line model of IOEO shown in Figure 3.1. Figure 3.1 represents the general model of the delay line oscillator. In Figure 3.1, A

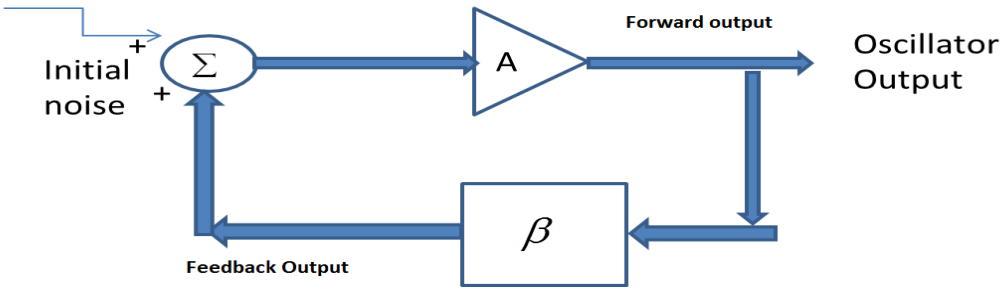

Figure 3.1: General model of the delay line oscillator

represents the forward gain and β represents the feedback gain of the oscillator. Initially a

random noise excites the oscillator. The noisy input passes through the forward path and amplifies the signal. The feedback signal is given as input to the forward path. To achieve the sustained oscillation at 40 GHz, the magnitude of $A\beta$ is maintained as 1. Figure 3.2 depicts the model of the designed IOEO with single IOMR consisting of electrical and all optical devices in the feedback path.

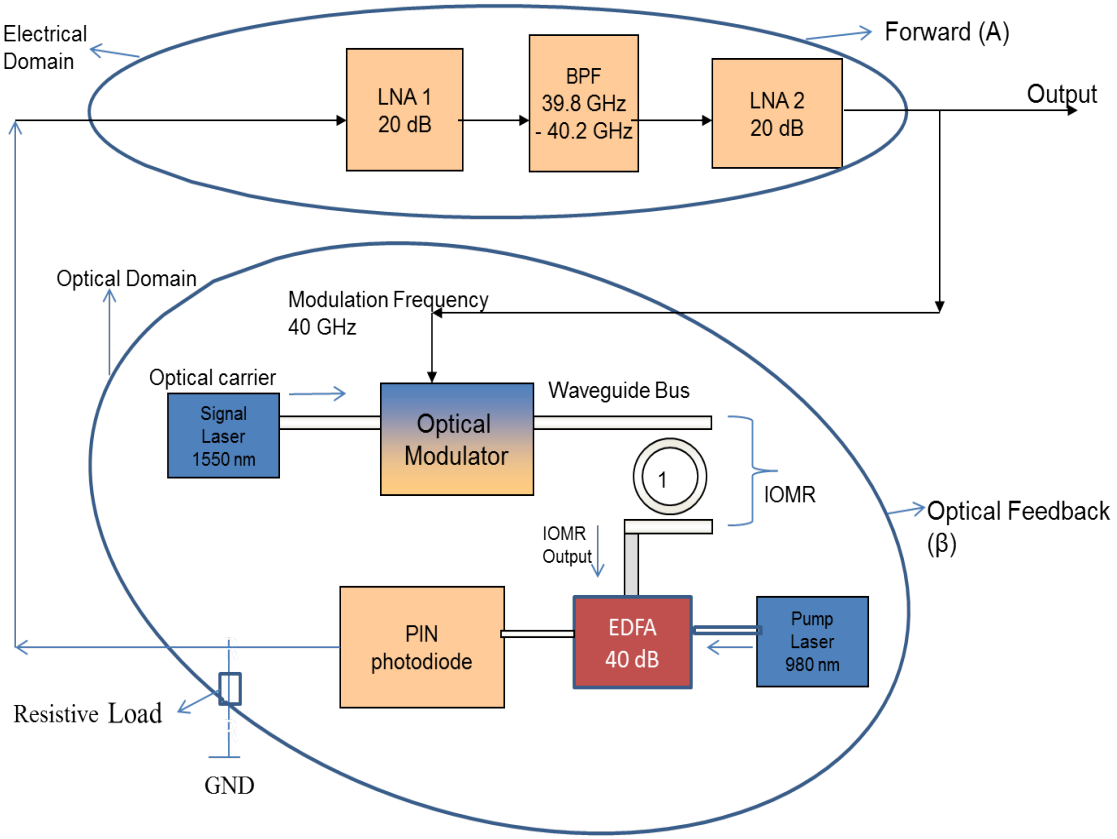

Figure 3.2: Schematic of IOEO with single IOMR

Figures 3.4 and 3.5 depict the simulation model of IOEOs with single IOMR having Okamoto model and Pollock model respectively. As per the delay line modeling of the IOEOs, Forward Gain (A) consists of Low Noise Amplifier (LNA1), Band Pass Filter (BPF) and Low Noise Amplifier (LNA2). Feedback gain (β) consists of Optical Modulator (OM), IOMR, EDFA and Photo Diode (PD). In both the architectures of IOEO, initial noise excites the oscillator. The noise excitation is shown in Figure 3.3. In the first iteration of

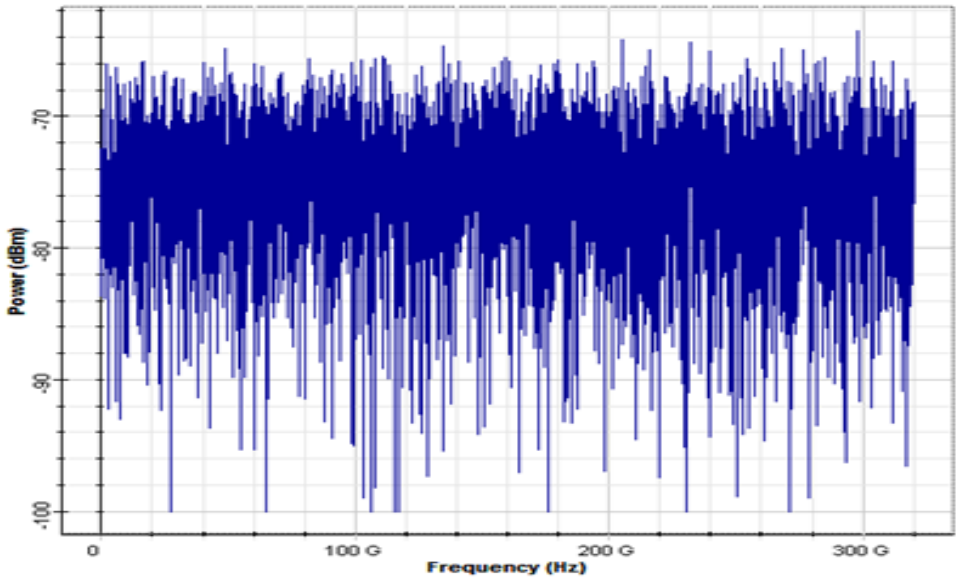

Figure 3.3: Noise excitation of IOEO using Optisystem version 7.0

the simulation, the output of the LNA2 is fed to the MZIM directly. In the second iteration of the simulation, the output of the photo diode is connected to the LNA1. Simulation of IOEO with single IOMR and array of 26 IOMR follows the same working principle. Figure 3.6 depicts the designed IOEO model with an array of 26 IOMR consisting of electrical and all optical devices in the feedback path. Figure 3.7 depicts the simulation model of IOEOs with an array of 26 IOMR.

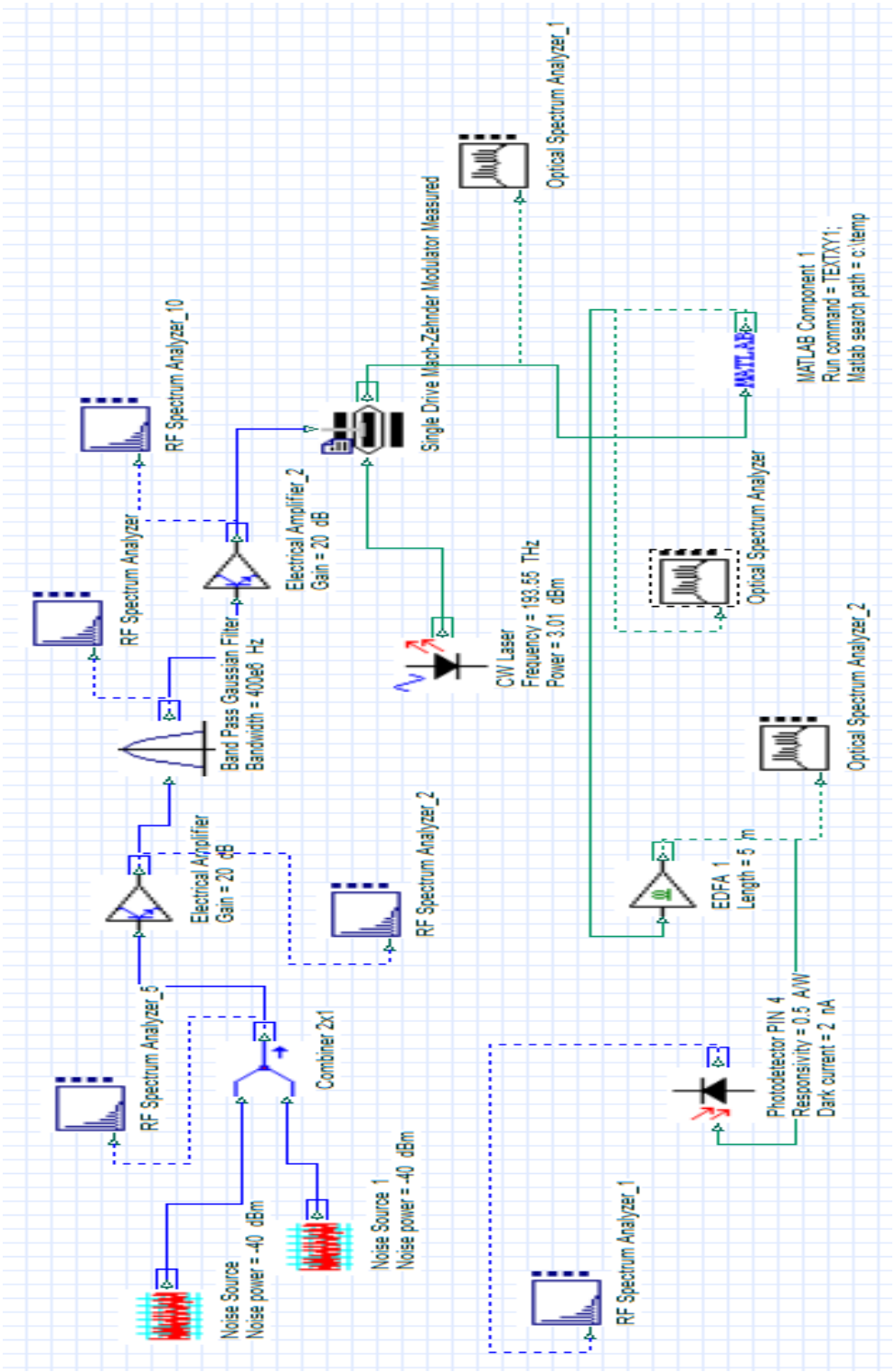

Figure 3.4: Simulation model of IOEO with single IOMR (Okamoto, 2010) using Optisystem version 7.0

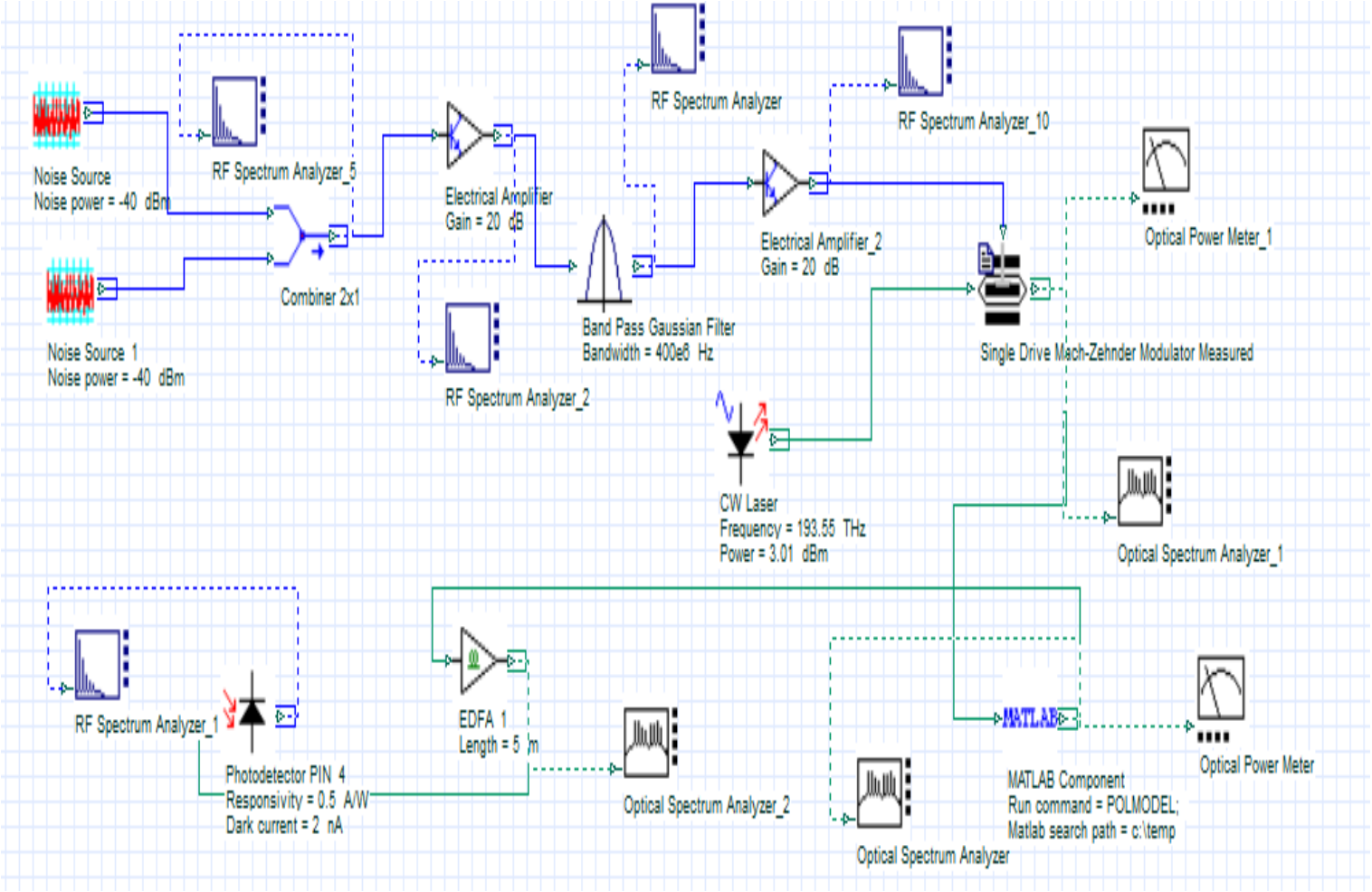

Figure 3.5: Simulation model of IOEO with single IOMR (Pollock and Lipson, 2003) using Optisystem version 7.0

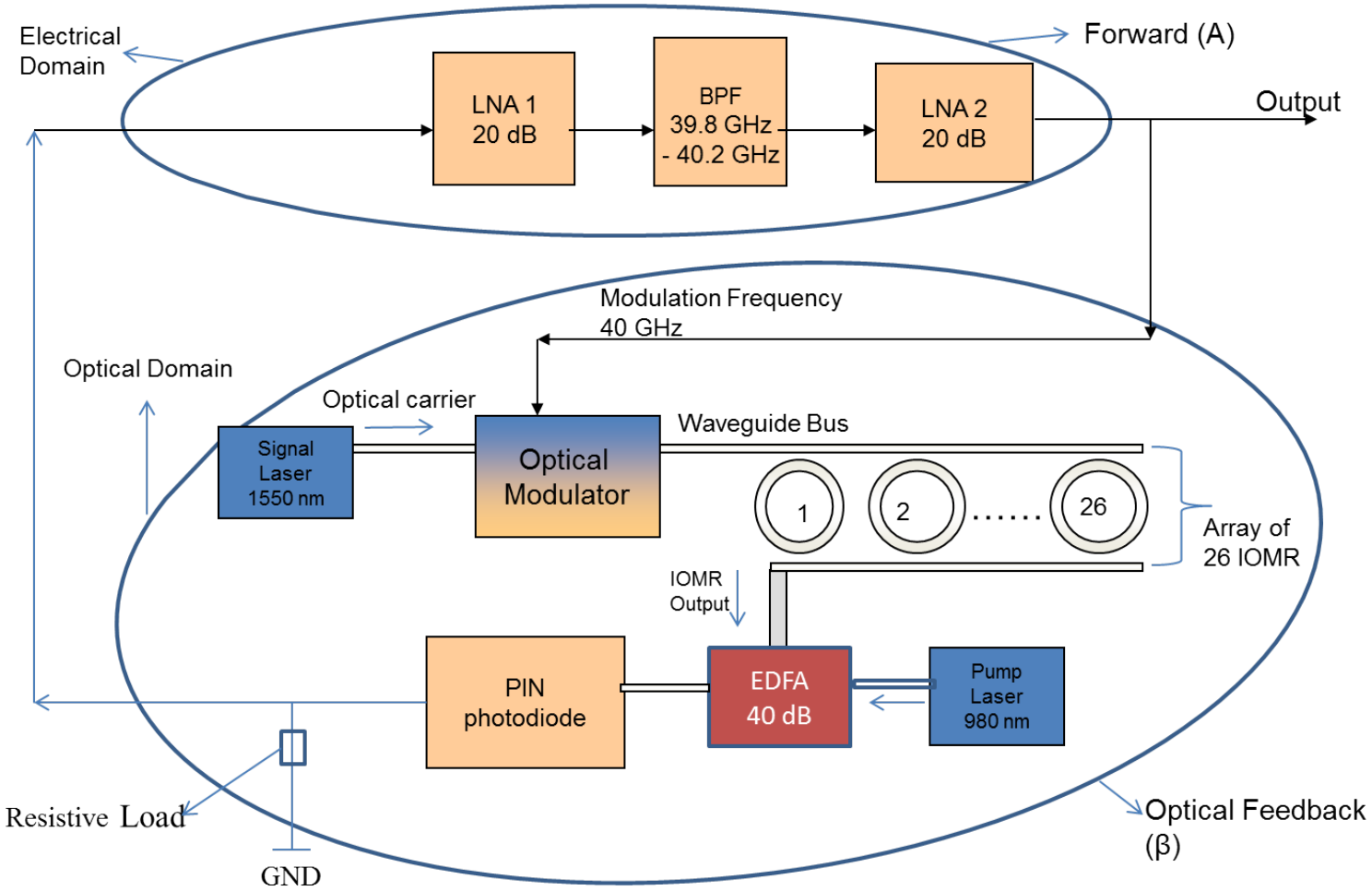

Figure 3.6: Schematic of IOEO with array of 26 IOMR

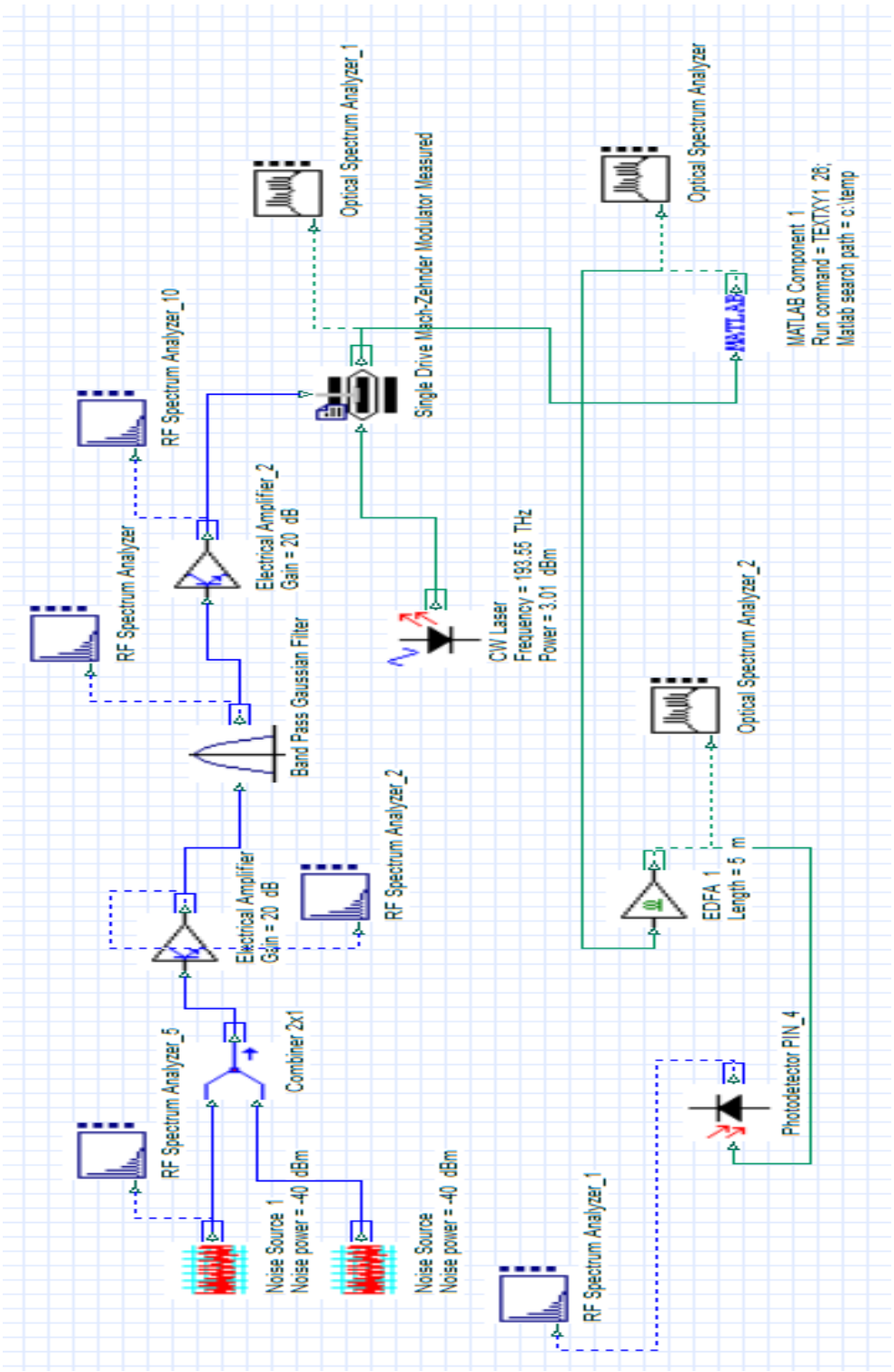

Figure 3.7: Simulatiom model of IOEO with array of 26 IOMR (Okamoto, 2010) using Optisystem version 7.0

The output of continuous wave laser at 193.55 THz with power of 3.01 dBm is fed to the MZIM. The output of LNA2 is also fed to the MZIM simultaneously. The modulated output is fed to the IOMR, which is a wavelength selective device and in the present case designed for the 1549.7 nm. The output of the IOMR gets attenuated drastically in case of single IOMR. Hence an array of 26 IOMRs has been used. The array of 26 IOMR offers an improvement in the optical output power of the IOMR as shown in Figure 3.8. The array

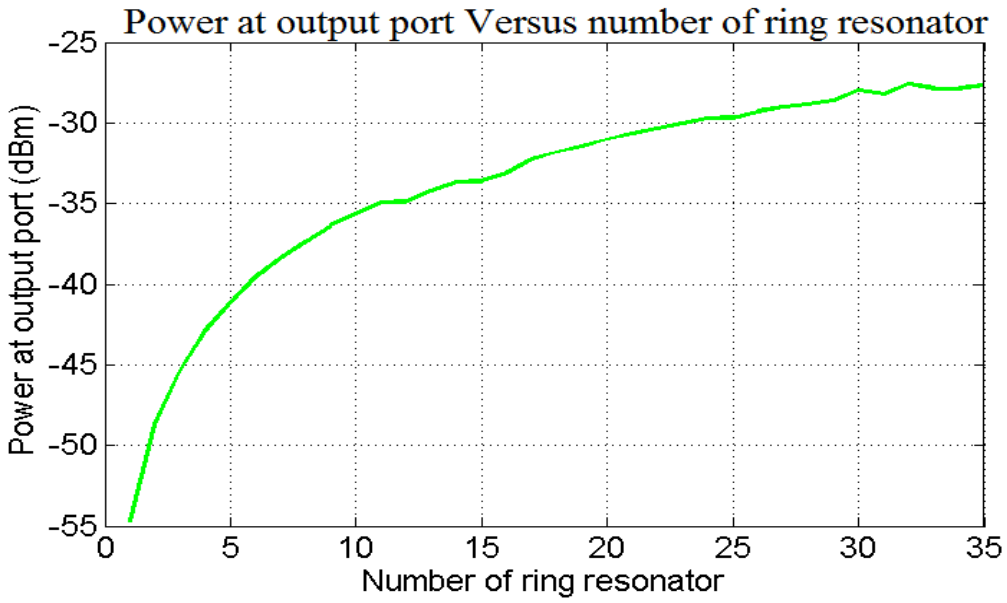

Figure 3.8: Power output (dBm) of array of IOMRs using Optisystem version 7.0

of 26 IOMRs offers an improvement in the optical output power relative to a single IOMR as shown in Figure 3.8. The array of 26 IOMRs has been designed using identical IOMRs resembling a cascaded structure. The individual IOMRs have been placed with the gap of $3l$, where l is the coupling length to ensure that interference does not occur between two consecutive IOMRs. For the simulation of results shown in Figure 3.8, an input signal with a power of -18.5 dBm at 1549.7 nm having a bandwidth of 7.85 nm is fed at the input of first IOMR and the output of the array with 26 IOMRs has been observed. It has been observed that further increase in the number of elements of the IOMR array beyond 26 does not show any further improvement in the power output. In addition, it results in the undesirable increase in bandwidth of frequency response characteristics. Therefore the number of elements in the IOMR array of IOEO is taken as 26 only. The bandwidth with an array of 26 IOMRs is found to be 2.5 nm, whereas the bandwidth with 35 IOMRs is

found to be 2.9 nm. The required power at the output of IOMRs has been obtained with an array of 26 IOMRs and hence only 26 IOMRs have been considered for the design of IOMR array. Before feeding to the photo diode, the output of the IOMR or IOMR array gets amplified in the optical domain itself through EDFA of 5 m length. The EDFA uses 980 nm as the pump signal. The amplified output of the IOMR/IOMR array is fed to the photo diode. The photo diode converts the optical signal into electrical signal. The output of the photo diode is found to be larger than 16 mA, which is sufficient enough for the LNA1 to function. In the next section, all the components and the simulation parameters of the IOEO used in the design of the model will be discussed.

3.3 Building Blocks of IOEO

In this section, a detailed discussion about the components of the designed IOEO are presented. Realization of the IOEO shown in Figures 3.2 and 3.6 needs detailed working of the individual blocks and integrated IOEO. Hence, studies have been carried out to get the details about the various components used in the IOEO. The analytical model of the designed IOEO is also presented. The formulation of the analytic model of the designed IOEO utilizes the transfer functions of the respective devices used in the design of the IOEO. Hence a detail study of the transfer function has been carried out. Finally a novel analytical model for the IOEO has been formulated and interpreted. The noise is one of the major criteria for the success of devices in the communication system. Hence, the noise associated with the components used in the design and modeling of the IOEO is discussed in the subsequent subsections.

3.3.1 Laser

The first important device used in the designed IOEO is the LASER. The LASER is an acronym for Light Amplification by Stimulated Emission of Radiation. In 1917 Einstein first predicted spontaneous and stimulated emission phenomenon. In 1960 Maiman demonstrated first Laser. Laser has been known for its high spectral purity or high temporal coherency. For the present case Laser is assumed to produce clean signal. Hence Continuous Wave (CW) Laser is used. It has both temporal and spatial coherency. Following parameters have been assumed for the simulation of InGaAsP Laser shown in Figure 3.4 using Optisystem version 7.0: wavelength of 1550 nm, frequency of 193.55 THz, power of 3.01 dBm with operating temperature of -20 to +70 degree Celsius. Its spectral width is 10

MHz and noise threshold is -100 dB. Figure 3.9 shows the power spectrum of laser source

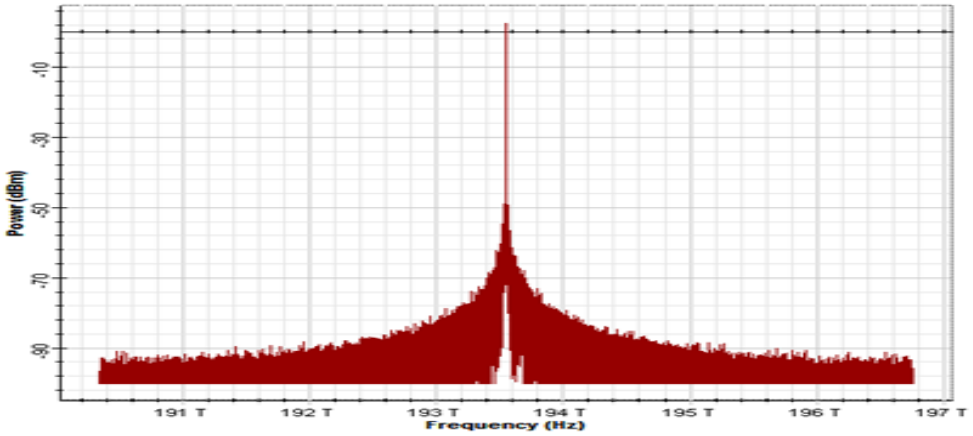

Figure 3.9: Power spectrum of the laser source with centre frequency of 193.55 THz using Optisystem version 7.0

used in the IOEO simulation. The center frequency is 193.55 THz. Following assumptions are associated with the chosen Laser: Zero reflection noise, No speckle at the output of the Laser and minimal mode partition noise.

3.3.2 Optical Modulator

Second significant device in IOEO is the Optical Modulator (OM). In the the optical communication system, there are two ways of modulating an optical signal: direct modulation and external modulation. In direct modulation a circuit is designed to modulate the current injected into the device. As the output of the source is controlled by the injected current, one can achieve the desired modulation. The upper modulation frequencies are limited to about 40 GHz. In external modulation, an optical signal from the source is passed through a material whose optical properties can be altered by external means. The device speed is controlled by the property of modulator. In the optical communication system, data is encoded in the form of the variation of some property of the optical output of a Light-Emitting Diode (LED) or a LASER. This property may be the intensity or the phase of the optical signal or the width of the pulses being transmitted.

In the designed IOEO an external single drive MZI on a Ti-diffused Lithium-Niobate intensity modulator is used. Figure 3.10 represents the cross sectional view of the single drive MZI on a Ti-diffused Lithium-Niobate intensity modulator. In the designed IOEO

model, the OM is assumed to be noise free. The structural details of the OM are shown in Figure 3.10. The OM works up to 40 GHz. In the designed OM, $LiNbO_3$ is the substrate

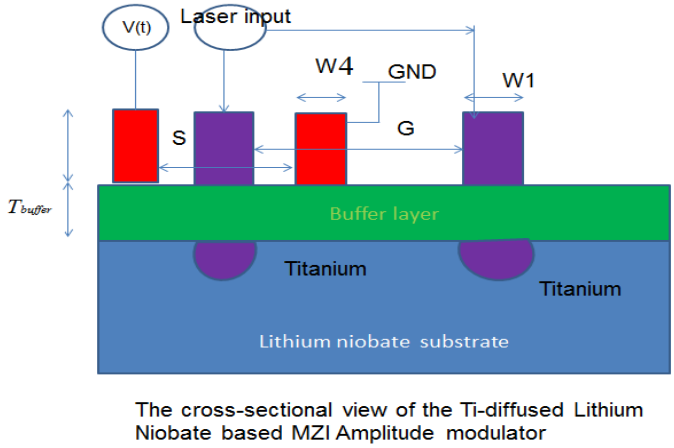

Figure 3.10: Cross sectional view of the single drive MZIM amplitude modulator (Binh, 2008)

material and diffused Ti acts as core of the optical waveguide. $Si0_2$ is the buffer layer and electrodes are made up of Gold. S is gap between modulating signal $v(t)$) electrode and ground electrode having width $W4$. G is gap between laser input and the electrode having width $W1$. T_{buffer} is the thickness of the buffer layer.

Transfer function of the OM is discussed in (Binh, 2008). The transfer function (Binh, 2008) of the MZIM is given by

$$T_{MZIM} = 0.5\{1 + \frac{2E_1E_2}{p_{in1}} cos[\pi \frac{v(t)}{V_\pi}] + \phi\} \tag{3.1}$$

$$T_{MZIM} = 0.5\{1 + 2 * r * cos[\pi \frac{v(t)}{V_\pi}] + \phi\} \tag{3.2}$$

where,

$$r = \frac{E_1E_2}{p_{in1}} \tag{3.3}$$

$r = 1$, if $E_1 = E_2$ i.e when input optical power p_{in1} gets equally distributed into the two arm of MZIM. E_1 and E_2 are the electric field input at the two arms of MZIM. ϕ is defined as DC phase due to bias voltage of the MZIM and given as $\phi = \Pi \frac{V_B}{V_\Pi}$.

Where, V_B is the DC bias voltage and V_π is the voltage required to generate a total phase change of π radians at DC bias .

Figure 3.11 shows the spectral response of the MZIM used in the IOEO simulation. The

bandwidth of the MZIM is observed as 193 THz to 194 THz. The value of peak power is found to be -2 dB at 193.5 THz. Following parameters have been assumed for the simulation of single drive MZIM: splitting ratio of 1; bias voltage of -2.8 V; V_π of -2.8 V; modulation voltage of 1.5 V and input optical power (p_{in1}) of 3.01 dB at 193.55 THz.

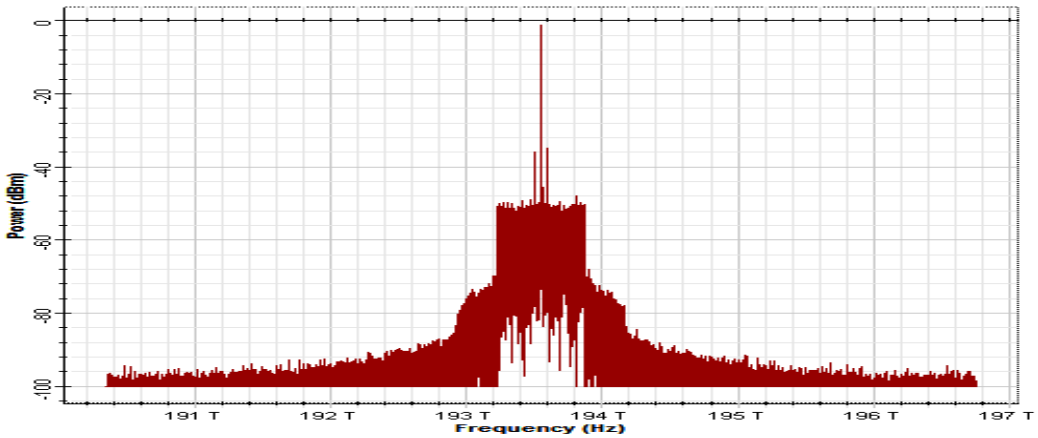

Figure 3.11: Power spectrum of the Mach-Zenhder Intensity Modulator (MZIM) using Optisystem version 7.0

3.3.3 Integrated Optical Micro-Ring Resonator

The third significant device used in the design of the IOEO is the IOMR. The IOMR used in the IOEO is of Silicon-on-Insulator (SOI) strip waveguide and laterally coupled architecture. The material for the manufacturing of the optical ring resonator is as follows: $Si0_2$ is the cladding layer for the bus waveguide and ring wave guide. Si is the substrate and also core of bus waveguide and core the ring wave guide.

A relevant 3D model of the IOMR has been drawn using software OptiFDTD version 8.0 and the 3D model is shown in Figure 3.12. The schematic has two straight waveguides and one ring waveguide. The ring waveguide has radius (R) and is separated by gap d from the straight waveguide on both sides. The IOMR has four ports namely input, through, drop and output port. The input port receives the optical input from the OM. At the through port, transmitted optical signal is received. The output port is the port where desired output is tapped and is fed to the EDFA. The remaining power gets transmitted at the drop port, which is the loss.

The total length of the straight bus waveguide should be multiple of coupling length l,

which is defined as the parallel running length between the two waveguides. The other straight waveguide length is also of equal length. The width of the bus waveguide and ring waveguide is kept the same (500 nm). The thickness of the core and clad is considered as 235 nm and 500 nm respectively.

The transfer function of IOMR of Figure 3.12, has been addressed (Okamoto, 2010)

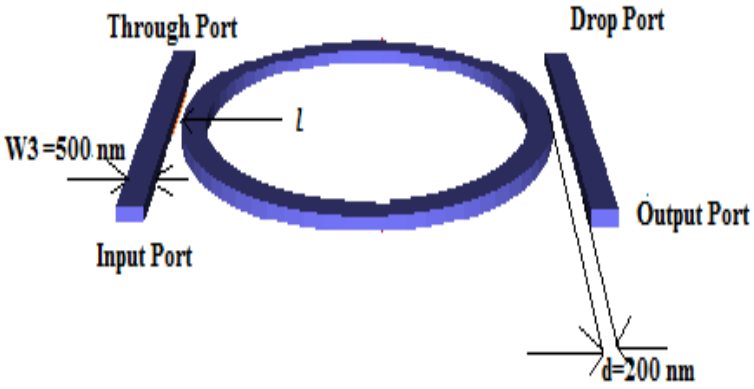

Figure 3.12: 3D model of an IOMR using OptiFDTD version 8.0

for its better coupling of the power from the input port to the output port at the desired wavelength in IOMR. The intensity transmittance of the optical ring resonator (Okamoto, 2010) is given by

$$T(\phi) = |\frac{E}{E_0}|^2$$

$$T(\phi) = \frac{p}{p_0} \tag{3.4}$$

$$T(\phi) = (1-\gamma)\frac{x_1^2(1-y_1)^2}{(1-x_1^2y_1^2)+4x_1^2y_1^2sin^2(\frac{\phi}{2})} \tag{3.5}$$

Where, the parameters x_1, y_1, and ϕ are defined by Equations (3.6), (3.7) and (3.8) respectively.

$$x_1 = (1-\gamma)^{\frac{1}{2}}exp(\frac{-\rho L}{2}) \tag{3.6}$$

$$y_1 = cos(kl) \tag{3.7}$$

$$\phi = \beta L \tag{3.8}$$

γ is intensity insertion loss, L is the circumference of the ring, ρ is intensity attenuation coefficient, β is the wave number, l is the coupling length and k is the coupling coefficient. The output power of the IOMR at the output port is given by.

$$P_{IOMR} = p_0(1-\gamma)\frac{x_1^2(1-y_1)^2}{(1-x_1^2y_1^2)+4x_1^2y_1^2sin^2(\frac{\phi}{2})} \tag{3.9}$$

Figure 3.13 shows the simulated output of IOMR used in the IOEO simulation. The IOMR works as a filter and allows only the signal of its resonated frequency at the output. The resonated frequency has been shown in Figure 3.13. Noise in the IOMR is a critical issue,

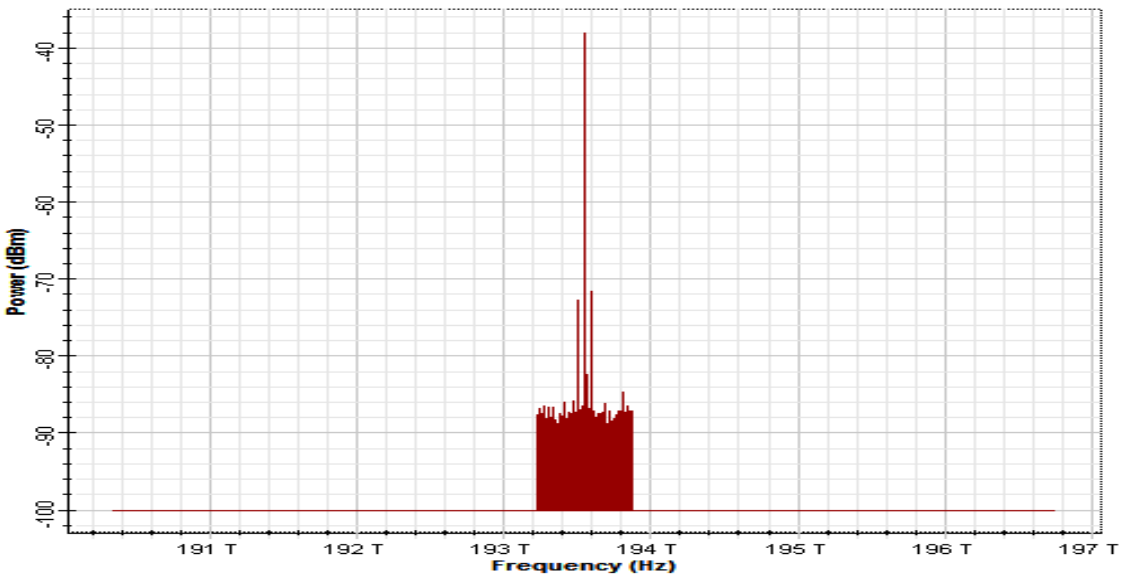

Figure 3.13: Output power spectrum of IOMR (Okamoto Model) using Optisystem version 7.0

which has been analysed extensively in this research work. Since IOMR is wavelength selective device, it introduces phase noise. The propagation of light inside the IOMR undergoes several round trips and finally intensity of the selected light appearing at the output port is a measure of power of the signal.

3.3.4 Design of Erbium Doped Fiber Amplifier

In the optical communication system, digital or analog signals from a transmitter are coupled into the optical fiber. As they propagate along the length of the fiber, these signals get attenuated due to absorption and scattering. The utility of the length of the optical fiber gets restricted because of attenuation and dispersion effects, which render the signal too weak and consequently become difficult to detect. The shape and strength of the signals are restored using either re-generator or an optical amplifier at an appropriate point along the length of the fiber.

A re-generator is an Opto-Electronic device. It amplifies the optical signal in three steps. The first step is to convert an optical signal into an electrical signal and then amplify it electronically. The second step is to improve the signal pulses using re-timing and pulse shaping circuits. The third step is to reconvert the electrical signal into an optical signal. An optical amplifier operates solely in the optical domain. There are two main classes of optical amplifiers, namely semiconductor optical amplifier and fiber amplifier. The semiconductor amplifier utilizes stimulated emission from injected carriers. In the fiber amplifiers, the gain is provided by either rare-earth dopants or stimulated Raman scaterring. Various rare elements such as Erbium (Er), Holmium (Ho), Neodymium (Nd), Samarium(Sm), or Ytterbium (Yb) are used as the doping element for the fabrication of a suitable optical fiber amplifier. The length of the optical fiber is generally about (10-30 m) for optical fiber amplifier. The optical amplifier doped with Erbium is known as EDFA (Khare, 2004). The design of EDFA with appropriate and desired length has been carried out for the IOEO, as shown in Figure 3.14. Equation 3.10, has been used for the design of EDFA (Keiser, 2013).

$$p_{signal,input} \leq \frac{\frac{\lambda_{pump}}{\lambda_{signal}} * power_{pump}}{Gain - 1} \tag{3.10}$$

Where, λ_{pump} is wavelength of the pump power, λ_{signal} is the signal power and $power_{pump}$ is the power of the forward pump signal.

In the existing design of IOEO, the EDFA has been designed for the gain of 40 dB. Hence the power at the output of the EDFA is given as

$$P_{EDFA} = 10000 * P_{inputatEDFA} \tag{3.11}$$

Following parameters have been considered for the design and simulation of the EDFA. The core radius of fiber is 2.2 μm; Er doping radius is 2.2 μm; Er metastable lifetime of

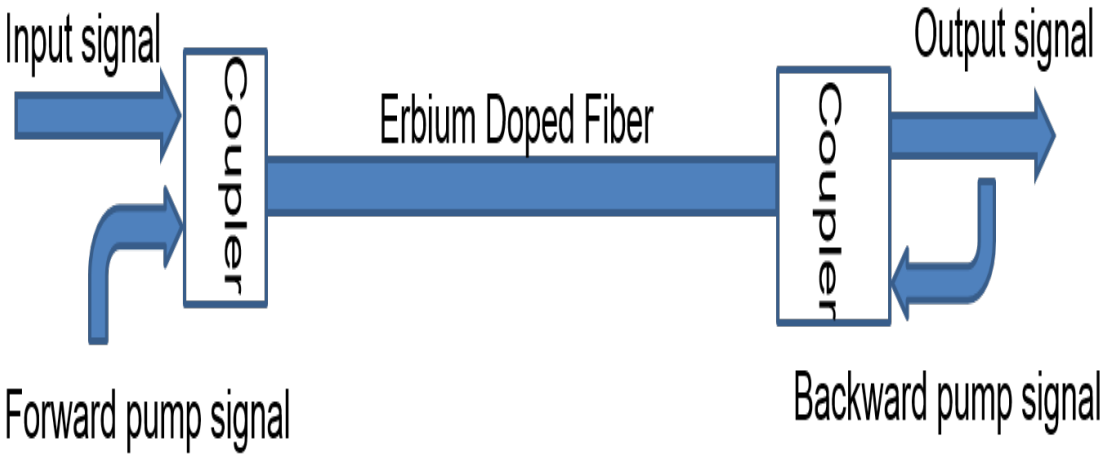

Figure 3.14: Schematic of EDFA

10 ms; numerical aperture of 0.24; loss at 1550 nm (λ_{signal})=0.1 dBm^{-1}; loss at 980 nm (λ_{pump})=0.2 dBm^{-1}; length of the fiber is 5 m; forward pump power of 100 mW; backward pump power of 0 mW; noise bandwidth of 13 THz and noise threshold of -100 dB. The computation of input signal power using Equation 3.10 results 6.32 μW. The input to the EDFA in the design of IOEO is -42 dBm, as shown in Figure 3.13, which satisfies the condition given in Equation (3.10). Figure 3.15 shows the output power spectrum of the

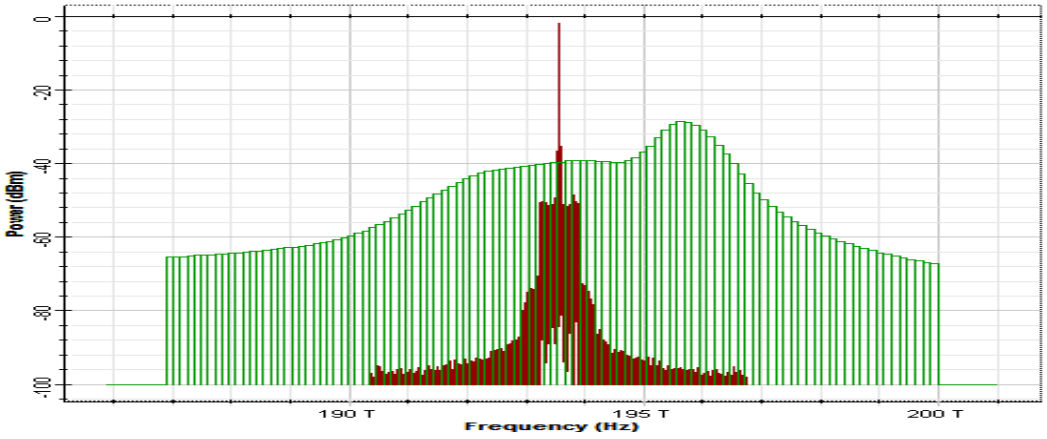

Figure 3.15: Output power spectrum of the EDFA using Okamoto model of IOMR using Optisystem version 7.0

EDFA. The noise along with the signal also gets amplified in the EDFA.

3.3.5 Photo Diode

In an Opto-Electronics system, it is required to convert an optical signals at the receiver end back into an electrical signals for further processing and display of the transmitted information. Figure 3.16 is a schematic representation of a photo diode. In the designed IOEO, photo diode is used to convert the output of optical EDFA into the electrical signal, which is ultimately fed to the LNA1. The requirements of photo diode are very similar to those of an Opto-Electronic source. It should have high sensitivity at operating wavelengths, high fidelity, fast response, high reliability, low noise and low cost. Further its size should be comparable with the immediate connecting device. The absorption of photons of a specific wavelength in a photo diode to produce electron-hole pairs and thus a photo current depends on the absorption coefficient of the semiconductor for that particular wavelength. If the total optical power incident on the photo diode is P_{in}, $V0$ is the biasing voltage of

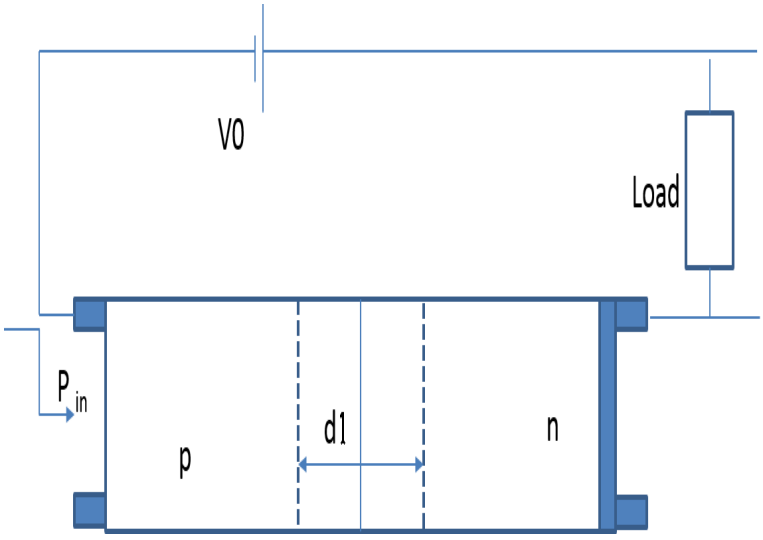

Figure 3.16: Schematic of photo diode

the photo diode and the Fresnel reflection coefficient at the air-semiconductor interface is R_3, then the optical power entering the semiconductor is $P_{in}(1-R_3)$. The power absorbed by the semiconductor is governed by $Beer's$ law (Khare, 2004). Thus, if the width of the absorption region is $d1$ and α is the absorption coefficient of the semiconductor at the incident wavelength, then the power absorbed by absorption region of width $d1$ is given by;

$$P_{abs} = P_{in}(1-R_3)[1-exp(-\alpha d1)] \tag{3.12}$$

The rate of photon absorption is given by Equation 3.13 (Khare, 2004), where, e is the electronic charge given as -1.602×10^{-19} Coulomb and h is Plancks constant given as $6.62607004 \times 10^{-34}\ m^2 kgs^{-1}$.

$$\frac{P_{abs}}{hf} = \frac{P_{in}(1-R_3)}{hf}[1-exp(-\alpha d1)] \tag{3.13}$$

The photo current (rate of flow of charge carriers) is represented as;

$$I_p = \frac{P_{in}e(1-R_3)}{hf}[1-exp(-\alpha d1)] \tag{3.14}$$

The Quantum efficiency of the photo diode is defined through;

$$\eta = \frac{\frac{I_p}{q}}{\frac{P_{in}}{hf}} \tag{3.15}$$

Where, q is the electronic charge. The responsivity of the photo diode is given by;

$$R_p = \frac{I_p}{P_{in}} = \frac{\eta q}{hf}[AW^{-1}] \tag{3.16}$$

The amplitude of optical signals at the receiver of an Opto-Electronic device is quite weak. Even the simplest kind of receiver requires good photo diode to be followed by an amplifier. (Keiser, 2013) Signal to Noise (S/N) ratio at the output of the receiver is given by;

$$\frac{S}{N} = \frac{SignalPower_{photocurrent}}{PD_{noisepower} + Amplifier_{Noisepower}} \tag{3.17}$$

$$\frac{S}{N} = \frac{I_p^2 M_1^2}{2e(I_p + I_d)\Delta f M_1^2 F(M_1) + \frac{4kT\Delta f}{R_L} + (i_{amp}^2)} \tag{3.18}$$

Where, I_d is the average primary dark current, which exists in PD without any input power, $< I^2 amp >$ is mean square noise current, $F(M_1)$ is the noise factor related to random nature of an avalanche process, Δf is the effective noise bandwidth, K is Boltzmann constant, R_L is the load resistance and M_1 is the multiplicative factor.

Photo diode is an optical component which converts the optical power into the electrical current. In the designed IOEO, PDCS12T 40 Gbs^{-1} InGaAs photo diode (Enablence, n.d.) has been used for the simulation. PDCS12T 40 Gbs^{-1} InGaAs photo diode is a high speed photo diode chip available with either a co-planar or a dual-pad layout. It has an optical aperture diameter of 12 μm. The photo diode has been optimized for single-mode data and

telecommunication applications up to 43 Gbs^{-1}. For wavelength of 1260 to 1620 nm, it exhibits a responsivity of 0.5 AW^{-1}. The photo diode has a low capacitance of less than 100 fF and has fast response of 0.5 AW^{-1} at a bias voltage of only 1.5 V. 50 ohm impedance is achieved through its co-planar pad structure, which provides matching condition when connected to a broadband amplifier. The PIN photo diode has the following features: it is top illuminated 40 Gbs^{-1} InGaAs photo diode, responsivity of 0.5 AW^{-1} at 1550 nm, capacitance of $<$100 fF, low dark current of 2 nA, low bias voltage of 1.5 V and operating temperature range of -40 to 85 degree Celcius. Figure 3.17 shows the simulated frequency response of the photo diode. The output of the photo diode is noisy. The noise power level is approximately same as the initial input excitation. It means it can be assumed that initial noise can be replaced by the output of the photo diode. This phenomenon substantiates that the designed IOEO works as an oscillator. The types of noise present in the Photo

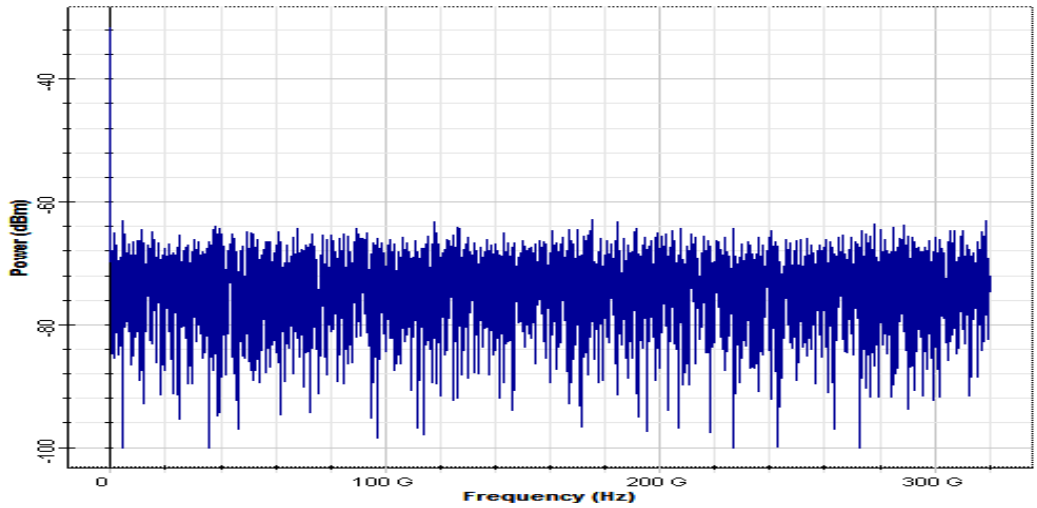

Figure 3.17: Frequency response of the photo diode using Okamoto model of IOMR using Optisystem version 7.0

diodes are quantum noise, thermal noise and dark current noise. The quantum noise is also known as shot noise. The types of noise in photo diodes are multiplicative in nature and are proportional to the input power of the photo diode. Thermal noise is the temperature dependent noise and is directly proportional to the square of the input power and the load resistance. In the simulation of photo diodes, dark current noise and thermal noise have been considered. For the simulation of the photo diode following parameters have been considered: input signal of -2 dBm with Amplified Spontaneous Noise (ASE) of EDFA,

responsivity of 0.5 AW^{-1}, dark current of 2 nA and thermal noise of $1 \times 10^{-22}\ WHz^{-1}$.

3.3.6 Low Noise Amplifier

Low Noise Amplifier (LNA) is a device to amplify a signal with very small amplitude. In the designed IOEO, the photo diode precedes the LNA so that the output of photo diode can be amplified to compensate the losses incurred in the preceding components. The LNA enables the possibility of retrieving the desired signal at various stages of the systems. It generally boosts the desired signal while adding insignificant level of noise in the system. The LNA should have low Noise Figure (NF) typically of 1 dB to 1.5 dB and a higher gain (about 20 dB). The performance metric of LNA are flatness of gain and stability. In addition, other parameters like Voltage Standing Wave Ratio (VSWR) and operating bandwidth are also equally important.

Because of the above stated need, Junction Gate Field-effect Transistor (JFET) and High Electron-Mobility Transistors (HEMTs) have been widely used in the design of LNA. These devices are high-current driven and helps in reduction of shot noise. The impedance matching circuits both at the input and output of LNA facilitate further increase in amplification. The four basic significant parameters in LNA design are: gain, noise figure, non-linearity and impedance matching.

Noise figure is a significant factor for determining the efficiency of a particular LNA. To have noise free reception of the signal, low noise figure of the LNA is must. Apart from the low noise figure, LNA should also have high gain for the post processing of signal. The low noise figure and high gain are required to avoid the attenuation in the LNA.

In this thesis, the RMLA31400 (Raytheon RF Components, 2002) has been used as LNA1 and LNA2 for the design of IOEO. The RMLA31400 is a three-stage MMIC LNA designed for 31 to 40 GHz operation. For the fabrication, GaAs MHEMT technique is important. Its application encompasses point to point as well as point to multi point scenario. A DC supply voltage of 1.9 V is required for its operation. The RMLA31400 has 16 mA supply current draw capability. The RMLA31400 LNA has the ability to achieve a small signal gain of 20 dB while maintaining a noise figure of 1.8 dB. The circuit contains individual source. This LNA has individual source vias, and the part is configured in a 2.5 mm x 1.25 mm x 100 μm package. Figure 3.18 shows the frequency response of the LNA1 used in the simulation of IOEO. The frequency response of LNA2 is the final output, which shows

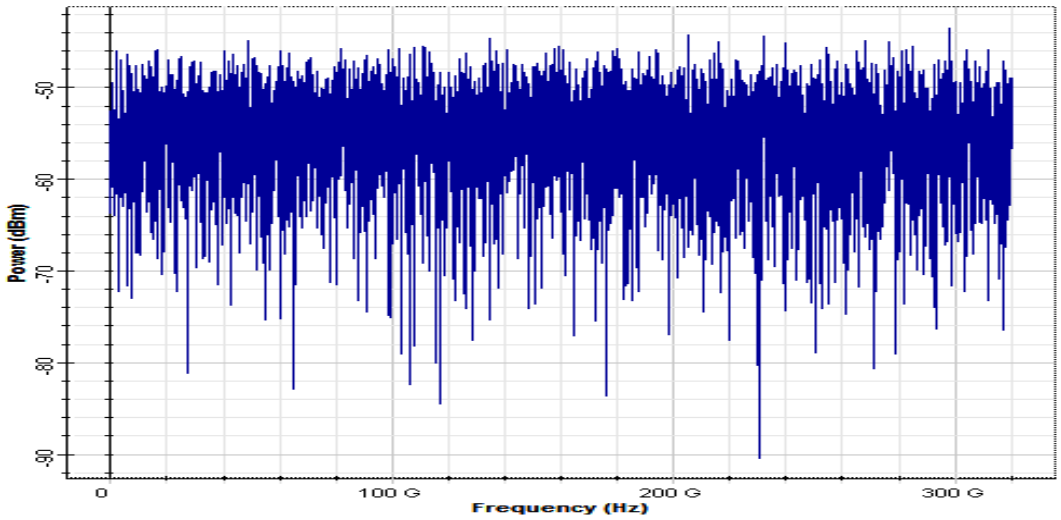

Figure 3.18: Output power spectrum of the LNA1 (Optisystem version 7.0 result)

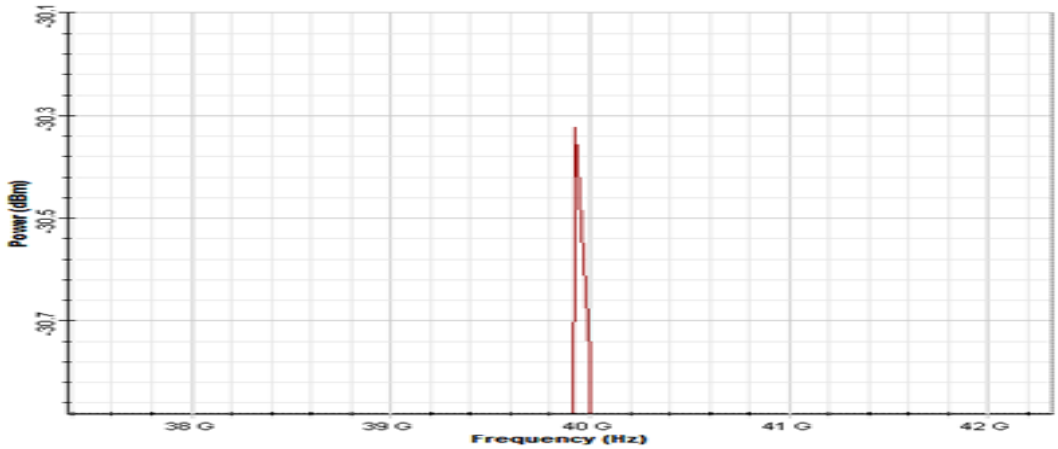

Figure 3.19: Output power spectrum of the LNA2 (Optisystem version 7.0 result)

the signal with -30 dBm of power at 40 GHz as shown in Figure 3.19.

3.3.7 Design of Band Pass Filter

Band Pass Filter (BPF) of 400 MHz bandwidth with a center frequency of 40 GHz has been used to filter the noise of the designed IOEO. The phase noise introduced by the band pass filter is significant in the present case. An integrated band pass filter of bandwidth of 400 MHz with a center frequency of 40 GHz can be fabricated on the same substrate where the other components of Opto-Electronic oscillators are fabricated. BPF has been realized using a combination of Low Pass Filter (LPF) and High Pass Filter (HPF). Equations 3.19 and 3.20 are used to calculate the cut-off frequency and the characteristic impedance of the LPF.

The schematic of Low Pass Filter is shown in Figure 3.20. The cut off frequency of low

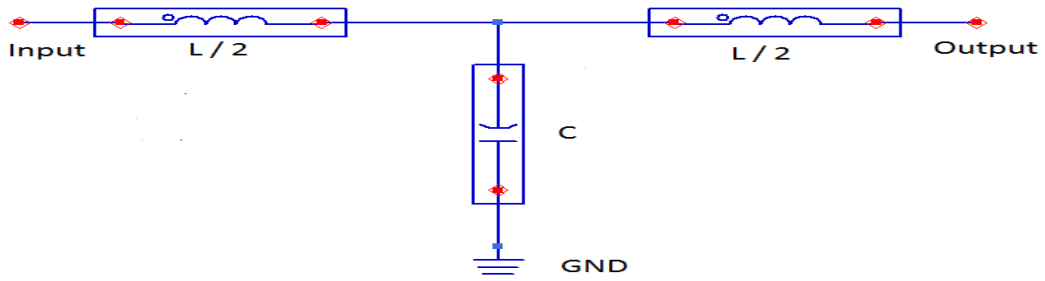

Figure 3.20: Schematic of T-Type low pass filter

pass filter (Pozar, 2009) is given as:

$$\omega_c = \frac{2}{\sqrt{LC}} \tag{3.19}$$

The characteristic input impedance is given as:

$$Z_0 = \sqrt{\frac{L}{C}} \tag{3.20}$$

The schematic of the High Pass Filer is shown in Figure 3.21. For the high pass filter, the analogous equations (Pozar, 2009) are:

$$\omega_c = \frac{1}{2\sqrt{LC}} \tag{3.21}$$

$$Z_0 = \sqrt{\frac{L}{C}} \tag{3.22}$$

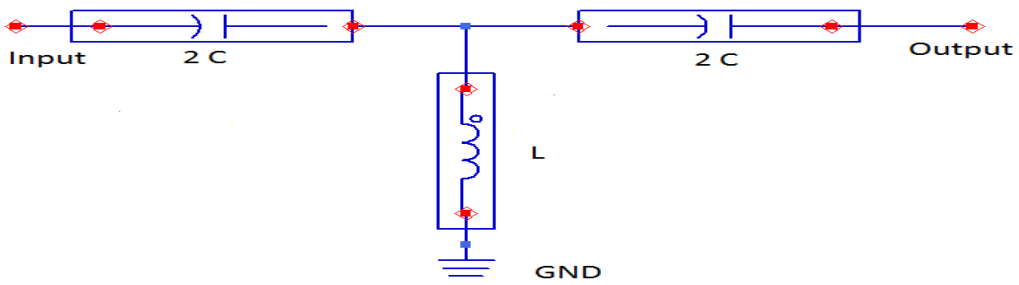

Figure 3.21: Schematic of T-Type high pass filter

A band pass filter is realized by cascading the LPF of Figure 3.20, with HPF of Figure 3.21.

The Figure 3.22 represents the schematic of BPF. The BPF has been realized using

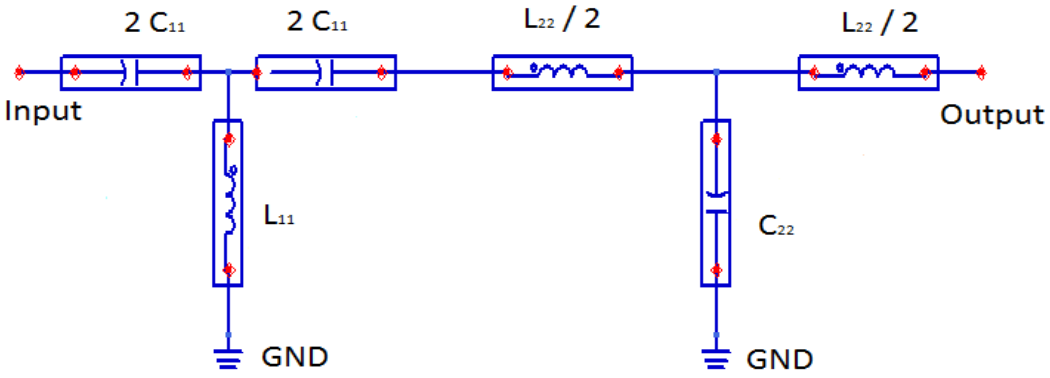

Figure 3.22: Schematic of band pass filter

HPF and LPF. The derivation of the voltage transfer function has been carried out using ABCD parameters of the BPF as shown in Figure 3.22. BPF has five cascaded elements Z_A, Z_B, Z_C, Z_D and Z_E respectively. All the five elements are defined as: $Z_A = \frac{1}{j\omega 2C_{11}}$, $Z_C = \frac{1}{j\omega 2C_{11}} + \frac{j\omega L_{22}}{2}$, $Z_D = \frac{1}{j\omega C_{22}}$, $Z_B = j\omega L_{11}$ and $Z_E = \frac{j\omega L_{22}}{2}$.

The system ABCD parameters of the Figure 3.22 has been calculated as follows.

$$\begin{pmatrix} A_{BPF} & B_{BPF} \\ C_{BPF} & D_{BPF} \end{pmatrix} = \begin{pmatrix} 1 & Z_A \\ 0 & 1 \end{pmatrix} * \begin{pmatrix} 1 & 0 \\ \frac{1}{Z_B} & 1 \end{pmatrix} * \begin{pmatrix} 1 & Z_c \\ 0 & 1 \end{pmatrix} * \begin{pmatrix} 1 & 0 \\ \frac{1}{Z_D} & 1 \end{pmatrix} * \begin{pmatrix} 1 & Z_E \\ 0 & 1 \end{pmatrix} \tag{3.23}$$

A methodology for the derivation of ABCD parameters of BPF has been discussed in Appendix A.4. The A_{BPF} of the BPF has been derived as follows:

$$A_{BPF} = (1 + \frac{Z_A}{Z_B}) + ((Z_C + \frac{Z_C Z_A}{Z_B}) + Z_A)\frac{1}{Z_D} \tag{3.24}$$

From the definition of ABCD matrix the voltage transfer function VTF_{BPF} of the system is defined as $= \frac{1}{A_{BPF}}$. Then the voltage transfer function of the BPF is given as

$$VTF_{BPF} = \frac{1}{(1 + \frac{Z_A}{Z_B}) + (Z_C + \frac{Z_C Z_A}{Z_B} + Z_A)\frac{1}{Z_D}} \tag{3.25}$$

Where,
$Z_A = \frac{1}{j\omega 2C_{11}}$, $Z_C = \frac{1}{j\omega 2C_{11}} + \frac{j\omega L_{22}}{2}$, $Z_D = \frac{1}{j\omega C_{22}}$, $Z_B = j\omega L_{11}$ and $Z_E = \frac{j\omega L_{22}}{2}$.

The power transfer function (PTF_{BPF}) of the BPF is given as:

$$PTF_{BPF} = 20 * log(VTF_{BPF}) \tag{3.26}$$

$$PTF_{BPF} = 20 * log(\frac{1}{(1 + \frac{Z_A}{Z_B}) + (Z_C + \frac{Z_C Z_A}{Z_B} + Z_A)\frac{1}{Z_D}}) \tag{3.27}$$

Capacitance and Inductance value of High Pass Filter: The capacitance and inductance to realize the HPF have been computed. Following data have been assumed for the computation: $R_0 = 50$ ohm, $\omega_c = 2\pi f$ and $f = 39.8 \times 10^9$ Hz.
The inductance value is computed as follows:

$$L_{11} = \frac{R_0}{2\omega_c} = 0.10002nH \tag{3.28}$$

The capacitance value is computed as follows:

$$C_{11} = \frac{1}{2\omega_c R_0} = 40.08fF \tag{3.29}$$

Capacitance and Inductance value of Low Pass Filter: The capacitance and inductance of the LPF have been computed. Following data have been assumed for the computation: $R_0 = 50$ ohm, $\omega_c = 2\pi f$ and $f = 40.2 \times 10^9$ Hz.

The inductance value is computed as follows:

$$L_{22} = \frac{2R_0}{\omega_c} = 0.39610nH \tag{3.30}$$

The capacitance value is computed as follows:

$$C_{22} = \frac{2}{\omega_c R_0} = 0.15884pF \tag{3.31}$$

Realization of Band Pass Filter:

The capacitance and inductance shown in the BPF of Figure 3.22 have been realized through microstrip line. A microstrip line is a planar transmission line, fabricated using photolithographic process. It can be easily integrated with other microwave devices. It consists of a conducting top layer of designed width and a conducting bottom layer serving as ground plane. The conducting top layer and the ground plane are separated by dielectric medium (usually FR-4) of desired height. The characteristic impedance of the microstrip line is a function of width of the top layer, dielectric constant of the medium and height of the dielectric medium. A short circuited microstripline (Pozar, 2009) has been used to realize the inductor and an open circuited microstripline has been used to realize the capacitor. The input impedance and the characteristic impedance of a shorted microstripline is given by:

$$Z_{in} = Z_0 \tan \frac{2\pi\sqrt{\varepsilon_{eff}}ll}{\lambda} \tag{3.32}$$

Where, Z_{in} is the input impedance, Z_0 is the characteristic impedance, λ is the wavelength, ε_{eff} is the effective dielectric constant of the medium and ll is the length of the microstripline.

To compute the length of the short circuited microstripline to realise the inductance L_{11} of Figure 3.22,

$$2\pi f L_{11} = Z_0 \tan \frac{2\pi\sqrt{\varepsilon_{eff}}ll}{\lambda} \tag{3.33}$$

Since $L_{11} = 0.10002$ nH, $f = 40$ GHz, $\lambda = \frac{3}{4}$ cm in free space and $Z_0 = 50\Omega$

Equation (3.33), can be rewritten as

$$25.137 = 50 \tan \frac{8\pi\sqrt{\varepsilon_{eff}}ll}{3} \tag{3.34}$$

Since,

$L_{11} = 0.10002$ nH, $\lambda f = c/\sqrt{\varepsilon}_{eff}$, where $\sqrt{\varepsilon_{eff}}$=$\sqrt{2.841}$ is the effective dielectric constant of the medium (For microstrip line width=0.0762 mm and FR-4 thickness of 0.3 mm) and c is speed of light given as 3×10^8 ms^{-1}.

Using Equation (3.34), one gets

$$\frac{25.137}{50} = \tan\frac{8\pi\sqrt{\varepsilon_{eff}}ll}{3} \tag{3.35}$$

Rearranging Equation 3.35, one gets

$$tan^{-1}\frac{25.137}{50} = \frac{8\pi\sqrt{\varepsilon_{eff}}ll}{3} \tag{3.36}$$

$$26.69\frac{\pi}{180} = \frac{8\pi\sqrt{\varepsilon_{eff}}ll}{3} \tag{3.37}$$

$$ll = \frac{26.69 \times 3}{8 \times 180 \times \sqrt{2.841}} \tag{3.38}$$

Hence the length of the short circuited microstripline to realise the inductor $L_{11} = 0.10002$ nH, is computed as $ll = 0.03297$ cm or (0.3297 mm).

Similarly a capacitor can be realised using an open circuited microstripline. The input impedance and the characteristic impedance of an open circuited transmission line is given by

$$Z_{in} = Z_0 cot\frac{2\pi\sqrt{\varepsilon_{eff}}ll}{\lambda} \tag{3.39}$$

and Impedance of the capacitance as $\frac{1}{2\pi f C_{11}}$ is used. Following data have been considered for the computation of length of the open circuited microstripline to realise the capacitor: $C_{11} = 40.08$ fF, $\lambda f = c/\sqrt{\varepsilon}_{eff}$, c is speed of light given as 3×10^8 ms^{-1}, $f = 40$ GHz and $\lambda = \frac{3}{4}$ cm in free space.

The length of the open circuited microstrip length to realise C_{11} of value 0.04008 pF of Figure 3.22, has been computed as follows:

$$\frac{1}{2\pi f C_{11}} = Z_0 cot\frac{2\pi\sqrt{\varepsilon_{eff}}ll}{\lambda} \tag{3.40}$$

Rearranging Equation (3.40), one gets $cot^{-1}\frac{99.27}{50} = \frac{8\pi\sqrt{\varepsilon_{eff}}ll}{3}$, which can be written as:

$$tan^{-1}\frac{1}{\frac{99.27}{50}} = \frac{8\pi\sqrt{\varepsilon_{eff}}ll}{3} \tag{3.41}$$

Equation (3.41) is further simplified as

$$26.73 = \frac{8\pi\sqrt{\varepsilon_{eff}}ll}{3} \tag{3.42}$$

$$26.73\frac{\pi}{180} = \frac{8\pi\sqrt{\varepsilon_{eff}}ll}{3} \tag{3.43}$$

On solving for the ll in Equation (3.43)

$$ll = \frac{26.73 \times 3}{8 \times 180 \times \sqrt{\varepsilon_{eff}}} \tag{3.44}$$

The length of the open circuited microstripline to realise a capacitance of 0.04008 pF has been computed as 0.03303 cm or 0.3303 mm.

Similarly computation of the inductor and and capacitance length for LPF has been computed as follows: To compute the length of the short circuited microstripline to realize the inductance L_{22} of value 0.39610 nH.

$$Z_{in} = Z_0 \tan\frac{2\pi\sqrt{\varepsilon_{eff}}ll}{\lambda} \tag{3.45}$$

Impedance of the inductance is also calculated as $2\pi f L_{22}$.

Hence one gets,

$$2\pi f L_{22} = Z_0 \tan\frac{2\pi\sqrt{\varepsilon_{eff}}ll}{\lambda} \tag{3.46}$$

Therefore,

$$2\pi f L_{22} = 50\tan\frac{8\pi\sqrt{\varepsilon_{eff}}ll}{3} \tag{3.47}$$

Since,

$Z_0 = 50$ ohm, $L_{22} = 0.39610$ nH, $\lambda f = c/\sqrt{\varepsilon}_{eff}$, c is speed of light given as $3 \times 10^8\ ms^{-1}$, $f = 40$ GHz and $\lambda = \frac{3}{4}$ cm.

Using Equation (3.47), we get

$$\frac{99.55}{50} = \tan\frac{8\pi\sqrt{\varepsilon_{eff}}ll}{3} \tag{3.48}$$

Rearranging Equation (3.48), one gets

$$tan^{-1}\frac{99.55}{50} = \frac{8\pi\sqrt{\varepsilon_{eff}}ll}{3}$$

From, the Equation (3.48), the length of the short circuited microstripline to realise the inductor $L_{22} = 0.39610$ nH has been computed and the length is computed as $ll = 0.07823$

cm or 0.7823 mm.

Similarly, the length of the open circuited microstripline for the capacitor $C_{22} = 0.15884$ pF, has been computed using,

$$Z_{in} = Z_0 cot \frac{2\pi\sqrt{\varepsilon_{eff}}ll}{\lambda} \tag{3.49}$$

and impedance of the capacitance as $\frac{1}{2\pi f C_{22}}$.

For the computation following data have been used: $C_{22} = 0.15884$ pF, $\lambda f = c/\sqrt{\varepsilon}_{eff}$, c is speed of light given as $3 \times 10^8\ ms^{-1}$, $f = 40$ GHz and $\lambda = \frac{3}{4}$ cm in free space.

The capacitor length computation is as follows:

$$\frac{1}{2\pi f C_{22}} = Z_0 cot \frac{2\pi\sqrt{\varepsilon_{eff}}ll}{\lambda} \tag{3.50}$$

Rearranging Equation (3.50), one gets $cot^{-1}\frac{25.05}{50} = \frac{8\pi\sqrt{\varepsilon_{eff}}ll}{3}$, which can be written as:

$$tan^{-1}\frac{1}{\frac{25.05}{50}} = \frac{8\pi\sqrt{\varepsilon_{eff}}ll}{3} \tag{3.51}$$

It is further simplified as:

$$63.38\frac{\pi}{180} = \frac{8\pi\sqrt{\varepsilon_{eff}}ll}{3} \tag{3.52}$$

Hence the length of the open circuited microstrip line to realize the capacitance of $C_{22} = 0.15884$ pF is computed as 0.07833 cm or 0.7833 mm.

The values of the capacitor, inductor and their corresponding length for the BPF as shown in Figure 3.22 have been calculated using microstripline concept. The value of microstripline length for the L_{22}, C_{22}, L_{11} and C_{11} have been computed. The schematic of the simulated BPF using Analog Design Simulator (ADS) version 2011.01 has been shown in Figure 3.23 and the s-parameters (s_{11} and s_{21}) have been shown in Figure 3.24. For the simulation following data are taken $C1 = 2C_{11}$, $C2 = 2C_{11}$, $L1 = L_{11}$, $L2 = L_{22}/2$, $L3 = L_{22}/2$ and $C3 = C_{22}$. From the results shown in Figure 3.23, it is obvious that the 3 dB bandwidth of the designed BPF is (34.5 GHz to 44.5 GHz) 10 GHz. Minimum reflection coefficient has been achieved at 40 GHz. However because of the large bandwidth, this designed filter is not used for the simulation of IOEO. Another BPF has been designed to get the narrower bandwidth of 400 MHz with 0 dB insertion loss. In order to design the BPF ADS version 2011.01 simulation environment has been used. The input and output ports have been terminated with the 50 ohms impedance for the frequency range of 39.8 GHz to 40.2

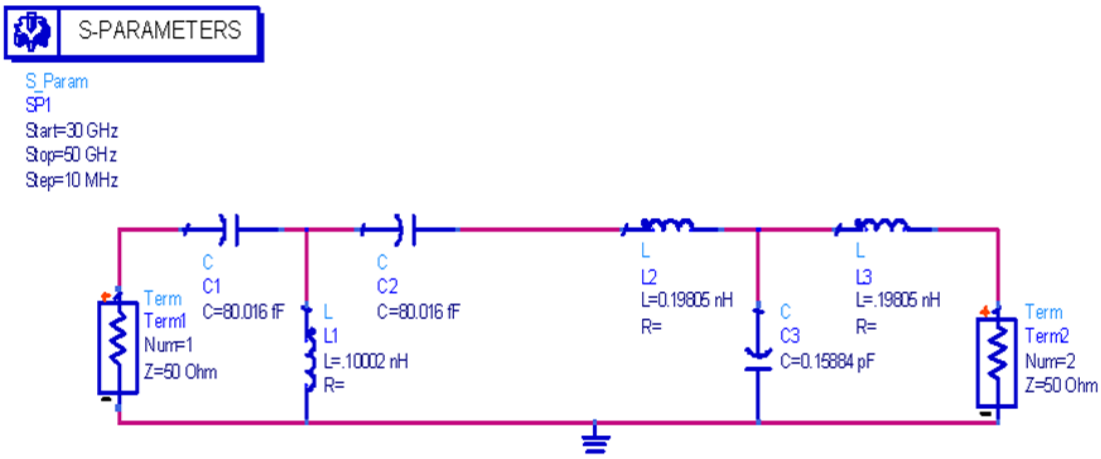

Figure 3.23: Schematic of band pass filter using ADS version 2011.01

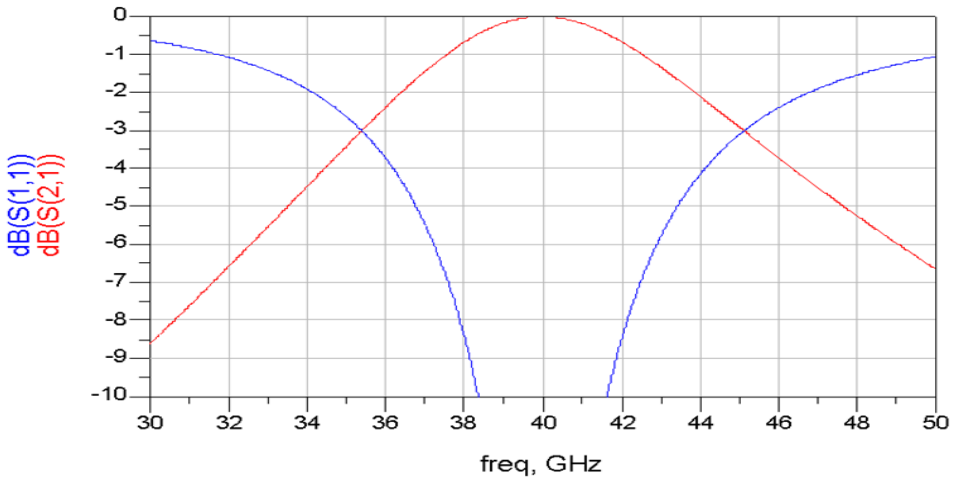

Figure 3.24: S_{11} and S_{21} profile of band pass filter using ADS version 2011.01

GHz. The BPF has twenty two elements. Figure 3.25 represents s_{11} and s_{21} profiles of the schematic of band pass filter as shown in the Figure 3.26. From the results of Figure 3.25, it is obvious that the 3 dB bandwidth of the designed RF band pass filter is (40.2 GHz-39.8 GHz) 400 MHz. Minimum reflection has been achieved at 40 GHz.

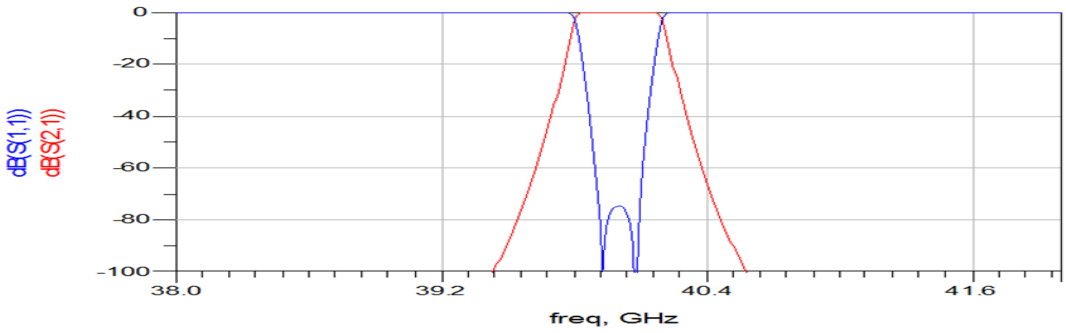

Figure 3.25: S_{11} and S_{21} profile of band pass filter using ADS version 2011.01

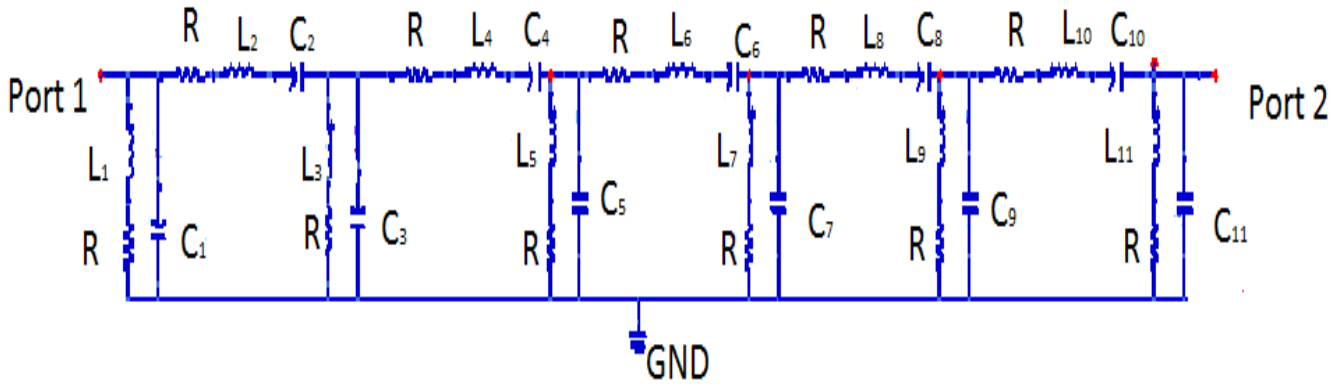

Figure 3.26: Schematic of band pass filter

The impedance of the individual cascaded elements for $f = 40$ GHz are given as follows:

$Z_1 = 1 \times 10^{-12} + 2 * 3.14 * f * L1;$

$Z_2 = (1./(2 * 3.14 * f * C1));$

$Z_3 = 1 \times 10^{-12} + 2 * 3.14 * f * L2;$

$Z_4 = (1./(2 * 3.14 * f * C2)\ ;$

$Z_5 = 1 \times 10^{-12} + 2 * 3.14 * f * L3;$

$Z_6 = (1./(2 * 3.14 * f * C3))\ ;$

$Z_7 = 1 \times 10^{-12} + 2 * 3.14 * f * L4;$

$Z_8 = (1./(2 * 3.14 * f * C4));$

$Z_9 = 1 \times 10^{-12} + 2 * 3.14 * f * L5;$

$Z_{10} = (1./(2 * 3.14 * f * C5));$

$Z_{11} = 1 \times 10^{-12} + 2 * 3.14 * f * L6;$

$Z_{12} = (1./(2 * 3.14 * f * C6));$

$Z_{13} = 1 \times 10^{-12} + 2 * 3.14 * f * L7;$

$Z_{14} = (1./(2 * 3.14 * f * C7));$

$Z_{15} = 1 \times 10^{-12} + 2 * 3.14 * f * L8;$

$Z_{16} = (1./(2 * 3.14 * f * C8));$

$Z_{17} = 1 \times 10^{-12} + 2 * 3.14 * f * L9;$

$Z_{18} = (1./(2 * 3.14 * f * C9));$

$Z_{19} = 1 \times 10^{-12} + 2 * 3.14 * f * L10;$

$Z_{20} = (1./(2 * 3.14 * f * C10));$

$Z_{21} = 1 \times 10^{-12} + 2 * 3.14 * f * L11;$

and $Z_{22} = (1./(2 * 3.14 * f * C11));$

Where,

$L_1 = 6.991246 \times 10^{-12} H;\ C_1 = 2.264522 \times 10^{-12} F;$

$L_2 = 16.52527 \times 10^{-9} H; C_2 = 0.958038 \times 10^{-15} F;$

$L_3 = 1.519343 \times 10^{-12} H\ ; C_3 = 10.420183 \times 10^{-12} F;$

$L_4 = 33.46519 \times 10^{-9} H\ ; C_4 = 0.473084 \times 10^{-15} F\ ;$

$L_5 = 1.036962 \times 10^{-12} H;\ C_5 = 15.267509 \times 10^{-12} F;$

$L_6 = 39.78048 \times 10^{-9} H; C_6 = 0.397983 \times 10^{-15} F;$

$L_7 = 1.036962 \times 10^{-12} H; C_7 = 15.267509 \times 10^{-12} F;$

$L_8 = 33.46510 \times 10^{-9} H\ ; C_8 = 0.473084 \times 10^{-15} F;$

$L_9 = 1.519343 \times 10^{-12} H; C_9 = 10.420183 \times 10^{-12} F;$

$L_{10} = 16.52527 \times 10^{-9} H; C_{10} = 0.958038 \times 10^{-15} F$;
$L_{11} = 6.991246 \times 10^{-12} H$; and $C_{11} = 2.284522 \times 10^{-12} F$;
All the inductors L_1 to L_{11} have been modelled with internal resistance of 1 p Ω in series with inductive elements.

The minimum capacitance and inductance required for the design of BPF with a pass band of 39.8 to 40.2 GHz are 0.397 fF and 1.0369 pH respectively. The achievable minimum length pertaining to the length of the conductive trace of the existing multilayer PCB is 0.0762 mm (Best Technology, n.d.). With FR4 as dielectric material of the PCB with a height of 0.3 mm and dielectric constant of 4.22, the minimum values of capacitance and inductance which can be realized through a microstrip line of length of 0.0762 mm are 0.1494 fF and 0.3754 pH respectively. The minimum value of inductance required for the design of BPF is 1.0369 pH which is larger than the minimum realizable inductance of 0.3754 pH. Similarly the minimum value of capacitance required for the design of BPF is 0.397 fF is larger than the minimum realizable capacitance of 0.1494 fF. Therefore all the inductors and capacitors needed in the design of BPF required in IOEO can be realised with existing precision of PCB technology. The computation of values of inductance and capacitance has been discussed in the Appendix A.7.

Apart from the PCB approach, the feasibility study on the fabrication of minimum values of capacitance and inductance required to realise the BPF of designed IOEO has also been carried out in Silicon-On-Insulator (SOI) processes. Using 0.18 μm (180 nm) SOI technology (X-FAB, n.d), the minimum realizable capacitance is 0.13 fF, but the minimum capacitance required in the BPF of designed IOEO is 0.397 fF and hence it can be fabricated with the precision realizable in the prevalent 180 nm SOI technology. With the existing 45 nm SOI technology from Cadence Virtuoso version 6.1.6, the minimum integrated planar inductance of 79 pH can be modelled. Therefore the inductance of 1.0369 pH which is the minimum required inductance in BPF of designed IOEO cannot be realised using 45 nm SOI technology. In the report from Global Foundries on 22 nm FD-SOI platform (GLOBALFOUNDRIES, 2016), it is stated that the platform is suitable for RF applications. Hence the realization of inductance of 1.0369 pH can be explored using integrated planar 2D or 3D structure with the existing 22 nm/ 14 nm/7 nm/5 nm SOI technologies.

The ABCD parameters of the BPF as shown in Figure 3.26 has been calculated using all the cascaded elements.

$$\begin{pmatrix} A_{NEWBPF} & B_{NEWBPF} \\ C_{NEWBPF} & D_{NEWBPF} \end{pmatrix} = \begin{pmatrix} 1 & 0 \\ \frac{1}{Z_1} & 1 \end{pmatrix} \begin{pmatrix} 1 & 0 \\ \frac{1}{Z_2} & 1 \end{pmatrix} \begin{pmatrix} 1 & Z_3 \\ 0 & 1 \end{pmatrix} \begin{pmatrix} 1 & Z_4 \\ 0 & 1 \end{pmatrix} \times \begin{pmatrix} 1 & 0 \\ \frac{1}{Z_5} & 1 \end{pmatrix} \begin{pmatrix} 1 & 0 \\ \frac{1}{Z_6} & 1 \end{pmatrix} \begin{pmatrix} 1 & Z_7 \\ 0 & 1 \end{pmatrix} \begin{pmatrix} 1 & Z_8 \\ 0 & 1 \end{pmatrix} \times \begin{pmatrix} 1 & 0 \\ \frac{1}{Z_9} & 1 \end{pmatrix} \begin{pmatrix} 1 & 0 \\ \frac{1}{Z_{10}} & 1 \end{pmatrix} \begin{pmatrix} 1 & Z_{11} \\ 0 & 1 \end{pmatrix} \begin{pmatrix} 1 & Z_{12} \\ 0 & 1 \end{pmatrix} \times \begin{pmatrix} 1 & 0 \\ \frac{1}{Z_{13}} & 1 \end{pmatrix} \begin{pmatrix} 1 & 0 \\ \frac{1}{Z_{14}} & 1 \end{pmatrix} \begin{pmatrix} 1 & Z_{15} \\ 0 & 1 \end{pmatrix} \begin{pmatrix} 1 & Z_{16} \\ 0 & 1 \end{pmatrix} \times \begin{pmatrix} 1 & 0 \\ \frac{1}{Z_{17}} & 1 \end{pmatrix} \begin{pmatrix} 1 & 0 \\ \frac{1}{Z_{18}} & 1 \end{pmatrix} \begin{pmatrix} 1 & Z_{19} \\ 0 & 1 \end{pmatrix} \begin{pmatrix} 1 & Z_{20} \\ 0 & 1 \end{pmatrix} \times \begin{pmatrix} 1 & 0 \\ \frac{1}{Z_{21}} & 1 \end{pmatrix} \begin{pmatrix} 1 & 0 \\ \frac{1}{Z_{22}} & 1 \end{pmatrix} \quad (3.53)$$

From the definition of ABCD matrix, the voltage transfer function VTF_{NEWBPF} of the BPF is defined as $= \frac{1}{A_{NEWBPF}}$. Using the voltage transfer function VTF_{NEWBPF} of the ADS generated BPF, the S parameters such as S_{11} and S_{12} have been plotted as shown in Figure 3.25. Figure 3.27 depicts the output of the BPF shown in Figure 3.26. The power of 40 GHz signal has been observed as -50 dBm.

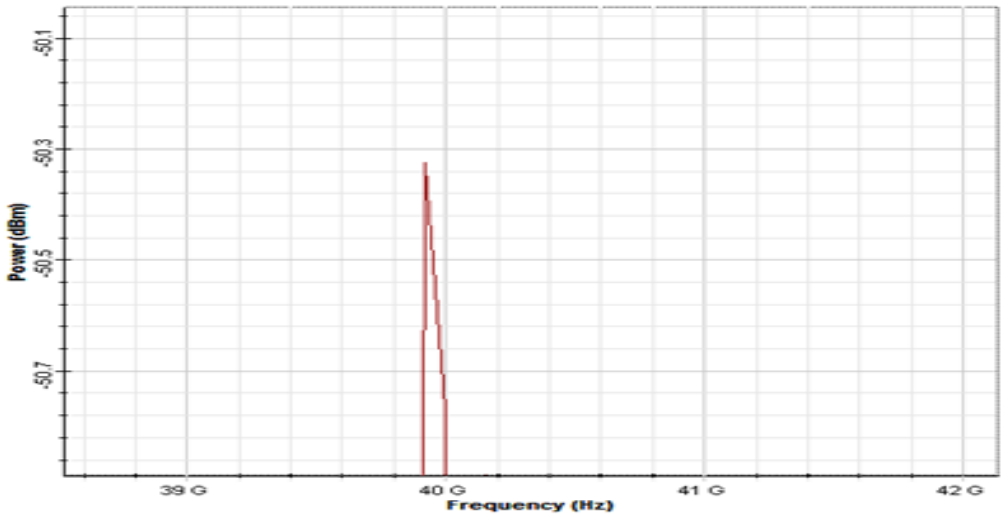

Figure 3.27: Power spectrum of the band pass filter

3.4 Principles of IOEO

In the previous sections, all the individual components or sub systems of IOEO depicted in the schematic representation of proposed IOEO shown in Figure 3.2 have been explained. The simulation results on the key performance parameters of the sub systems have also been presented. The initial excitation of an oscillator is by the thermal noise in the forward path. The feedback is taken from the output of the forward path and is fed to the optical modulator. In the designed IOEO, 1550 nm (193 THz) has been chosen as the optical carrier and it is also fed to the optical modulator. The output of the optical modulator is fed to the array of 26 IOMR or single IOMR. The output port of the IOMR is connected to the EDFA. The EDFA of 40 dB gain has been used at the output of the modulator. EDFA is purely an optical amplifier and is generally used to amplify the signal level significantly. The pump signal for the EDFA is at a wavelength of 980 nm. The output of the EDFA is fed to the PIN photo diode. A 50 Ω load resistance is used at the output of the photo diode. The output of the photo diode is an input to the LNA. The output of the first stage LNA is given to the microstrip based integrated band pass filter of 400 MHz bandwidth. The output of the BPF is again fed to the second stage LNA. The final output of the second stage LNA is connected to the optical modulator.

Various optical and electrical devices could be used to customize the performances of the designed architecture of IOEO. The low noise amplifier which is a gain element and the

microstrip based band pass filter have been used in the electrical domain of the system. In the designed IOEO, the Continuous Wave (CW) laser has been used which generates signal at 1550 nm, and the optical modulation has been achieved through Mach-Zehnder Interferometer (MZI).

In the IOEO, phase, amplitude and polarization modulators can be used and minimum dissipation loss in the optical domain could be achieved. In the present IOEO design, intensity modulation technique has been used for the simulation. Since the quality factor (Q) is dependent on the length of fiber, the designed IOEO with high Q is achieved through the circulations of the light energy in the designed IOMR. The variation in the operating frequency is possible in IOEO. The band pass filter could be used to tune the operating frequency of the IOEO. The variable frequency could be achieved by changing the wavelength of the laser source. In the designed IOEO, a novel architecture for the BPF has been used to realize the operating frequency as 40 GHz. The optical gain of IOMR is coupled to electrical part of the IOEO via optical modulator. This type of configuration is known as Coupled Opto-Electronic Oscillator (COEO).

The gain of the delay line oscillator is represented by Equation (3.54). To provide sustained oscillation, an oscillator must satisfy Barkhausen criteria. The Barkhausen criteria for the sustained oscillation are dealt in (Millman and Halkias, 1972) are given by

$$Gain = \frac{A}{1 - \mid A\beta \mid} \tag{3.54}$$

where A is forward path gain and β is the reverse path gain. For the oscillator stability it should satisfy the condition of magnitude $\mid A\beta \mid = 1$ and phase $\mid A\beta \mid = 0^0$ respectively. If $\mid A\beta \mid < 1$, then the oscillation dampens fast. If $\mid A\beta \mid > 1$, then the gain of oscillation builds up. Hence Equation (3.54) must be satisfied to achieve sustained oscillation.

3.5 Analytical Formulation of the IOEO

In this section, analytical formulation of the designed IOEO has been carried out. An expression of output voltage $v(t)$ has been derived for the designed IOEO. The derived voltage expression depicts the behaviour of the designed oscillator. As discussed in the previous section, the designed IOEO consists of electrical (LNA1, BPF and LNA2) as well as optical components (OM, IOMR, EDFA and PD). The Photo Diode (PD) is basically an opto electronic components of IOEO which converts optical power into electrical current and a voltage gets developed across the load (R_L) of the PD. The voltage V_p across the

Photo Diode (PD) used in IOEO (Figure 3.2) has been computed using ohm's law as shown in Equation (3.55).

$$V_p = I_p * R_L \tag{3.55}$$

Where,

I_p is the photo current and the load resistance R_L is 50Ω.

The photocurrent of the PD is given by

$$I_p = p_{in}\frac{\eta q}{hf} \tag{3.56}$$

Where,

f is frequency of operation, h is the planck's constant, η is the quantum efficiency of PD, q is the electronic charge and P_{in} is the total optical power incident on the photo diode.

Substituting the value of I_p and R_L in Equation (3.55), V_p is written as:

$$V_p = p_{in}\frac{\eta q}{hf} * R_L \tag{3.57}$$

Derivation of P_{in}

A derivation for the optical power P_{in} which is the optical power at the input of the PD is as follows:

The output of EDFA (P_{EDFA}) is fed to the PD. Since the gain of the EDFA (G_{EDFA}) is 40 dB or 10000, the EDFA output is considered as $G_{EDFA} * P_{inputatEDFA}$, Hence P_{in} is written as

$$P_{in} = P_{EDFA} = G_{EDFA} * P_{inputatEDFA} \tag{3.58}$$

Where,

$P_{inputatEDFA}$ is the input to the EDFA

P_{EDFA} is the output power of EDFA

$P_{inputatEDFA}$ is computed as $P_{inputatEDFA} = P_{IOMR}$, P_{IOMR} is the output power of the IOMR and given as $P_{IOMR} = T(\phi) * p_0$. The $T(\phi)$ is the transmittance of IOMR and p_0 is the modulated output power of Optical Modulator.

The expression of p_{in} can be rewritten as:

$$P_{in} = G_{EDFA} * P_{IOMR} = G_{EDFA} * T(\phi) * p_0 \tag{3.59}$$

The modulated output power of Optical Modulator (p_0) is represented through

$$p_0 = 0.5\{1 + 2 * r * cos[\pi\frac{v(t)}{V_\pi}] + \phi\} \tag{3.60}$$

and $T(\phi)$ is given by

$$T(\phi) = 1-\gamma)\frac{x_1^2(1-y_1)^2}{(1-x_1^2y_1^2)+4x_1^2y_1^2sin^2(\frac{\phi}{2})} \tag{3.61}$$

Substituting the value of $T(\phi)$ and p_0 in Equation (3.59), the expression of the p_{in} is derived as:

$$P_{in} = G_{EDFA}*(1-\gamma)\frac{x_1^2(1-y_1)^2}{(1-x_1^2y_1^2)+4x_1^2y_1^2sin^2(\frac{\phi}{2})}*p_0 \tag{3.62}$$

Substituting the value of p_0 in Equation (3.62), the P_{in} is given as:

$$P_{in} = G_{EDFA}*(1-\gamma)\frac{x_1^2(1-y_1)^2}{(1-x_1^2y_1^2)+4x_1^2y_1^2sin^2(\frac{\phi}{2})}*0.5\{1+2*r*cos[\pi\frac{v(t)}{V_\pi}]+\phi\} \tag{3.63}$$

Derivation of V_p

The expression for the voltage across the PD can be derived through the following steps. Substituting the value of derived P_{in} in Equation (3.57), the voltage across the photodiode V_p is given as:

$$V_p = G_{EDFA}*(1-\gamma)\frac{x_1^2(1-y_1)^2}{(1-x_1^2y_1^2)+4x_1^2y_1^2sin^2(\frac{\phi}{2})}*0.5\{1+2*r*cos[\pi\frac{v(t)}{V_\pi}]+\phi\}\frac{\eta q}{hf}*R_L \tag{3.64}$$

In the designed IOEO, the output (V_p) is fed to the forward path of Figure 3.2 and then the final output is measured at the output of *LNA*2.

The output voltage $v(t)$ which is an output of *LNA*2 is expressed finally as

$$v(t) = G_{EDFA}*(1-\gamma)\frac{x_1^2(1-y_1)^2}{(1-x_1^2y_1^2)+4x_1^2y_1^2sin^2(\frac{\phi}{2})}*0.5\{1+2*r*cos[\pi\frac{v(t_0)}{V_\pi}]+\phi\}\frac{\eta q}{hf}*R_L*G_F \tag{3.65}$$

Where, G_F is the gain of the forward path and $v(t_0)$ is the initial voltage output at *LNA*2. The initial modulating signal $v(t_0)$ is the electrical output from the *LNA*2. To get the initial modulating signal, the *LNA*1 is excited with the thermal noise p_{noise} and it is then fed to the Band Pass Filter and finally fed to the input of *LNA*2. Hence, the $v(t_0)$ is defined as

$$v(t_0) = p_{noise}*G_{_{LNA1}}*VTF_{BPF}*G_{LNA2} \tag{3.66}$$

Where,

p_{noise} is the thermal excitation noise, the gain of $G_{_{LNA1}}$ and G_{LNA2} is 20 dB, VTF_{BPF} is the

voltage transfer function of the band pass filter, which in the present case is negligible (in the range of 10^{-25}). The forward gain G_F can be approximated as the value of gain of cascaded G_{LNA1} and G_{LNA2}.

The expression for the $v(t)$ is further simplified by assuming following data: p_{noise} is the thermal excitation noise ; the gain of $LNA1$ and $LNA2$ is 20 dB; n=2.44 refractive index of the medium;$\gamma = 0.023$ W; $x = (1-\gamma)^1/2 * exp(-\rho * L1/2)$; $\rho = 0.023 * 10^2$ Watt/m; $y = cos(k*l)$; k is coupling coefficient of (638 mm^{-1}) and l is coupling length of $(0.262k^{-1})$.

where,

R is ring radius given as R=3.5973 μm, $\phi = \beta * L1$,

$L1 = 2*3.14*$ R, $\beta = ((2*3.14)/(\lambda))$ and $r = 1$ in case of single drive MZIM.

The output voltage $v(t)$ which is the output of $LNA2$ in the designed IOEO is expressed finally as

$$v(t) = G_{EDFA} * 0.2328 * 0.5\{1 + 2*1*cos[\pi\frac{v(t_0)}{V_\pi}] + \phi\}\frac{\eta q}{hf} * R_L * G_F \tag{3.67}$$

$$v(t) = 0.12G_{EDFA}\{1 + 2cos[\pi\frac{v(t_0)}{V_\pi}] + \phi\}\frac{\eta q}{hf} * R_L * G_F \tag{3.68}$$

3.6 Summary

In this chapter a novel Linear Time Invariant (LTI) architecture of IOEO has been proposed and analysed. In the proposed architecture, the long optical fiber has been replaced by an optical micro-ring resonator (IOMR). Use of IOMR significantly reduces the size of the oscillator and thereby facilitating its integration on a single chip. The replacement of long optical fiber by a compact micro ring resonator leads to significant reduction in the propagation loss which in turn increases the quality factor (Q) of the oscillator.

To facilitate better appreciation of the underlying principles of the architecture of the proposed IOEO, a technical description of all the sub components of the functional block of IOEO has been presented with requisite and pertinent details. The simulation results emphasising the important performance attribute of each sub system or block have also been presented. Keeping in view the feasibility and the practical relevance of the proposed architecture, for the simulation of performance measures of various components/devices, fairly well known and published structural configurations of devices have been chosen. A significant deviation of the architecture of proposed IOEO is the placement of components

belonging to optical domain in the feedback path which in turn reduces the size of the IOEO, increases the quality factor and thermal stability. It also reduces the phase noise of the IOEO.

CHAPTER 4

THE ANALYSIS OF AN INTEGRATED OPTICAL MICRO-RING RESONATOR

4.1 Introduction

In this chapter design and analytical study on the performance parameters of IOMR are presented. The design and quantification of the various parameters such as Quality factor (Q), Ring radius (R), Free Spectral Range (FSR) and Phase noise have been discussed through the development of expressions relating them. The CMT which is a fundamental principle explaining the transfer of power from the one port to another in the optical domain has also been addressed. An application of the CMT to analyse the significance of the gap between the straight waveguide and the curved waveguide on the performance of IOMR relevant to IOEO has been analyzed through a development of an analytical model. The IOMR is well known for its high quality factor and negligibly small phase noise. The usage of the IOMR in the generation of the sinusoidal frequency has been reported extensively in the literature. This chapter further substantiates the utility of IOMR for the generation of a signal at frequency as high as 40 GHz.

4.2 Analysis of Integrated Optical Micro Ring Resonator

The traditional Fabry-Perot (FP) resonators, introduced by Charles Fabry and Alfred Perot in 1899 (Renk, 2012) are complex and expensive devices, bulky in size, tough in assembly and susceptible to instability. The conventional FP exhibits low quality factor and hence is not used in optical communication application. Search for the resonator with high quality factor has resulted in monolithic resonators such as Whispering Gallery Mode Resonators (WGMR), in which the closed trajectories of light follow total internal reflection in curved and polygon structures. The circular optical modes in such resonators are WGM supported by total internal reflection (A. B. Matsko and Ilchenko, 2006).

Lord Rayleigh extensively explored propagation of sound over a curved gallery surface

of WGM. The WGM has unique spectral properties such as narrow line width, tunability and high stability. The high quality factor could be achieved in WGM with small volume. The simplest geometry of such resonator is either ring or cylinder or sphere. There are various optical resonator structures available to be used for the generation of pure sinusoidal frequency. To name a few one can use race track resonator, filled disk and optical delay line. The small size and better mechanical stability make race track resonator, filled disk and optical delay line suitable for many engineering applications such as oscillator and phase shifters. The WGMR can be used in OEO. It generates microwave signals using photonics techniques. Fabrication of WGMR claiming low threshold and low power consumption (Savchenkov et al., 2010) have been reported in the literature. The disadvantages of WGMR are low output power and high phase noise.

There are single bus and dual bus configurations of IOMR. The dual bus architecture of the IOMR is shown in the Figure 4.1. In dual bus architecture of IOMR, there are two straight waveguides and one circular waveguide. The width and thickness of each waveguide are kept same. The gap between straight and curved waveguides is shown by d. $W3$ is the width of each waveguide. k_{ab} represents the coupling coefficient between straight and curved waveguides, l is the coupling length. The resonance condition of the IOMR depends

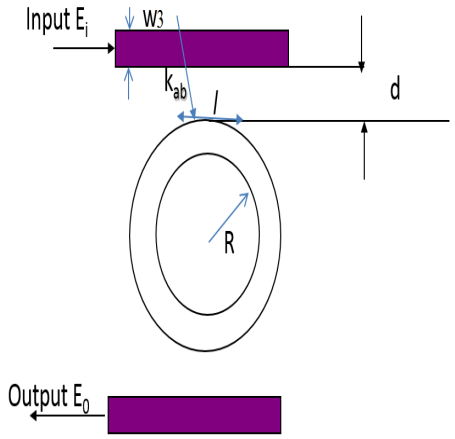

Figure 4.1: Schematic of the single IOMR

on the geometry (De Vos et al., 2007) of the device. The basic equation describing the resonance condition of the IOMR is given by

$$m\lambda = 2\pi nR \tag{4.1}$$

Where,

m is the mode number, λ is the resonance wavelength, n is the effective refractive index

and R is the ring radius. Various structures of the optical ring resonator are in use such as elliptical, race track and circular geometry.

The finesse is another key specification of the IOMR and it is defined (Kominato et al., 1992) as

$$F = \frac{FSR}{\Delta\lambda_{FWHM}} \tag{4.2}$$

$$F = \frac{\pi}{2sin^{-1}(\frac{1-R_1}{2\sqrt{R_1}})} \tag{4.3}$$

where,

$R_1 = e^{-\alpha}(1-K_2)$, α is the total amplitude attenuation coefficient for each round trip of the circular waveguide of IOMR, and K_2 is the normalized coupling coefficient between straight and curved waveguides of the IOMR separated by distance d.

FSR stands for the Free Spectral Range which signifies the separation between two resonance conditions of the same IOMR. The other significant parameter of IOMR is the Quality factor (Q) which deals with the power dissipation capability. Higher the Q, lesser dissipative the IOMR is. Other factors such as Field Enhancement (FE), Full Width Half Maximum (FWHM) also have their own significance in the analysis of the IOMR.

Parameters such as FSR and Quality factor (Q) of the IOMR have been analysed by, (Binh, 2008) through simulation. The mathematical expressions for the FSR and Q of the ring resonator have been given in Equations (4.4) and (4.5) respectively.

$$FSR = \frac{\lambda^2}{n_r L} \tag{4.4}$$

$$Q = \frac{\pi n_r L \pi\sqrt{ar}}{\lambda(1-ar)} \tag{4.5}$$

$$a = exp\frac{-\rho L}{2} \tag{4.6}$$

Where, λ is resonance wavelength, a is attenuation factor, ρ is propagation loss, n_r is effective refractive index, r is transmission factor and L is the circumference of the optical ring resonator. The propagation loss ρ has been computed as

$$\rho = \frac{2log(a)}{L} \tag{4.7}$$

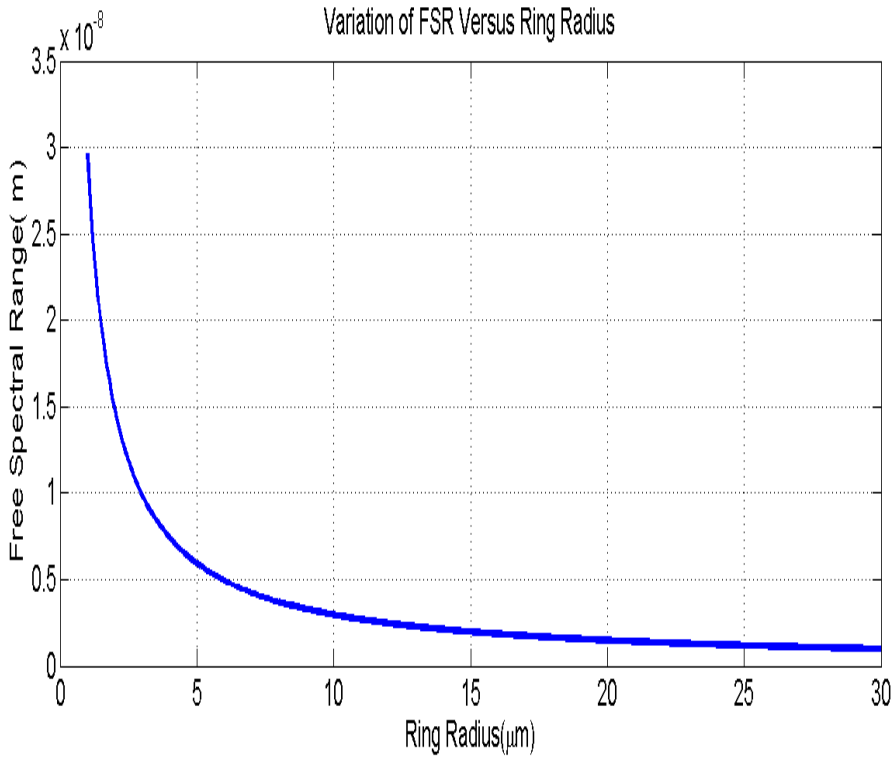

Figure 4.2: Variation of FSR with change in ring radius

The variation of FSR of a IOMR with change in its radius is shown in Figure 4.2 through simulation study. In this simulation following parameters have been assumed. Effective refractive index of IOMR (n_r) of 2.44, refractive index of silica (Keiser, 2013) of 1.44, refractive index of silicon dioxide of 3.56, clad height of 500 nm and core height of 235, attenuation factor (a) of 0.5, transmission factor (r) of 0.5 and ring radius of range (R): 1 μm to 30 μm. The simulated results for the relationship between FSR and R and Q and R have been shown in the Figures 4.2 and 4.3 respectively. It is observed from the Figure 4.3, that if the radius of ring increases, Q also increases. Whereas FSR decreases with the increase in the ring radius of IOMR as shown in Figure 4.2. Hence increasing the ring radius can lead to decrease in the FSR, which finally leads to interference between the two resonant wavelength. Hence, in order to achieve the required Q, the R must be minimum. The miniaturized ring of the IOMR should also be manufacturable. To fabricate a successful optical IOMR, one must be able to couple the optical wave to straight as well as ring waveguide of the IOMR. Optical micro ring is one of the waveguides, in which task of realising coupling of a optical wave is a challenge. Hence to achieve minimum radiation loss the formation of the bends in the IOMR should be carried out carefully. Marcatili and

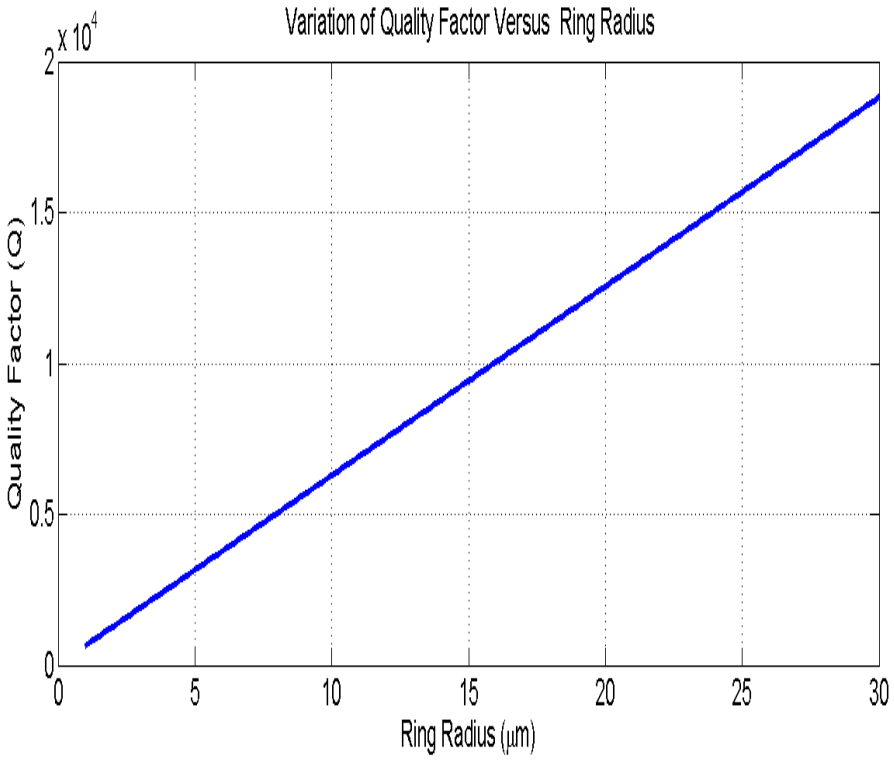

Figure 4.3: Variation of quality factor with change in ring radius

Miller (Reed and Knights, 2004) have analysed the bend loss coefficient (radiation loss) of bend waveguide. They showed that the loss coefficient α_{BEND} from the bend is of the form given by

$$\alpha_{BEND} = P_1 exp(-P_2 R) \tag{4.8}$$

Where,

R is the bend radius (Ring radius), P_1 and P_2 are related to the dimensions of straight and curved waveguides of Figure 4.1. The constants P_1, and P_2 are given by Equations (4.9) and (4.10) respectively.

$$P_1 = \frac{\lambda_0 cos^2(k_{xg}\frac{W3}{2}) exp(k_{xs}W3)}{W3^2 k_{xs} n_{effp}[\frac{W3}{2} + \frac{1}{2k_{xg}} sin(W3k_{xg}) + \frac{1}{k_{xs}} cos^2(\frac{W3}{2})k_{xg}]} \tag{4.9}$$

$$P_2 = 2k_{xs}(\frac{\lambda_0 \beta}{2\pi n_{effp}} - 1) \tag{4.10}$$

Where,

β is the z directed propagation constant, k_{xg} is the x directed propagation constant, k_{xs} is the x directed decay constant representing the evanescent field, $W3$ is waveguide width,

n_{effp} is the effective index outside the waveguide and λ_0 is the free space wavelength. The loss coefficient α_{BEND} depends on the radius of curvature of the bend. Thus the radius of curvature should be as large as feasible. Reduction of the parameter k_{xs} leads to lower value of constant P_1 and P_2. Hence it leads to reduced loss. The loss coefficient is dependent upon the radius of curvature of the bend. Thus the radius of curvature should be large enough so that loss could be minimized. However, for the IOEO application, a device with small footprint is needed and this can be achieved through small ring radius. Furthermore, the constants P_1 and P_2 critically rely on the x-directed loss coefficient, k_{xs}. Hence the dimension of the IOMR has to be designed such that it minimizes the bend loss. Also, the trade off between FSR and Q has to be taken into consideration during miniaturization of the IOMR. The Silicon-on-Insulator (SOI) based IOMR has found to be potentially a better candidate for small bend dimension, as IOMR is highly optical light confining technology because of large index contrast between core and cladding.

4.2.1 Relation Among Effective Refractive Index, Dimension and Mode Profile of IOMR

The geometry and material properties play a vital role in the performance of the IOMR. In this section suitable geometry, material and effective refractive index of the IOMR have been obtained. The geometry of the straight wave guide of the proposed IOMR is shown in Figure 4.4. This is SOI based device having lower cladding SiO_2, core silica and upper cladding as air. The schematic is of a dual bus configuration having two straight bus waveguides and one ring waveguide. Figure 4.5 is the cross section view of the straight waveguide of IOMR shown in Figure 4.4. In Figure 4.5, $W3$ is the width of the waveguide for both straight and ring waveguides. h_2 is the sum of the height of lower cladding and the core. h_1 is the height of the lower clad. $h_2 - h_1$ indicates the height of the core. In this configuration, the $W3$ is considered to be greater than height of the core. The range of value of the $W3$ is taken as 450 nm to 500 nm for the simulation. The minimum height of the core suitable for the IOMR is assumed to be 220 nm. Figure 4.6 shows the refractive index of the IOMR. In this simulation model, the IOMR is in the X-Z plane. Following are the simulation parameters of the IOMR: the wavelength used is (C-Band) 1550 nm window. The silicon is chosen as core material with refractive index of 3.476. Silicon dioxide SiO_2 is chosen as lower cladding material with refractive index of 1.48. Air is chosen as upper cladding with refractive index of 1.0. The analysis of effective refractive

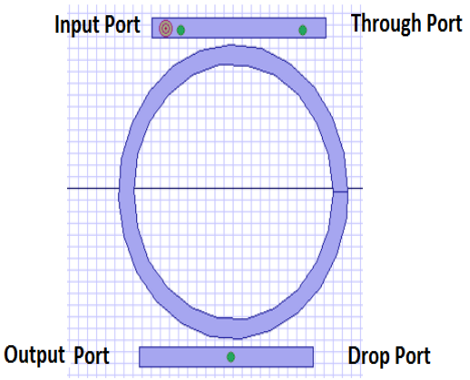

Figure 4.4: Schematic of the IOMR using OptiFDTD version 8.0

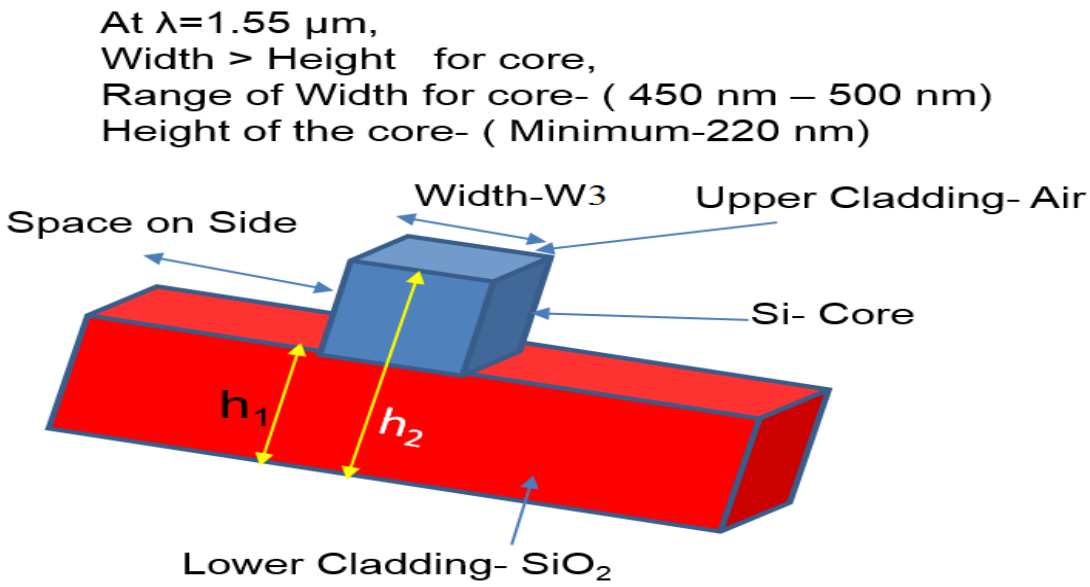

Figure 4.5: Cross sectional view of straight waveguide of IOMR

index has been carried out at $(h_2 - h_1)$ of 500 nm clad height and varying core height (h_1) using Eigen solver @ Photonic Research Laboratory (Photonics Research Laboratory, n.d.) open source code. The effective refractive index of the straight wave guide at the core height of 235 nm and clad height of 500 nm is found to be 2.448 at 1549.7 nm wavelength.

Table 4.1: Variation of effective refractive index$-n_{eff}$ with change in height of core (nm)

Height of core (nm)	Effective refractive index
200	2.299
210	2.344
220	2.38
235	**2.448**
240	2.46
250	2.49
300	2.63
350	2.72
400	2.79
450	2.85
500	2.89

The effective refractive index at various heights of the clad is shown in Table 4.1. For the

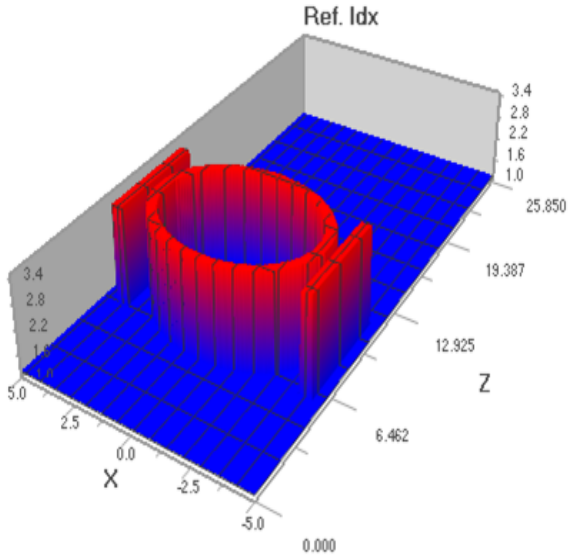

Figure 4.6: Refractive index profile of the IOMR

computation of effective refractive index of IOMR, the refractive index of of core (n_{core}) is taken as = 3.476, core height of 500 nm, refractive index of clad (n_{clad}) of 1.44 and wavelength (λ) of 1549.7 nm are used. The mode profile of the waveguide shown in Figure 4.7 are for 500 nm of core height and 235 nm of clad height. The results of Figure 4.7 have been obtained using Eigen solver @ Photonic Research Laboratory (Photonics Research Laboratory, n.d.) open source code. All the modes of IOMR have been shown as magnetic

components (Hx, Hy and Hz) and Electrical Components (Ex, Ey and Ez). The Y-axis and X-axis represent the core height and clad height of the strip waveguide (straight waveguide of IOMR) respectively.

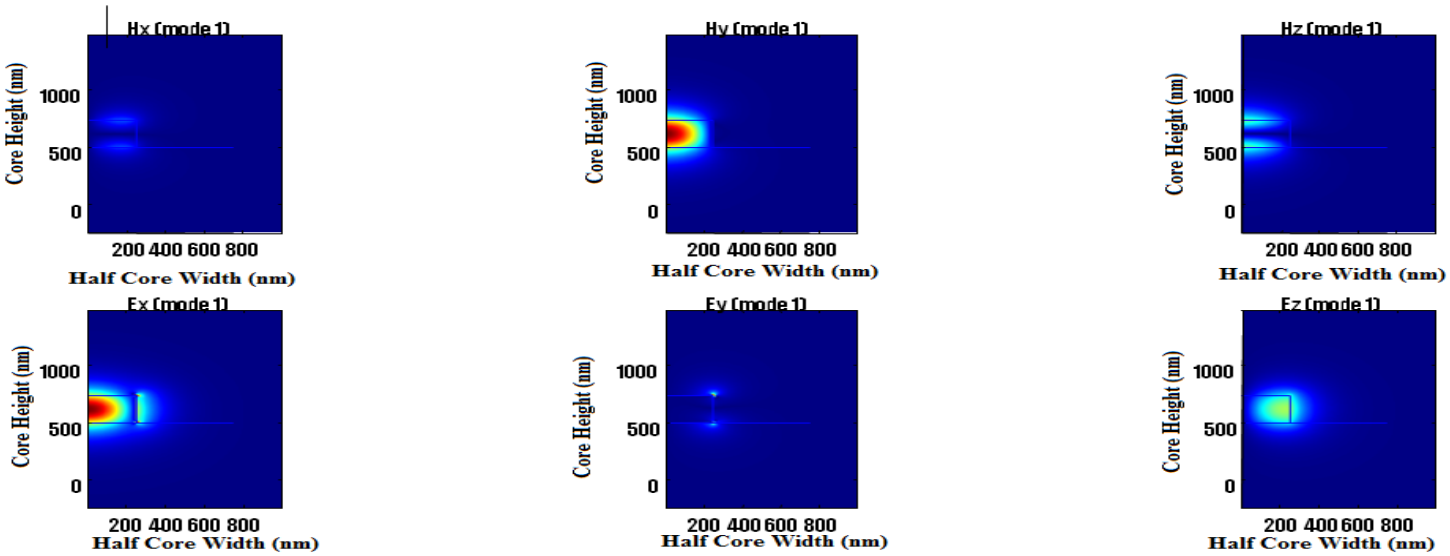

Figure 4.7: Mode plot for wave guide with 500 nm clad height, 235 nm core height, 500 nm core width and 500 nm of side spacing

The confined fundamental mode has been observed in the Figure 4.7.

4.2.2 Influence of Coupling Coefficient and Coupling Length on Power Transmission of IOMR

In this subsection, the relation among the power transmission, coupling co-efficient and coupling length has been obtained for the IOMR. To accomplish this the proposed design of IOMR described in the previous section is analyzed through simulation. The *Okamoto's* Transfer function (Okamoto, 2010) has been considered for the IOMR structure. The intensity transmittance of the open type of ring resonator is given by

$$T(\phi) = \mid \frac{E}{E_0} \mid^2 \tag{4.11}$$

$$\mid \frac{E}{E_0} \mid^2 = \frac{p}{p_0} \tag{4.12}$$

$$T(\phi) = (1-\gamma)\frac{x_1^2(1-y_1)^2}{(1-x_1^2y_1^2)+4x_1^2y_1^2sin^2(\frac{\phi}{2})} \tag{4.13}$$

Where, the parameters x_1, y_1, and ϕ are defined by Equations (4.14), (4.15) and (4.16) respectively.

$$x_1 = (1-\gamma)^{\frac{1}{2}}exp(\frac{-\rho L}{2}) \tag{4.14}$$

Where, γ is intensity insertion loss, L is the circumference of the ring, ρ is intensity attenuation coefficient, β is the wave number, l is the coupling length and k is the coupling coefficient.

$$y_1 = cos(kl) \tag{4.15}$$

$$\phi = \beta L \tag{4.16}$$

Following parameters have been considered for the simulation: Insertion loss (γ) of 0.023 W, Propagation loss (ρ) of 0.023 Wcm^{-1} or (2.3 Wm^{-1}), $k \times l$=0.262 (product of coupling coefficient and coupling length), optical modulator output of -5 dB, Laser power source power of -13.86 dB, Sinusoidal signal of 1 V with SNR of 10 dB and variable coupling length of $\frac{2*\pi*R}{N}$;
Where N=1, 2, 3 etc. is positive integer and R is the ring radius.
Equation (4.1) justifies that to get any standing wave in an optical ring waveguide, the input

wavelength must be equal to the $\frac{2\pi nR}{m}$.
Since, in the IOMR the material properties of medium change, the wavelength also gets changed accordingly. The m in Equation (4.1) decides the ring radius (R), but the selection of coupling length (l) shown in Figure 4.1, decides the power at the output port. If the product of l and coupling coefficient (k) is taken as 0.262 (Okamoto, 2010), the performance of IOMR is very good in terms of the power at the output port. But for the smaller ring radius, the coupling length seems to be impractical from the manufacturing perspective. The variable coupling length, gives the power drop in the range of -300 dB at the output port. Hence to achieve the best output power at the output port, following dimensions of the ring structure are considered: clad height of 500 nm, core height of 235 nm, and effective refractive index of 2.444, mode order(m) of 35 and k of 0.638 mm^{-1}.
Computation of practical coupling length considering $Okomato's$ transfer function (Okamoto, 2010) for the IOMR has been performed using following parameters: Insertion loss (γ) of 0.023 W, Propagation loss ρ of 0.023 Wcm^{-1} or (2.3 Wm^{-1}), $k \times l$=0.262, coupling coefficient=0.638 mm^{-1}, Optical modulator power of -5 dB, Laser power of -13.86 dB and sinusoidal signal of 1 V with SNR of 10 dB. It has been observed that coupling length required for the power of -40 dB at the output port of the optical ring resonator is in the range of 410.66 μm for the ring radius of 3.5397 μm.

4.2.3 Simulation of IOMR Suitable for the IOEO Application

In this section the simulation of the IOMR suitable for the IOEO application to generate 40 GHz has been carried out. The simulation of the IOMR has been carried out for two different cases of m (mode order).
In Case I, the following data are assumed:

- Effective Refractive index $n_{eff} = 2.44$ for mode order (m)=1
- Optical Ring Radius = 0.1013 μm,
- Width of the waveguide = 0.5 μm
- Core height of 235 nm and gap (d) of 200 nm
- Wavelength is 1.5497 μm of Amplitude 1 Volt, (Gaussian modulated wave)
- Half width of the Gaussian modulated wave is 6.5×10^{-14} second

The effective refractive index of any photonic device is important since it directly affects various performance metrics of the optical device. For the design and simulation of accurate IOMR, the knowledge of accurate effective refractive index value is needed. Hence, Table 4.2 representing the variation of effective refractive index (n_{eff}) with the ring radius (R) for mode order (m) of 1 is included. The results of Table 4.2 have been plotted in Figure 4.8.

Using the results of Figure 4.8, IOMR, has been designed and simulated. The simulated

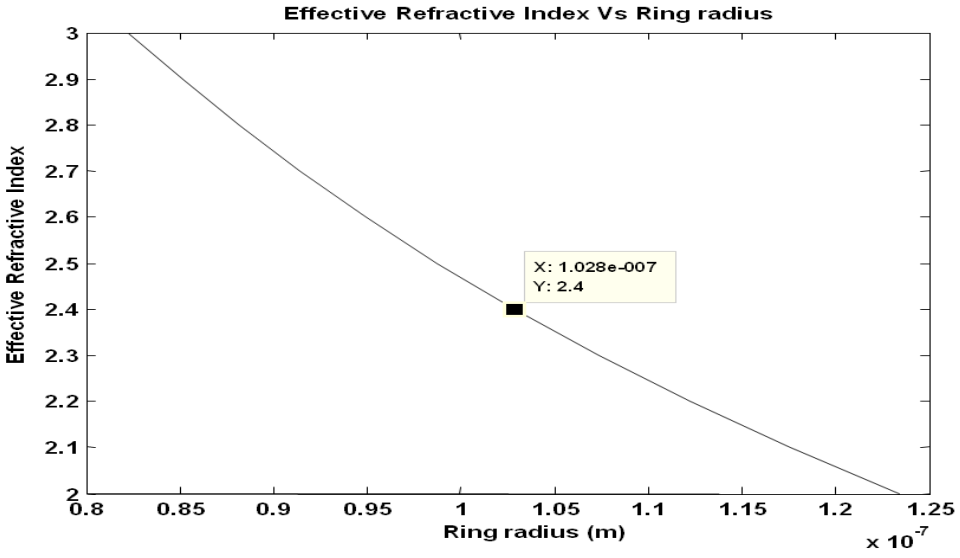

Figure 4.8: Variation of effective index with change in ring radius of IOMR for mode order (m) of 1

results have been depicted in the Figures 4.9, 4.10 and 4.11. In the Figures 4.9, 4.10 and 4.11, observation point *A* represents power at source (input port of IOMR), observation point *B* represents power at transmitted port of IOMR and observation point *C* represents the power at output port of IOMR. It has been observed that for mode order of (m) of 1, the loss between source and output ports is in the range of 17 dB .

Case II:

In Case II, the following parameters have been considered: Effective refractive index (n_{eff}) of 2.44, mode order(m) of 35, optical ring radius of 3.5397μm, gap (d) of 200 nm, width of the bus waveguide and the ring waveguide is 0.5 μm and core height of 235 nm for both straight and ring wave guides. The Gaussian modulated wave of amplitude 1 Volt at wavelength (λ) of 1.5497 μm is considered for the simulation. The half width for the

Table 4.2: Variation of effective refractive index with change in ring radius (μm) of IOMR

Effective refractive index n_{eff}	Ring radius (μm)
2	0.12338
2.01	0.12277
2.02	0.11217
2.03	0.12156
2.05	0.12037
2.06	0.11921
2.07	0.11921
2.25	0.10967
2.3	0.10729
2.4	0.10282
2.44	0.10113

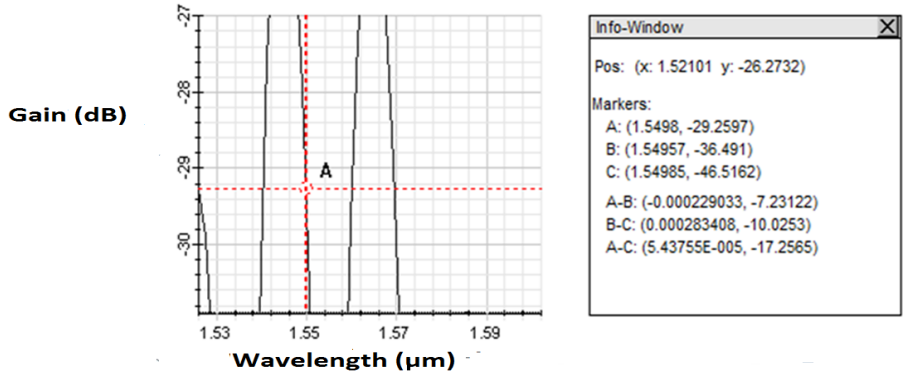

Figure 4.9: Source power at input port of IOMR (observation point A) using OptiFDTD 8.0

Gaussian modulated wave is observed as 9.5×10^{-14} second. The obtained simulation results shown in Figure 4.12 validate the designed IOMR. In the Figure 4.12 the observation point *C* represents the source power at input port, observation point *B* represents the transmitted power at through port and observation point *A* represents the power at the output port of the IOMR. It has been observed that for the mode order(m) of 35, the loss between source and output ports is in the range of 29.43 dB. The effect of Half Width

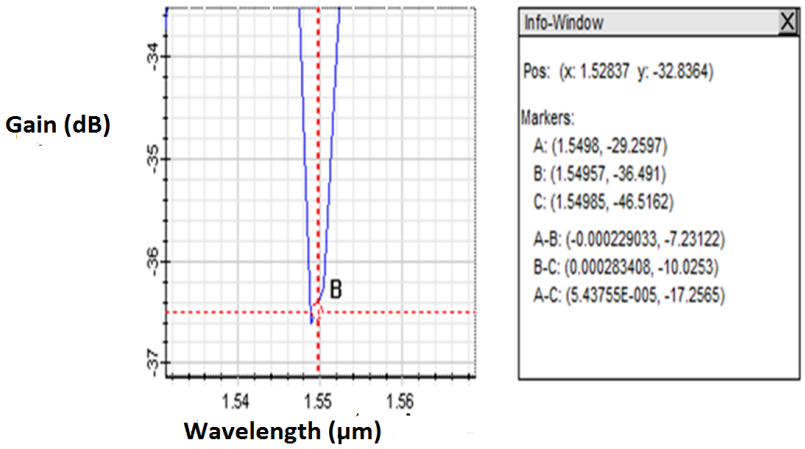

Figure 4.10: Transmitted output power at through port of IOMR (observation point B) using OptiFDTD 8.0

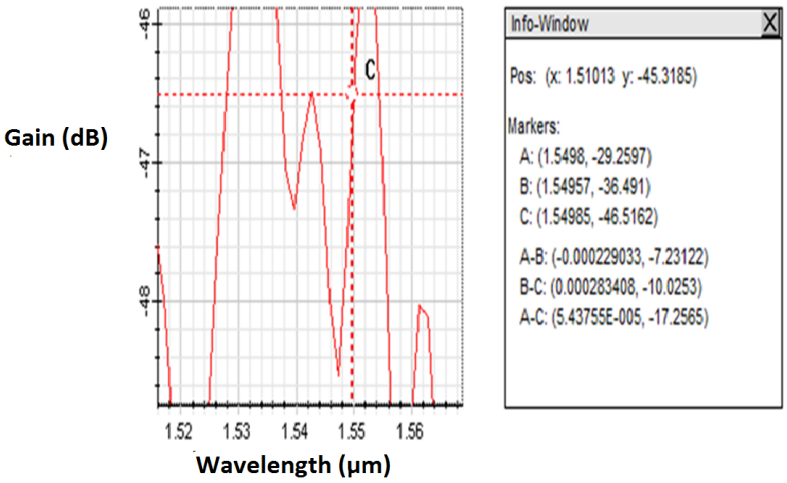

Figure 4.11: Power at output port of IOMR (observation point C) using OptiFDTD 8.0

(HW) time of the Gaussian modulated wave on the performance of IOMR has also been observed. The HW of 9.5×10^{-14} sec provides improved power at output port of IOMR than 6.5×10^{-14} sec. This justifies the usage of the designed IOMR in the proposed IOEO.

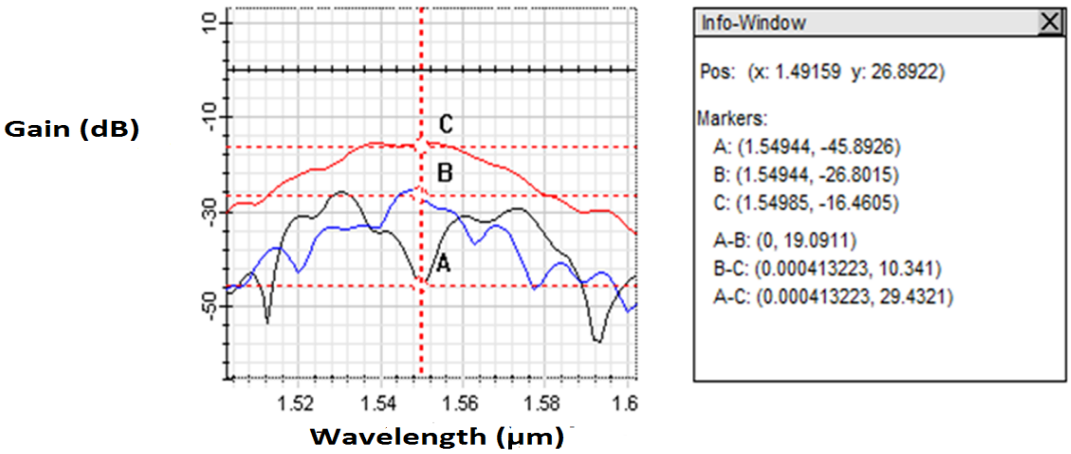

Figure 4.12: Observation point C, B and A represents source, transmitted and output port power using OptiFDTD version 8.0

4.2.4 Fabrication Tolerance of the IOMR

The fabrication tolerance is an important factor for the manufacturing of the IOMR. This factor is extremely significant since the dimensions of IOMR under consideration are extremely small of the order of (nm). This section presents computation of the fabrication tolerance of the designed IOMR. First an analytic model has been proposed for the designed IOMR. Then using the derived analytic model the fabrication tolerance has been computed.

A schematic representation of an instantaneous wave vector of straight and curved waveguides of a dual bus configuration of IOMR is shown in Figure 4.13. In the Figure 4.13, d is the distance between straight and curved waveguides, k is the coupling coefficient, l is the coupling length, Δl is the incremental coupling length. L is the total ring circumference and R is inner radius of ring.

The relationship between the coupling length l and coupling coefficient (k) of IOMR under phase matched condition given by (Yariv, 1973) is written as

$$l = \frac{\pi}{2k} \tag{4.17}$$

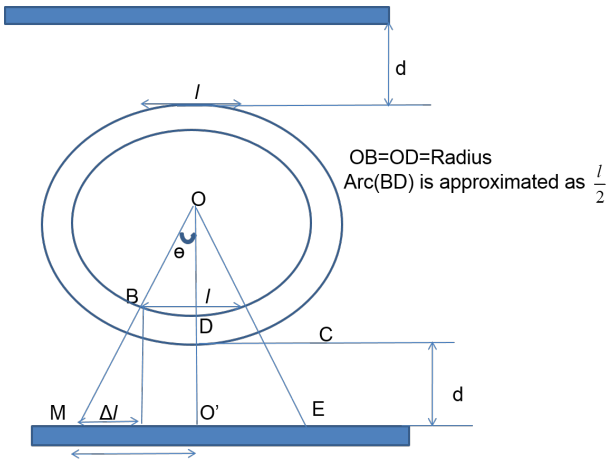

Figure 4.13: Instantaneous wave vectors between straight and curved wave guide in dual bus IOMR

In this section an equation to relate R, l and d has been presented. In Figure 4.13, considering triangles OBD and OMO', one gets

$$tan(\theta) = \frac{\frac{l}{2}}{R} \tag{4.18}$$

and

$$tan(\theta) = \frac{\frac{l}{2} + \Delta l}{R + d} \tag{4.19}$$

Equating Equations (4.18) and (4.19)

$$\frac{\frac{l}{2}}{R} = \frac{\frac{l}{2} + \Delta l}{R + d} \tag{4.20}$$

Equation (4.20) is simplified as

$$\frac{R}{l} = \frac{d}{2\Delta l} \tag{4.21}$$

Using Equations (4.17) and (4.21), one gets

$$d = \frac{4R\Delta lk}{\pi} \tag{4.22}$$

$$k = \frac{d\pi}{4R\Delta l} \tag{4.23}$$

If $l = N\Delta l$, where N is any positive integer

Then,

$$k = \frac{d\pi N}{4Rl} \tag{4.24}$$

Equation (4.24) shows the relationship between d, l, k and R. Considering the change in d as d' and l as Δl, one gets the Equation (4.25) to relate the coupling coefficient(k) with gap (d'), R and Δl.

$$k = \frac{\pi d'}{4R\Delta l} \tag{4.25}$$

The fabrication of the IOMR as per the IOEO requirements is a challenging task. The small deviation in the dimension of the IOMR can occur during the fabrication, which is defined as the misalignment. In the IOMR, the gap between straight and curved waveguides (d) and the Ring radius (R) are important parameters. Hence the deviations in the (d) and the (R) are studied. Using Equation (4.25), the variation of coupling coefficients with respect to misalignment in gap between straight and curved wave guides is shown in Figure 4.14. In the simulation of the results of Figure 4.14, the following parameters have been considered. The refractive index n_{eff} of 2.44, mode order(m) of 35, optical ring radius of 3.5397μm, width of the bus waveguide and the ring waveguide is 0.5 μm and core thickness of 235 nm for both straight and ring waveguides.

Similarly, the variation in coupling coefficient with misalignment of center of curved

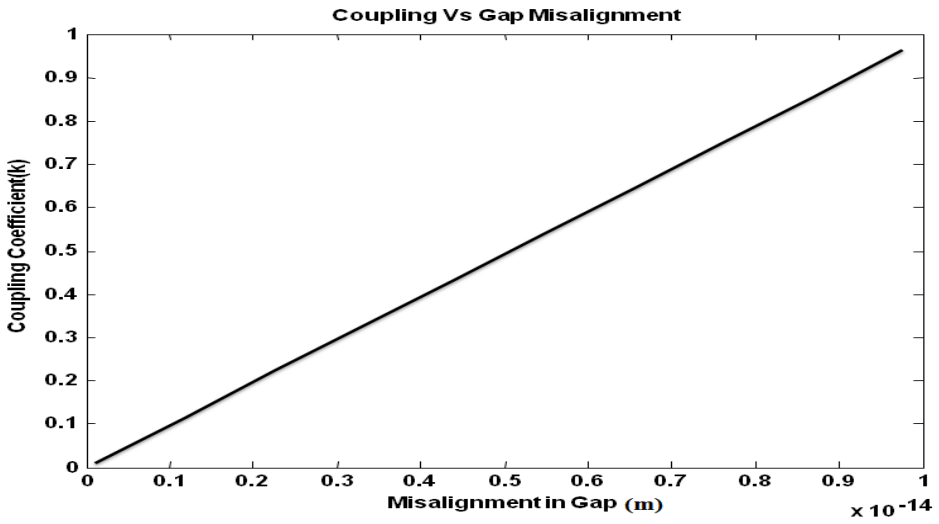

Figure 4.14: Variation of coupling coefficient with misalignment in Gap (d) of IOMR

waveguide is shown in Figure 4.15. For the results of Figure 4.15, the following parameters have been considered for the simulation: effective refractive index (n_{eff}) of 2.44, mode

order(m) of 35, optical ring radius of 3.5397μm, width of the bus waveguide and the ring waveguide is 0.5 μm and core thickness of 235 nm for both straight and ring waveguides. The results of the Figure 4.14 and 4.15 depict the effect of minute inaccuracies in the

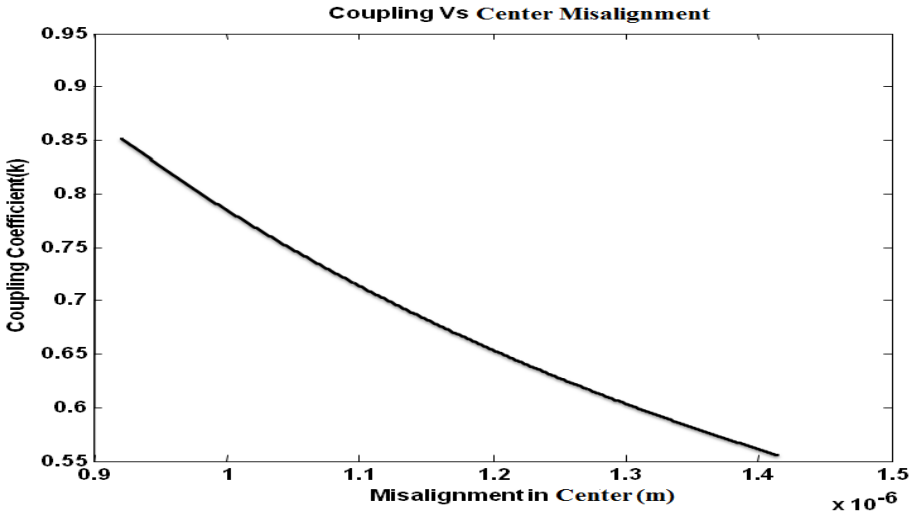

Figure 4.15: Variation of coupling coefficient with misalignment in center of IOMR

tolerance of IOMR related to the straight waveguide on the coupling coefficient. The permissible variations in the value of the d and R are observed. The minimum and maximum gaps allowed are $\frac{d}{1005}$ and $\frac{d}{11}$ respectively for the fixed ring radius and coupling length. The minimum and maximum coupling lengths are found to be $13 * l$ and $20 * l$ respectively for the fixed ring radius (R) and gap(d).

The fabrication tolerance has been computed for the gap of 15 nm between straight and curved waveguides of an IOMR. Figure 4.14 shows the variation of coupling coefficient with the change in misalignment of the gap (d). Figure 4.15 shows the variation of coupling coefficient with the misalignment of center of the ring of IOMR. In Figures 4.14 and 4.15, the change in the gap (d) is in the range of fm, whereas the change in radius of ring is in μm. For the gap (d) of 15 nm between straight and curved waveguides, even a variation of a few fm affects the coupling. At the same time a misalignment of a few μm in the center of the ring of IOMR also affects the coupling. The results of Figures 4.14 and 4.15 indicate the tolerable variation in gap (d) and location of the center of ring of IOMR to get desirable output power from IOMR. The minimum realizable gap (d) reported is 150 nm between

straight and curved waveguides (Steglich et al., 2017) of an IOMR. From the perspective of practical implementation of the IOEO, an IOMR with the gap (d) of 200 nm has been simulated and fabrication of such device is presently possible. For the fabrication of IOMR following features been considered: core height of 235 nm, clad height of 500 nm, width of 500 nm for both the straight and curved waveguides and ring radius of 3.5973 μm. An IOMR with these dimensional parameters can be realised with the reported existing precision (Steglich et al., 2017).

4.2.5 Analysis of Butt-coupling and Numerical Modelling of IOMR with Smaller Gap

In this section an analytical model of modified resonance condition of the IOMR has been proposed considering Butt coupling coefficient. Using the developed analytic expression the influence of the Butt-coupling coefficient on the coupling coefficient and resonance is discussed. In Figure 4.4, if the distance between straight and ring waveguides is lesser than 100 nm, the excitation of the Butt coupling coefficient takes place. Now if the field disturbance is assumed to be zero ($\chi = 0$), then following conditions can be written for the study of the coupled mode equations of IOMR. Conditions are as follows:$\chi = 0$, $c_{12} = c_{21} = c$ and $k_{12} \neq k_{21}$:

$$\frac{\partial A}{\partial z} + c\frac{\partial B}{\partial z} + jk_{12}B = 0 \tag{4.26}$$

$$\frac{\partial B}{\partial z} + c\frac{\partial A}{\partial z} + jk_{21}A = 0 \tag{4.27}$$

Where,

A and B are the Electric fields in the straight and curved waveguides respectively. Equations (4.26) and (4.27) can be written as,

$$\frac{\partial A}{\partial z} = jMA - jNB \tag{4.28}$$

$$\frac{\partial B}{\partial z} = jMB - jNA \tag{4.29}$$

Where,

$$M = k_{21}\frac{c}{1-c^2} \tag{4.30}$$

$$N = k_{12}\frac{1}{1-c^2} \tag{4.31}$$

Taking the second derivative of Equations (4.28) and (4.29), and further simplifying, second order differential equations for the Butt-coupling coefficients are:

$$\frac{\partial^2 A}{\partial z^2} - 2\frac{\partial A}{\partial z} jM - (M^2 - N^2)A = 0 \tag{4.32}$$

$$\frac{\partial^2 B}{\partial z^2} - 2\frac{\partial B}{\partial z} jM - (M^2 - N^2)B = 0 \tag{4.33}$$

Solution to the second order differential equation for Butt coupling coefficients, are written as:

$$A(z) = C_1 exp[j(M+N)z] - C_2 exp[j(M-N)z] \tag{4.34}$$

$$B(z) = C_1 exp[j(M+N)z] + C_2 exp[j(M-N)z] \tag{4.35}$$

Co-efficients C_1, and C_2, are calculated by considering the boundary conditions:

$$A(0) = 1 \tag{4.36}$$

$$B(0) = B(l) exp(j\beta L) \tag{4.37}$$

The C_1, and C_2 co-efficient are written as:

$$C_1 = \frac{1 + B(l) exp(j\beta L)}{2} \tag{4.38}$$

$$C_2 = \frac{-1 + B(l) exp(j\beta L)}{2} \tag{4.39}$$

The modified resonance condition of IOMR with the consideration of Butt-coupling coefficients is represented as

$$n_{eff} L + \lambda(\frac{Ml}{2\pi}) = m\lambda_R \tag{4.40}$$

where, m= $1, 2, 3...$ and λ_R is the new resonance wavelength. Equation (4.40) is a modification of Equation (4.1) to determine the resonant condition of IOMR when the proximity of the bus waveguide and curved waveguide is considered. Electromagnetic field distributions of IOMR are computed using OptiFDTD Version 8.0 and dependence of Butt-coupling coefficient, resonant wavelength shift on width of bus waveguide width is analysed. The factor (M), resonance shift λ_R, coupling coefficient (k) and Butt-coupling Coefficient (c)

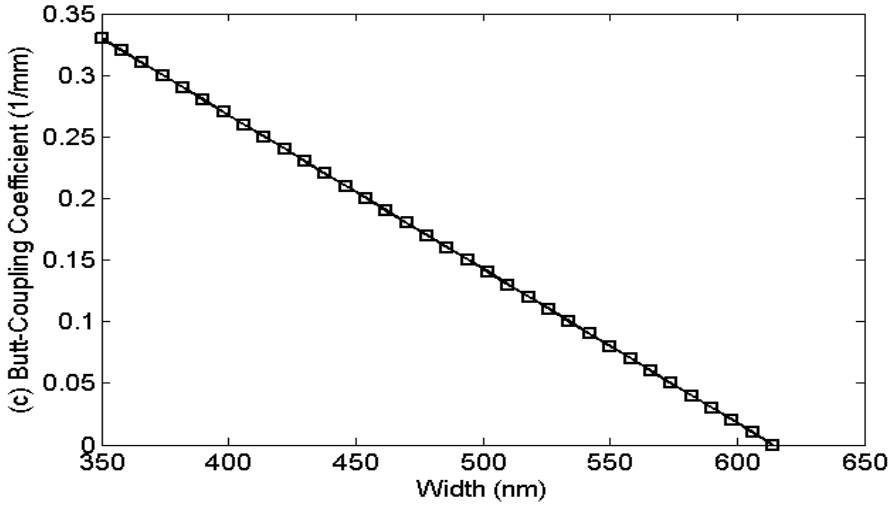

Figure 4.16: Variation of Butt-coupling coefficient with change in width of bus waveguide of IOMR

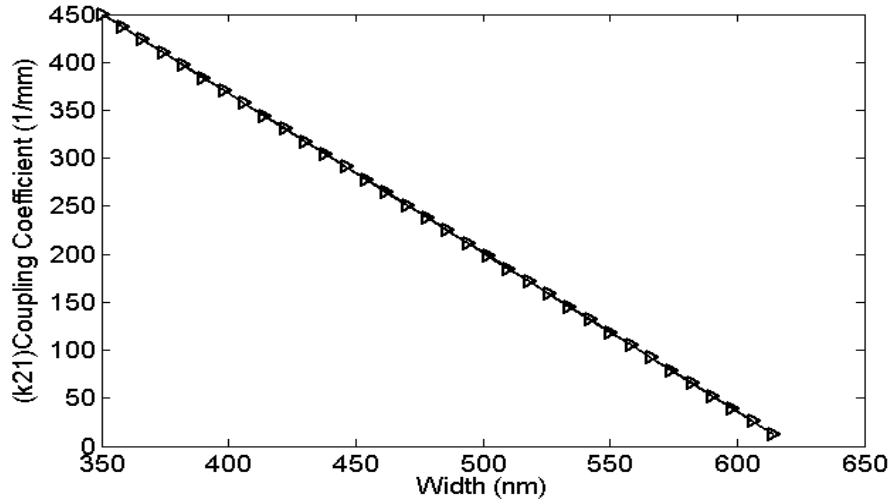

Figure 4.17: Variation of coupling coefficient with change in width of IOMR

are calculated for different values of width of bus waveguide. Figure 4.16 depicts the variation of Butt coupling coefficient with respect to width of bus waveguide. Figure 4.17 depicts the results on variation of coupling coefficient with respect to waveguide width. The results on shift in resonance with respect to width of bus wavegude is illustrated in Figure 4.18, whereas the variation in factor M with change in width of bus waveguide has been shown in Figure 4.19. The factor M decreases exponentially with waveguide width and the variation is negligible above 600 nm. Coupling coefficient and resonant wavelength vary linearly with width of bus waveguide. Thus it is evident that inclusion of

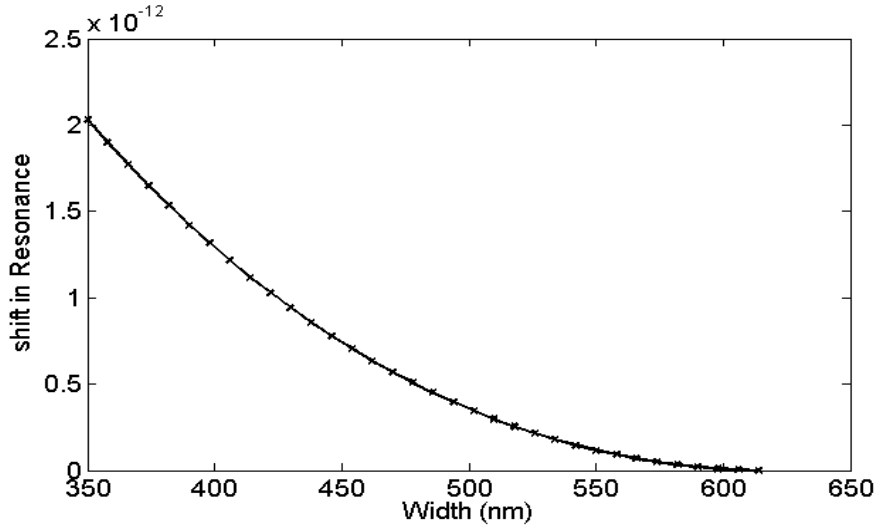

Figure 4.18: Shift in resonance of IOMR with change in width of IOMR

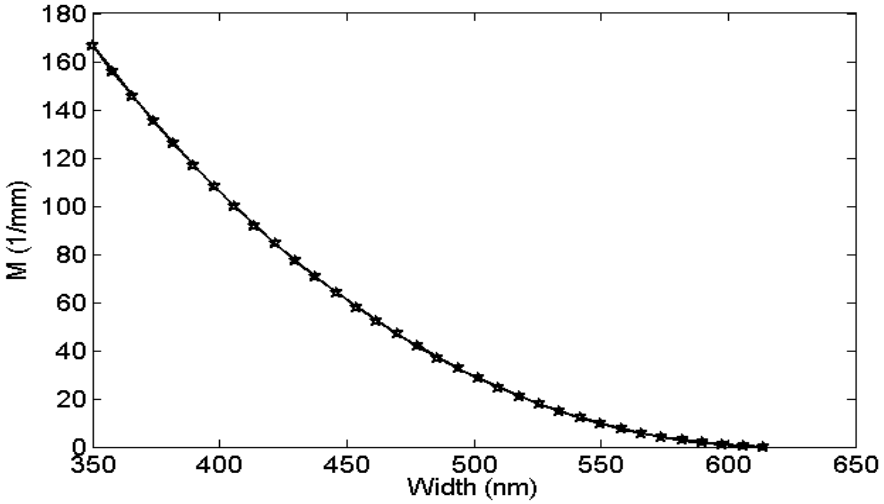

Figure 4.19: Variation in the factor M with change in the width of IOMR

Butt-coupling, waveguide coupling coefficient and perturbation are important in the design of IOMR with smaller gap between straight waveguide and the ring waveguide. Therefore the proposed analysis is useful in the realization of integrated optic devices such as OEOs, sensors and multiplexers.

4.3 Influence of Butt-coupling co-efficient on the Phase Noise, FSR, Power and Quality Factor

In this section analytic study of the influence of the Butt coupling co-efficient on the phase noise, FSR, Power and Quality factor has been discussed. When the gap d between the straight and the curved wave guides is reduced to a certain value, the effect of the Butt coupling coefficient can be observed. The shift in the resonance wavelength is one such significant outcome of this observation. The shift in the resonant wavelength is found to be more for the lower mode order m as compared for the higher order. For the high order such as m=35, shift in the resonance is very small. The small drift in the resonance can be easily reduced with the help of thermo-optic properties of the silicon of SOI. The change in the resonant wavelength leads to change in the phase noise behaviour of the IOEO.

Recently Pollock (Pollock and Lipson, 2003) has analysed the effect of gap d on the coupling coefficient k, where, k is defined as':

$$k = \frac{2k_{xc}^2 k_{xs} exp(-k_{xs}S)}{\beta w3(k_{xs}^2 + k_{xc}^2)} \tag{4.41}$$

Where, k_{xc} is the x directed propagation constant in the core, k_{xs} is the x directed decay constant (between the waveguides), $w3$ is the wave guide width, and S is the wave guide separation. The analysis of Pollock's model does not discuss the impact of the k on the phase noise of the IOMR. This model does not consider the radius of the ring. In the present research, ring radius is a significant parameter, which basically influences the effective refractive index of the IOMR.

In this section, the analyses of the phase noise, FSR and quality factor of the IOEO have been carried out at various values of coupling coefficient k. The Okamoto model (Okamoto, 2010) has been chosen and the phase noise, FSR and Q have been compared with derived equation for the IOMR. Inclusion of Butt-coupling coefficient (c) has also been taken into account to analyse the effect on phase noise, FSR and quality factor of the IOEO system. For the analysis two analytic approaches denoted as Case I and Case II have been discussed and the associated results are interpreted.

Case I:

In this approach the derived relation among d, R and l and the Okamato's model of the resonance condition is considered. Equation (4.42) represents the derived equation which relate d, R and l (Section 4.2.4)

$$k = \frac{d\pi N}{4Rl} \tag{4.42}$$

The radius of ring of IOMR is computed using the model of (Okamoto, 2010)

$$R = \frac{m\lambda}{2\pi n_{eff}} \tag{4.43}$$

Substituting the value of R of Equation (4.43) in the Equation (4.42), the coupling coefficient k can be represented by

$$k = \frac{d\pi N 2\pi n_{eff}}{4ml\lambda} \tag{4.44}$$

Using $\beta = \frac{2\pi}{\lambda}$, Equation (4.44) gets modified and is represented as:

$$k = \frac{d\pi N\beta n_{eff}}{m4l} \tag{4.45}$$

The Equation for β is rewritten as:

$$\beta = \frac{km4l}{d\pi N n_{eff}} \tag{4.46}$$

The phase change ϕ is computed as $\phi = \beta L$. Using the modified Equation of β

$$\phi = \frac{km4l}{d\pi N n_{eff}} L \tag{4.47}$$

Then for the designed IOMR, the intensity transmittance of the open type of ring resonator gets modified and is represented as Equations (4.73) and (4.74).

$$T(\phi) = \mid \frac{E}{E_0} \mid^2 = \frac{p}{p_0} \tag{4.48}$$

$$T(\phi) = (1-\gamma)\frac{x_1^2(1-y_1)^2}{(1-x_1^2y_1^2)+4x_1^2y_1^2 sin^2(\frac{\frac{km4l}{d\pi N n_{eff}}L}{2})} \tag{4.49}$$

The parameters x_1 and y_1, are defined by Equations (4.50) and (4.51) respectively.

$$x_1 = (1-\gamma)^{\frac{1}{2}} exp(-\frac{\rho L}{2}) \tag{4.50}$$

where, γ is intensity insertion loss, L is the length of ring, and ρ is intensity attenuation coefficient.

$$y_1 = cos(kl) \tag{4.51}$$

The model in (Okamoto, 2010) has been invoked to compute the following performance parameter of IOMR. The FWHM, Quality factor and FSR are represented as Equations

(4.52), (4.53) and (4.54) respectively for the modified intensity transmittance of the IOMR.

$$FWHM = \frac{2(1-x_1y_1)}{\sqrt{x_1y_1}} \tag{4.52}$$

$$Q = \frac{\lambda_{res}}{FWHM} \tag{4.53}$$

$$FSR = -\frac{\lambda^2}{N_gL} \tag{4.54}$$

$$N_g = \frac{\partial\beta}{\partial k} \tag{4.55}$$

$$N_g = n_{eff} + k\frac{\partial n}{\partial k} \tag{4.56}$$

Case II:

In case I, Butt-coupling coefficient was not considered to analyse the parameters of IOMR. In case II the effect of Butt-coupling coefficients has been considered to analyse the performance parameters of IOMR. When the Butt-coupling coefficient (c) is taken into consideration, the resonance condition gets changed. The equation for the coupling coefficient k of the IOMR is modified as:

$$n_{eff}L + \lambda(\frac{Ml}{2\pi}) = m\lambda_R \tag{4.57}$$

After substituting $L = 2\pi R$

$$n_{eff}2\pi R + \lambda(\frac{Ml}{2\pi}) = m\lambda_R \tag{4.58}$$

The modified expression of radius R can be written as

$$R = \frac{m\lambda_R - \lambda(\frac{Ml}{2\pi})}{n_{eff}2\pi} \tag{4.59}$$

Where, m $= 1, 2, 3....$

The coupling coefficient k is given by

$$k = \frac{d\pi N}{R4l} \tag{4.60}$$

Substituting the Equation (4.59) in Equation (4.60), the expression for the coupling is written as:

$$k = \frac{d\pi N}{\frac{m\lambda_R - \lambda_R(\frac{Ml}{2\pi})}{(\frac{}{n_{eff}2\pi})4l}} \tag{4.61}$$

On further simplification and rearrangement of the terms, the expression for k is written as:

$$k = \frac{d\pi N n_{eff} 2\pi}{(m\lambda_R - \lambda_R(\frac{Ml}{2\pi}))4l} \tag{4.62}$$

Since $\beta = \frac{2\pi}{\lambda_R}$, Equation (4.62) is rewritten as:

$$k = \frac{d\pi N n_{eff}\beta}{(m - (\frac{Ml}{2\pi}))4l} \tag{4.63}$$

$$\beta = \frac{k((m - (\frac{Ml}{2\pi}))4l)}{d\pi N n_{eff}} \tag{4.64}$$

The modified β affects the intensity transmittance as shown in Equation (4.94) of the IOEO and in turn FWHM, Quality factor and FSR also get changed. The modified expressions for FWHM, Quality factor and FSR considering the Butt-coupling coefficients are:

$$FWHM = \frac{2(1 - x_1 y_1)}{\sqrt{x_1 y_1}} \tag{4.65}$$

Where, $y_1 = cos(\frac{d\pi N n_{eff}\beta}{(m - (\frac{Ml}{2\pi}))4l} l)$

$$Q = \frac{\lambda_{res}}{FWHM} \tag{4.66}$$

$$FSR = -\frac{\lambda^2}{N_g L} \tag{4.67}$$

Where, $N_g = n_{eff} + k\frac{\partial n}{\partial k}$.
The modified expression for intensity transmittance of the IOMR can be represented as:

$$T(\phi) = \mid \frac{E}{E_0} \mid^2 = \frac{p}{p_0} \tag{4.68}$$

$$T(\phi) = (1-\gamma)\frac{x_1^2(1-y_1)^2}{(1-x_1^2y_1^2)+4x_1^2y_1^2sin^2(\frac{k((m-(\frac{Ml}{2\pi}))4l)}{d\pi Nn_{eff}})} \tag{4.69}$$

The variation in coupling coefficient considering varying gap between straight and curved waveguides is shown in Figure 4.20. Figure 4.21 shows the variation of Butt-coupling

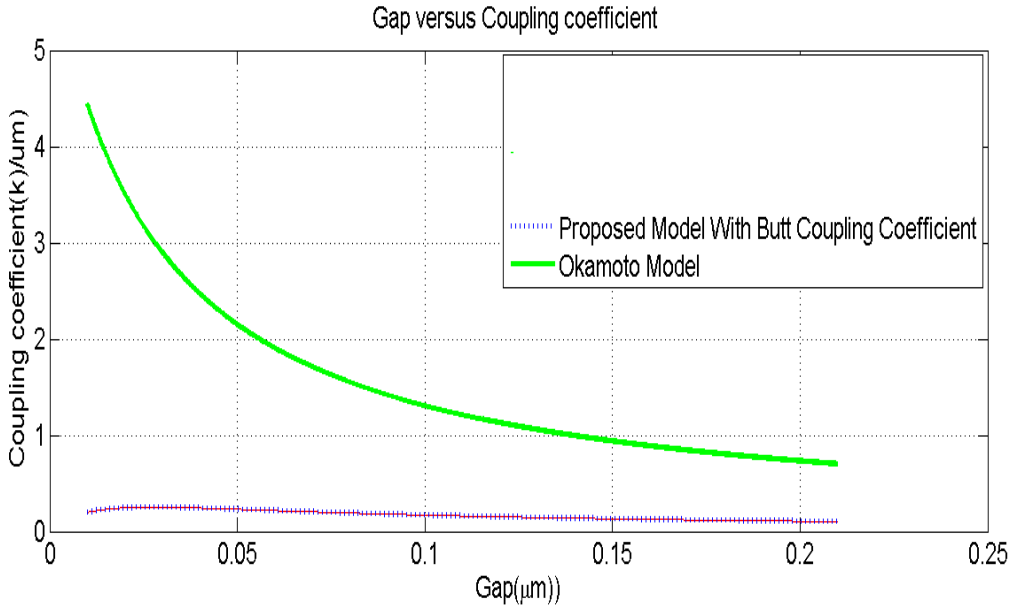

Figure 4.20: Variation of coupling coefficient with change in Gap (d) of IOMR

for the gap d between straight and curved waveguides. According to fabrication tolerance discussed in section 4.2.4, an IOMR with a gap between the straight and curved waveguides below 50 nm does not have a feasibility of fabrication in the near future. The variations of the E_y and H_x fields are taken into consideration for the computation of the Butt-coupling coefficient.

The Butt-coupling coefficient (c) deceases as the gap (d) between straight and curved waveguides increases. The derived expression for Butt-coupling coefficient does not hold for the value of d greater than 200 nm, as it is defined for the narrow gap between the straight and curved waveguides of the IOMR.

The variation in FSR with change in the the variation in the gap (d) between straight and curved waveguides is depicted in Figure 4.22. Figure 4.23 depicts the variation of quality factor with change in the gap between straight and curved waveguides. The quality factor higher than 650 has been obtained at the lowest manufacturable gap (presently, 200 nm).

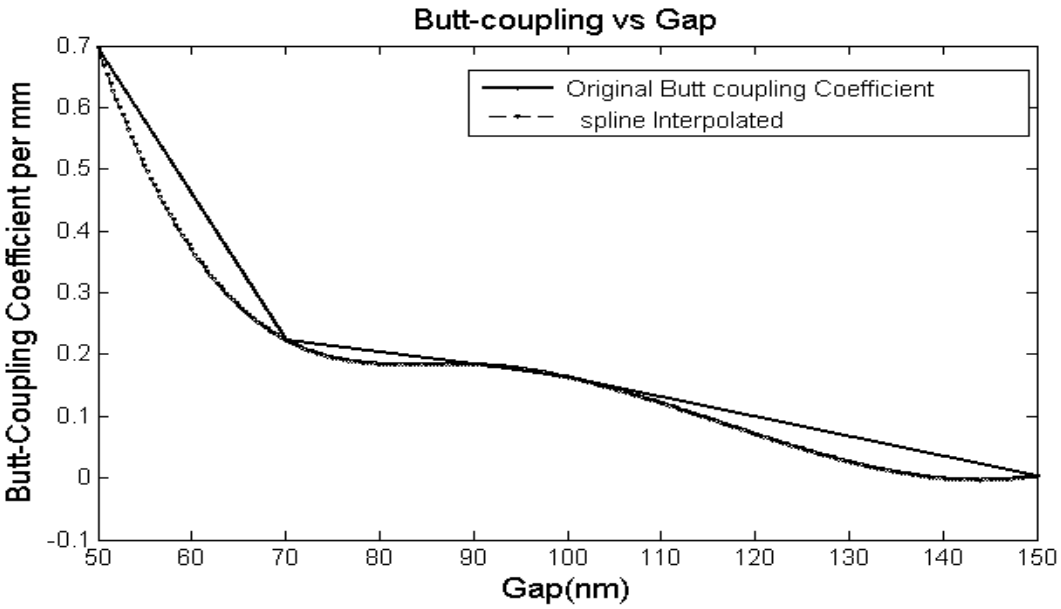

Figure 4.21: Variation of Butt-coupling coefficient with change in Gap (d) of IOMR

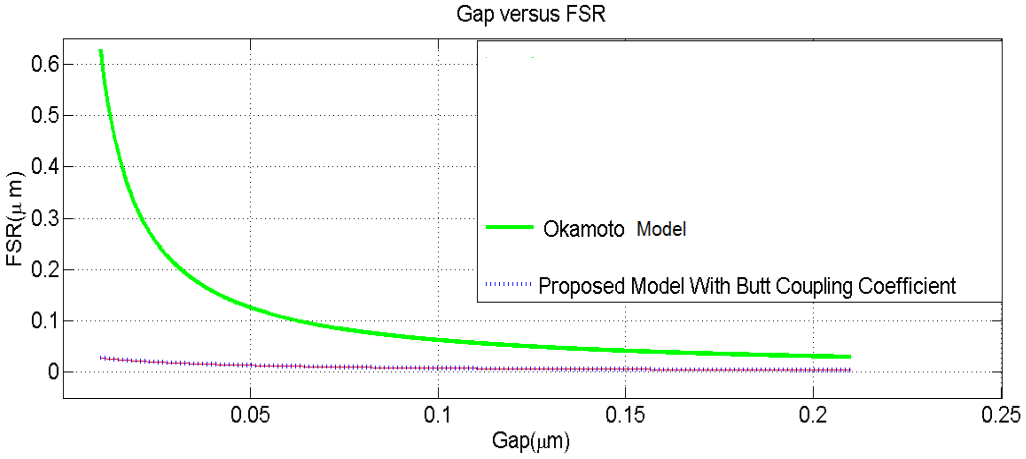

Figure 4.22: Variation of FSR with change in Gap (d) of IOMR

The quality factor generally increases as the gap *d* between straight and curved waveguides changes. Similar trend has been observed in the simulation results shown in Figure 4.23 for the IOMR. The phase noise at different offset frequencies has been plotted for the range of gap (d) of the IOMR as shown in Figure 4.24. The minimum phase noise has been observed in the Okamoto's model (Okamoto, 2010). Figure 4.24 depicts the the effect of *k* on the phase noise of IOMR. The effect of phase noise due to *k* is found to be insignificant in Okamoto model as well as the proposed model with But coupling coupling

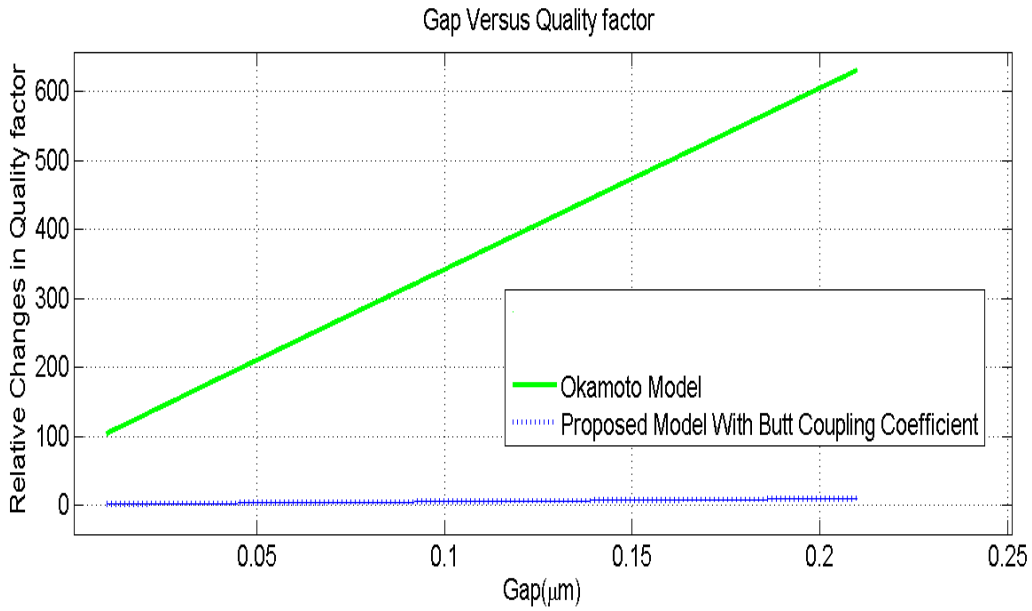

Figure 4.23: Variation of quality factor with change in Gap (d) of IOMR

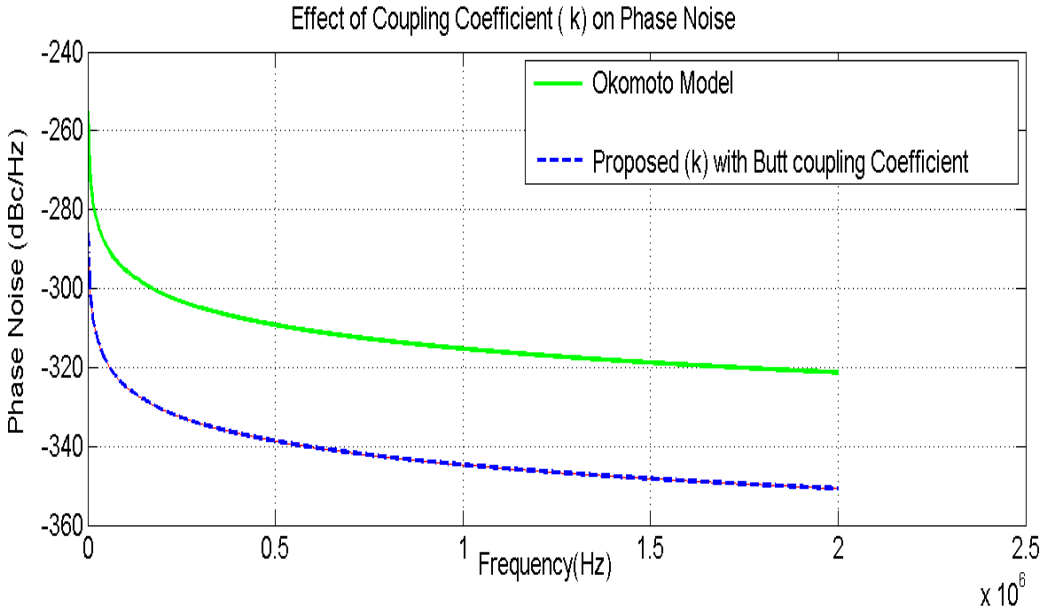

Figure 4.24: Variation of phase noise with change in width of IOMR

coefficient. Phase noise is extremely low and found to be in the range of -280 $dBcHz^{-1}$ to -300 $dBcHz^{-1}$ at different offset frequencies with a carrier of 40 GHz.

4.4 Summary

In this chapter various design and performance parameters of the IOMR have been explored. The significance and the usability of these parameters in the application like oscillators have been analysed through both through analytical expressions as well as through simulation studies. In the process the quantification of the design parameters of IOMR is also discussed. The computation of the effective refractive index and their corresponding waveguide dimension and mode profile has been carried out using Eigen solver @Photonic Research Laboratory (Photonics Research Laboratory, n.d.) as per the IOEO requirements. A novel analytical model for the IOMR with straight and curved waveguides has been explored. Relation between ring radius, coupling length, gap between straight and curved waveguides and coupling coefficient is established. The developed analytical model of IOMR is found to be suitable for the IOEO application. Its utility in the calculation of quality factor, coupling length and gap between straight and curved waveguides of the ring resonator has been substantiated. The coupling coefficient, coupling length and their influence on the power transmission at the output port of IOMR have been analysed. The designed IOMR can be fabricated and the fabrication tolerance of the designed IOMR has been analysed using OptiFDTD version 8.0 simulator.

The CMT which is basically the physics of the device has been discussed. A novel analytic approach with physical insight of the CMT in the IOMR has been explored. The CMT has been analysed by including the Butt-coupling coefficient. The effect of Butt-coupling coefficient on the output power at the output port, quality factor and FSR has been analysed. The analysis of the effect of gap d between straight and curved waveguides from the perspective of output power brings new insight into the physics of the device. The effect of bend waveguide on loss coefficient has been analysed for the designed IOMR. The effect of waveguide thickness on the performance of the strip waveguide has also been studied. This analysis facilitates better understanding of design of IOMR from the point view of the requirements of IOEO for communication applications.

Finally the effect of the phase noise on the designed IOMR taking Butt-coupling coefficient into consideration is also analysed. The study of Butt-coupling coefficients paves way for the future development of miniaturized IOMR with narrow gap. The effect of phase noise is found to be in the range of -280 $dBcHz^{-1}$ to -300 $dBcHz^{-1}$, which is insignificant for any communication application.

CHAPTER 5

THE ANALYSIS OF AN INTEGRATED OPTO-ELECTRONIC OSCILLATOR

5.1 Introduction

In this chapter performance analysis of the designed IOEO with single IOMR as well as array of IOMR has been carried out. The phase noise, thermal and short term frequency stability of IOEO with single IOMR have also been addressed. The effect of the single IOMR on the phase noise of the IOEO has also been discussed using analytical method. A two port network concept is invoked to develop a model for the analysis of phase noise of the subsystems of IOEO and that of IOEO. An analytical approach for the determination of ABCD parameters of the constituent subsystems of IOEO and composite IOEO has also been presented. Widely used and well known relationship between the ABCD matrix and the S-matrix of a two port network model has been invoked to address the stability analysis of the designed IOEO.

5.2 Performance Analysis of IOEO using Single and Array of IOMR

In this section performance analysis of IOEO using single and array of IOMR is discussed. The schematic of the IOEO design with a single IOMR is shown in Figure 3.1 and an analogous schematic of the IOEO design with 26 IOMRs is shown in Figure 3.4 of Chapter 3. The improvement of 20 dB in the output power has been observed in case of an array of 26 IOMRs, as shown in Figures 5.1 and 5.2. Since the improvement in the output power is very significant with an array of 26 IOMRs, this configuration can be used for the development of application such as optical beam steering. All the IOMRs in the array are similar with respect to material and structure.

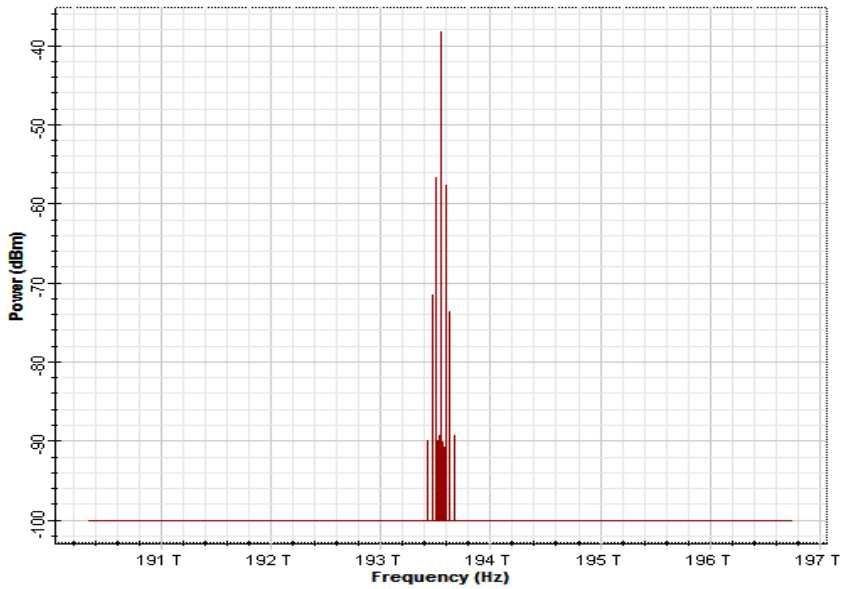

Figure 5.1: Output power spectrum of the single IOMR (Okamoto model) in the IOEO

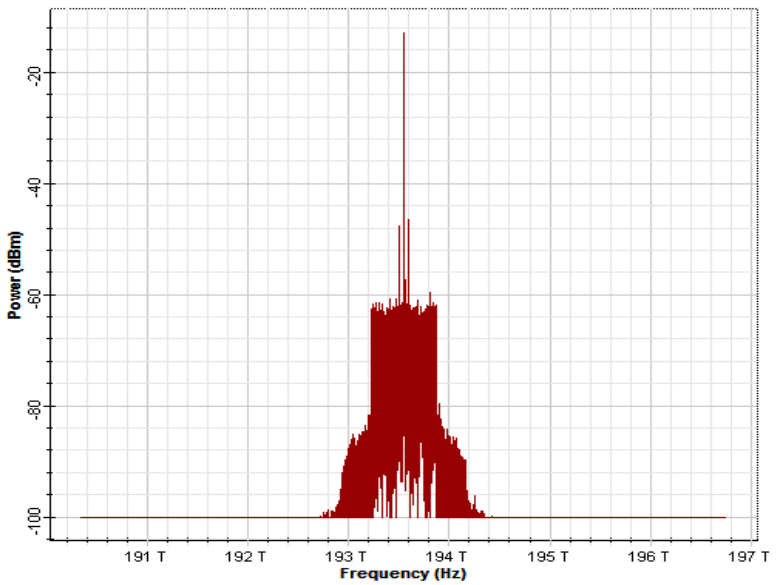

Figure 5.2: Output power spectrum of array of 26 IOMRs (Okamoto model) in the IOEO

The major disadvantages of the array of 26 IOMRs architecture is the wider bandwidth (1.6 THz) as compared to the single IOMR (0.25 THz) as shown in Figures 5.1 and 5.2. Because of the presence of other wavelength, noise at the output of EDFA is comparatively more. This is due to the amplification of noise also by EDFA. But the EDFA gain requirement gets reduced by using an array of 26 IOMRs. However in the next section, an architecture

with single IOMR has been considered for the phase noise and stability analysis.

5.3 Introduction to Phase Noise

In this section fundamentals of phase noise have been discussed. Present state of the art technology in communication needs reference microwave sources with very good stability and high spectral purity. The frequency synthesis at high frequency range is unsatisfactory because of the insufficient spectral purity. Integrated photonic devices could provide solutions to the problem of inadequate spectral purity. Examples of such devices are mode-locked lasers, OEO and optical micro-cavities.

Literature (Chembo et al., 2009) reports the usage of optical fiber as a delay line for the generation of stable and high spectrally pure Giga Hertz frequency. The optical fiber has been a better choice due to the following advantages. A long delay such as 100 μs could be achieved because of low loss (0.2 $dBkm^{-1}$ at 1.55 μm and 0.35 $dBkm^{-1}$ at 1.31 μm). It shows very low background noise, that is close to the limit imposed by the shot and thermal noise at the output of detector. In spite of all these advantages, the lengthy fiber makes the system bulky and unsuitable to be used at the micro level. The other performance metrics of fiber are the phase noise and quality factor which have been proved to be the limiting factors for so many application such as Wavelength Division Multiplexing based optical steering and bio-sensing. Hence the device to be used in such application should have very low phase noise and high quality factor.

The phase noise is generally measured as the average Power Spectral Density (PSD) of the output noise of any system. The single-sided PSD is preferred over two sided PSD because of the redundancy in negative frequencies. It has been observed that the power law model shown in Equation 5.1 and the coefficients in the Table 5.1 (Rubiola, 2008) describe phase noise of oscillator accurately. The various types of noise in any oscillators are listed in Table 5.1 along with the designated coefficients (Rubiola, 2008).

$$S_{\varphi}(f) = \sum_{m=-4}^{0} b_m f^m \tag{5.1}$$

The power law relies on the fact that white noise f_0 and flicker noise f^{-1} exist. The phase noise defined through power law also depends on the phase integration present in the oscillator. The frequency fluctuations in the spectrum of oscillator can be described using the power law. Figure 5.3 depicts the generic linear phase noise model (Rubiola, 2008) of the oscillator. The linear model has an amplifier of gain A and a feedback transfer

Table 5.1: Noise available in oscillator

Coefficient	Noise type	Noise Origin and offset frequency
b_{-4}	Frequency random walk	Device non-linearity, 1 mHz-100 mHz
b_{-3}	Flicker of Frequency	Device non-linearity, 100 mHz-10 Hz
b_{-2}	White Frequency Noise	Device non-linearity, 10 Hz-1 kHz
b_{-1}	Flicker of Noise	Near DC Frequency, 1 kHz-10 kHz
b_0	White Phase Noise	Thermal and Shot noise, $>$ 10 kHz

function $B(jf)$ in closed loop. The gain A compensates for the losses, while $B(jf)$ selects the oscillation frequency. In the linear model of the oscillator, the Barkhausen condition for stationary oscillation is verified at the carrier frequency using feedback gain control mechanism. Under this hypothesis, the phase noise is modelled by the scheme shown in Figure 5.3. This linear phase noise model has been used for the computation of the phase noise of the designed IOEO. The forward path consists of LNA1, BPF and LNA2, whereas the feedback path comprises OM, IOMR, EDFA and PD. In the next section the phase noise computation of IOEO using linear model has been presented.

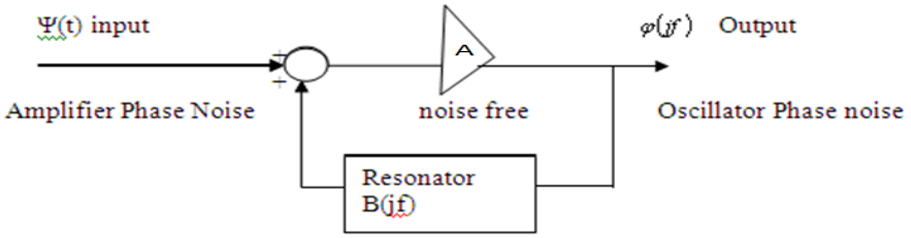

Figure 5.3: Oscillator linear phase noise model

5.3.1 Analysis of Phase Noise of Linear Model for IOEO using Variance Method

In this section, phase noise of IOEO has been computed using the linear model of IOEO and analysed using variance method. An oscillator is defined by three parameters: phase

(ϕ), amplitude (A_0), and frequency (f_0). In an oscillator both phase (ϕ) and amplitude A_0 get affected by noise over a period of time (t). The generated frequency is expressed as in Equation 5.2.

$$\omega(t) = A_0(t)cos(2\pi t f_0 + \varphi(t)) \tag{5.2}$$

The nonlinear dynamics of an oscillator make the amplitude $A_0(t)$ relatively constant thereby rendering the amplitude noise to be considerably less significant than phase noise. Further, if the modulation does not affect the amplitude, then the receiver can also ignore the amplitude noise. However, phase noise cannot be overlooked and it is actually a defining parameter for performance quality of an oscillator. Single Side Band PSD is a measure of oscillator phase noise. The phase noise at a frequency which is offset from the carrier is generally specified. The PSD is normalized to the power of the RF signal and has units of $dBcHz^{-1}$. Often, the phase noise is quoted as a single value measured at a frequency offset f_m from the carrier phase noise $\phi(t)$ for a free running oscillator is a non-stationary random variable. The PSD, denoted as $P_x(f)$, (Perez Serna et al., 2010) is given by

$$p_x(f) = \frac{\sigma_\phi^2}{(2\pi f)^2 + (\frac{\sigma_\phi^2}{2})^2} \tag{5.3}$$

where, σ_ϕ^2 is the unit variance of the random phase noise process, so that the total variance is measured by $\sigma_\phi^2(t)$. In terms of PSD, the phase noise is represented by

$$L(f_m) = 10log_{10}(P_x(f_m)) \tag{5.4}$$

Where, $L(f_m)$ is the phase noise in units of dB_cHz^{-1}. The simplified form of the phase noise can be written as

$$L(f_m) = 20log(\frac{\sigma_\phi}{2\pi f_m}) \tag{5.5}$$

for smaller values of $\frac{\sigma_\phi^2}{f_m^2}$.
Where, (f_m) is the frequency offset and σ_ϕ (standard deviation) is the constant that defines the noise level of the oscillator. In practice all free-running oscillators exhibit a noise roll-off of -20 decibels per decade when the operating frequency is other than the fundamental frequency (Perez Serna et al., 2010). The phase noise computed using variance method (Perez Serna et al., 2010) has been shown in the Figure 5.4. The results of Figure 5.4 pertain to the phase noise of the linear model of the IOEO with single IOMR as discussed in the previous section and the simulation result has been obtained using Equation 5.5. The

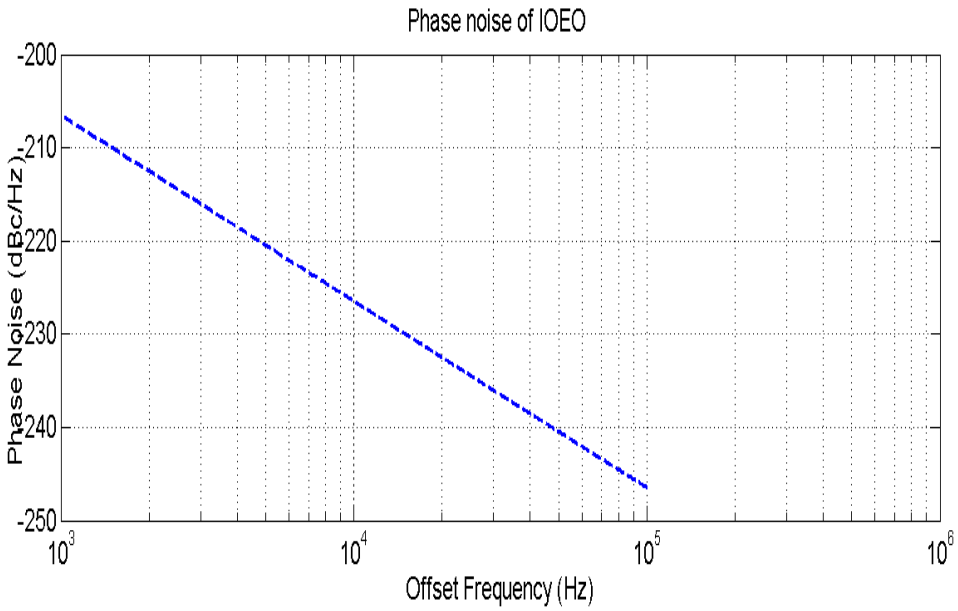

Figure 5.4: Phase noise of IOEO (using Okamoto or Pollock model of IOMR) (optisystem Results)

variance σ_ϕ^2 of output voltage of the LNA2 has been computed. The power at the output of LNA2 is shown in Figure 5.5. The variance σ_ϕ^2 has been computed using expression given

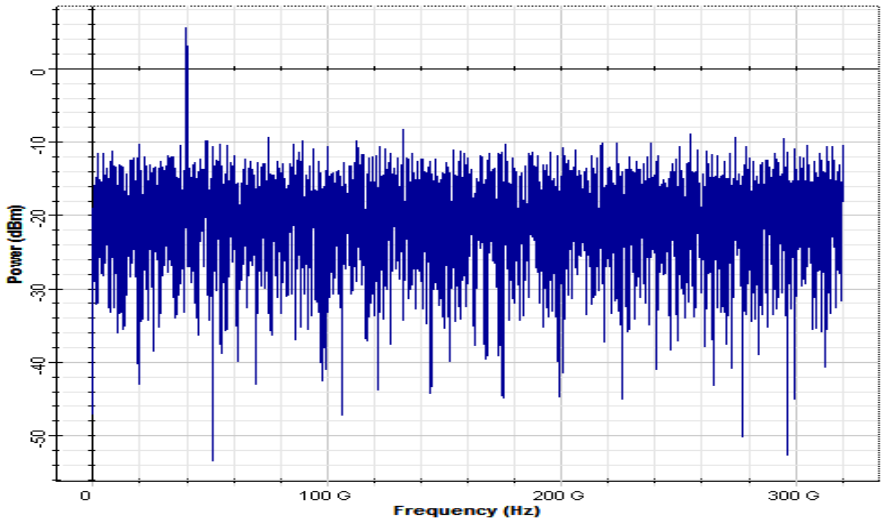

Figure 5.5: Power spectrum at LNA2 of IOEO using Okamoto model of IOMR

by:

$$\sigma_\phi^2 = \frac{\Sigma\{X-\mu\}}{N_{sample}}$$

Where,

X is the output signal sample of the LNA2 which varies from 1.8402 volt to 2.6180 volt, μ is the mean of the output signal sample given as 2.1198 Volt, N_{sample} is the total number of output signal samples. The total number of samples N_{sample} is considered to be 100 for the simulation.

For the phase noise computation, range for f_m has been considered to be 1 Hz to 100 kHz. Equation (5.5) has been used to compute $L(f_m)$, which is expressed in dB_cHz^{-1} unit. Finally, the output of $L(f_m)$ versus offset frequency (f_m) has been plotted to obtain phase noise. The results are found to be very optimistic and minimum comparatively to the exiting Opto-Electronic oscillator (Chembo et al., 2009). The minimum phase noise observed is as low to -245 dB_cHz^{-1} at the 100 kHz offset.

5.3.2 Stability Analysis of IOEO using Allan Variance

Short term stability is generally carried out using Allan variance method. This method has been in use for the characterization of the designed oscillator (Rubiola, 2008). The computation of Allan variance is carried out from the phase noise spectra of the designed oscillator. Generally any phase noise spectra can have five types of noise termed as Random walk frequency noise, flicker frequency noise, white frequency noise, flicker phase noise and white phase noise respectively. The Allan variance is generally expressed as follows:

$$\sigma_y^2(\tau) = \frac{3f_H h_2}{(2\pi)^2}\tau^{-1} + [1.038 + 3ln(2\pi f_H \tau] \times \frac{h_1}{(2\pi)^2}\tau^{-1} + \frac{h_0}{2}\tau^{-1} + 2ln(2)h_{-1} + \frac{(2\pi)^2}{6}h_{-2}\tau \tag{5.6}$$

Where,

$h_2 = \frac{b_0}{f_0^2}$,

$h_1 = \frac{b_{-1}}{f_0^2}$,

$h_0 = \frac{b_{-2}}{f_0^2}$,

$h_{-1} = \frac{b_{-3}}{f_0^2}$ and

$h_{-2} = \frac{b_{-4}}{f_0^2}$.

f_0 is the resonance frequency, f_H is the low-pass cutoff frequency and τ is the time.

The coefficients b_0, b_{-1}, b_{-2}, b_{-3} and b_{-4} represent various noise types as shown in Table 5.1. These coefficients are computed from the phase noise spectra using 0 $dBdec^{-1}$, -10 $dBdec^{-1}$, -20 $dBdec^{-1}$, -30 $dBdec^{-1}$ and -40 $dBdec^{-1}$ roll off rate from the phase noise

spectra respectively. The method discussed by Rubiola in (Rubiola, 2008) for Allan variance computation has been used for the short term stability of the designed IOEO. Figure 5.4 depicts the phase noise of the designed IOEO. The phase noise plot shows the -20 $dBdec^{-1}$ roll off, hence only white frequency noise is predominant in the designed IOEO. From the results shown in Figure 5.6, it is evident that the Allan Variance is constant

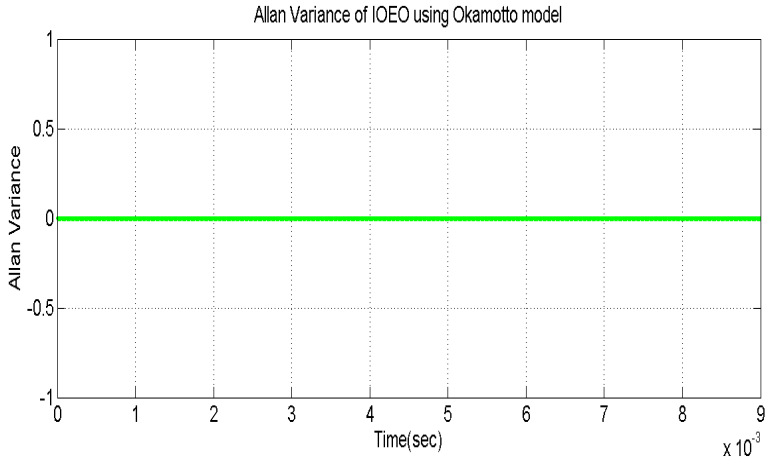

Figure 5.6: Allan variance of IOEO

as a function of time and hence it is concluded that the designed IOEO (Figure 3.2) exhibits short term stability.

5.3.3 Analysis of Phase Noise using Two Port Network Model

In this section, the phase noise of the IOEO has been analysed using two port network method. All the components of the IOEO belong to a model of two port network. The performance of a composite two port network which comprises a cascade of many two port networks can be analysed invoking the concept of ABCD matrix or parameters. Therefore the phase noise computation through ABCD parameters can also explored and its accuracy can be compared with the linear model of the IOEO. P. K. Webb of British Post Office Research Department has been pioneer to define the ABCD matrix for Telephony four-wire Transmission Systems in 1977. The defined ABCD matrix for the two-port network model finds its utility in mathematical techniques for circuit analysis.

Once any linear circuit satisfies the port conditions and does not have an independent source, then the circuit can be defined as a two-port network. A two-port network is described by its properties stated by a matrix of numbers (Ghosh, 2005). The use of ABCD matrix simplifies the response of the network to signals applied at the port of the

two port network. Even though all voltages and currents are not calculated, it is possible to get the response of two port network using ABCD matrix.

For the mathematical modeling of any two-port network, 2 by 2 square matrix of complex elements is used. This is applicable to any two port linear network provided the linear superposition of various short-circuit and open circuit conditions exist. The matrix is usually expressed in matrix notation, and they establish relationship between the variables V_1 voltage across port 1, I_1 current into port 1, V_2 voltage across port 2 and I_2 current into port 2. These current, voltage, and power variables are useful in the analysis of two port linear network model.

In the designed IOEO, the IOMR is a photonic device that replaces a long fiber and is basically a symmetrical SOI based device. The most common definitions of ABCD parameters for the reciprocal networks or symmetrical networks, are defined as $A = D$ (Laughton, and Say, 2013). In case of reciprocal network and loss less network, A and D are real, while B and C are found to be imaginary. Hence the phase noise contribution of the IOMR in the IOEO has been analysed using two port network theory.

The optical power of IOMR for the frequency range of $1.932 \times 10^{14} Hz$ to $1.938 \times 10^{14} Hz$ is shown in Figure 5.7. The linearity of the IOMR has been observed and is shown in Figure

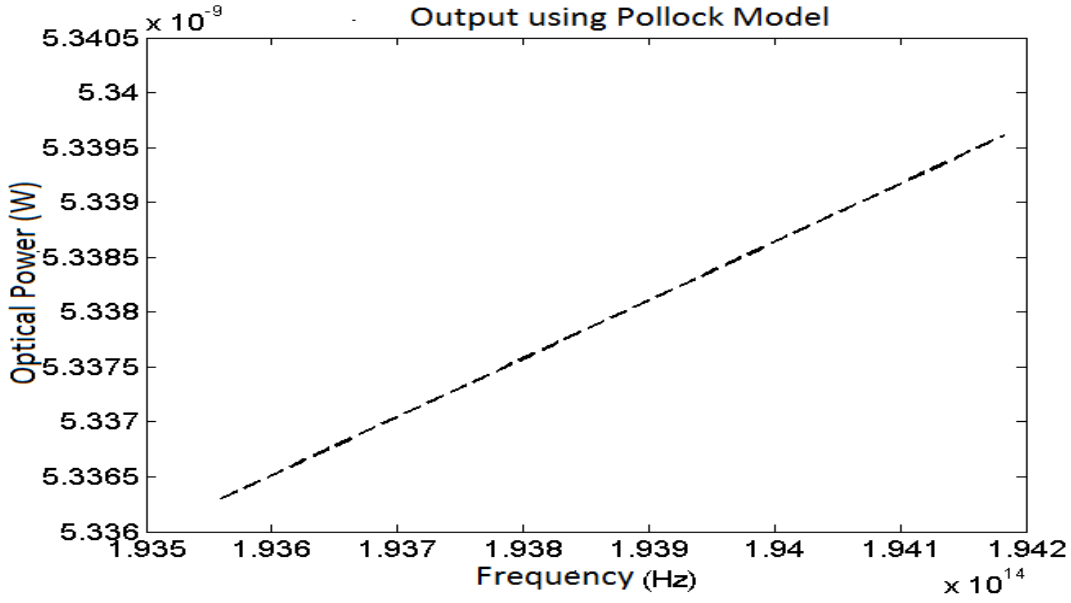

Figure 5.7: Variation of optical power of IOMR with change in frequency

5.7. The lineraity of the IOMR in the above stated frequency range makes it suitable for

the two port network analysis. The ABCD parameters of the IOMR have been computed for IOMR using both Okamoto and Pollock models. The contribution of phase noise due to IOMR of the IOEO has been computed assuming that both the Okamoto and Pollock models are linear in the frequency range of 1.932×10^{14} Hz to 1.938×10^{14} Hz for the IOMR.

5.3.4 Analytical Formulation of Phase Noise Contribution of IOMR in IOEO using Okamoto Model

In this section, Okamoto's model (Okamoto, 2010) of the SOI based IOMR has been considered for the analysis. The transfer function of the Okamoto model of dual bus ring configuration (Okamoto, 2010) can be applied to the schematic depicting the 4 port model of IOMR shown in Figure 5.8. The complete analysis is based on the assumption that IOMR is linear device as shown in Figure 5.7. The Figure 5.8 shows the schematic of the IOMR. The various ports of the IOMR are input, output, through and drop port. For the present analysis the refractive index and the Electric field at the various port have been considered. Let the electric field at the input port 1 be E_1 and the Electric field at the through port 2 be E_2. Let E_3 denote the Electric field at output port 3. Likewise E_4 represents the Electric field at port 4 (drop port). The characteristic impedance of free

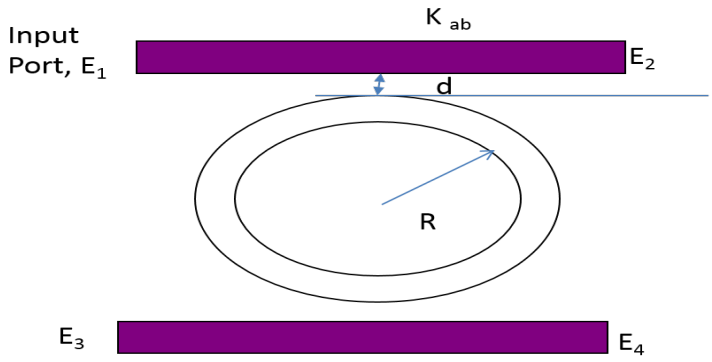

Figure 5.8: Schematic of IOMR

space is given by the Equation 5.7.

$$Z_0 = \sqrt{\frac{\mu_0}{n^2 \varepsilon_0}} \tag{5.7}$$

The input impedance of the IOMR at the port 1 has been computed using Equation (5.7) and is expressed as

$$Z_{input} = \frac{Z_0}{n} \tag{5.8}$$

Where, $Z_0 = 377ohm$, n is the refractive index.
E_1 is the input Electric Field and is defined as

$$E_1 = A_0 cos(\omega t) \tag{5.9}$$

The transfer function given by the Okamoto model (Okamoto, 2010) of dual bus ring model has been used to analyse the effect of the phase noise on the IOEO system due to presence of IOMR. The transfer function of intensity of IOMR is given by Equation (5.13). Various parameters of IOMR such as x_1, y_1 and ϕ are defined by Equations (5.14), (5.15) and (5.16) respectively.

$$T(\phi) = |\frac{E_3}{E_1}|^2 \tag{5.10}$$

$$|\frac{E_3}{E_1}|^2 = (1-\gamma)\frac{x_1^2(1-y_1)^2}{(1-x_1^2y_1^2)^2 + 4x_1^2y_1^2 sin^2(\frac{\phi}{2})} \tag{5.11}$$

$$|\frac{E_3}{E_1}|^2 = \frac{p_3}{p_1} \tag{5.12}$$

$$T(\phi) = (1-\gamma)\frac{x_1^2(1-y_1)^2}{(1-x_1^2y_1^2)^2 + 4x_1^2y_1^2 sin^2(\frac{\phi}{2})} \tag{5.13}$$

$$x_1 = (1-\gamma)\frac{1}{2}exp(-\frac{\rho L}{2}) \tag{5.14}$$

Where,
γ is the intensity insertion loss, L is the length of ring resonator and ρ intensity attenuation coefficient.

$$y_1 = cos(kl) \tag{5.15}$$

$$\phi = \beta L \tag{5.16}$$

The Equation (5.17) defines the ratio of E_1 and E_3.

$$\frac{E_3}{E_1} = \sqrt{(1-\gamma)\frac{x_1^2(1-y_1)^2}{(1-x_1^2y_1^2)^2 + 4x_1^2y_1^2 sin^2(\frac{\phi}{2})}} \tag{5.17}$$

The output intensity E_3 is expressed as

$$E_3 = E_1 \sqrt{(1-\gamma)\frac{x_1^2(1-y_1)^2}{(1-x_1^2y_1^2)^2+4x_1^2y_1^2sin^2(\frac{\phi}{2})}} \tag{5.18}$$

V_1 and V_2 are the voltages at port 1 and port 2 of IOMR respectively. Similarly the voltages at port 3 and port 4 are denoted by V_3 and V_4 respectively. Then,

$$V_1 = -E_1 l \tag{5.19}$$

$$V_1 = -A_0 l cos(\omega t) \tag{5.20}$$

$$V_3 = -E_3 l \tag{5.21}$$

$$V_3 = E_1 * l \sqrt{(1-\gamma)\frac{x_1^2(1-y_1)^2}{(1-x_1^2y_1^2)^2+4x_1^2y_1^2sin^2(\frac{\phi}{2})}} \tag{5.22}$$

$$V_2 = -E_2 l \tag{5.23}$$

$$E_2 = (1-\gamma)^2 \frac{cos(kl)-(1-\gamma)^2 exp(\frac{-\rho L}{2}-j\beta L)}{1-(1-\gamma)^2 exp(\frac{-\rho L}{2}-j\beta L)cos(kl)} \tag{5.24}$$

and V_2 is given by the Equation (5.25).

$$V_2 = -lE_2 \tag{5.25}$$

From the fundamental law of conservation of energy, one can have the Equation (5.26) for the designed IOMR.

$$E_1 = E_2 + E_3 + E_4 \tag{5.26}$$

The expression for E_4 can be written as

$$E_4 = E_1 - E_2 - E_3 \tag{5.27}$$

$$E_4 = -V_1 l + V_2 l + V_3 l \tag{5.28}$$

Using the Equations (5.27) and (5.28), one gets,

$$V_4 = -E_4 l \tag{5.29}$$

$$V_4 = -[(-V_1 l + V_2 l + V_3 l)]l \tag{5.30}$$

The current at the input and output ports of the IOMR shown in Figure 5.2 are calculated using Equations (5.31) and (5.32):

$$I_1 = \frac{V_1}{Z_{input}} \tag{5.31}$$

$$I_3 = \frac{V_2}{Z_{output}} \tag{5.32}$$

As stated in previous section, the ABCD parameters are defined only for two port network. IOMR is a 4 port network. Therefore ABCD parameters or ABCD matrix of IOMR seems not possible. However for simplicity, the port 2 and port 4 can be grounded, assuming the potential across these port to be zero. Now principles of two port network theory can be invoked to explore the possibility of deriving ABCD matrix of IOMR. It is well known that the ABCD parameters can be derived only for a linear device. In section 5.3.3, it has been shown that IOMR exhibits linear response features over a span of wavelength of operation. In this section, an analytic formulation is presented for the derivation of ABCD matrix of IOMR. In the first stage, the port 2 and port 4 are grounded as shown in Figure 5.9. For the first stage, ABCD parameters can be written as

$$\begin{pmatrix} A1_{Oka} & B1_{Oka} \\ C1_{Oka} & D1_{Oka} \end{pmatrix} \tag{5.33}$$

$$A1_{Oka} = \frac{V_1}{V_3} \tag{5.34}$$

with $I_3 = 0$

$$B1_{Oka} = \frac{V_1}{I_3} \tag{5.35}$$

with $V_3 = 0$

$$C1_{Oka} = \frac{I_1}{V_3} \tag{5.36}$$

with $I_3 = 0$

$$D1_{Oka} = \frac{I_1}{I_3} \tag{5.37}$$

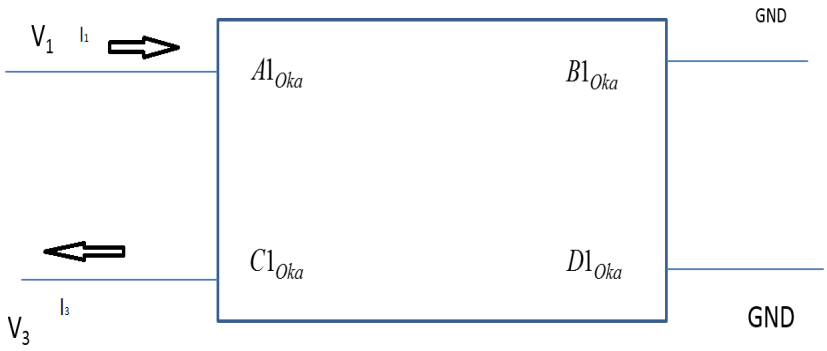

Figure 5.9: First stage of IOMR as two port network with port 2 and port 4 grounded

with $V_3 = 0$.

Here $V_1 = V_{input}$ and $V_3 = V_{output}$

$$I_1 = \frac{V_1}{Z_{input}} \tag{5.38}$$

$$I_3 = \frac{V_3}{Z_{out}} \tag{5.39}$$

The ABCD parameters of IOMR, an optical two port network can be calculated as:

$$\begin{pmatrix} A_{Oka} & B_{Oka} \\ C_{Oka} & D_{Oka} \end{pmatrix} = \begin{pmatrix} A1_{Oka} & B1_{Oka} \\ C1_{Oka} & D1_{Oka} \end{pmatrix} \tag{5.40}$$

The voltage gain V_{Gain} of Okamoto model of IOMR is given by:

$$V_{Gain} = \frac{1}{A_{Oka}} \tag{5.41}$$

The phase noise computation of the designed IOMR has been carried out using Equation (5.5) of section 5.3.1.

$$L(f_m) = 10log(\frac{\sigma_\phi^2}{2\pi f_m^2})$$

Where,

f_m is the frequency offset and σ_ϕ^2 is the variance of the output signal of IOMR.

The phase noise computation of the designed IOMR has been carried out using the calculated ABCD parameters as follows:

The variance σ_ϕ^2 of output voltage of the IOMR has been computed. The output voltage of IOMR has been computed as the product of voltage gain and the optical modulated output. The power at the output port of IOMR is shown in Figure 5.10. The variance σ_ϕ^2 has been computed using the expression:

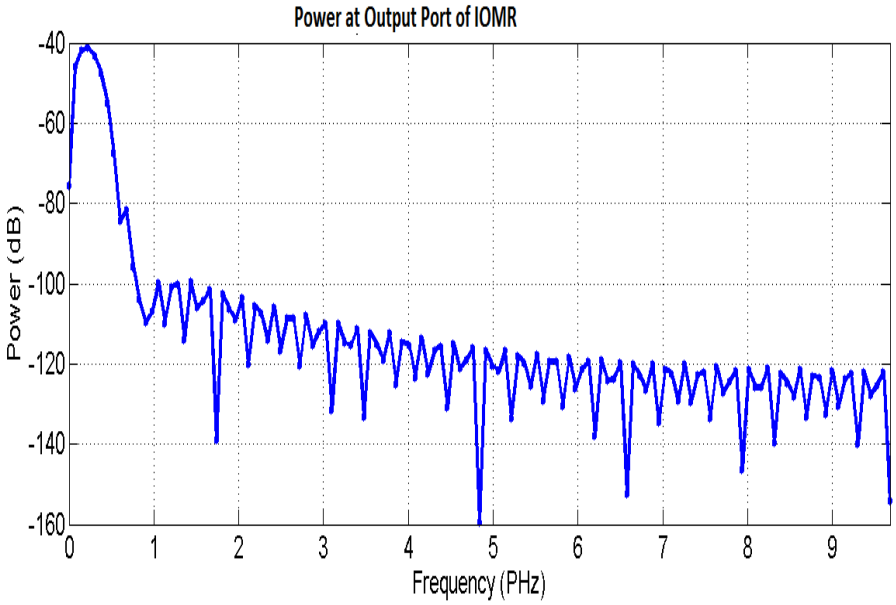

Figure 5.10: Power at the output port of IOMR using Okamoto model

$$\sigma_{\phi}^{2} = \frac{\sum\{X-\mu\}}{N_{sample}}$$

Where,

X is the output signal sample of the IOMR which varies from -0.0125 Volt to 0.0125 Volt, μ is the mean of the output signal sample given as -4.4684×10^{-9} Volt, N_{sample} is the total number of output signal samples. The total number of sample N_{sample} is considered to be 100 for the simulation. For the phase noise computation, range for f_m has been considered to be 1 Hz to 100 kHz. Equation (5.5) has been used to compute $L(f_m)$, which is expressed in dB_cHz^{-1} unit. Finally, the output of $L(f_m)$ versus offset frequency (f_m) has been plotted to obtain phase noise. The results of such a computation is shown in Figure 5.11. From the results shown in Figure 5.11, it is observed that the contribution of the IOMR to the phase noise of the system is insignificant and it is in the range of -250 dB_cHz^{-1} to -280 dB_cHz^{-1} at the various frequencies of offset.

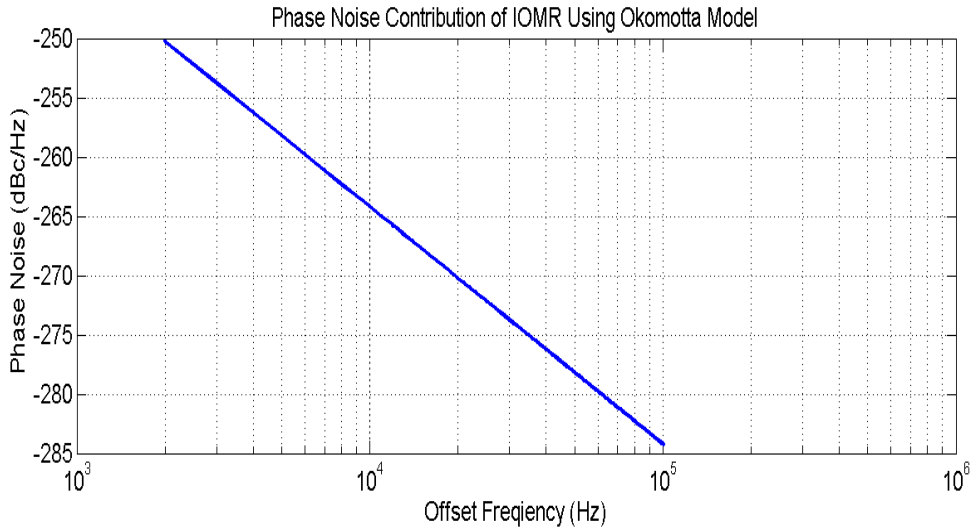

Figure 5.11: Phase noise contribution of IOMR using Okamoto model

5.3.5 Analytical Formulation of Phase Noise Contribution of IOMR in IOEO using Pollock Model

Analysis of IOMR using Pollock model is similar to the Okamoto model of IOMR described in section 5.3.4. ABCD parameters of pollock model of IOMR shown in Figure 5.12, can also be derived following logic described earlier. In this section, Pollock's model (Pollock and Lipson, 2003) of the SOI based IOMR has been considered for the analysis. The complete analysis is based on the assumption that IOMR is a linear device as shown in Figure 5.7. The Figure 5.12 shows the schematic of the IOMR used for the Pollock's model. The input port of the IOMR is termed as S_1. The three output ports of the IOMR are termed as S_{-2}, S_{-3}, and S_{-4}. All the waveguides in the Pollock model are considered to be operating in a single mode. For the present analysis, the refractive indices and the electric fields present at the input and output ports are considered. For the IOMR shown in Figure 5.12, the characteristic impedance of free space is given by Equation (5.42):

$$Z_0 = \sqrt{\frac{\mu_0}{n^2 \varepsilon_0}} \tag{5.42}$$

From the characterization impedance, the input impedance has been computed using Equation (5.43).

$$Z_{input} = \frac{Z_0}{n} \tag{5.43}$$

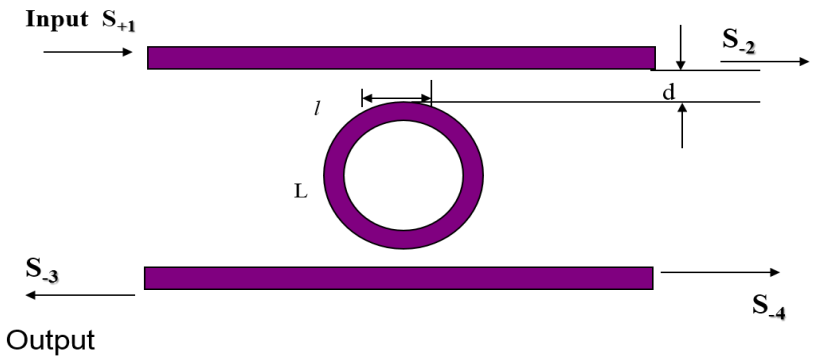

Figure 5.12: Schematic of IOMR for Pollock model

Where, $Z_0 = 377$ ohm, and n is the refractive index.
The currents I_1 and I_2 are defined in Equations (5.44) and (5.45) respectively:

$$I_1 = \frac{V_1}{Z_{input}} \tag{5.44}$$

$$I_2 = \frac{V_2}{Z_{out\,put}} \tag{5.45}$$

s_{+1} is the input Electric Field at input port. All the other are ports do not have any incoming field initially. The electric field s_{+1} is defined as

$$S_{+1} = Acos(\omega t) \tag{5.46}$$

According to (Pollock and Lipson, 2003),amplitude of the outgoing waves S_{-1}, S_{-2}, S_{-3} and S_{-4} are given by Equations (5.47), (5.48), (5.49) and (5.50) respectively.

$$S_{-1} = e^{-j\beta L}\frac{k_1 k_2}{\frac{1}{\tau_e}+\frac{1}{\tau_f}+\frac{1}{\tau_0}}S_{+1} \tag{5.47}$$

$$S_{-2} = e^{-j\beta L}(1-\frac{k_1 k_2}{\frac{1}{\tau_e}+\frac{1}{\tau_f}+\frac{1}{\tau_0}})S_{+1} \tag{5.48}$$

$$S_{-3} = e^{-j\beta L}\frac{k_1 k_2}{\frac{1}{\tau_e}+\frac{1}{\tau_f}+\frac{1}{\tau_0}}S_{+1} \tag{5.49}$$

$$S_{-4} = e^{-j\beta L}\frac{k_1 k_2}{\frac{1}{\tau_e}+\frac{1}{\tau_f}+\frac{1}{\tau_0}}S_{+1} \tag{5.50}$$

Where, L is the Ring circumference, k_1 and k_2 are the coupling coefficients in the forward direction; $\frac{1}{\tau_0}$ is the decay rate due to the propagation loss; $\frac{1}{\tau_e}$ and $\frac{1}{\tau_f}$ are the decay rates due to the coupling to the bus waveguide and the resonator respectively.

Using the formulation of CMT, the outgoing amplitudes S_{-1}, S_{-2},S_{-3} and S_{-4} are denoted by V_1, V_2, V_3 and V_4 respectively. They can be represented through Equations (5.52), (5.54), (5.56) and (5.58) respectively.

$$V_1 = -S_{+1}l \tag{5.51}$$

$$V_1 = -A_0 l cos(\omega t) \tag{5.52}$$

$$V_2 = -S_{-2}l \tag{5.53}$$

$$V_2 = -e^{-j\beta L}(1 - \frac{k_1 k_2}{\frac{1}{\tau_e} + \frac{1}{\tau_f} + \frac{1}{\tau_0}})S_{+1}l \tag{5.54}$$

$$V_3 = -S_{-3}l \tag{5.55}$$

$$V_3 = e^{-j\beta L}\frac{k_1 k_2}{\frac{1}{\tau_e} + \frac{1}{\tau_f} + \frac{1}{\tau_0}}S_{+1}l \tag{5.56}$$

$$V_4 = -S_{-4}l \tag{5.57}$$

$$V_4 = -e^{-j\beta L}\frac{k_1 k_2}{\frac{1}{\tau_e} + \frac{1}{\tau_f} + \frac{1}{\tau_0}}S_{+1}l \tag{5.58}$$

Following an approach similar to Okamoto model of IOMR, ABCD parameters of Pollock model of IOMR (Pollock and Lipson, 2003) shown in Figure 5.12 can also be derived.

In the first stage of IOMR, the ports S_{-2} and S_{-4} are grounded. The ABCD parameters of the first stage of IOMR are

$$\begin{pmatrix} A1_{Pol} & B1_{Pol} \\ C1_{Pol} & D1_{Pol} \end{pmatrix} \tag{5.59}$$

$$A1_{Pol} = \frac{V_1}{V_3} \tag{5.60}$$

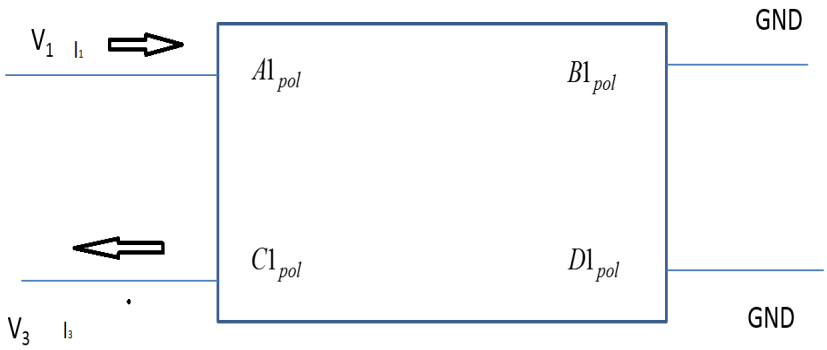

Figure 5.13: First stage of IOMR using Pollock model with port S_{-2} and port S_{-4} grounded

with $I_3 = 0$

$$B1_{Pol} = \frac{V_1}{I_3} \tag{5.61}$$

with $V_3 = 0$

$$C1_{Pol} = \frac{I_1}{V_3} \tag{5.62}$$

with $I_3 = 0$

$$D1_{Pol} = \frac{I_1}{I_3} \tag{5.63}$$

with $V_3 = 0$

Using the principles of a two port network, ABCD parameters of single stage of Pollock model of IOMR, are obtained as:

$$\begin{pmatrix} A_{Pol} & B_{Pol} \\ C_{Pol} & D_{Pol} \end{pmatrix} = \begin{pmatrix} A1_{Pol} & B1_{Pol} \\ C1_{Pol} & D1_{Pol} \end{pmatrix} \tag{5.64}$$

The voltage gain V_{Gain} of Pollock model of IOMR is given by :

$$V_{Gain} = \frac{1}{A_{Pol}} \tag{5.65}$$

The phase noise computation of the designed IOMR has been carried out using Equation (5.5) of section 5.3.1.

$$L(f_m) = 10log(\frac{\sigma_\phi^2}{2\pi f_m^2})$$

Where,

f_m is the frequency offset and σ_ϕ^2 is the variance of the output signal of IOMR.

The phase noise computation of the designed IOMR has been carried out using the calculated ABCD parameters as follows:

The variance σ_ϕ^2 of output voltage of the IOMR has been computed. The output voltage of IOMR has been computed as the product of voltage gain and the optical modulated output. The power at output port IOMR has been shown in Figure 5.14. The variance σ_ϕ^2 has been

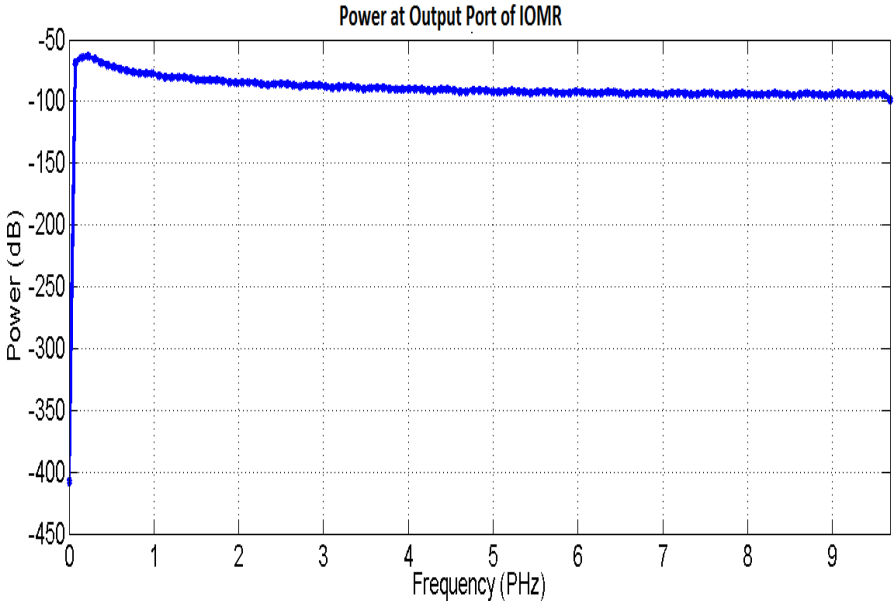

Figure 5.14: Power at output port of IOMR using Pollock model

computed using the expression given as:

$$\sigma_\phi^2 = \frac{\Sigma\{X-\mu\}}{N_{sample}}$$

Where,

X is the output signal sample of the IOMR and varies from -6.2613×10^{-4} Volt to 6.2613×10^{-7} Volt, μ is the mean of the output signal sample given as -1.8181×10^{-11} Volt and N_{sample} is the total number of output signal samples. The total number of sample N_{sample} is assumed to be 100 for the simulation.

For the computation of phase noise, range for f_m has been considered to be 1 Hz to 100 kHz. Equation (5.5) has been used to compute $L(f_m)$, which is expressed in dB_cHz^{-1} unit. Finally, the variation of $L(f_m)$ versus offset frequency (f_m) has been computed to obtain phase noise. Result of the computation of phase noise of IOMR through Pollock model is shown in Figure 5.15. From the results of Figure 5.15, it is evident that the contribution of the IOMR to the phase noise of the system is insignificant and it is in the range of -280 dB_cHz^{-1} to -310 dB_cHz^{-1} at the various frequencies of offset. Using the results phase noise analysis is carried out for the IOMR, as shown in Figure 5.15. The Okamoto model

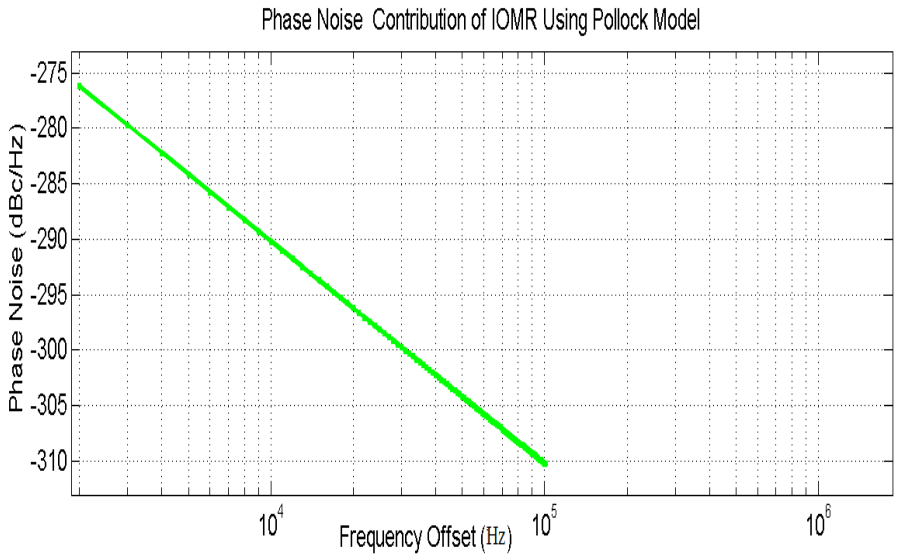

Figure 5.15: Phase noise contribution of IOMR using Pollock model

is found to be ideal one showing minimum phase noise contribution similar to the designed IOEO itself. The Pollock model also shows similar trend. The Okamoto model does not consider the effect of gap between straight and ring waveguides on the power coupling between straight and curved waveguides. Okamoto model considers the intensity insertion loss of ring resonator and the effect of coupling coefficient. In case of Pollock model, it considers the effect of coupling coefficient between straight and curved waveguides and decay rates. The Pollock model shows extremely minimum contribution to the phase noise of the IOEO by IOMR. Hence it is concluded that both the models of IOMR (Okamoto and Pollock models) exhibit similar trends of insignificant contribution to the phase noise of IOEO.

5.4 Thermal Stability of the Designed IOEO

In this section, thermal stability analysis of the designed IOEO has been carried out. For the prediction of the effect of temperature on the stability of IOMR, an analytical method has been used. It is widely proven that the refractive index is a function of both wavelength and temperature. The refractive indices of the fused silica and silicon have been explored for a wide range of temperature (Keiser, 2013). In this study, thermal stability of the IOEO using the Sellmeier model is used (Leviton and Frey, 2006) and the study covers wide

range of temperature. The temperature dependent Sellmeier model is represented as

$$n^2(\lambda,T)-1=\sum_{i=1}^{m}\frac{S_i\cdot(T)\lambda^2}{\lambda^2-\lambda_i^2(T)} \tag{5.66}$$

Where,
n is the refractive index, T is the temperature in Kelvin, S_i are the strengths of the resonance features in the material at wavelength λ_i.
According to temperature dependent Sellmeier model, if the resonance wavelength of the material is known, then the model can be approximated with a few terms. With such an approximation, effects of S_i and λ_i are used to fit the empirical data. IOEO using SOI based IOMR has generated considerable interest because of its capability of generating stable high frequency as high as 40 GHz. The high refractive index contrast of silicon and SiO_2 (n_{Si} -$n_{SiO_2} > 1.9$) has been explored and demonstrated in the literature for the IOMR having radii as small as $1\mu m$ with low bending loss (Rouger et al., 2010).
IOMR is highly attractive, especially because of its notch filter characteristics. IOMR helps in the selection of the desired wavelength of operation based on its structure. However, the study of the thermal effects on IOMR as a performance metric of the IOEO has not been discussed in the literature. In this section, a model for the thermal analysis of the IOEO based on the Sellmeier model is presented.
For the thermal stability analysis of IOEO, following assumptions are made:

- IOEO is based on single IOMR
- Refractive index is wavelength and temperature dependent
- Influence of the thermal expansion is small and hence is negligible
- Only the fundamental transverse electric mode exist in the IOMR.

For the analysis of IOEO, the temperature dependent Sellmeier model, can be simplified to three terms. The contributions of other higher order terms of S_i and λ_i on the model are insignificant. Hence for the analysis of designed IOEO, 4^{th} order temperature dependencies in all three terms in each of S_i and λ_i are adequate. The simplified Sellmeier model can be represented as

$$n^2(\lambda,T)-1=\sum_{i=1}^{3}\frac{S_i\cdot(T)\lambda^2}{\lambda^2-\lambda_i^2(T)} \tag{5.67}$$

Where,

$$S_i(T) = \sum_{J=0}^{4} S_{ij} \cdot T^j \tag{5.68}$$

and

$$\lambda_i(T) = \sum_{J=0}^{4} \lambda_{ij} \cdot T^j \tag{5.69}$$

The Sellmier model considered through Equation (5.67) and the refractive index for the Si and SiO_2 (at the 1550 nm and 150 K-300 K) (Leviton and Frey, 2006) have been used to analyse the effect of changes in the refractive index on the frequency offset of IOMR. As can be seen from the results of Figure 5.16, the relationship between the resulting frequency offset of IOMR and change in refractive index is non-linear.

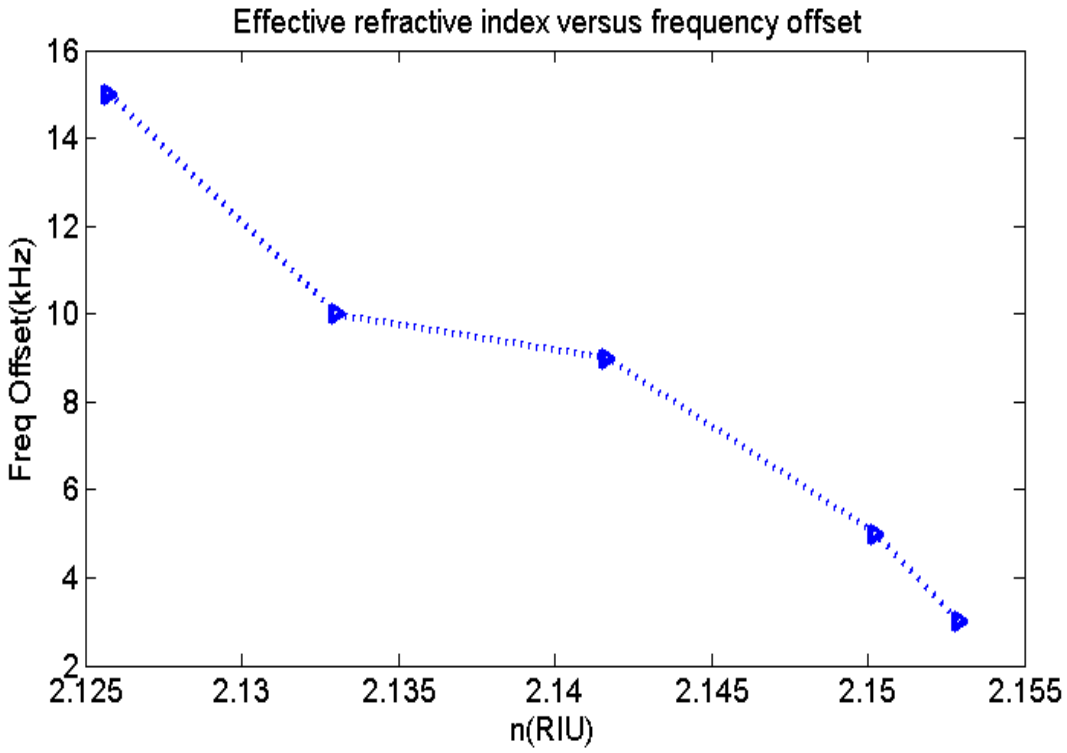

Figure 5.16: Variation of frequency Offset (kHz) with the change in effective refractive index (RIU) at 40 GHz)

The variation in effective refractive index with change in temperature of IOMR is illustrated in Figure 5.17.

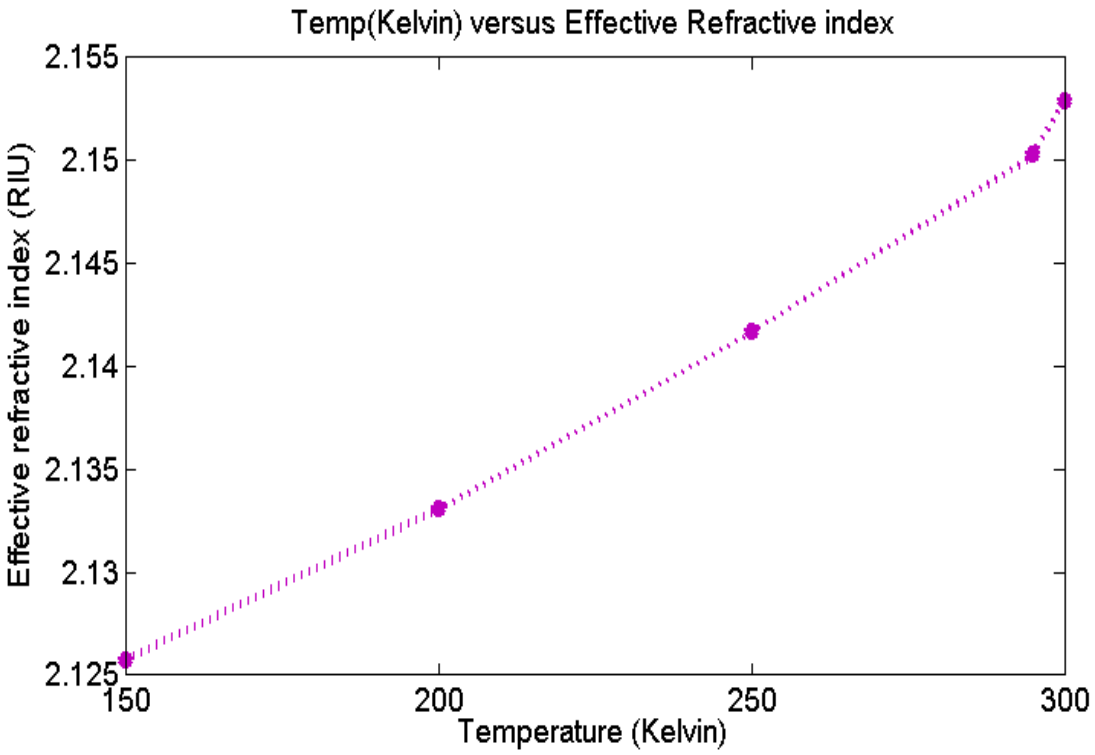

Figure 5.17: Variation of effective refractive index (RIU) with change in temperature (K) at oscillating frequency of 40 GHz)

The results of Figure 5.17 reveal almost a steady and linear variation except for the region of very high temperature. Figure 5.18 depicts the variation in offset frequency with change in temperature. The designed IOEO oscillates at 40 GHz with the minimum phase noise of -245 dB_cHz^{-1} at the 100 kHz offset. In the simulation, effective refractive index of IOMR is varied from 2.125 to 2.155 and the corresponding frequency shift in the IOEO is computed. With the rise in temperature, the resonant frequency of the oscillator decreases. The designed IOEO exhibits thermal stability of ± 0.325 $ppmK^{-1}$. Thermal stability of IOEO has been computed using

$$\pm ppm = \frac{\Delta f \times 10^6}{f_0}$$

Where,

Δf is the variation in offset frequency, f_0 is the desired frequency.

On substituting the value of Δf of 13 kHz (Figure 5.18) and f_0 of 39.9986×10^9 Hz, one

gets,

$$\pm ppm = \frac{0.000013 \times 10^6}{39.9986}$$

$$\pm ppm = 0.325$$

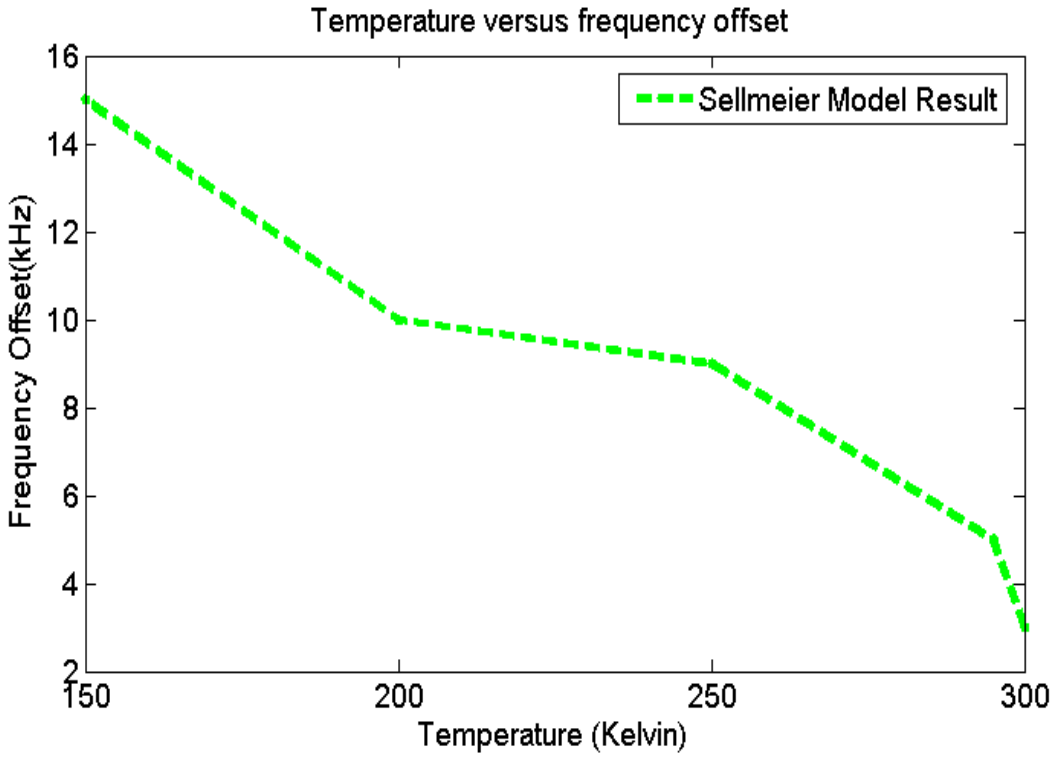

Figure 5.18: Variation of frequency offset (kHz) with change in temperature (K)

The thermal stability analysis presented in this section quantifies the temperature effects on the IOEO. It also paves the way for the application of IOEO in the design of sensors featured with high sensitivity and wider operating temperature range sensor.

5.5 Stability Analysis of the Designed IOEO

This section presents an analytical fromulation for the stability of IOEO described in chapter 3. The stability of a two port network has been analysed in (Odyniec, 1999) using the S-parameters. The Rollets factor (K1) is generally computed to establish the unstability of the forward elements (Amplifier). In the present case amplifier is considered to be stable

and is used only for the amplification purpose. The stability of the forward path has been ensured through computation of Rollets factor (K1). In this section, ABCD parameters of the forward and feedback paths have been computed to evaluate the gain of the designed IOEO. The block diagram of the IOEO is shown in Figure 3.2 of chapter 3. In the Figure 3.2, all the sub systems other than IOMR are two port network. Since all the subsystem of IOEO have to be considered as a two port network, and its ABCD-parameters need to be determined, the following steps have been followed for the realization of the same.

- A 4 port device (IOMR) has been equivalently transformed into two port device invoking the analysis in sections 5.3.3 and 5.3.4.
- The ABCD parameters of all the subsystems of IOEO have been determined using the approximate parameters (design and geometrical) of the individual subsystem
- The ABCD matrix of the forward path and the feedback path of IOEO is obtained by successive multiplication of the associated two successive subsystems.

The designed IOEO consists of various two port components. Hence designed IOEO can be linearised and expressed in terms of forward and feedback elements. The IOMR, EDFA, PD and OM are the feedback elements in the IOEO. The LNA1, BPF and LNA2 constitute the forward elements of the linear feedback system. The ABCD parameters of all the subsystems of IOEO have been derived.

5.5.1 ABCD Matrix of IOMR

The ABCD parameters of the SOI based IOMR (feedback element) have already been derived in section 5.3. For the derivation of ABCD parameters of IOMR, following parameters have been considered: The bus waveguide and ring waveguides have been taken as 500 nm wide. The core thickness of the waveguides is 235 nm. The radius of the ring is 3.5397 μm and effective refractive index is 2.44. From the analysis presented in section 5.3, the ABCD parameters of the IOMR using Okamoto model and Pollock model are written as

$$\begin{pmatrix} A_{IOMR} & B_{IOMR} \\ C_{IOMR} & D_{IOMR} \end{pmatrix} = \begin{pmatrix} A_{Oka} & B_{Oka} \\ C_{Oka} & D_{Oka} \end{pmatrix} \tag{5.70}$$

and

$$\begin{pmatrix} A_{IOMR} & B_{IOMR} \\ C_{IOMR} & D_{IOMR} \end{pmatrix} = \begin{pmatrix} A_{Pol} & B_{Pol} \\ C_{Pol} & D_{Pol} \end{pmatrix} \tag{5.71}$$

The ABCD parameters of IOMR can be written using Okamoto and Pollock model as:

$$\begin{pmatrix} A_{IOMR} & B_{IOMR} \\ C_{IOMR} & D_{IOMR} \end{pmatrix} = \begin{pmatrix} A_{IOMR_Okomotto} & B_{IOMR_Okomotto} \\ C_{IOMR_Okomotto} & D_{IOMR_Okomotto} \end{pmatrix} \tag{5.72}$$

$$\begin{pmatrix} A_{IOMR_Okomotto} & B_{IOMR_Okomotto} \\ C_{IOMR_Okomotto} & D_{IOMR_Okomotto} \end{pmatrix} = \begin{pmatrix} 69.1459 & 1.0684 \times 10^4 \\ 0.4475 & 69.1459 \end{pmatrix} \tag{5.73}$$

Similarly for Pollock,

$$\begin{pmatrix} A_{IOMR} & B_{IOMR} \\ C_{IOMR} & D_{IOMR} \end{pmatrix} = \begin{pmatrix} A_{IOMR_Pollock} & B_{IOMR_Pollock} \\ C_{IOMR_Pollock} & D_{IOMR_Pollock} \end{pmatrix} \tag{5.74}$$

$$\begin{pmatrix} A_{IOMR_Pollock} & B_{IOMR_Pollock} \\ C_{IOMR_Pollock} & D_{IOMR_Pollock} \end{pmatrix} = \begin{pmatrix} 1.1925 \times 10^3 & 1.8425 \times 10^5 \\ 7.7178 & 1.1925 \times 10^3 \end{pmatrix} \tag{5.75}$$

5.5.2 ABCD Matrix of LNA

In this section, the ABCD parameters of LNA used in IOEO are derived using the dimensional and other parameters of LNA. In the computation of ABCD matrix of the LNA (Raytheon RF Components, 2002), the following parameters of LNA have been considered: In this thesis, the RMLA31400 (Raytheon RF Components, 2002) has been used as LNA1 and LNA2 for the design of IOEO. Typical frequency range of 31-40 GHz, nominal gain of 20 dB, nominal noise figure of 1.8 dB, single supply of +1.9 Volt, supply current of 16 mA and chip size of 2.25 mm x 1.25 mm x 100 μm.

The ABCD matrix of LNA1 is derived from the S-parameters of the LNA1. The S-parameters of LNA1 in (dB) at 40 GHz are given as:

$$\begin{pmatrix} S_{11-LNA1} & S_{12-LNA1} \\ S_{21-LNA1} & S_{22-LNA1} \end{pmatrix} = \begin{pmatrix} -4.5 & -37.5 \\ 20 & -13 \end{pmatrix} \tag{5.76}$$

The S parameters linear unit) are given by:

$$\begin{pmatrix} S_{11-LNA1} & S_{12-LNA1} \\ S_{21-LNA1} & S_{22-LNA1} \end{pmatrix} = \begin{pmatrix} 0.5956 & 0.0133 \\ 10 & 0.2238 \end{pmatrix} \tag{5.77}$$

The ABCD parameters have been derived from the S parameters of the LNA1 using the conversion formula given in (Pozar, 2009):

$$\begin{pmatrix} A_{LNA1} & B_{LNA1} \\ C_{LNA1} & D_{LNA1} \end{pmatrix} = \begin{pmatrix} 0.0686 & 4.5492 \\ 0.0002 & 0.0314 \end{pmatrix} \tag{5.78}$$

Similarly, the ABCD matrix of LNA2 is computed.

$$\begin{pmatrix} A_{LNA2} & B_{LNA2} \\ C_{LNA2} & D_{LNA2} \end{pmatrix} = \begin{pmatrix} 0.0686 & 4.5492 \\ 0.0002 & 0.0314 \end{pmatrix} \tag{5.79}$$

5.5.3 ABCD Matrix of BPF

In this section, the ABCD parameters of the BPF (Figure 3.22 of chapter 3) have been derived. This is based on the microstrip and consists of HPF and LPF. The derived ABCD parameters of the BPF are:

$$\begin{pmatrix} A_{BPF} & B_{BPF} \\ C_{BPF} & D_{BPF} \end{pmatrix} = \begin{pmatrix} A_L & B_L \\ C_L & D_L \end{pmatrix} \tag{5.80}$$

Where,

- $A_L = 1 + \frac{Z_A}{Z_B} + \{Z_C + \frac{Z_C Z_A}{Z_B} + Z_A\}\frac{1}{Z_D}$
- $B_L = Z_E\{1 + \frac{Z_A}{Z_B} + (Z_C + \frac{Z_C Z_A}{Z_B} + Z_A)\frac{1}{Z_D}\} + Z_C(1 + \frac{Z_A}{Z_B}) + Z_A$
- $C_L = \frac{1}{Z_B} + (\frac{Z_C}{Z_B} + 1)\frac{1}{Z_D}$
- $D_L = \frac{1}{Z_E}\{\frac{1}{Z_B} + (\frac{Z_C}{Z_B} + 1)\frac{1}{Z_D}\} + \frac{Z_C}{Z_B} + 1$

Where,
$Z_A = \frac{1}{j\omega 2C_{11}}$, $Z_C = \frac{1}{j\omega 2C_{11}} + \frac{j\omega L_{22}}{2}$, $Z_D = \frac{1}{j\omega C_{22}}$, $Z_B = j\omega L_{11}$ and $Z_E = \frac{j\omega L_{22}}{2}$.
Following data have been considered for the computation of the ABCD parameters of BPF: $R_0 = 50$ ohm, $\omega_c = 2\pi f$ and $f = 39.8 \times 10^9$ Hz, $L_{11} = 0.10002$ nH, $C_{11} = 0.04008$ pF, $L_{22} = 0.39610$ nH and $C_{22} = 0.15884$ pF.
The ABCD parameters of the designed BPF have been computed as

$$\begin{pmatrix} A_{BPF} & B_{BPF} \\ C_{BPF} & D_{BPF} \end{pmatrix} = \begin{pmatrix} 2.57 & 33.41 \\ 0.0238 & 1.3818 \end{pmatrix} \tag{5.81}$$

Similarly,

The ABCD parameters of the designed ADS generated BPF (Figures 3.26) have been computed from the S-parameters (dB) of the BPF as shown:

$$\begin{pmatrix} S_{11-BPF} & S_{12-BPF} \\ S_{21-BPF} & S_{22-BPF} \end{pmatrix} = \begin{pmatrix} -75 & 0 \\ 0 & -75 \end{pmatrix} \tag{5.82}$$

The S-parameters of BPF in linear unit can be written as:

$$\begin{pmatrix} S_{11-BPF} & S_{12-BPF} \\ S_{21-BPF} & S_{22-BPF} \end{pmatrix} = \begin{pmatrix} 1.77 \times 10^{-4} & 1 \\ 1 & 1.77 \times 10^{-4} \end{pmatrix} \tag{5.83}$$

The ABCD parameters of the BPF is computed as:

$$\begin{pmatrix} A_{BPF} & B_{BPF} \\ C_{BPF} & D_{BPF} \end{pmatrix} = \begin{pmatrix} 1.0000 & 0.0089 \\ -0.0000 & 1.0000 \end{pmatrix} \tag{5.84}$$

5.5.4 ABCD Matrix of OM

The ABCD parameters of optical modulator are derived in this section. The MXAN-LN-40 (iXblue, n.d.) optical modulator, which basically is an intensity modulator for the K_a-band has been considered for the computation of the ABCD parameters. A two port representation of an MXAN-LN-40 (iXblue, n.d.) optical modulator is shown in Figure 5.19. The S-parameters (in dB) of the optical modular have been found to be

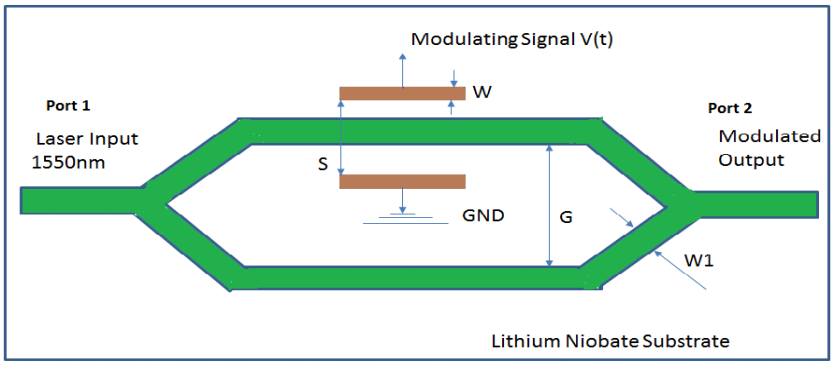

Figure 5.19: Two port network representation of the OM

$$\begin{pmatrix} S_{11-OM} & S_{12-OM} \\ S_{21-OM} & S_{22-OM} \end{pmatrix} = \begin{pmatrix} -16 & -6 \\ -6 & -16 \end{pmatrix} \tag{5.85}$$

The S-parameters (Linear unit) Of optical modulator can be written as:

$$\begin{pmatrix} S_{11-OM} & S_{12-OM} \\ S_{21-OM} & S_{22-OM} \end{pmatrix} = \begin{pmatrix} 0.1584 & 0.5011 \\ 0.5011 & 0.1584 \end{pmatrix} \tag{5.86}$$

The ABCD parameters of single drive MZIM can be derived from the S-parameters and are given as follows:

$$\begin{pmatrix} A_{OM} & B_{OM} \\ C_{OM} & D_{OM} \end{pmatrix} = \begin{pmatrix} 1.2233 & 54.4197 \\ 0.0091 & 1.2233 \end{pmatrix} \tag{5.87}$$

5.5.5 ABCD Matrix of EDFA

This section deals with the formulation and simulation of ABCD-parameters of EDFA. The s-parameters of the EDFA have been calculated using Optisystem. The length of the EDFA is 5 m. The Rayleigh scattering constant has been taken into consideration. The signal of wavelength 980 nm is used as pump signal with 100 mW power. Since isolators are at input and output of the EDFA as shown in Figure 3.11, the return loss of the EDFA is same as isolators. The gain of the EDFA is found to be 42 dB. The return loss for the chosen isolator (AMONICS, n.d.) is -55 dB. The computed S_{11} of the isolator is found to be 3.162×10^{-6}. Since the EDFA uses isolator at both input and output ports, the S_{11} and S_{22} are assumed to be same. The S_{12} is assumed to be 0.008, since the EDFA is operating in co-propagating mode. Therefore S_{12} should ideally be insignificantly small.
The S-parameters (linear unit) of the EDFA have been assumed to be

$$\begin{pmatrix} S_{11-EDFA} & S_{12-EDFA} \\ S_{21-EDFA} & S_{22-EDFA} \end{pmatrix} = \begin{pmatrix} 0.00177 & 0.008 \\ 125.89 & 0.00177 \end{pmatrix} \tag{5.88}$$

The ABCD parameters of the EDFA have been computed from its S-parameters. The ABCD parameters are given as

$$\begin{pmatrix} A_{EDFA} & B_{EDFA} \\ C_{EDFA} & D_{EDFA} \end{pmatrix} = \begin{pmatrix} 0.0080 & -0.0007 \\ -0.0000 & 0.0080 \end{pmatrix} \tag{5.89}$$

5.5.6 ABCD Matrix of PD

The Photo Diode (PD) is an important constituent of the designed IOEO. The PD converts the optical power into the electrical power. An equivalent circuit model of an PD discussed in (Wang et al., 2002) has been considered to derive ABCD matrix of the PD. Figure 5.20

Figure 5.20: Cross section of PIN photo diode (Wang et al., 2002)

shows the cross section of PD. Figure shows 5.21 the electrical equivalent circuit for the PIN PD. The two port model of a PD has been further simplified as shown in Figure 5.22.

Figure 5.21: Electrical equivalent circuit with parasitic elements for PIN photo diode

The ABCD matrix of PD is given by;

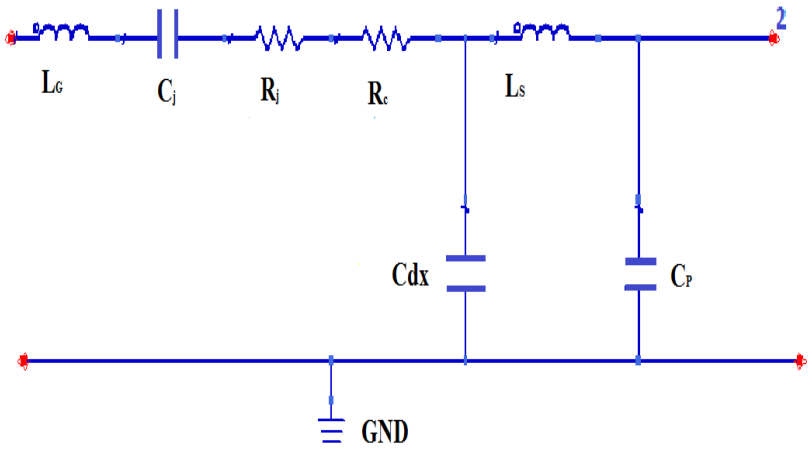

Figure 5.22: The equivalent circuit for the PD device

$$\begin{pmatrix} A_{PD} & B_{PD} \\ C_{PD} & D_{PD} \end{pmatrix} = \begin{pmatrix} 1 & Z_F \\ 0 & 1 \end{pmatrix} \begin{pmatrix} 1 & 0 \\ \frac{1}{Z_5} & 1 \end{pmatrix} \begin{pmatrix} 1 & Z_6 \\ 0 & 1 \end{pmatrix} \begin{pmatrix} 1 & 0 \\ \frac{1}{Z_7} & 1 \end{pmatrix} \tag{5.90}$$

Where,

$$Z_F = Z_1 + Z_2 + Z_3 + Z_4$$

$$Z_1 = j\omega L_G$$

$$Z_2 = \frac{1}{j\omega C_j}$$

$$Z_3 = R_j$$

$$Z_4 = R_c$$

$$Z_5 = \frac{1}{j\omega Cdx}$$

$$Z_6 = j\omega L_s$$

$$Z_7 = \frac{1}{j\omega C_p}$$

In the simulation of ABCD matrix of PD at f=40 GHz, the following parameters have been assumed (Wang et al., 2002). L_G=0.04 nH, $C_p + Cdx$=23 fF, L_s=0.03 nH, $\omega = 2\pi f$ and $R_j + R_c = 95\Omega$. The ABCD parameters of the PD then can be written as

$$\begin{pmatrix} A_{PD} & B_{PD} \\ C_{PD} & D_{PD} \end{pmatrix} = \begin{pmatrix} 1.6903 & 138.7784 \\ 0.0057 & 0.9905 \end{pmatrix} \tag{5.91}$$

5.5.7 ABCD Matrix of Forward Elements of IOEO

In this thesis ABCD matrix of the designed IOEO has been computed. The ABCD matrix of the forward (electrical) and feedback (optical) elements have been computed. The computed ABCD matrix of the forward and feedback elements have been used in the analysis of the oscillation of the designed IOEO. The schematic of designed IOEO can be analysed further from oscillation conditions. The IOEO can be represented by the block diagram shown in Figure 5.23. The oscillation condition is required to adopt the scheme

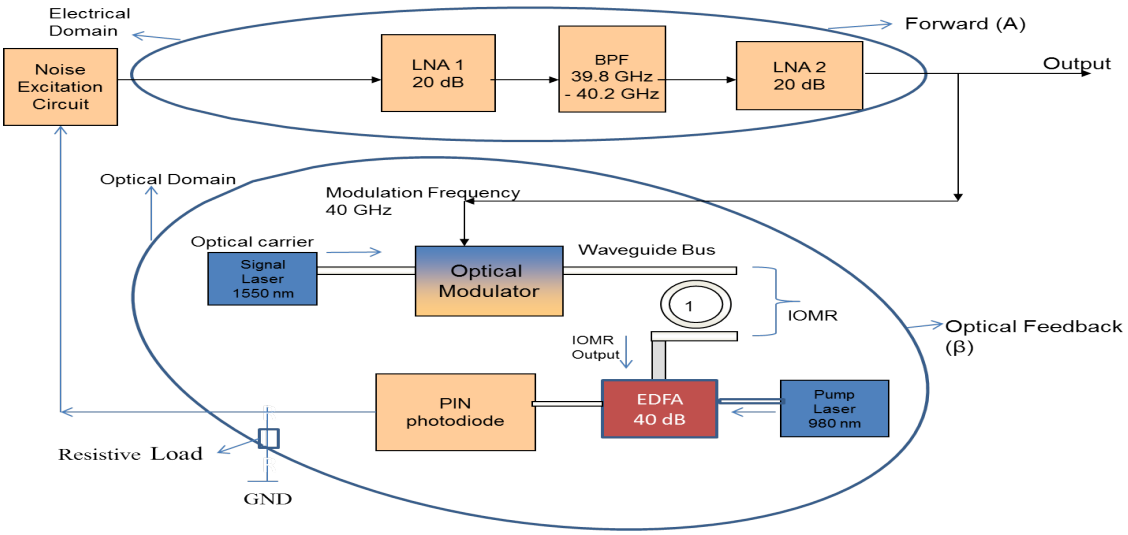

Figure 5.23: Pre oscillation condition in IOEO

suggested in (Odyniec, 1999) for the stability analysis of IOEO. The composite ABCD matrix of all the blocks in the forward path of IOEO is:

$$\begin{pmatrix} A_{forward} & B_{forward} \\ C_{forward} & D_{forward} \end{pmatrix} = \begin{pmatrix} A_{LNA1} & B_{LNA1} \\ C_{LNA1} & D_{LNA1} \end{pmatrix} \cdot \begin{pmatrix} A_{BPF} & B_{BPF} \\ C_{BPF} & D_{BPF} \end{pmatrix} \cdot \begin{pmatrix} A_{LNA2} & B_{LNA2} \\ C_{LNA2} & D_{LNA2} \end{pmatrix}$$

The ABCD parameters of the forward element are computed as :

$$\begin{pmatrix} A_{forward} & B_{forward} \\ C_{forward} & D_{forward} \end{pmatrix} = \begin{pmatrix} 0.0055 & 0.4547 \\ 0.0000 & 0.0018 \end{pmatrix}$$

5.5.8 Stability Analysis of IOEO

The conversion of ABCD parameters into S-parameters is required to compute the stability of the IOEO. S-matrix of a network can be derived from the corresponding ABCD matrix (Pozar, 2009). In a two port network

$$S_{11} = \frac{A + \frac{B}{Z_0} - CZ_0 - D}{A + \frac{B}{Z_0} + CZ_0 + D} \tag{5.92}$$

$$S_{12} = \frac{2(AD - BC)}{A + \frac{B}{Z_0} + CZ_0 + D} \tag{5.93}$$

$$S_{21} = \frac{2}{A + \frac{B}{Z_0} + CZ_0 + D} \tag{5.94}$$

$$S_{22} = \frac{-A + \frac{B}{Z_0} - CZ_0 + D}{A + \frac{B}{Z_0} + CZ_0 + D} \tag{5.95}$$

Using Equations (5.92) to (5.95) the S-matrix of the forward path of IOEO at 40 GHz is given as:

$$\begin{pmatrix} S_{11-forward} & S_{12-forward} \\ S_{21-forward} & S_{22-forward} \end{pmatrix} = \begin{pmatrix} 0.6870 & 0 \\ 115.398 & 0.2582 \end{pmatrix} \tag{5.96}$$

The stability of the forward path has been calculated using Rollets factor $(K1)$. The Rollets factor determines whether the proposed forward path is stable for a given frequency of operation. In the designed IOEO, the Rollets factor $(K1)$ is calculated from the following Equations.

$$K1 = \frac{1 - S_{11}^2 - S_{22}^2 + \triangle^2}{2S_{12}S_{21}} \tag{5.97}$$

Where,

$$\triangle = S_{11} * S_{22} - S_{12} * S_{21}$$

Computation of the stability factor leads to a conclusion that the forward path is stable. The $K1$ is found to be 10.2941, which is greater than 1. Since the forward path is stable, the instability required for oscillator is provided by the optical feedback path. The oscillation phenomenon of the designed IOEO has also been validated using Barkheusen criteria (Millman and Halkias, 1972) as discussed in chapter 3 .

5.6 Phase Noise and Stability of IOEO using Two Port Network Model

In this section the phase noise of the IOEO has been computed using two port network model. The ABCD-parameters of the forward path and the feedback path have been derived using two port network theory. Initially the forward path is excited by the thermal noise as shown in Figure 5.24 and then output is fed to the feedback path. Finally the output of the feedback path is fed to the forward path to get the final output of the IOEO. The phase noise plot of the IOEO having Okamoto model for IOMR is shown in Figure 5.25.

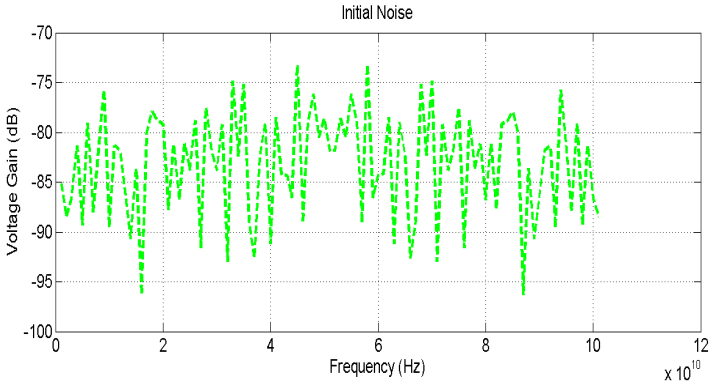

Figure 5.24: Thermal noise excitation

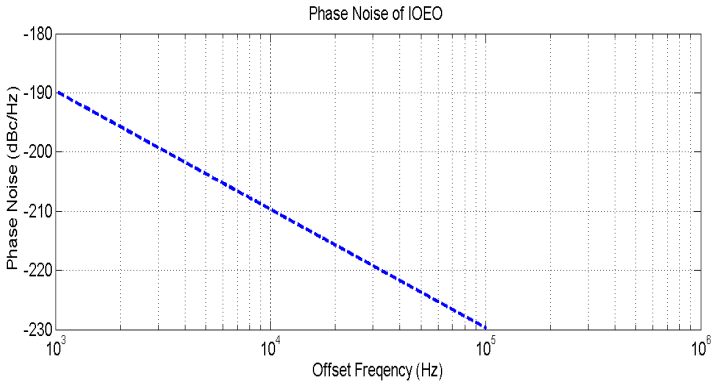

Figure 5.25: Phase noise of IOEO using Okamoto model

The Allan variance for the IOEO using Okamoto model for IOMR has also been computed as shown in Figure 5.26. Similarly, the phase noise of the IOEO has also been computed having Pollock model of IOMR using ABCD parameters. The ABCD- parameters of the forward path and the feedback path have been derived using two port network theory. The phase noise plot of the IOEO using Pollock model for IOMR is shown in Figure 5.27. The Allan variance for the IOEO using Pollock model for IOMR has also been computed as

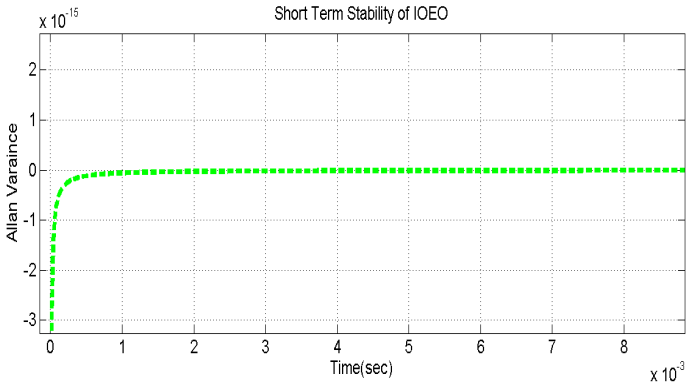

Figure 5.26: Allan varaince of IOEO using Okamota model

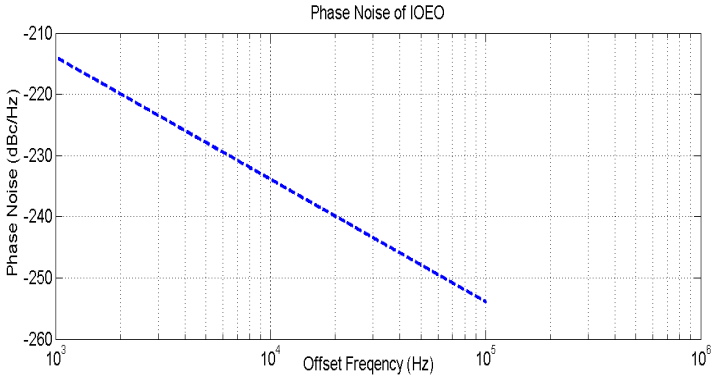

Figure 5.27: Phase noise of IOEO using Pollock model

shown in Figure 5.28. Figures 5.29 and 5.30 depict the phase noise comparison of IOEO

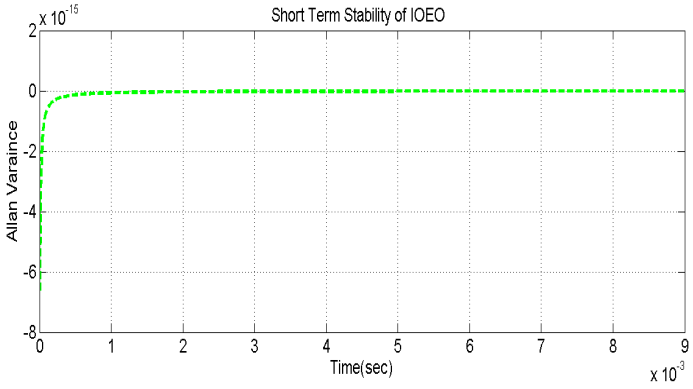

Figure 5.28: Allan variance of IOEO using Pollock model

using Okamoto and Pollock model. The designed IOEO has been simulated using both Okamoto and Pollock Model. For the simulation of the designed IOEO three approaches have been followed. The first approach is the transfer function method, where the transfer

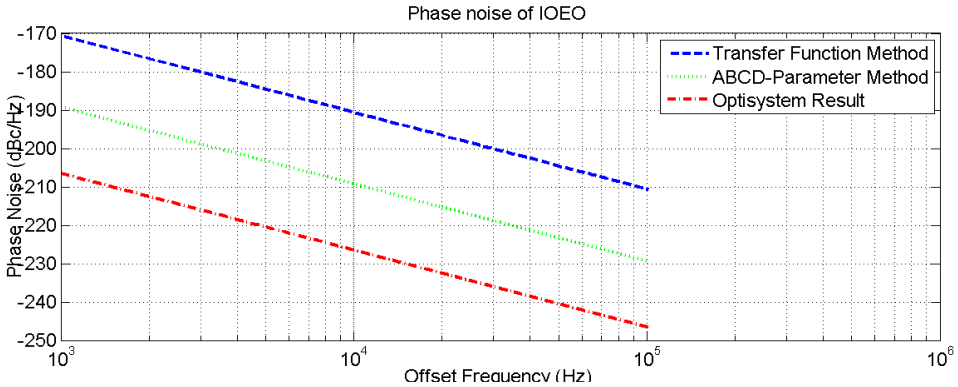

Figure 5.29: Phase noise comparison of IOEO using Okamoto model

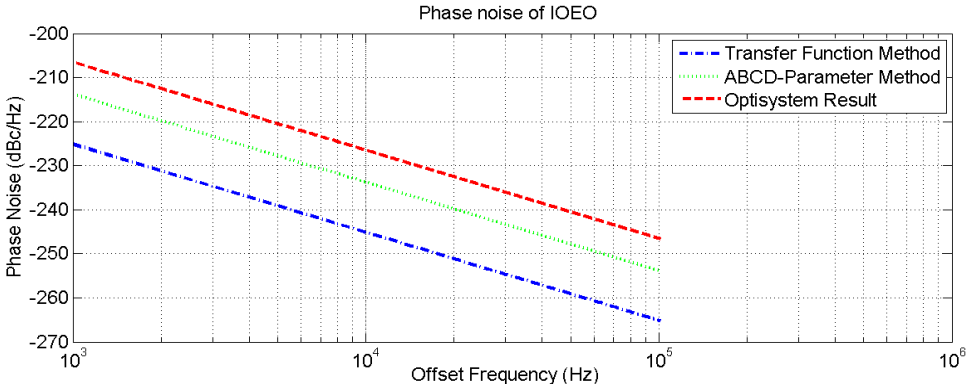

Figure 5.30: Phase noise comparison of IOEO using Pollock model

function of each constituent component has been taken into consideration. The second approach is the ABCD-parameters approach, where each component has been modelled as two port network. The third approach is the use of the Optisystem version 7.0 simulator for the validation of the simulated results.

5.7 ABCD Parameters of IOMR using Okamoto Model with Butt-coupling Coefficient

In this section, the variation in ABCD parameters has been carried out by including the Butt coupling coefficient of the IOMR. Butt coupling occurs when the gap, between the straight and curved waveguides of the IOMR is very small (of the order of 100 nm). Variation in A-parameter of IOMR with the change in gap between straight and curved waveguides is shown in Figures 5.31. Variation in B-parameter of IOMR with the change in gap between

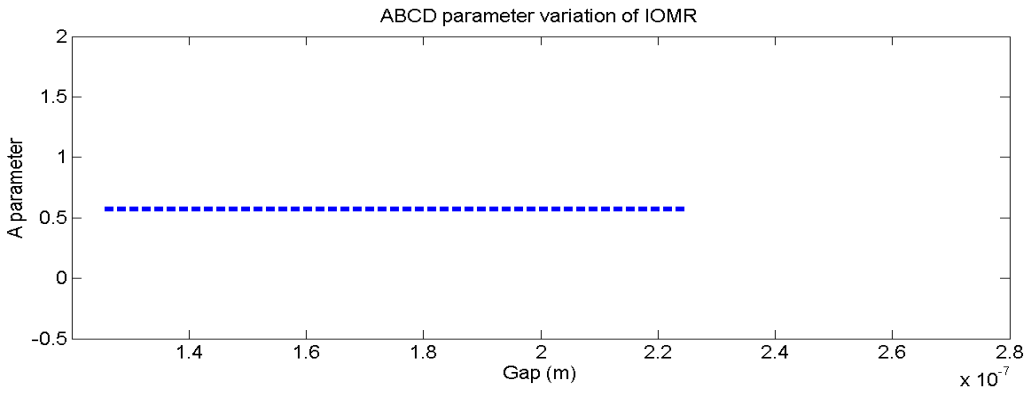

Figure 5.31: Variation of A-parameter of IOMR with change in Gap (d)

straight and curved waveguides is shown in Figure 5.32. Similarly, variation in C-parameter

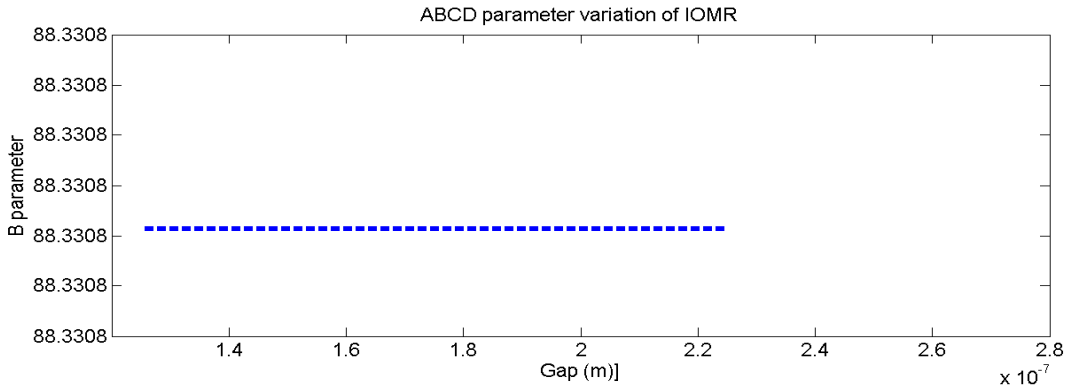

Figure 5.32: Variation of B-parameter of IOMR with change in Gap (d)

of IOMR with the change in gap between straight and curved waveguides is shown in Figure 5.33. Figure 5.34 illustrates the variation of D-parameter of IOMR with the change in gap between straight and curved waveguides. From the results of Figures 5.31-5.34, it is concluded that the inclusion of the Butt-coupling coefficient does not have any impact on the ABCD parameters of the IOMR.

5.8 ABCD Parameters of IOMR using Pollock Model with Butt-coupling Coefficients

In section (5.5), the ABCD parameters of IOMR have been derived using Okamoto model (Okamoto, 2010). The ABCD parameters of IOMR have also been computed using

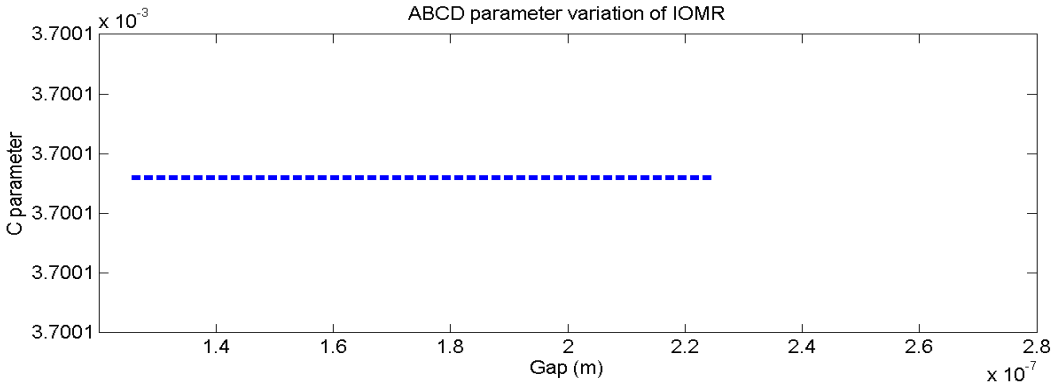

Figure 5.33: Variation of C-parameter of IOMR with change in Gap (d)

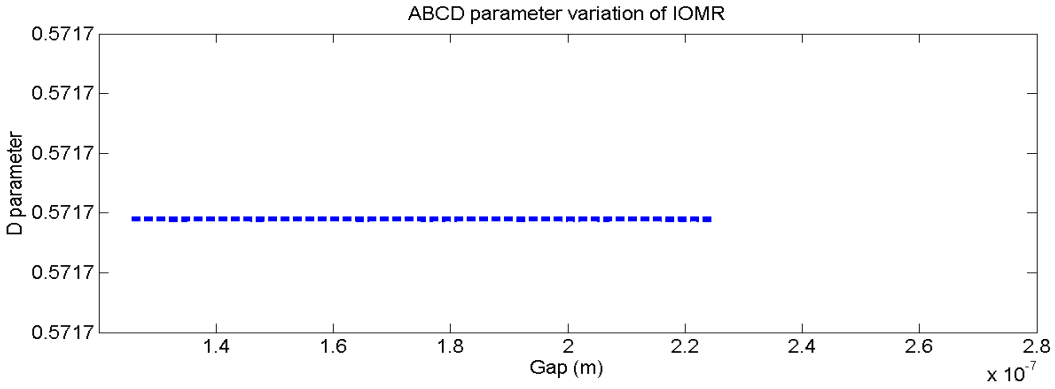

Figure 5.34: Variation of D-parameter of IOMR with change in Gap (d)

the Pollock model of IOMR. From the analysis of Pollock model of IOMR, the ABCD parameters of IOMR (section 5.3.4) are given by

$$\begin{pmatrix} A_{IOMR_{Pollock}} & B_{IOMR_{Pollock}} \\ C_{IOMR_{Pollock}} & D_{IOMR_{Pollock}} \end{pmatrix} = \begin{pmatrix} 1.1925 \times 10^3 & 1.8425 \times 10^5 \\ 7.7178 & 1.1925 \times 10^3 \end{pmatrix}$$

For the ABCD parameters of the IOMR using Pollock model the gap(d) is varied from 125 nm to 225 nm. This has been performed to facilitate the computation of effect of Butt coupling coefficient on the ABCD parameters of IOMR. Figure 5.35 depicts the variation of A-parameter with change in gap(d). The variation in B-parameter of IOMR with change in gap(d) is shown in Figure 5.36. Figure 5.37 illustrates the variation in C-parameter of IOMR with change in gap(d). Figure 5.38 depicts the variation in D-parameter of IOMR with change in gap (d). The inclusion of Pollock model of IOMR does not alter the feedback path of IOEO. The variation of the A-parameter of the IOMR is found to approximately

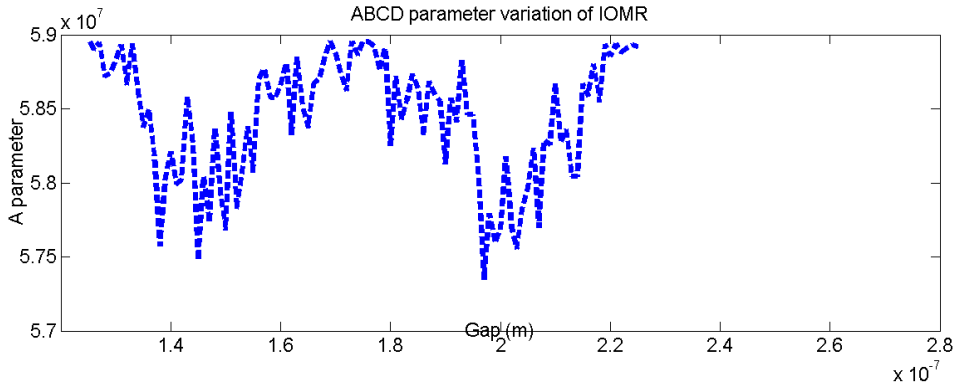

Figure 5.35: Variation of A-parameter of IOMR (Pollock Model) with change in Gap (d)

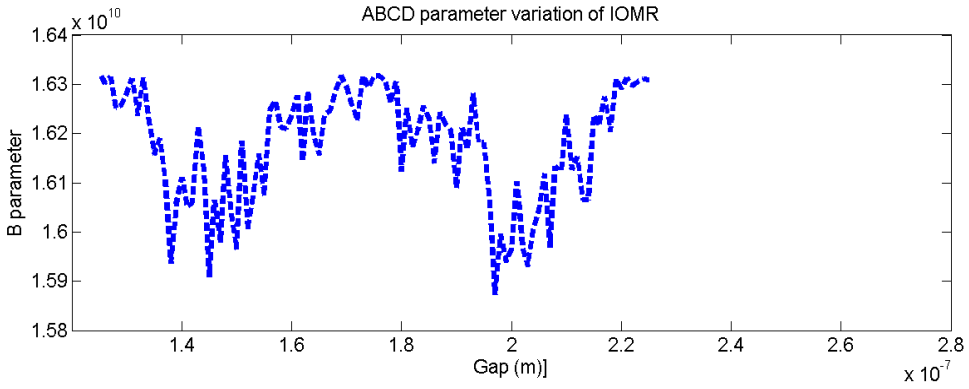

Figure 5.36: Variation of B-parameter of IOMR (Pollock Model) with change in Gap (d)

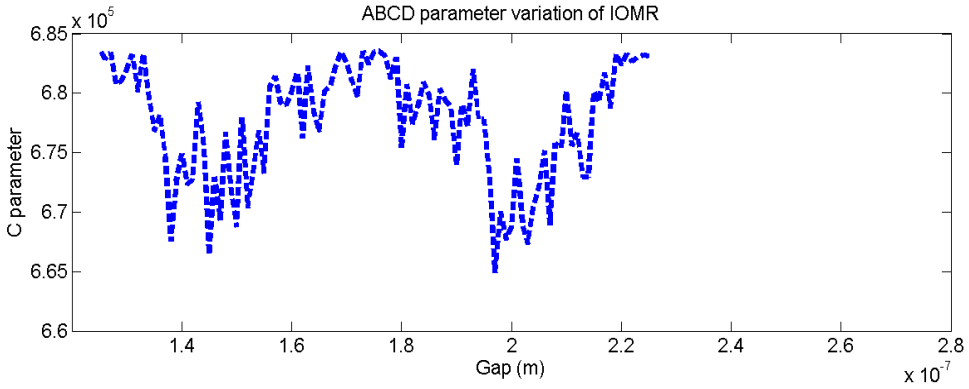

Figure 5.37: Variation of C-parameter of IOMR (Pollock Model) with change in Gap (d)

1 percent. Figures 5.35, 3.36, 3.37 and 3.38 depict the variation of ABCD-parameters of IOMR due to inclusion of effect of Butt coupling coefficients between straight and curved

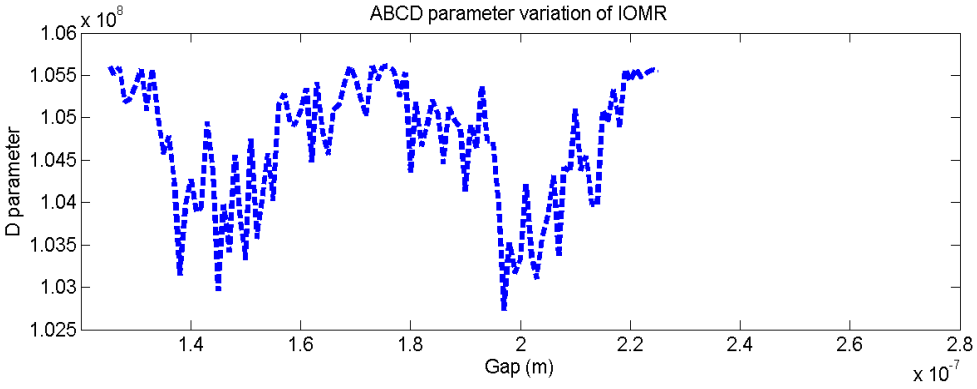

Figure 5.38: Variation of D-parameter of IOMR (Pollock Model) with change in Gap (d)

waveguides of the designed IOMR.

5.9 Summary

This chapter has presented numerous analytical formulations to analyse the performance metrics of IOEO such as phase noise, thermal stability and stability with variation in design input parameters such as refractive index and offset frequency. The relative advantage of array of IOMR over single IOMR pertaining to the output power of IOEO has been discussed in this chapter.

The contribution of IOMR to the phase noise of IOEO has not been addressed in the literature. Hence a novel model for the phase noise analysis of IOEO has been proposed and the phase noise of IOEO has been computed. The phase noise analysis using variance method has been discussed and found to be suitable for the IOEO application in optical beam steering and Bio-sensor. The results show that the designed IOEO has minimum phase noise -245 $dBcHz^{-1}$ at 100 kHz offset. This is minimum phase noise as compared to -163 $dBcHz^{-1}$ as in the the existing literature (Chembo et al., 2009)

The ABCD parameters have been explored to analyse the phase noise contribution of the IOMR in designed IOEO. To address this a novel ABCD parameter approach has been been presented using Pollock and Okamoto models for SOI based IOMR. The simulation results indicate that the contribution of the IOMR to the phase noise in the designed IOEO is insignificant and negligibly small (of the order of -280 $dBcHz^{-1}$).

Thermal analysis of the designed IOEO has been carried out to ensure long term stability of IOEO. In the simulation, effective refractive index of IOMR has been varied from 2.125

to 2.155 and the corresponding frequency shift in the IOEO is determined. With the rise in temperature, the resonant frequency of the oscillator decreases. The designed IOEO exhibits thermal stability of $\pm$ 0.325 $ppmK^{-1}$.

The stability analysis of the designed IOEO has been carried out. Since the stability analysis involves the scattering parameters, a two port network theory has been used and ABCD parameters of the constituent subsystems of IOEO have been computed. From the ABCD matrices of the subsystems, the ABCD matrices of the forward path and feedback path of IOEO have been arrived at. From the arrived ABCD matrices, the associated S-parameters have been obtained. With the computed S-parameters of Forward path, Rollets stability criteria has been computed. The short term stability of IOEO has been assessed using Allan Variance. Study on the effect of Butt-coupling coefficient on the ABCD-parameters of the IOMR has also been presented. Additional simulation results on IOEO and its subsystem (components) are presented in Appendix-A.

CHAPTER 6

THE IOEO BASED BEAM STEERING AND BIO-SENSOR

This chapter is intended to discuss the potential utility of the proposed IOEO for possible diverse systems applications. To substantiate this feature, two applications namely optical beam steering and Bio-sensor have been considered. The conceptual implementation of the proposed IOEO in the above referred applications has been addressed with architectural schematics and requisite technical details to facilitate better appreciation of the versatile novel features of the IOEO proposed in this thesis.

6.1 Introduction to Application of the IOEO as an Optical RF Phase Shifter for Beam Steering

In this section, designed IOEO has been explored further for its application such as RF phase shifter for beam steering. Designed IOEO system is useful in the development of RF phase shifter for optical beam steering. An optical phase shifter is used to achieve the desired phase shift in the modulating frequency with high accuracy. Photonics integrated devices have been used in the development of optical RF phase shifter for beam steering. The Integrated Photonic Device (IPD) provides features such as light weight and accuracy to realise beam forming networks preferred in satellite communication. The IPDs have an inherent property of being light weight and they are also immune to EMI. Hence IPD is an appropriate technology for the beam forming network. Lightweight, remote delivery to feed antennas and immunity to electromagnetic interference are the key requirements in satellites (Vidal et al., 2012). The parameters such as broad bandwidth and fast signal processing could be achieved through IPDs. These features of the IPDs pave way for the advancement of novel satellite systems. The optical beam forming architectures having IPDs are used for satellite applications especially where fast beam steering is required.
The optical beam forming systems pose challenges in the integration of beam forming module, laser source, modulators and photo detector (Meijerink et al., 2007). The optical beam steering can be used for many high speed communication application such

as Earth observation satellites. In case of LEO, store and forward technique is used for the transmission of data to ground (earth) station. This technique is useful in the remote sensing application.

Internet traffic on satellite mobile phones also utilizes fast beam steering networks. The Very Small Aperture Terminal (VSAT) generally invokes the concept of frequency reuse. The frequency reuse technique is applied to realise fast beam steering system. The flexibility of the fast beam steering systems enables many satellites for broadband applications.

Various architectures proposed so far for the optical beam forming can deal important issues specific to a given application scenario only. The context and the specificity of the application determine the choice of appropriate beam forming architecture (Meijerink et al., 2007). Especially for the array antenna in K_a-band or millimeter-wave use, it is important to reduce the size, weight and insertion loss of the beam forming network. One of promising technologies to overcome these difficulties is application of the optically controlled array antenna for the satellite-borne system. In the optically controlled array antenna, the RF signals are optically modulated and then transmitted via optical fiber. The phase and amplitude of each RF signal are controlled by using optical beam forming network.

Optical dispersion techniques having true-time delay characteristics suitable for wide-bandwidth operation have already been proposed and verified for optical beam steering. However these techniques have temperature instability due to optical fiber. The Wavelength Division Multiplexing (WDM) based optically controlled array antenna consists of WDM optical sources and an optical dispersion fiber is fundamentally investigated aiming for future millimetre wave satellite communication (Ohuchi et al., 2007).

6.2 Design of an Optical RF Phase Shifter for Beam Steering using Designed IOEO

In this section, an architecture has been proposed for IOEO based optical RF phase shifter to be used for antenna beam steering. WDM facilitates simultaneous transmission of the optical signals of different wavelengths over a single fiber (Ohuchi et al., 2007). Technically, the International Telecommunication Union for Telemetry (ITU-T) recommendation G.692 specifies a channel spacing of 100 GHz (0.8 nm at 1552 nm) for Dense Wavelength Division Multiplexing (DWDM). Presently, one can transmit as many as 300 channels over the single fiber.

Phase shifters find extensive applications in phased arrays. Phased arrays are under the

purview of analog beamformers to steer the main beam along a desired direction. Satellite and radar communication systems are some of the examples for system applications of Phased array. phased array satellite antenna with beam steering is used to cover wide service area (Vidal et al., 2012). But increase in the number of antenna elements leads to increase in the weight, feed loss and complexity in beam forming network. One of the promising technologies to overcome these difficulties is application of the WDM based optically controlled array antenna. Optically controlled array antennas using optical delay lines with different length and spatial light modulator have earlier been proposed and experimentally verified at modulating frequency 40 GHz (Ohuchi et al., 2007).
Figure 6.1 represents the schematic of the WDM based optically controlled transmitter for the phased array antenna. The transmitting system consists of a bank of laser diodes, optical

Figure 6.1: Schematic of the transmitting system (Ohuchi et al., 2007)

muliplexer, optical modulator, single mode fiber, optical amplifier, optical demultiplexer, a bank of photo diodes and antenna elements. The outputs of the bank of laser diodes are multiplxed using wavelength division multiplexer. The multiplexed modulating signal at 40 GHz is modulated by optical modulator (Ohuchi et al., 2007). The modulated signal is transmitted through the single mode optical fiber. Since the signal gets attenuated in the single mode fiber, the optical amplifier is used to improve the SNR of the signal to the desired level. The differing wavelengths of the signal are further De-multiplexed using

the optical De-multiplexer. The De-multiplexed signals (of varying wavelength) are fed to bank of photo diodes. The desired phase shifted modulating signals of varying wavelength are retrieved through photo diode. The output of each photo diode is connected to an antenna element.

Figure 6.2 represents the schematic of the WDM based optically controlled receiver (Ohuchi et al., 2007) for the phased array antenna. The receiver system consists of antenna

Figure 6.2: Schematic of the recieving system (Ohuchi et al., 2007)

elements, laser diode, optical modulator, optical multiplexer, single mode fiber, optical amplifier and photo diode. The antenna elements of the receiving system receive the phase shifted modulating signal. The phase shifted modulating signal received by each receiving antenna element is fed to the associated optical modulator. Since there are multiple receive antenna elements, there is a bank of optical modulators. The outputs from the bank of optical modulators are then fed to the multiplexer. The multiplexed signals are transmitted over single mode fiber. The signal is amplified in the optical domain itself. The modulating signal is retrieved by a photo diode

In both the transmitting and receiving antennas of the existing system (Ohuchi et al., 2007), delay time difference between the adjacent wavelengths can be expressed as

$$\tau = D_0 L_0 \Delta\lambda_{opt} \tag{6.1}$$

Where,

D_0 is the wavelength dispersion, L_0 is the length of the Single Mode Fiber, $\Delta\lambda_{opt}$ is the wavelength spacing.

The phase difference $\Delta\phi$ between antenna elements can be expressed as

$$\Delta\phi = 2\pi D_0 L_0 \Delta\lambda_{opt} f_{RF} \tag{6.2}$$

Where,

f_{RF}, is the modulating frequency.

Since the wavelength dispersion varies over wide range of bandwidth, the relative phase difference at each antenna input is also different. A schematic of the Optical beam steering using 40 GHz IOEO is shown in Figure 6.3. The proposed system shown in Figure 6.3 has many advantages over the existing architecture (Ohuchi et al., 2007).

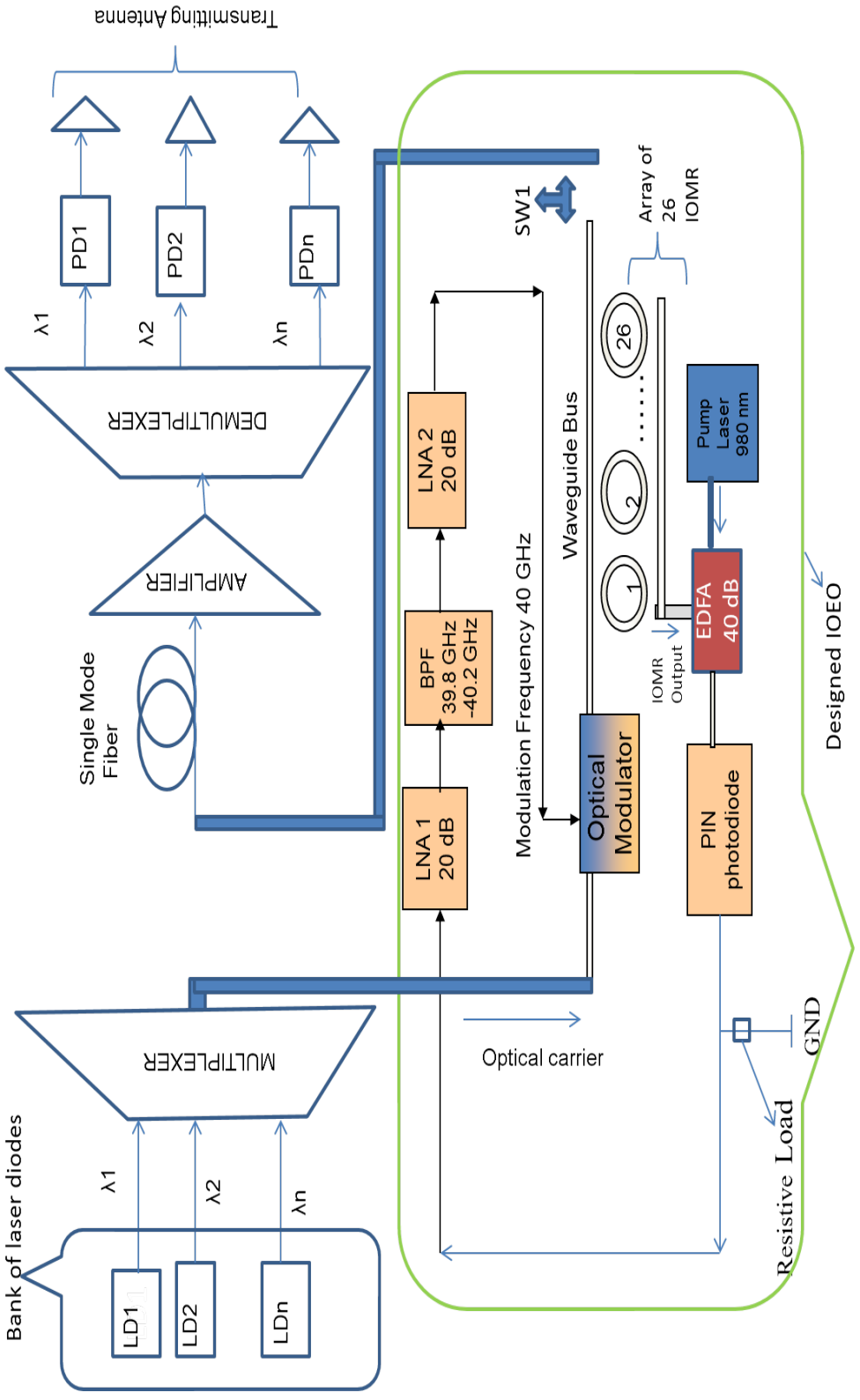

Figure 6.3: Optical beam steering using designed 40 GHz IOEO

In this section, an architecture of the WDM-based optically controlled transmitting array antenna using an integrated 40 GHz IOEO has been proposed. In the designed WDM based RF phase shifter for optical beam steering, the integrated 40 GHz IOEO works as optical modulator as well as 40 GHz source. The designed IOEO is used for the modulation as well as in generation of the 40 GHz with high spectral purity and high quality factor. Among the entire optical carrier, the first carrier 193.1 THz has been used to generate modulating signal of 40 GHz. Initially in the first cycle of operation, the system generates the 40 GHz signal and then the modulation takes place with the entire optical carrier. The IOEO generates 40 GHz as long as the laser and WDM subsystem operate. The architecture can use large number of laser diodes as per the requirement. The entire optical carrier Laser Diodes LD_1 to LD_n are excited simultaneously.
Initially the switch (SW1) shown in Figure 6.3 is kept open for the first cycle of the IOEO. The first laser 193.1 THz is used to generate the required modulating frequency of 40 GHz. The switch (SW1) is closed after the first cycle and remains closed forever. The optical modulator used in the IOEO is used to generate the modulated output and transmit it to the Single Mode Fiber (SMF). The outputs of SMF are amplified, de-muxed and de-modulated using photo diode. Equations (6.1) and (6.2) hold for the designed WDM based optical phase shifter for beam steering. The designed architecture has been simplified by having four isotropic antenna elements for the simulation. Hence all the four isotropic antennas receive a different phase delayed modulating signal of 40 GHz. In the next section detail simulation study of the four antenna elements and optical phase shifter has been discussed.

6.2.1 Simulation of the Designed Optical RF Phase Shifter for Beam Steering

The simulation of the designed system has been carried out and results have been verified using simulator (Opti-System). A simulation model of IOEO based optical beam steering system with four antenna elements is shown in Figure 6.4. Following parameters have been considered for the simulation of the IOEO based optical beam steering system as shown in Figure 6.4: The four individual laser sources required for the four antenna elements are assumed to operate at 1500 nm, 1550 nm, 1600 nm and 1650 nm respectively. The reference dispersion at 1550 nm is 16.75 ps/nm/Km. The differential group delay is 0.2 $nsKm^{-1}$. The attenuation in the fiber is assumed to be 0.2 $dBKm^{-1}$. The bandwidth of the Multiplexer and Demultiplxer of WDM are 10 GHz, with noise threshold of -100 dB. Responsivity of the PIN photo diode is 0.5 AW^{-1} with dark current of 2 nA.

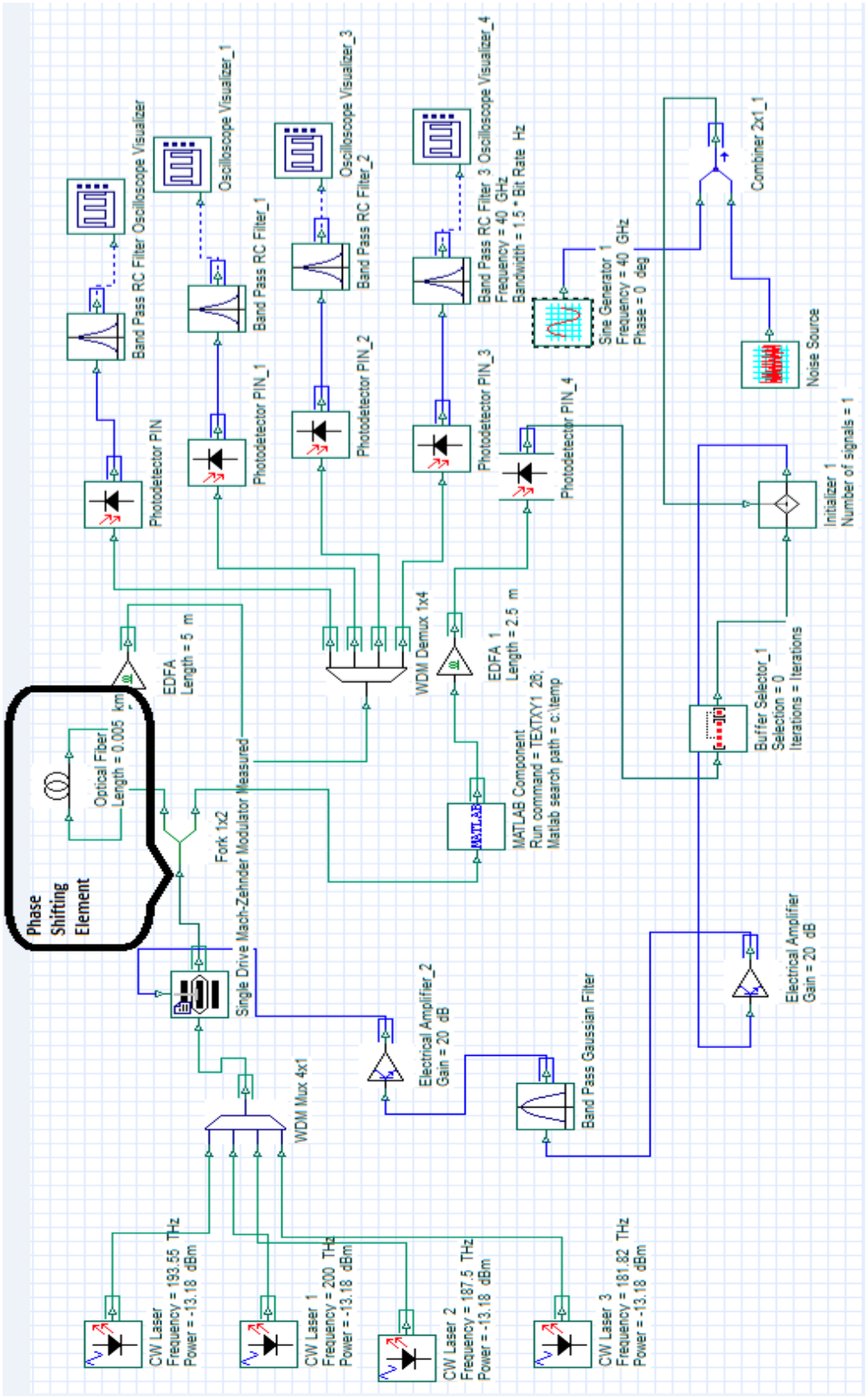

Figure 6.4: Simulation of designed beam forming architecture using Optisystem version 7.0

Thermal noise of PIN diode is assumed to have $1 \times 10^{-22}\ WHz^{-1}$. Band pass RC filter of frequency 40 GHz with 0 dB insertion loss. The designed system uses four laser sources emitting at different wavelengths 1500 nm, 1550 nm, 1600 nm and 1650 nm respectively as shown in Figure 6.5. In the designed IOEO, the IOMR serves as optical filter and it

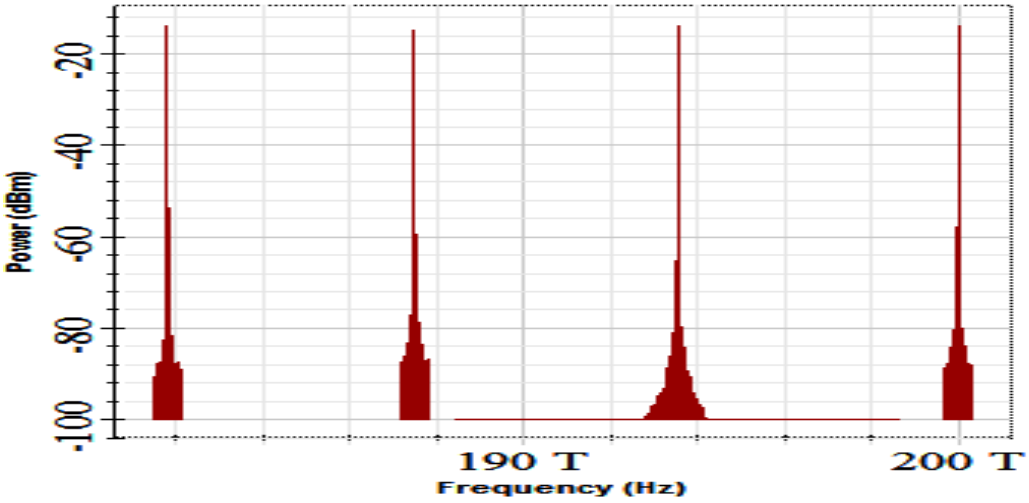

Figure 6.5: Output power spectrum of the WDM using Optisystem version 7.0

resonates at specified resonant frequency. Figure 6.6 depicts the output at the IOMR used in the IOEO. In case of designed IOEO based optical RF phase shifter, the modulating

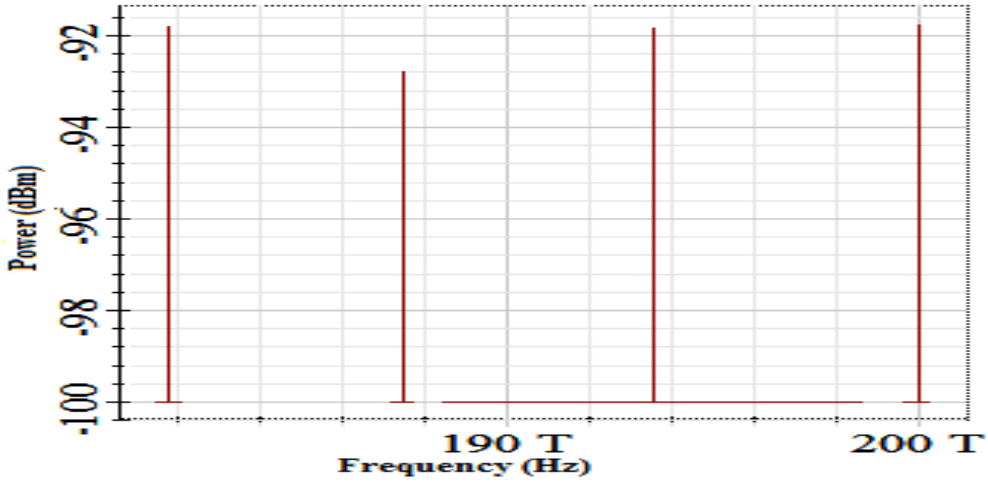

Figure 6.6: Output power spectrum of the IOMR using Optisystem version 7.0

signal of 40 GHz with the required phase shift is fed to the input of isotropic antenna elements. All the phase shifted modulating signals at the antenna elements are shown in Figures 6.7, 6.8, 6.9 and 6.10 respectively.

The phase difference in degree for the designed RF phase shifter system having antenna

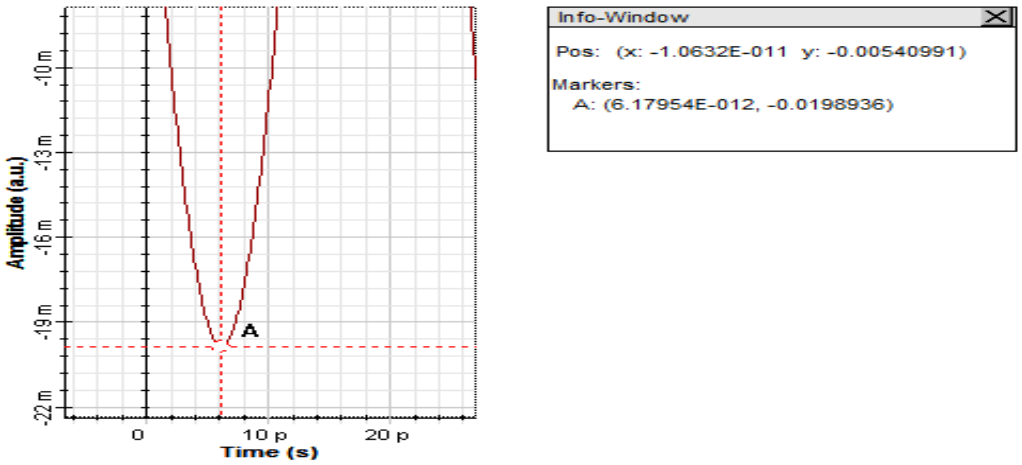

Figure 6.7: Amplitude time response of first photo diode using Optisystem version 7.0

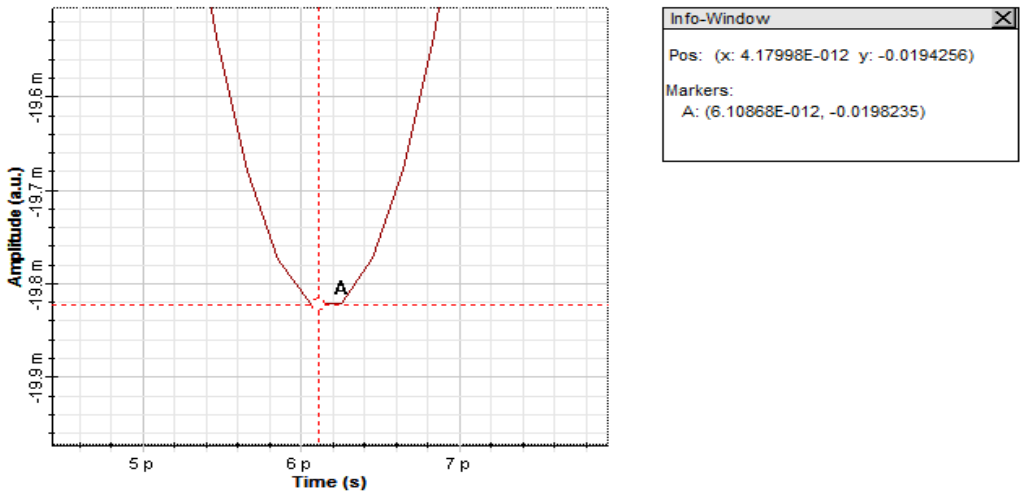

Figure 6.8: Amplitude time response of second photo diode using Optisystem version 7.0

spacing($d3$), where, $d3 = \frac{\lambda}{2}$ have been computed and are given as follows:

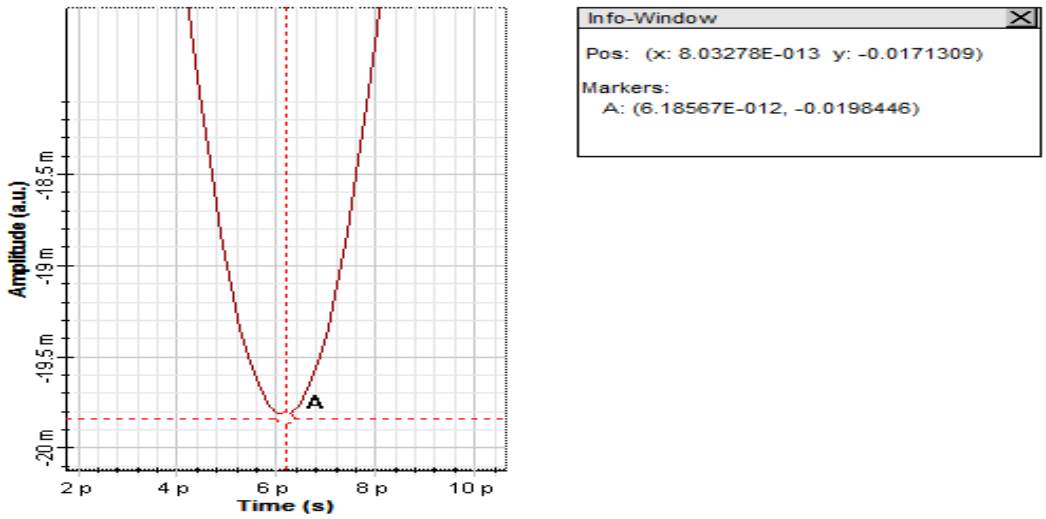

Figure 6.9: Amplitude time response of third photo diode using Optisystem version 7.0

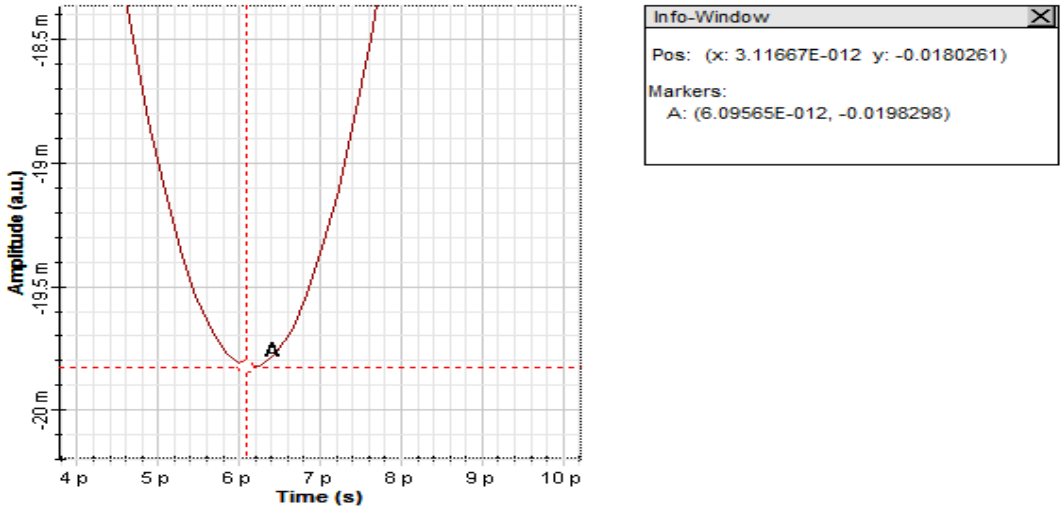

Figure 6.10: Amplitude time response of fourth photo diode using Optisystem version 7.0

The phase difference at an antenna element has been calculated using Equation (6.3).

$$\phi = 2\pi f \triangle t \tag{6.3}$$

Where, $\triangle t$ is the time delay and $f$is the frequency of the output RF signal. The time delay between antenna 1 and antenna 2 is 0.08 ps, between antenna 2 and antenna 3 is 0.08 ps and between antenna 3 and antenna 4 is 0.08 ps respectively as shown in Figures 6.7, 6.8, 6.9 and 6.10.

The phase differences(radians) are given as:

$$\phi_{12} = 2\pi 40 \times 10^9 \times 0.08 \times 10^{-12}$$

$$\phi_{23} = 2\pi 40 \times 10^9 \times 0.08 \times 10^{-12}$$

$$\phi_{34} = 2\pi 40 \times 10^9 \times 0.08 \times 10^{-12}$$

It is concluded that equal phase difference are achieved between successive isotropic antenna elements. The beam steering angle (θ) of the antenna elements is calculated using Equation (6.4).

$$\phi = 2\pi(\frac{d3}{\lambda})sin\theta \tag{6.4}$$

The beam steering angle is calculated as:

$$2\pi 40 \times 10^9 \times 0.08 \times 10^{-12} = 2\pi(\frac{d3}{\lambda})sin\theta$$

At $d3 = \frac{\lambda}{2}$

$$\theta = 0.366^\circ$$

The beam steering angle (θ) obtained is 0.366 degree. The beam steering output of the

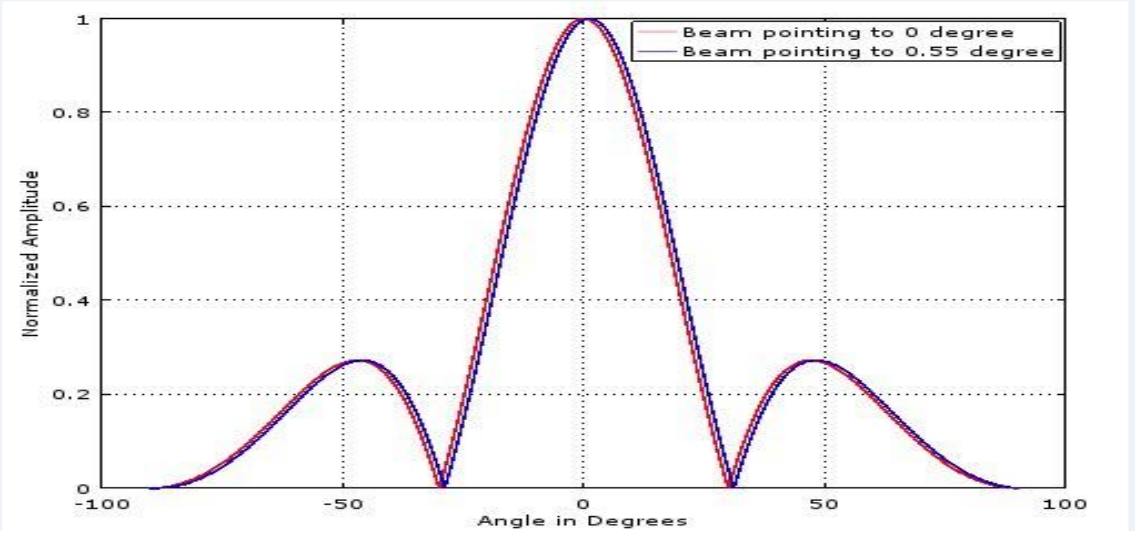

Figure 6.11: Output of beamformer with 4 isotropic antenna elements using MATLAB version 7. 12 (R2011a)

four antenna elements has been shown in the Figure 6.11. The expanded view of the shift

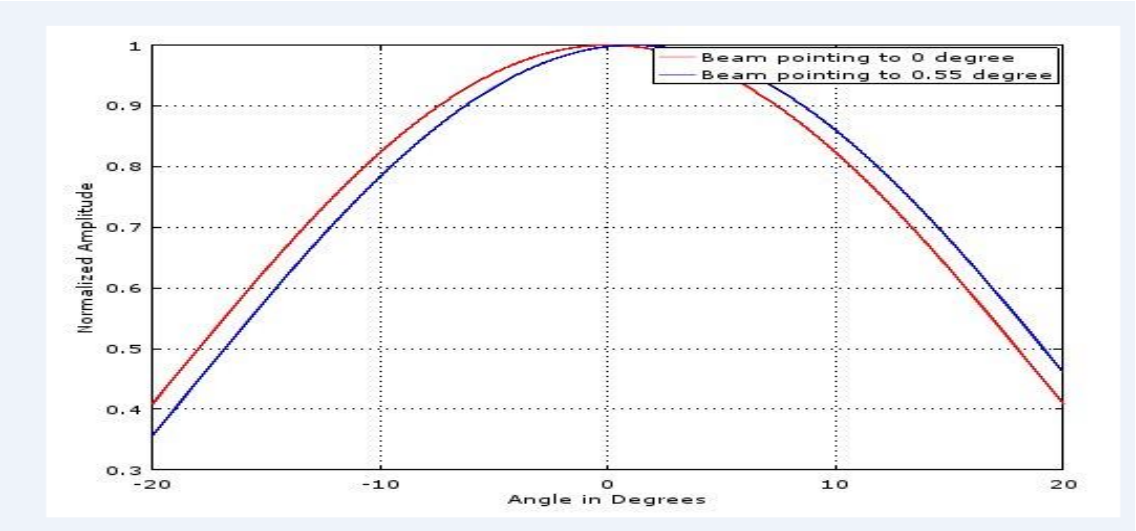

Figure 6.12: Expanded view of output beamform of 4 antenna elements using MATLAB version 7. 12 (R2011a)

in the beam has been shown in the Figure 6.12. The variation of the SMF length L_0 of Equation (6.2) results in the change in the phase of the modulated signal. Therefore one can achieve the desired phase shift at the output of the bank of photo diodes as shown in Figure 6.3.

The realised 0.366^0 of beam steering can be useful in Elastography (Rao et al., 2006), which is a medical imaging modality that maps the elastic properties of soft tissue. The 0.366^0 of beam forming also can find its utility in the conformal sub-aperture beam steering (McManamon, 2009) using Liquid Crystal (LC) for radar imaging. The range of angle of beam steering is significant for a beam forming network. With the designed beam forming architecture beam steering of 0.5^0, 1^0, 2^0 and 4^0 has also been achieved at 40 GHz. To achieve the beam steering of 0.5^0, 1^0, 2^0 and 4^0 at 40 GHz, a Single Mode Fiber (SMF) has been introduced in the designed beam steering system using IOEO. The SMF is placed before each photo diode elements of the designed beam steering system using IOEO. The details have been shown in Table A.1 of Appendix A.5. Hence the proposed beam steering system using IOEO can be used in the Elastography and Radar imaging applications.

6.2.2 Summary:

This section summarizes the application of the designed IOEO as the optically beam steering system. The proposed optical RF phase shifter for beam steering has advantages

of generating stable and pure modulating signal of 40 GHz with minimum phase noise of -245 $dBcHz^{-1}$ at 100 kHz offset. The designed beam steering system also generates and modulates simultaneously using a single optical modulator. Using the designed optical beam steering one can achieve the desired phase shift by varying the length of SMF. An optical beam steering system with 4 successive isotropic antenna elements has been simulated and a phase shift of 0.4 degree has been obtained.

6.3 Introduction to the Application of IOEO in Bio-sensors:

At present the global market for the Bio-sensor is very attractive and therefore photonics scientists are perusing research and development aimed at near ideal Bio-sensor with compactness and better sensitivity. In this section, design and simulation of the Bio-sensor based on the designed IOEO is discussed. The designed Bio-sensor can find its application in many areas like clinical diagnosis, drug development and food quality control.

There are two types of sensing technologies for the integrated photonic device; first one is surface sensing (labeled) and other one is bulk sensing (label free). In case of surface sensing the target molecule is used as the adlayer. In bulk sensing, the target molecule (analyte) is selectively captured by a Bio-recognition agent immobilized on the surface of the sensor.

It has been shown in the literature that WGM resonators can be used as good label-free Bio-sensors (A. Matsko et al., 2003). They are made entirely with low-loss dielectrics and for this reason, they exhibit a much sharper resonances. WGM resonators are widely used because of very high quality factor and miniaturized size down to a few tens of micrometers in diameter. It can be integrated with photonic waveguides easily and hence complex system could be realized. Since realization of small integrated and functional optical chips are possible, WGM is preferred for Bio-sensor device.

There are a few advantages such as reduction in both costs and the time of manufacturing and use. In these devices, a large number of multiplexed sensors are placed within a few square millimeters. Label-free sensors based on Silicon Oxynitride (SiON) ring resonators integrated with an inexpensive Vertical Cavity Surface Emitting Laser (VCSEL) light source have been reported in (Guider et al., 2015). These Bio-sensors are able to distinguish small changes in the refractive index of bulk solutions flowing over their surface.

He in 2012, has also showed the feasibility of creating a Bio-sensor based on an intensity-

interrogated planar waveguide double ring resonator (He, 2012). Intensity-interrogated planar waveguide double ring resonator uses a low-cost broadband light source combined with simple intensity measurements without requiring an external bulky and expensive tunable laser.

Intensity-interrogated planar waveguide double ring resonator based sensor has various advantages such as high sensitivity, simplicity and speed of analysis, temperature insensitivity, compactness, and suitability for high-density array integration. The low-cost practical applications of these planar waveguide ring-resonator Bio-sensors need further research work in terms of sensitivity, simplicity and speed of analysis, temperature insensitivity, compactness, and suitability for high-density array integration.

Biochemical sensing using the concept of ring resonator has been discussed in (Sun and Fan, 2011). Rigorous research in the field of Biochemical sensors is the driving factor for utilizing ring resonator sensors in healthcare, environmental monitoring, food industry and pharmaceuticals. To simulate these sensors, sensitive and high speed analytical tools are required.

In the optical ring resonator sensor, light and analyte interaction takes place and optical signals are measured. Interaction of the analytes near the resonator surface and the evanescent field of the ring resonator takes place during multiple round trips in IOMR. The evanescent field of the ring resonator generally extend upto several hundred nanometers into the surrounding medium (liquid, gas, and polymer coatings) and interacts repeatedly with the analytes near the resonator surface. The evanescent field is a fraction of guided mode that extends to the cladding layer and the substrate layer of the waveguide.

The IOMR based sensor has a few significant advantages. In case of IOMR based sensor, the encircling nature of the resonant mode creates an extremely long effective interaction length which is not possible in the conventional linear waveguide or fiber-based sensors. Quality factor of the various ring resonators configuration ranges from 10^4 to 10^8 (Sun and Fan, 2011).

The effective interaction length of an IOMR is a few tens of centimeters. This small interacting length of the IOMR is capable of delivering improved sensing performance, smaller footprint, and higher multiplexing capability while using less analyte. Also IOMR fabricated with dielectric materials (for example Silicon-on-Insulator) on a silicon wafer, can be mass produced using micro/nano-fabrication technology and scaled up to an array format for multiplexed detection.

In the optical IOMR having high quality factor, light intensity near its surface remains

high, because light continues to encircle inside the resonator. This encircling of light in the IOMR has been exploited for sensing applications as shown in Figure 6.13. Various optical

Figure 6.13: IOMR as sensing element (Sun and Fan, 2011))

properties have been explored previously in ring resonator sensors to generate the sensing signal, including Refractive Index (RI), fluorescence, Raman, and optical absorption. RI detection is also called label-free detection, because it does not involve any sample labeling. Presently many small sensors use the RI detection methods.

Depending on the origin of sensing signal, bulk or surface sensing is defined. In the case of surface sensing a thin layer typically a few nanometer thickness is coated on the top surface of the IOMR. In surface sensing, analytes come very close to the decay length of evanescent field of the ring resonator surface. In case of bulk sensing, the anlaytes available around evanescent field of IOMR produces modified optical signal.

6.3.1 Design of Bio-sensor Based on Designed IOEO

The issues such as thermal stability, frequency stability and sensitivity of IOMR based Bio-sensors have been potential areas of research. The designed IOEO in chapter 3 of this thesis, has been found to be thermal and frequency stable. In this section, an optical Bio-sensor with improved bulk sensitivity has been presented. The sensor uses IOMR, which has been used in the designed IOEO as the sensing element. IOEOs have been widely used in various optical communication systems since last two decades. IOEO bridges microwave components and optical components of a communication system. Apart

from communication systems, IOEOs can also be used in contemporary applications such as Bio/ chemical sensing.

Duy and his research team of France (Duy et al., 2008) have reported IOEO based sensor with a fiber loop as sensing element. Similar structures with micro ring resonator and microspheres are also reported in (Quan and Guo, 2005) and (Schweinsberg et al., 2007). In this section, a novel configuration of Bio-sensor is proposed wherein the fiber loop of the existing scheme has been replaced with Silicon On Insulator (SOI) based IOMR, which essentially reduces device size. Conventionally, OEOs have electrical components in the feedback. The proposed IOEO has all-optical feedback, which provides frequency stability and low phase noise suitable for various applications such as satellite communication and sensing.

In this section, analysis of micro ring waveguide structures and Bio-sensor based on an IOEO has been carried out. Strip and rib wave guide geometries are the two prevalent structures on SOI material. Rib waveguide has a thickness of 1 μm (device layer) and the slab width varies from 500 nm to 900 nm for single mode variation. Strip waveguide geometry for the single mode condition has a dimension of 400 nm x 220 nm. Hence micro ring resonator with strip geometry is the more compact than the Rib waveguide. As compactness is one of the important criteria, strip geometry has been chosen. Single optical mode is supported by strip and rib structure and has a height of 220 nm and width in the range of 400-500 nm. The Bio-material is applied as a cover on the resonator and bus waveguide as shown in Figures 6.14 and 6.15.

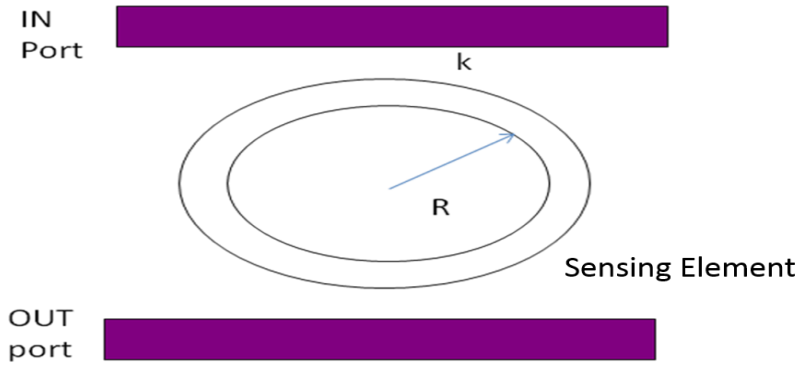

Figure 6.14: Schematic of IOMR as sensing element

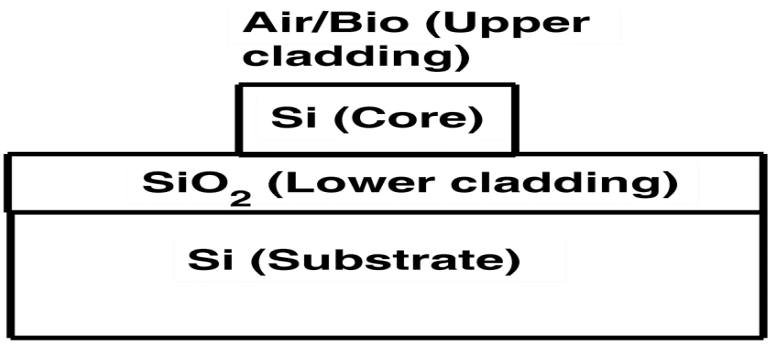

Figure 6.15: Schematic of cross section of sensing element

The IOMR which is placed in the feedback path of the IOEO acts as a sensing element. The evanescent field of the ring resonator interacts with the upper cladding layer which modifies the effective index of the propagating mode. This in turn changes the resonant wavelength of the IOMR. The change in resonant wavelength / frequency of the IOMR influences the PIN photo diode in the feedback loop which results in shift in resonant frequency of IOEO. Glucose solution as the Bio layer above the ring structure has been considered. The structure has been simulated with a Bio-material, whose refractive indices lie in the range 1.3332 to 1.3340 based on glucose concentration (Liu, Hering, and Scully, 1992).

The conventional unit used for monitoring of actual blood serum or blood plasma in a diabetic condition is $(\frac{mg}{100ml})$ (Desai, 2014). The normal glucose concentration value of the human blood is 80-120 $(\frac{mg}{100ml})$. For the simulation studies presented in chapter 6, an aqueous glucose concentration has been considered. For the purpose of analysis, the range of concentration of an aqueous glucose from 0 to 1 g/100 ml has been considered (Liu, Hering, and Scully, 1992). The corresponding readings in terms of the normal units of blood glucose concentration are [0,200, 300, 500, 600, 700, 800, 900 and 1000] $(\frac{mg}{100ml})$. Only for the purpose of the response analysis of designed Bio-Sensors using IOEO, higher values of aqueous glucose concentration have been considered. In some diabetic condition, the glucose concentration value reaches to 450 $(\frac{mg}{100ml})$ also.

The Glucose concentration for the given range of refractive index varies from 0 to 1000 $(\frac{mg}{100ml})$ at 20 degree Centigrade temperature as shown in Figure 6.16 where, *mg* is milligram.

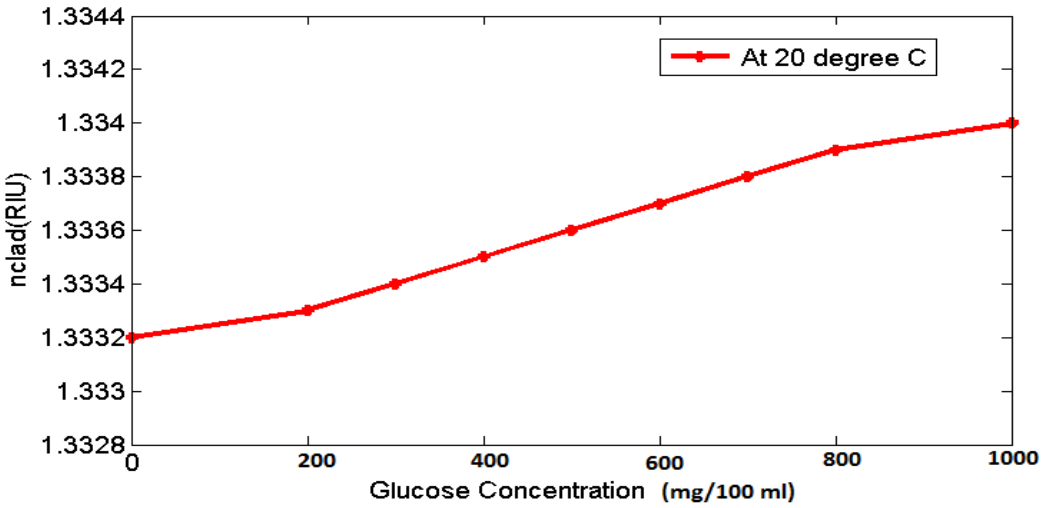

Figure 6.16: Variation of refractive index with change in Glucose concentration ($\frac{mg}{100ml}$)

The schematic diagram of the proposed micro-ring resonator based IOEO is depicted in Figure 6.17. The IOEO consists of Laser, Optical-modulator, Optical micro ring resonator, Photo diode, Low noise amplifier and Filter. The proposed Laser in the IOEO system oscillates at 1550 nm. The optical modulator drives the micro-ring resonator which is the sensing element of the IOEO.

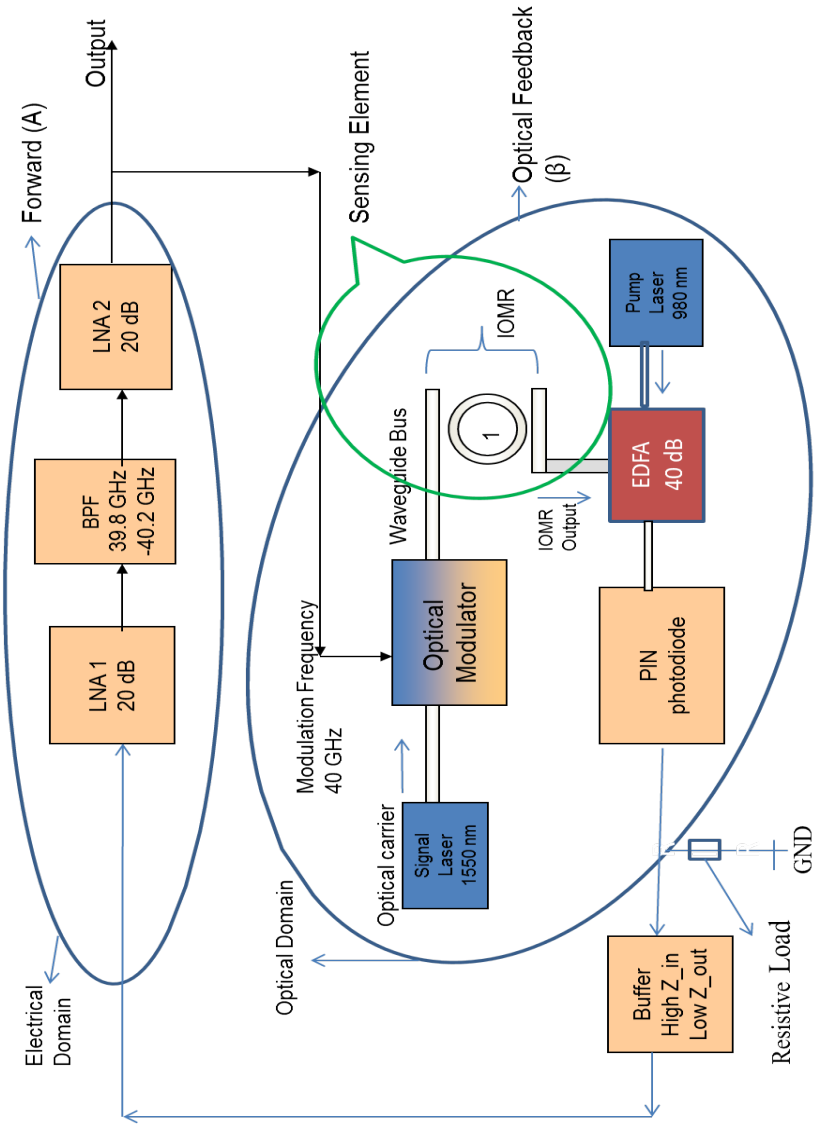

Figure 6.17: Schematic of IOEO based Bio-sensor

The output of the ring resonator is further amplified by the EDFA of 40 dB gain. The pump signal for the EDFA is given at wavelength of 980 nm. The resonant wavelength of IOMR depends on the geometry of the ring waveguide, bus wave guide and the cladding material.

The output of IOEO is defined by $v(t)$ by Equation (6.5) (Section 3.5)

$$v(t) = 0.12G_{EDFA}\{1 + 2cos[\pi\frac{v(t_0)}{V_\pi}] + \phi\}\frac{\eta q}{hf} * R_L * G_F \tag{6.5}$$

6.3.2 Analysis and Simulation of the IOEO Based Bio-sensor

In this section, an analytical modelling of the IOEO based sensor has been presented. Conventionally the resonant wavelength of a micro-ring/race-track resonator is given by

$$n_{eff}L = m\lambda_0 \tag{6.6}$$

Where,

n_{eff} is the effective refractive index, L is the perimeter of ring resonator of IOMR and λ_0 is the resonant wavelength and m is the order of resonance.

The FSR of the micro ring resonator is given by Equation (6.8). Where c is the velocity of light in free space and n_g is the group index.

$$\lambda_0 = \frac{c}{n_g f_0} \tag{6.7}$$

$$FSR = \frac{c}{n_g L} \tag{6.8}$$

Where,

FSR is the Free Spectral Range, n_g is the group index and c is the velocity of light in free space.

The mode propagating in high index contrast SOI based ring resonator and bus wave guides experiences the strong dispersion effect. Hence the group index of the mode n_g rather than effective index n_{eff} has been considered. The expression for the change in output frequency of the Bio-sensor is derived as follows: Substituting the value of λ_0 from Equation 6.7 and L from Equation 6.8 in Equation 6.6, one gets

$$n_{eff}\frac{c}{n_g \times FSR} = m\frac{c}{n_g \times f_0} \tag{6.9}$$

Simplifying the Equation 6.9 one gets,

$$\Delta f_0 = \frac{m \times FSR}{\Delta n_{eff}} \tag{6.10}$$

Change in effective refractive index of the ring resonator due to Bio-material results in a shift in resonant frequency indicated in Equation (6.10). The frequency shift $\triangle f_0$ of the IOMR results in deviation of center frequency of the IOEO based sensor and consequently drift in the $v(t)$ is observed. In this analysis, the effect of refractive index of Bio-material on the sensitivity of the IOEO is analyzed. The estimation of the effective refractive index in the waveguide for the variation in upper clad refractive index has been performed using mode solver (Fallahkhair, Li, and Murphy, 2008) from Photonics Research Laboratory (Photonics Research Laboratory, n.d.) and the results are shown in Figure 6.18.

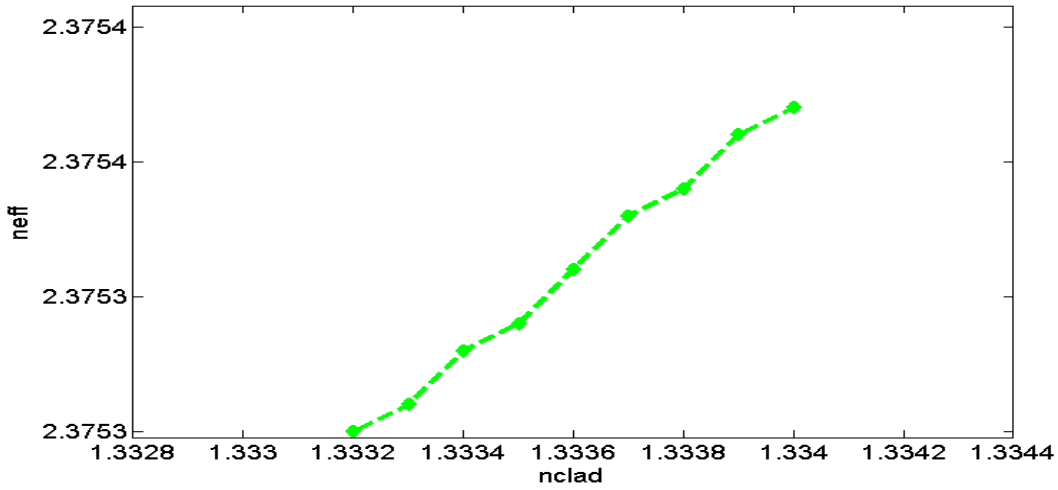

Figure 6.18: Variation of effective refractive index with clad refractive index

The shift in resonant wavelength of micro-ring resonator by varying the upper cladding refractive index with a Bio-material (Glucose Solution) has been observed. Frequency offset or shift in resonant frequency of IOEO varies linearly with change in refractive indices of upper cladding as depicted in Figure 6.19. Figure 6.20 depicts the change in frequency offset with change in glucose concentration.

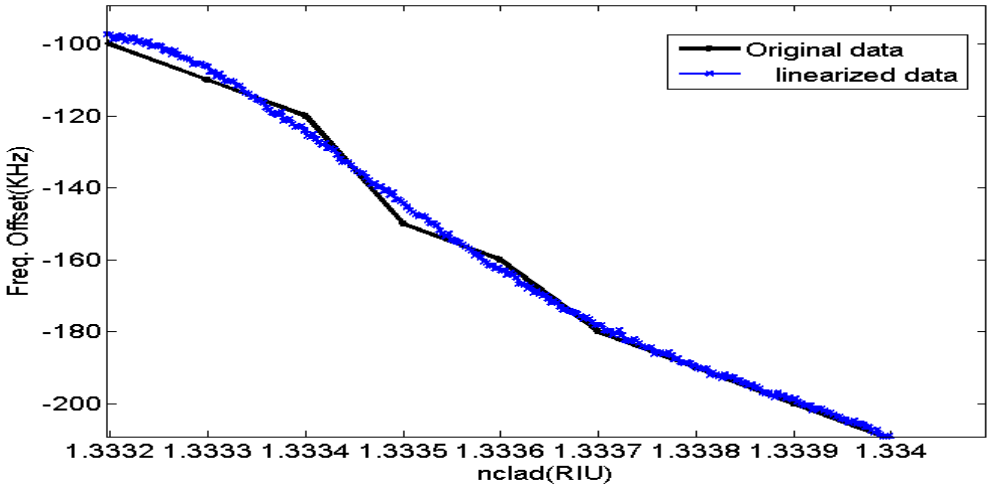

Figure 6.19: Variation of frequency offset with clad refractive index

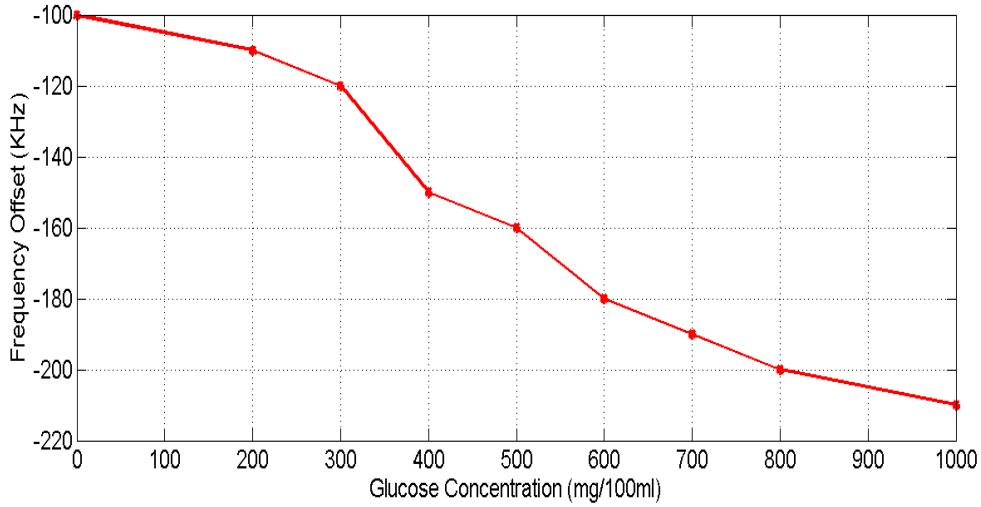

Figure 6.20: Variation of frequency offset with change in Glucose concentration

An architecture for Bio-sensor based on IOEO has been proposed. IOEO oscillates at 40 GHz with a lowest phase noise of -245 $dBcHz^{-1}$ at 100 kHz offset. Liu et al. have tabulated (Liu, Hering, and Scully, 1992) the variation in cladding refractive index with change in Glucose concentration. These tabulated values are represented in first and third column of Table 6.1. The change in resonant frequencies with change in refractive index of clad is

Table 6.1: Variation of cladding refractive index, Glucose concentration (mg/100ml) and frequency shift (kHz)

Cladding refractive index	Frequency shift (kHz)	Glucose concentration (mg/100ml)
1.3332	-100	0
1.3333	-110	200
1.3334	-120	300
1.3335	-150	400
1.3336	-160	500
1.3337	-180	600
1.3338	-190	700
1.3339	-200	800
1.3340	-210	1000

also tabulated in Table 6.1. With the tabulation depicted in Table 6.1, the shift in resonant frequency is directly related to the corresponding Glucose concentration thereby serving as a Bio-marker for blood sugar monitoring. In the simulation, cladding index of the IOMR is varied from 1.3332 to 1.3340 (Refractive index of Glucose) and the corresponding shift in resonant frequency of IOEO is observed. With the rise in refractive index of upper cladding, the resonant frequency of the oscillator decreases. The proposed sensor exhibits a bulk refractive index sensitivity of -140 $MHzRIU^{-1}$. Table 6.1 depicts the variation of cladding refractive index, Glucose concentration and frequency shift in the output of designed IOEO. As the concentration of the Glucose increases, the shift in the resonant frequency of IOEO has been observed. From the above discussions, it is observed that the change in glucose concentration leads to variation in refractive index of the cladding surface on which the glucose is placed. The change in the refractive index of the cladding surface leads to shift in resonant frequency of the IOEO. Thus the change in the concentration of the glucose can be directly related to the resulting shift in the resonant frequency of the IOEO. Conversely, the observed shift in resonant frequency of the IOEO can be directly correlated to the concentration level of the Glucose. Thus the validity of the underlying principle behind the functionality of the Bio-sensor is substantiated.

6.4 Summary

Novel architecture for Bio-sensor based on Integrated IOEO has been proposed. The proposed Bio-sensor falls under the category of label-free optical Bio-sensor which elim-

inates the need and cumbersome effects of labeling techniques. The simulated IOEO oscillates at 40 GHz with a lowest phase noise of -245 $dBcHz^{-1}$ at 100 kHz offset has all-optical components in the feedback path. The proposed configuration of Bio-sensor has the desirable features of compactness and high thermal stability of $\pm 0.325\ ppmK^{-1}$.

An IOMR in the feedback path of the IOEO acts as a sensing element. The Bio-material acts as the cladding layer of the IOMR with which the evanescent tail of the propagating fundamental mode interacts. This interaction changes the effective index of the mode and resonant wavelength of the IOMR. The proposed ring resonator geometry on Silicon-on Insulator platform enables miniaturization. The structure has been simulated with a Bio-material, whose refractive indices lie in the range 1.3332 to 1.3340 based on Glucose concentration. Refractive index of the cladding layer eventually modifies the oscillating frequency of the IOEO. The proposed sensor exhibits a bulk refractive index sensitivity of -140 $MHzRIU^{-1}$.

CHAPTER 7

CONCLUSIONS AND FUTURE RECOMMENDATION

7.1 Summary

In this chapter conclusions derived from the research study of this thesis have been presented. The original research contributions of this thesis to the specific domains of OEO and IOMR have also been discussed. The contributions related to design and simulation of 40 GHz IOEO, design and analysis of IOMR, CMT for IOMR, two port network theory applicable to IOEO, various models of IOMR and utility of designed IOEO in applications such as beam steering and Bio-sensors have been summarized. A suggestion for the possibility of exploring further some of the key research findings of this thesis has also been presented.

7.2 Conclusion

The key research contributions of this thesis can be discussed succinctly by emphasizing the following specific technical aspects.

1. Design, simulation and analysis of all optical feedback path based 40 GHz IOEO
2. Development of simulation model of IOMR using Coupled Mode Theory
3. Formulation of an analytical approach for the computation of phase noise of IOMR and IOEO
4. Application of proposed IOEO for Optical beam Steering and Bio-Sensor
5. Fabrication of BPF and IOMR

A summary description of the research findings of this thesis under the purview of the above cited topics is presented in the following paragraphs.

1. Design, simulation and analysis of all optical feedback path based 40 GHz IOEO

A Linear Time Invariant (LTI) architecture for the generation of 40 GHz sinusoidal frequency with high spectral purity, high Quality factor, minimum phase noise, better

thermal and frequency stability has been proposed. The need and the requirement of the IOEO have been explored keeping the perspective of requirement of the present photonics communication systems as well as the latest trends in the integrated photonic communication industries.

In the proposed LTI architecture of IOEO, the long optical fiber has been replaced by an optical ring resonator (micro-ring resonator). Use of optical ring resonator significantly reduces the size of the oscillator and thereby facilitating its integration on a single chip. The replacement of long optical fiber by a compact micro ring resonator leads to significant reduction in the propagation loss which in turn increases the quality factor (Q) of the oscillator.

The proposed architecture of IOEO has all optical components in the feedback path. After the initial excitation, the forward path (with all electrical components) and feedback path (with all optical components) form the closed loop system and the oscillation sets in. The proposed IOEO has the possibility of adjusting the gain through design of LNA, EDFA and IOMR. The design of novel BPF also leads to the improved filtering and rejection of the unwanted side modes of the IOMR.

To facilitate better appreciation of the underlying principles of the architecture of the proposed IOEO, a technical description of all the components of the functional block of IOEO has been presented with requisite and pertinent details. The simulation results emphasising the important performance attribute of each sub system or block have also been presented. Keeping in view the feasibility and the practical relevance of the proposed architecture, for the simulation of performance measures of various components/devices, fairly well known and published structural configurations of devices have been chosen. A significant deviation of the architecture of proposed IOEO is the placement of components belonging to optical domain in the feedback path which in turn leads to:

- Reduction in the size of the IOEO
- Increased quality factor
- Improved thermal stability
- Reduction in the phase noise of the IOEO

The effect of the phase noise on the designed IOMR taking Butt-coupling coefficient into consideration is also analysed. The study of Butt-coupling coefficients paves way

for the future development of miniaturized IOMR with narrow gap. The phase noise is found to be in the range of -280 $dBcHz^{-1}$ to -300 $dBcHz^{-1}$, which is insignificant for any communication application.

Numerous analytical formulations to analyse the performance metrics of IOEO such as phase noise, thermal stability and stability with variation in design input parameters such as refractive index and offset frequency have been discussed in the thesis. The relative advantage of array of IOMR over single IOMR pertaining to the output power of IOEO has been discussed in this thesis. The improvement of 20 dB in the output power has been observed in case of array of 26 IOMRs.

In this thesis, performance analysis of the designed IOEO with single and array of IOMRs has been presented. The phase noise, thermal and frequency stability of IOEO with single IOMR have also been addressed. The effect of the IOMR on the phase noise of the IOEO has also been discussed using analytical method.

The phase noise analysis using variance method has been discussed and found to be suitable for the IOEO application in optical beam steering and Bio-sensor. The simulation results show that the designed IOEO has minimum phase noise -245 $dBcHz^{-1}$ at an offset frequency of 100 kHz. This is minimum phase noise as compared to -163 $dBcHz^{-1}$ as in the the existing literature (Chembo et al., 2009)).

Thermal analysis of the designed IOEO has been carried out. In the simulation, effective refractive index of IOMR has been varied from 2.125 to 2.155 and the corresponding frequency shift in the IOEO is determined. With the rise in temperature, the resonant frequency of the oscillator decreases. The designed IOEO exhibits thermal stability of $\mp 0.325\ ppmK^{-1}$.

The stability analysis of the designed IOEO has been carried out. Since the stability analysis involves the usage of Scattering parameters, a two port network theory has been used and ABCD parameters of the constituent subsystems of IOEO have been computed. From the ABCD matrices of the subsystems, the ABCD matrices of the forward path and feedback path of IOEO have been arrived at. From the arrived ABCD matrices, the associated S-parameters have been obtained. With the computed S-parameters of forward path, the stability of IOEO has been assessed. Study on the effect of Butt-coupling coefficient on the ABCD parameters of the IOMR has also been presented. The product of S-parameters of the elements of forward path of IOEO is used to compute the Rollets Stability factor (K1) and is found to be 10.2941.

2. Development of simulation model of IOMR using Coupled Mode Theory

The IOMR is well known for its high quality factor and negligibly small phase noise. The usage of the IOMR in the generation of the sinusoidal frequency has been reported extensively in the literature. This thesis further substantiates the utility of IOMR for the generation of a signal at frequency as high as 40 GHz.

The design and analytical study on the design and performance parameters of IOMR have been presented. The design and quantification of the various parameters such as Quality factor (Q), Ring radius (R), Free Spectral Range (FSR) and Phase Noise have been discussed through the development of analytical expressions relating them. The Coupled Mode Theory (CMT) which is a fundamental principle explaining the transfer of power from the one port to another in the optical domain has also been addressed. An application of the CMT to analyse the significance of the gap between the straight waveguide and the curved waveguide on the performance of IOMR relevant to IOEO has been analyzed through a development of an analytical model.

In this thesis various design and performance parameters of the IOMR have been explored. The significance and the usability of these parameters in the application like oscillator have been analysed both through analytical expressions as well as through simulation studies. The quantification of the design parameters of IOMR is also discussed. The computation of the effective refractive index and their corresponding wave guide dimension and mode profile has been carried out using Eigen solver at Photonic Laboratory Lab as per the IOEO requirements.

A novel analytical model for the IOMR with straight and curved waveguides has been explored. Relation among ring radius (R), coupling length (l), gap between straight and curved waveguides (d) and coupling coefficient (k) is established. The developed analytical model of IOMR is found to be suitable for the IOEO application. Its utility in the calculation of quality factor, coupling length and gap between straight and curved waveguides of the ring resonator has been substantiated. The coupling coefficient, coupling length and their influence on the power transmission at the output port of IOMR have been analysed. The designed IOMR can be fabricated and the fabrication tolerance of the designed IOMR has been analysed using OptiFDTD version 8.0 simulator.

The CMT which is basically the physics of the device has been discussed. An analytic approach with physical insight of the CMT in the IOMR has been explored. The CMT has been analysed by including the Butt-coupling coefficient. The effect of Butt-coupling coefficient on the output power at the output port, quality factor and FSR has been analyzed.

The analysis of the effect of gap d between straight and curved waveguides from the perspective of output power brings new insight into the physics of the device. The effect of bend waveguide on loss coefficient has been analysed for the designed IOMR. The effect of thickness of waveguide on the performance of the strip waveguide has also been studied. This analysis facilitates better understanding of design of IOMR from the point view of the requirements of IOEO for communication applications.

3. Formulation of an analytical approach for the computation of Phase Noise of IOMR, sub blocks of IOEO and IOEO

A novel model for the phase noise analysis of IOEO has been proposed and the phase noise of IOEO has been computed. The contribution of IOMR to the phase noise of IOEO has been addressed in the thesis. A two port network concept is invoked to develop a model for the analysis of phase noise of the subsystems of IOEO as well as that of IOEO. An analytical approach for the determination of ABCD parameters of the constituent sub-systems of IOEO and composite IOEO has also been presented. Widely used and well known relationship between the ABCD matrix and the S-matrix of a two port network model has been invoked to address the stability analysis of the designed IOEO.
The ABCD parameters have been explored to analyse the phase noise contribution of the IOMR in the designed IOEO. To address this, a novel ABCD parameter approach has been been presented using Pollock and Okamoto models for SOI based IOMR. The simulation results indicate that the contribution of the IOMR to the phase noise in the designed IOEO is insignificant and negligibly small (of the order of -280 dB_cHz^{-1}).

4. Application of proposed IOEO for Optical beam Steering and Bio Sensor

This thesis also illustrates the application of the designed IOEO for the optical beam steering system. The proposed optical RF phase shifter for beam steering has advantages of generating stable 40 GHz modulating signal with a reduced phase noise of -245 $dBcHz^{-1}$ at an offset frequency of 10 kHz. The designed beam steering system also generates and modulates simultaneously using a single optical modulator. Using the designed optical beam steering, one can achieve the desired phase shift by varying the SMF length. An optical beam steering system with 4 isotropic antennas has been simulated and a beam shift or steering of 0.4 degree has been obtained.
An architecture for Bio-sensor based on IOEO has been proposed. The proposed Bio-sensor falls under the category of label-free optical Bio-sensor which eliminates the need and

cumbersome effects of labeling techniques. The simulated IOEO oscillates at 40 GHz with a lowest phase noise of -245 $dBcHz^{-1}$ at 100 kHz offset and has all-optical components in the feedback path. The proposed configuration of Bio-sensor has the desirable features of compactness due to small size of IOMR (Radius of 3.5397 μm) and high thermal stability of $\mp$ 0.325 $ppmK^{-1}$.

An IOMR in the feedback path of the IOEO acts as a sensing element. The Bio-material acts as the cladding layer of the micro-ring resonator with which the evanescent tail of the propagating fundamental mode interacts. This interaction changes the effective index of the mode and resonant wavelength of the micro-ring resonator. The proposed ring resonator geometry on silicon-on insulator platform enables miniaturization. The structure has been simulated with a Bio-material, whose refractive indices lie in the range 1.3332 to 1.3340 based on Glucose concentration. Refractive index of the cladding layer eventually modifies the oscillating frequency of the IOEO. The proposed sensor exhibits a bulk refractive index sensitivity of -140 $MHzRIU^{-1}$.

5. Fabrication of BPF and IOMR

To facilitate manufacturing of the proposed IOEO, a technical description of fabrication tolerance of the IOMR as well as computation of the capacitance and inductance used in the BPF have been presented in chapter 3 with requisite and pertinent details. The capacitance and inductance required for the design of BPF with a pass band 39.8 to 40.2 GHz are 0.397 fF and 1.0369 pH respectively. The achievable minimum length pertaining to the length of the conductive trace of the existing multilayer PCB is 0.0762 mm (Best Technology, n.d.). With FR4 as dielectric material of the PCB with a height of 0.3 mm and dielectric constant of 4.22, the minimum values of capacitance and inductance which can be realized through a microstrip line of length of 0.0762 mm are 0.1494 fF and 0.3754 pH respectively. The value of inductance required for the design of BPF is 1.0369 pH which is larger than the minimum realizable inductance of 0.3754 pH. Similarly the value of capacitance required for the design of BPF is 0.397 fF is larger than the minimum realizable capacitance of 0.1494 fF. Therefore all the inductors and capacitors needed in the design of BPF required in IOEO can be realised with existing precision of PCB technology. The minimum realizable gap (d) reported is 150 nm between straight and curved wave guides of an IOMR (Steglich et al., 2017). From the perspective of practical implementation of the IOEO, an IOMR with the gap (d) of 200 nm has been simulated and fabrication of such device is presently possible. For the fabrication of IOMR following features have

been considered: core height of 235 nm, clad height of 500 nm, width of 500 nm for both the straight and curved wave guides and ring radius of 3.5973 μm. An IOMR with these dimensional parameters can be fabricated with the reported existing realizable precision in Silicon-On-Insulator (SOI) technology (Steglich et al., 2017).

7.3 Original Contributions

The list of original contributions of this thesis with its emphasis on IOEO at 40 GHz is as follows:

- Design architecture of IOEO at 40 GHz with its feedback path comprising all optical components
- Analytical formulation for the analysis of phase noise of IOEO and its constituent subsystems using two port network theory
- Analysis of IOMR with the consideration of Butt-coupling coefficient
- IOEO based optical beam steering scheme and label free Bio-sensor

7.4 Suggestions for Future Work

Research is a continual process thriving for perennial advancement and dissemination of knowledge through a scientific method of investigative study and its extension. Keeping in view of the philosophy of research, a few suggestions to explore further some of research ideas within the purview of broad research domain of IOEO have been proposed.

- In this thesis, the architecture of the proposed IOEO involves only one feedback loop. However, the IOEO could be designed with dual or multi-feedback loop architecture. The dual loop architecture could further suppress the side modes. Hence IOEO could be realized without BPF also. The multi-loop architecture could provide enough output power so that use of EDFA can be neglected. Therefore dual and multi-feedback loop architecture of IOEO is worth pursuing.
- In this thesis, considerable emphasis is on phase noise of IOEO. Noise from the sub system such as BPF, PD and IOMR have been considered. The thermal noise of the IOMR is also taken into consideration. The noise performance of the designed IOEO

could be analysed using noise transfer function of the various subsystem of the IOEO. The noise from the laser, EDFA, pump source and the LNA could be further studied and improved. The noise transfer function can be useful in interpreting noise output at various subsystems of the IOEO. Hence one can derive overall noise transfer function of the IOEO. The study can help in the estimation of total noise of IOEO.

- In the proposed thesis, the architecture of IOEO has been assumed to be Linear Time Invariant. However, from a practical stand point of view, the IOEO may encounter a time variant behaviour. In addition, the thesis also has an explicit assumption of linearity to invoke the two port network concept wherever applicable. The rigour of the proposed thesis can be enhanced by incorporating the non-linear and time variant features into the architecture of IOEO.

- This thesis addresses the influence of Butt-coupling coefficient in the performance analysis of IOMR. The thesis also presents a simulation model of IOMR invoking the CMT. Further analytical formulation can be attempted to link the CMT to determine the Butt-coupling coefficient of IOMR so that more accurate estimation of performance metrics of IOMR can be attempted.

APPENDIX A

THE SIMULATION RESULTS OF IOEO

This appendix presents additional simulation results on IOEO using Optisystem and MATLAB. Both Okamoto and Pollock models of IOMR are considered in the IOEO configuration.

A.1 Simulation Results for Pollock Model using Optisystem Version 7.0

In this section simulation results for IOEO using Pollock model for IOMR have been presented. The simulation has been carried out using Optisystem simulator. The Figures related to thermal noise and the output at each individual constituents of IOEO (such as LNA1, BPF, LNA2, OM, IOMR, EDFA and PD) have been shown. The phase noise and Allan variance of IOEO have also been illustrated.

Figure A.1 depicts the thermal noise which excites the initial oscillation in the IOEO through its forward path. The spectrum shown in Figure A.1 constitutes the input to the LNA1 of the forward path.

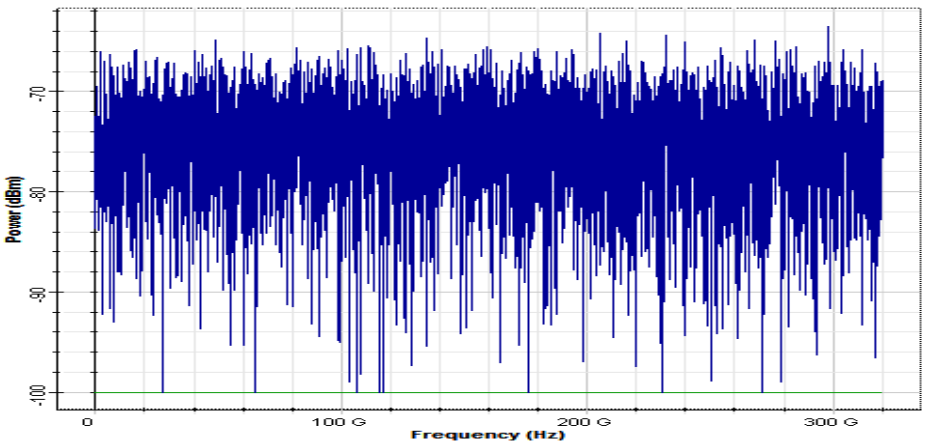

Figure A.1: Thermal noise excitation

Figure A.2 depicts the output of LNA1 which is the amplified thermal noise.

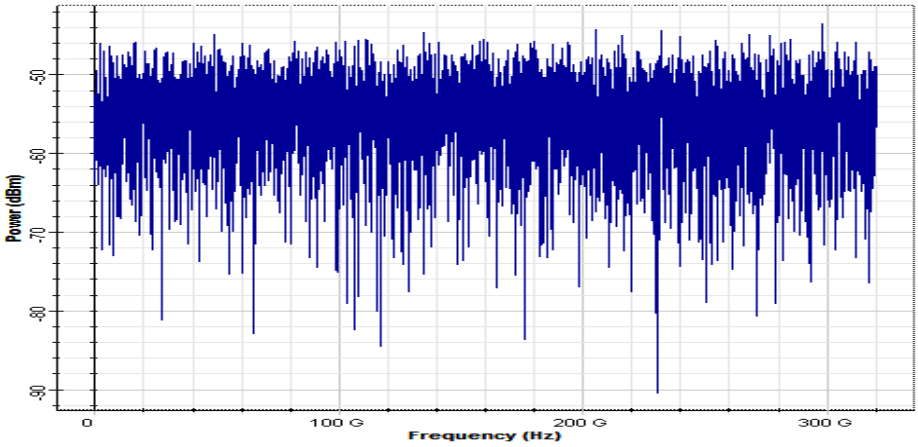

Figure A.2: Power spectrum of LNA1

The output of LNA1 is fed to the BPF. Figure A.3 illustrates the output spectrum of BPF.

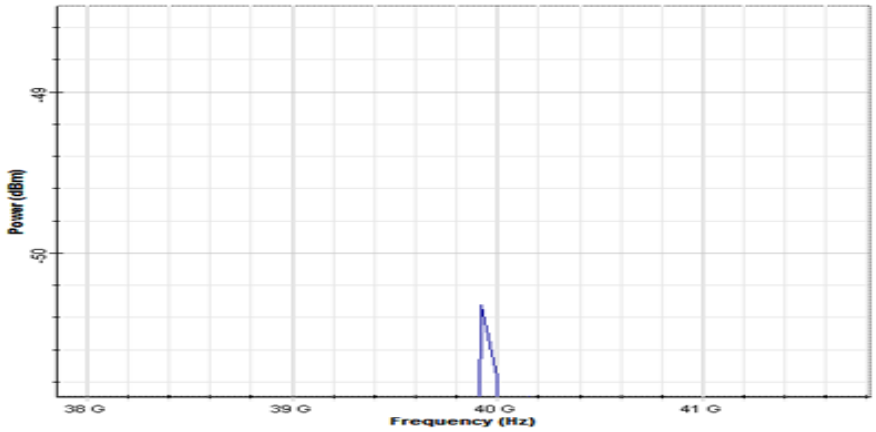

Figure A.3: Power spectrum of BPF

The output of BPF constitutes the input to the LNA2. The output spectrum of LNA2 is shown in Figure A.4.

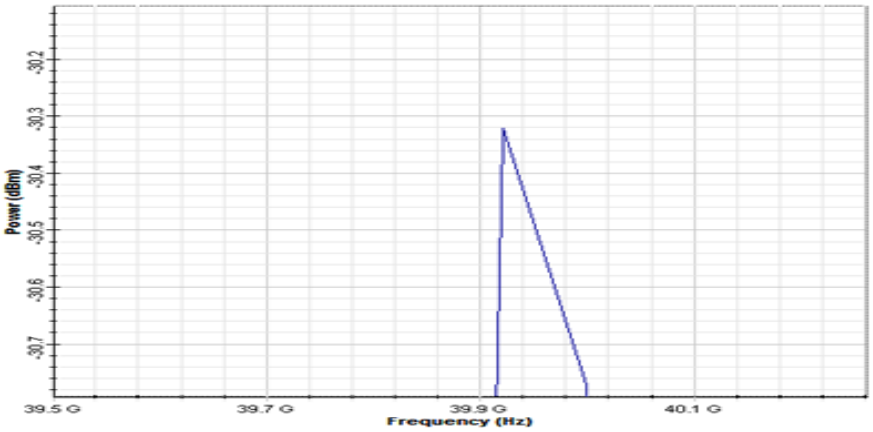

Figure A.4: Power spectrum of LNA2

The output of LNA2 is fed to optical modulator. Figure A.5 represents the optical carrier for optical modulator. The modulated output is fed to IOMR. Figure A.7 depicts the output spectrum of IOMR simulated through Pollock model. The frequency selection feature of IOMR is evident from the power spectrum shown in Figure A.7.

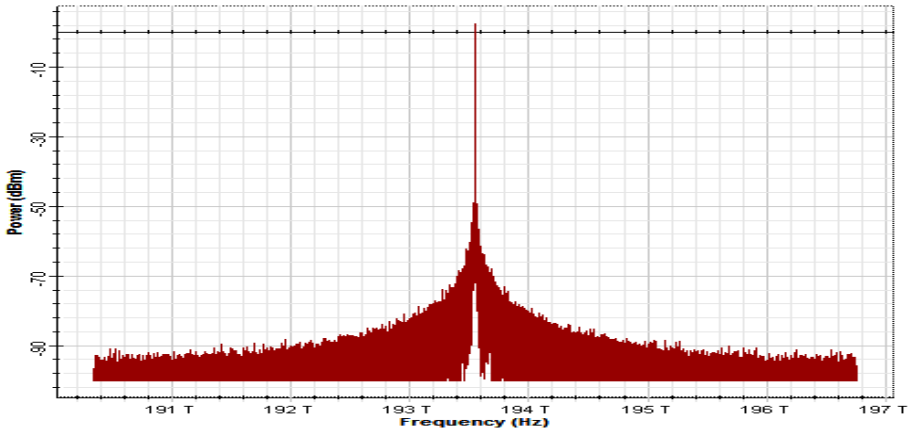

Figure A.5: Power spectrum of optical carrier

Figure A.6 depicts the modulated output from the optical modulator.

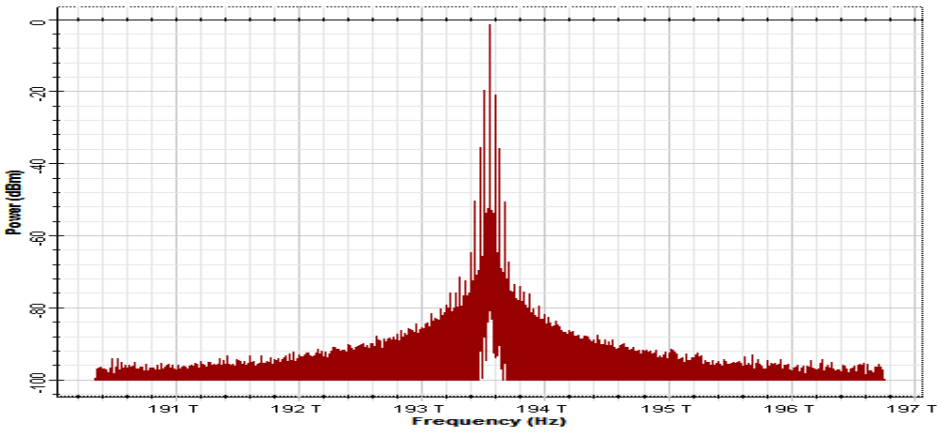

Figure A.6: Power spectrum of OM

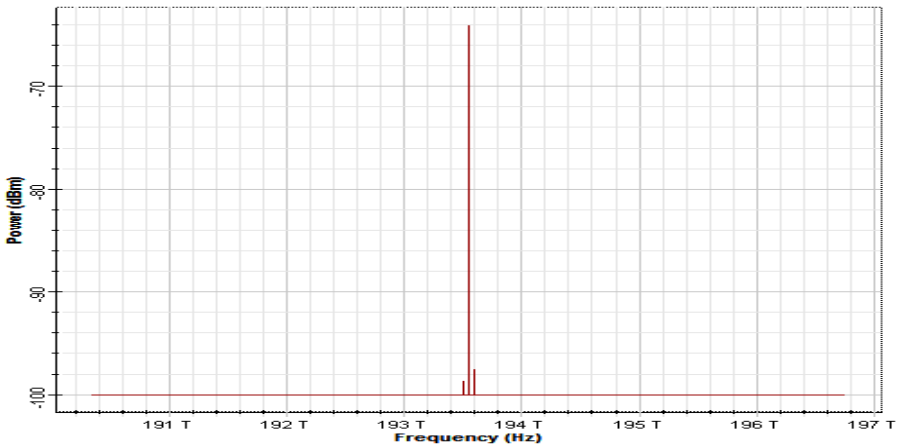

Figure A.7: Power spectrum of IOMR (Pollock model)

The power spectrum of IOMR constitutes the input to EDFA which is an amplifier. The output spectrum of EDFA is shown in Figure A.8.

The output of EDFA is fed to photo diode. The power spectrum of the output of the photo diode is illustrated in Figure A.9.

The phase noise of the designed IOEO is shown in Figure A.10. The IOMR of the IOEO is simulated through Pollock model.

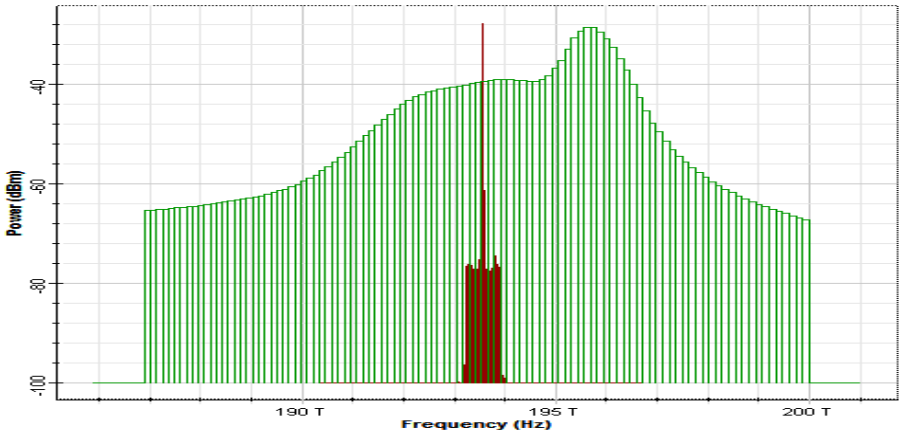

Figure A.8: Power spectrum of EDFA

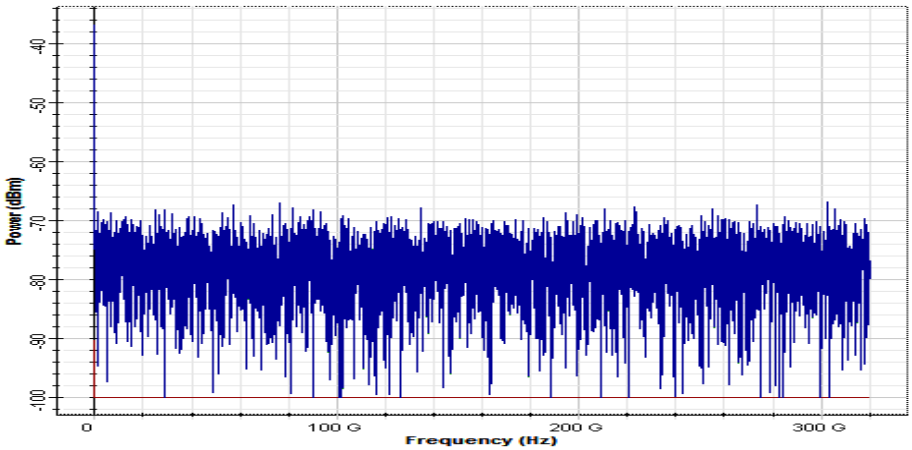

Figure A.9: Power spectrum of photo diode

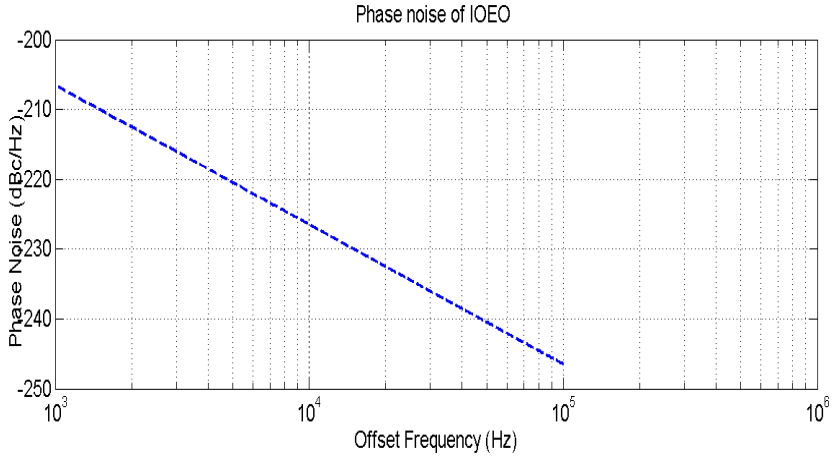

Figure A.10: Phase noise of IOEO using Pollock model of IOMR (Optisystem version 7.0 result)

The variation in Allan variance (short term stability) of IOEO is shown in Figure A.11. As seen from the results of Figure A.11, the short term stability of IOEO with Pollock model of IOMR is proved.

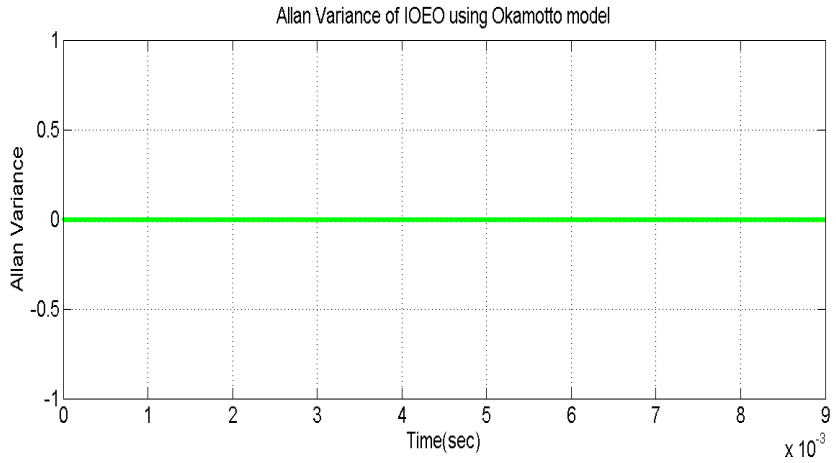

Figure A.11: Short term stability of IOEO using Pollock model (Optisystem version 7.0 result)

A.2 Simulation Results for Pollock Model using MATLAB Version 7.12 (R2011a)

In the previous section, simulation results of the constituents of IOEO and IOEO are obtained through Optisystem simulator. For a purpose of comparison, the simulation presented in the previous section has been repeated with MATLAB. In this section, simulation results for IOEO using Pollock model for IOMR have been presented using MATLAB simulator. The Figures related to thermal excitation noise and the output at each individual constituents of IOEO (such as LNA1, BPF, LNA2, OM, IOMR, EDFA and PD) have been shown. The phase noise and Allan variance have also been illustrated.
Analogous to the Figure A.1, Figure A.12 shows the thermal noise of IOEO which excites the oscillator to set initial oscillation.

Figure A.13 depicts the output spectrum of LNA1 which has been assumed to possess a gain of 20 dB.

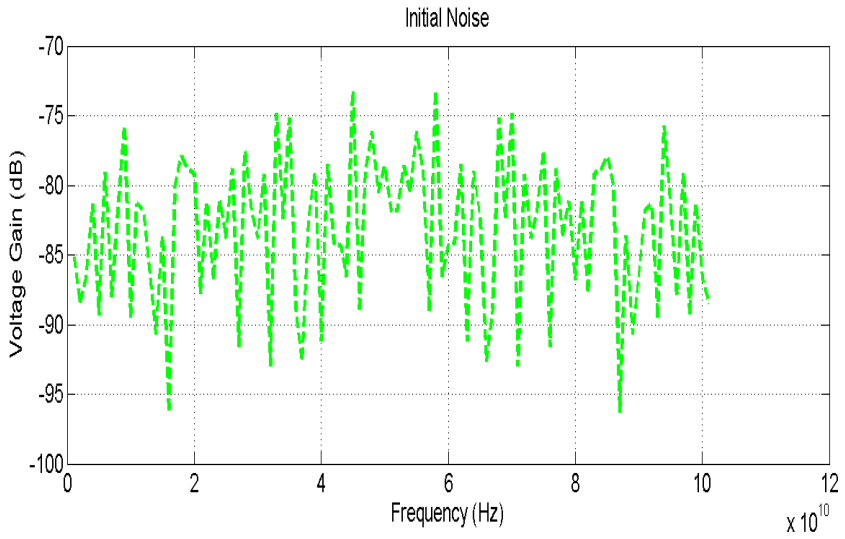

Figure A.12: Thermal noise excitation

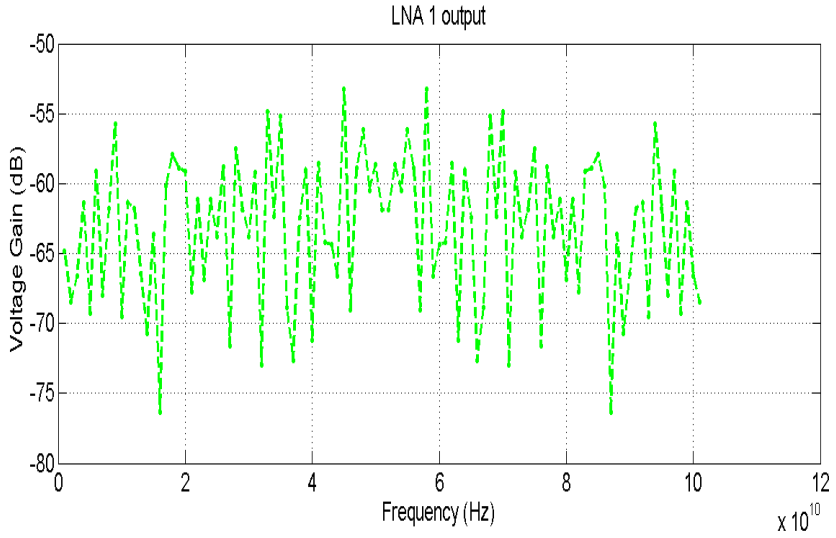

Figure A.13: Output spectrum of LNA1

The output of the LNA1 is fed to the BPF with a centre frequency of operation of 40 GHz. Figure A.14 illustrates the frequency response of BPF.

The output of the BPF constitutes an input to the LNA2 with a gain of 20 dB. Figure A.15 shows the frequency response of LNA2.

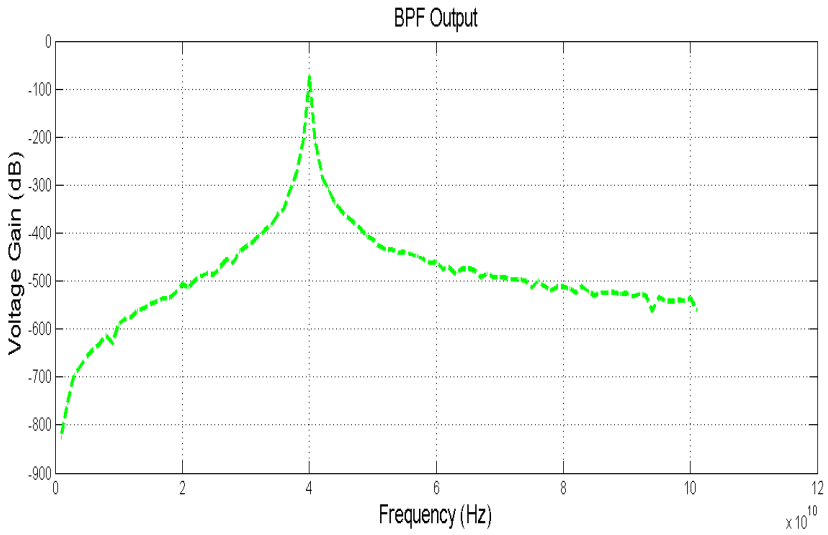

Figure A.14: Output spectrum of BPF

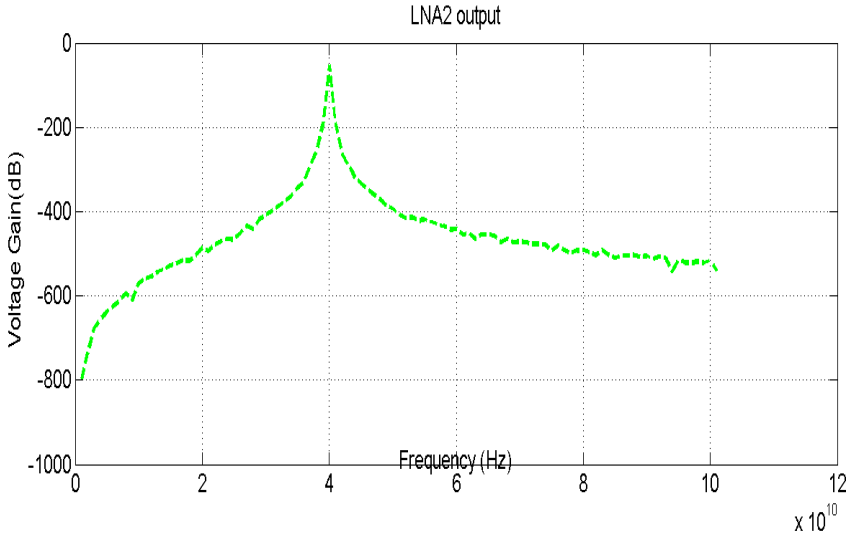

Figure A.15: Output spectrum of LNA2

Optical modulator derives its input from the output of LNA2. Figure A.16 depicts the output spectrum of optical modulator.

The output of optical modulator is fed to the IOMR simulated through Pollock model. Figure A.17 shows the output spectrum of IOMR.

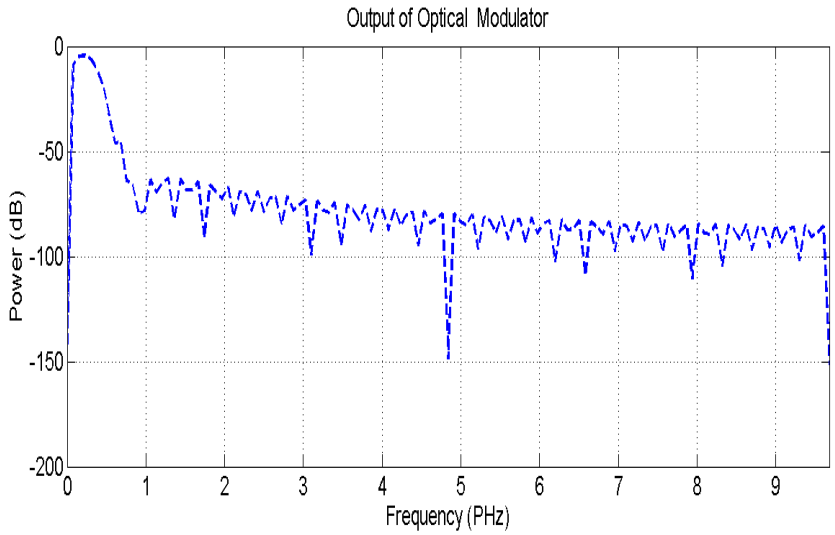

Figure A.16: Power spectrum of OM

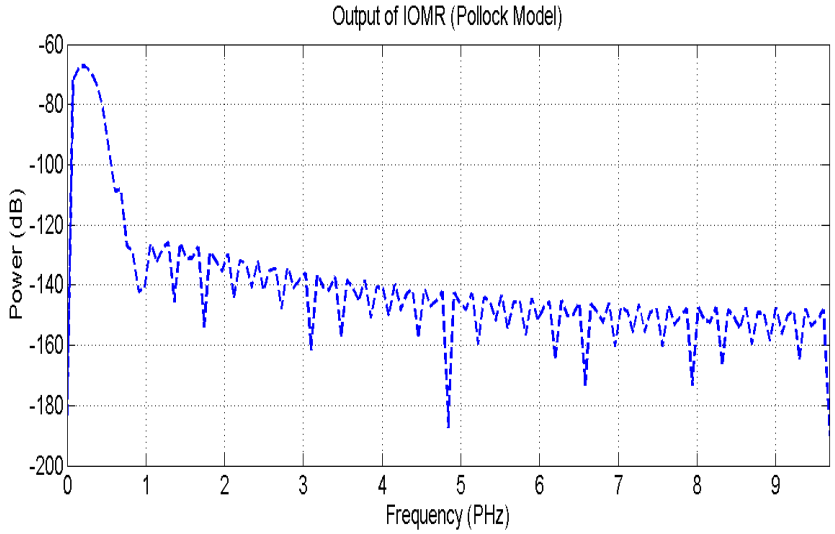

Figure A.17: Power spectrum of IOMR (Pollock model)

Output spectrum of IOMR forms an input to EDFA. Figure A.18 illustrates the frequency response of EDFA.

The input to the photo diode is obtained from the output of EDFA. Figure A.19 depicts the output spectrum of photo diode.

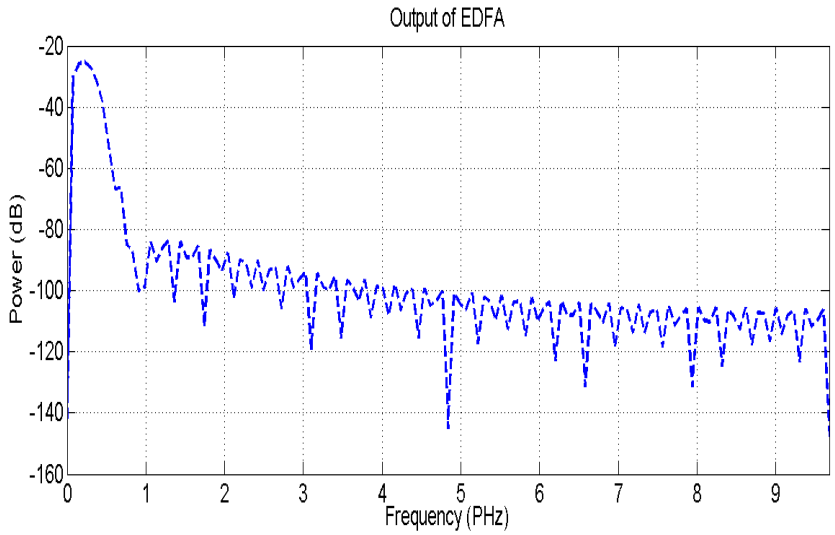

Figure A.18: Power spectrum of EDFA

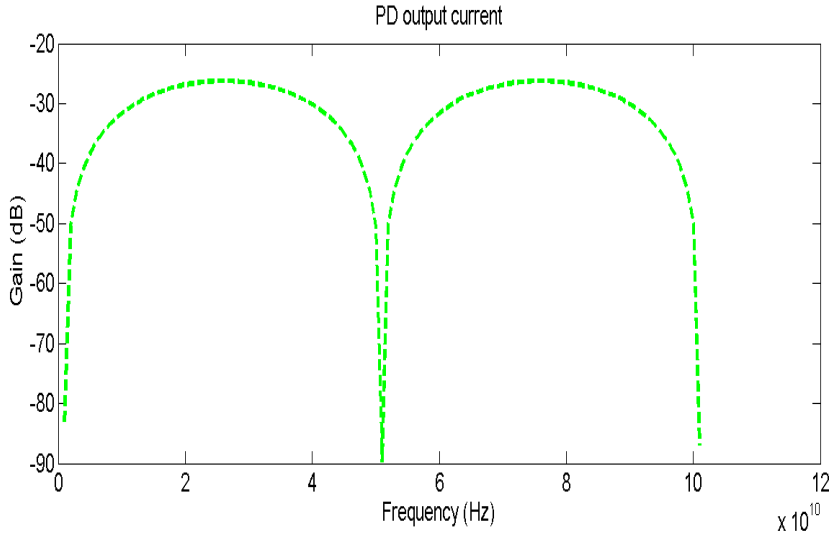

Figure A.19: Output spectrum of photo diode

Figure A.20 illustrates the simulated results on the phase noise of IOEO obtained with the Pollock model of IOMR.

Simulation result on the short term stability of the proposed IOEO obtained with Pollock model of IOMR is depicted in Figure A.21.

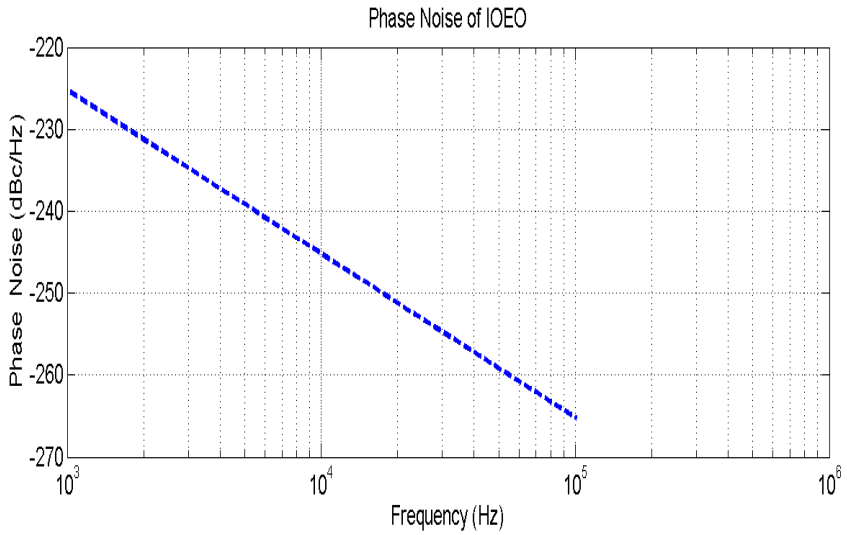

Figure A.20: Phase noise of IOEO using Pollock model of IOMR (MATLAB version 7.12 (R2011a) result)

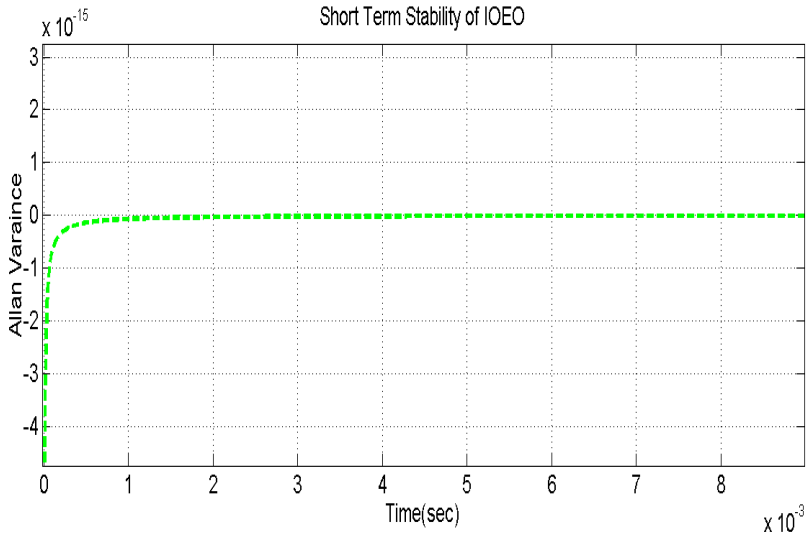

Figure A.21: Short term stability of IOEO using Pollock model of IOMR (Matlab result)

A.3 Simulation Results of Okamoto Model using MATLAB Version 7.12 (R2011a)

In this section simulation results for IOEO using Okamoto model for IOMR have been presented. The simulation has been carried out using MATLAB simulator. The Figures related to thermal noise and the output at each individual constituents of IOEO (such as LNA1, BPF, LNA2, OM, IOMR, EDFA and PD) have been shown. The phase noise and Allan variance have also been presented in this section.

Figure A.22 depicts the thermal noise which excites the initial oscillation in the IOEO

through its forward path. The spectrum shown in Figure A.22 constitutes the input to the LNA1 of the forward path.

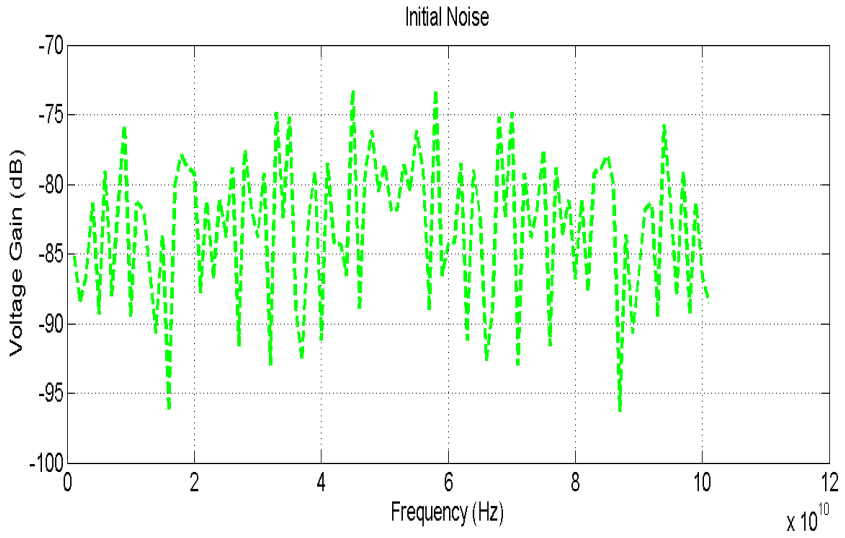

Figure A.22: Thermal noise excitation

Figure A.23 depicts the output spectrum of LNA1 which has been assumed to possess a gain of 20 dB.

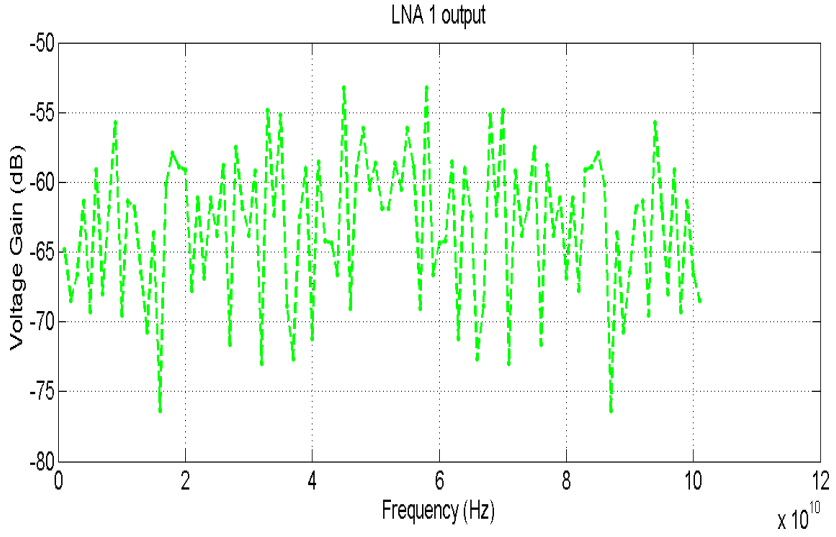

Figure A.23: Output spectrum of LNA1

The output of LNA1 forms an input to the BPF with the centre frequency of 40 GHz. Figure A.24 shows the frequency response of BPF indicating the functionality of the design of BPF.

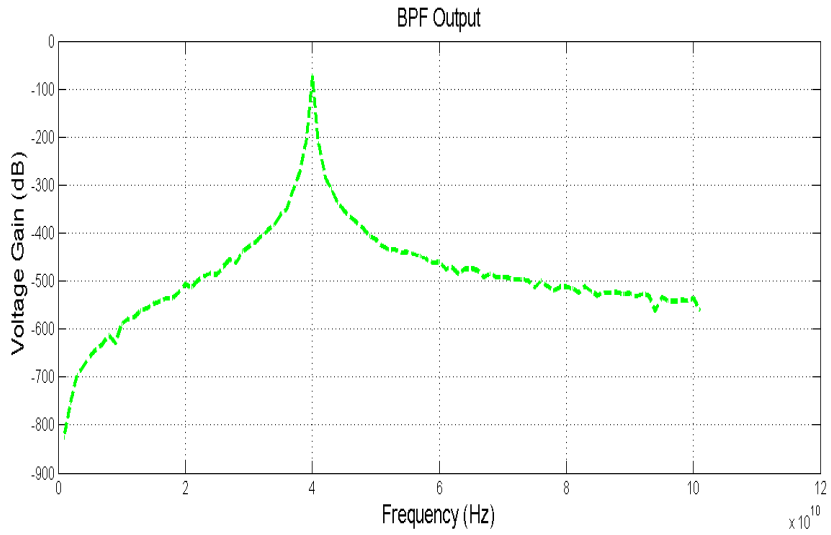

Figure A.24: Output spectrum of BPF

The output of the BPF constitutes input to the LNA2 with a gain of 20 dB. Figure A.25 shows the frequency response of LNA2.

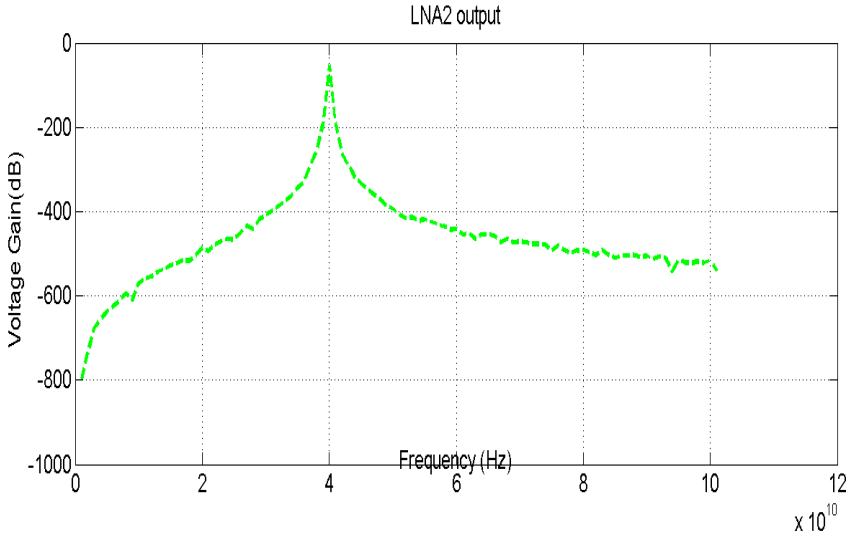

Figure A.25: Output spectrum of LNA2

The optical modulator is fed with the output of LNA2. The output spectrum of optical modulator is shown in Figure A.26.

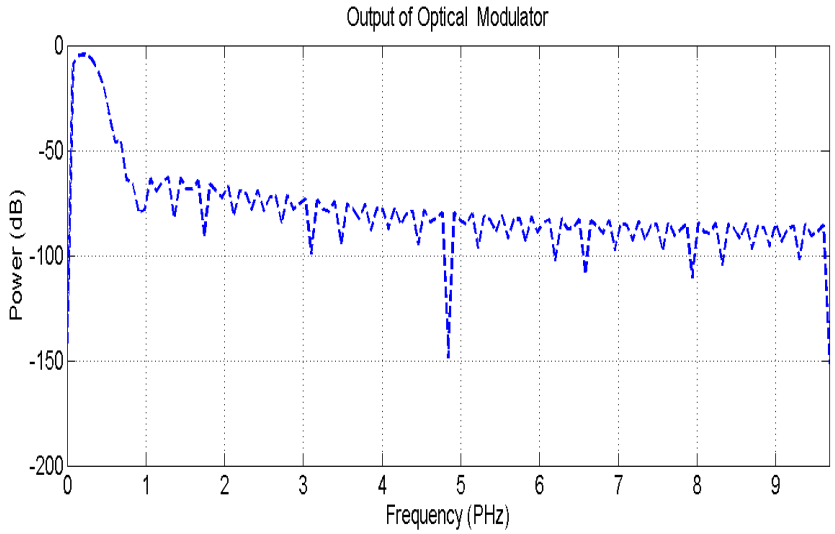

Figure A.26: Power spectrum of OM

The input of IOMR designed with Okamoto model is obtained from the output of optical modulator (modulated signal). The output spectrum of IOMR (Okamoto model) is shown in Figure A.27.

EDFA amplifies the output signal of IOMR. The output spectrum of the EDFA is shown in Figure A.28.

The output of EDFA constitutes the input to the photo diode. Figure A.29 depicts the output spectrum of photo diode.

The phase noise characteristic of IOEO with its IOMR simulated through Okamoto model is shown in Figure A.30.

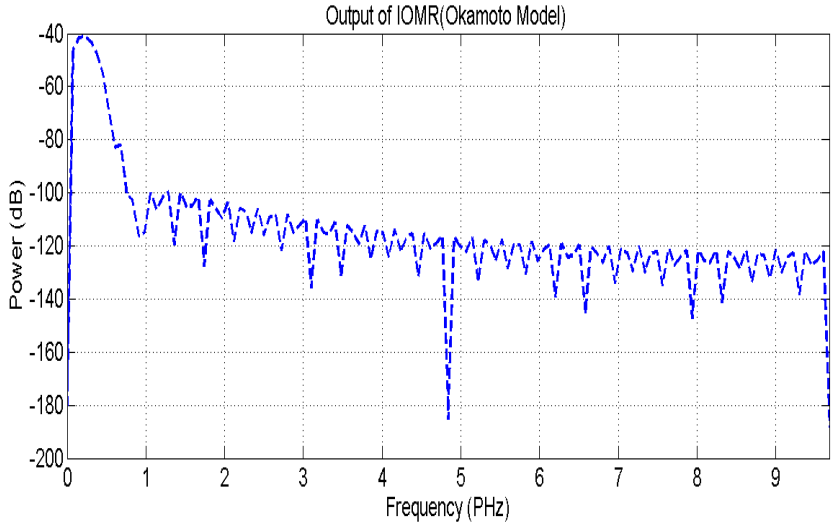

Figure A.27: Power spectrum of IOMR (Okamota model)

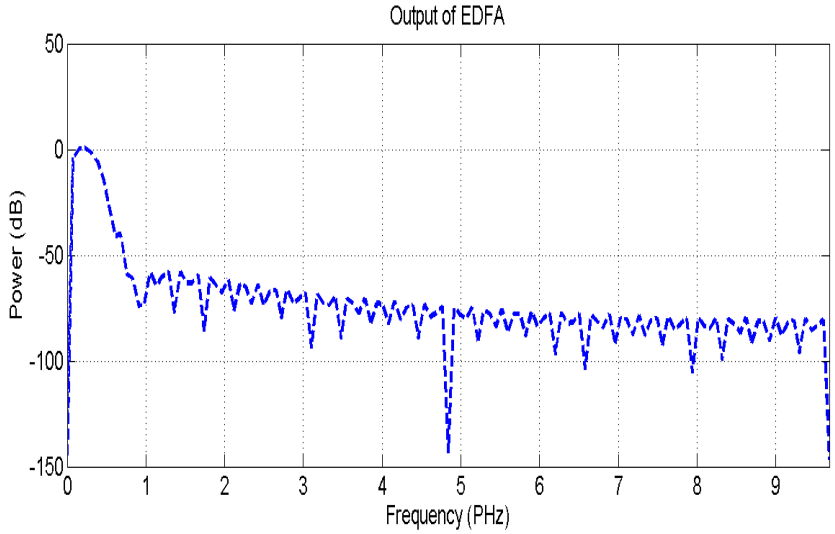

Figure A.28: Power spectrum of EDFA

The short term stability of an oscillator is analysed through Allan variance. Allan variance exhibited by the IOEO with its IOMR simulated through Okamoto model is illustrated in Figure A.31. Simulation result shown in Figure A.31 clearly reveal that the proposed IOEO simulated through IOMR with Okamoto model attains stability after 1 ms.

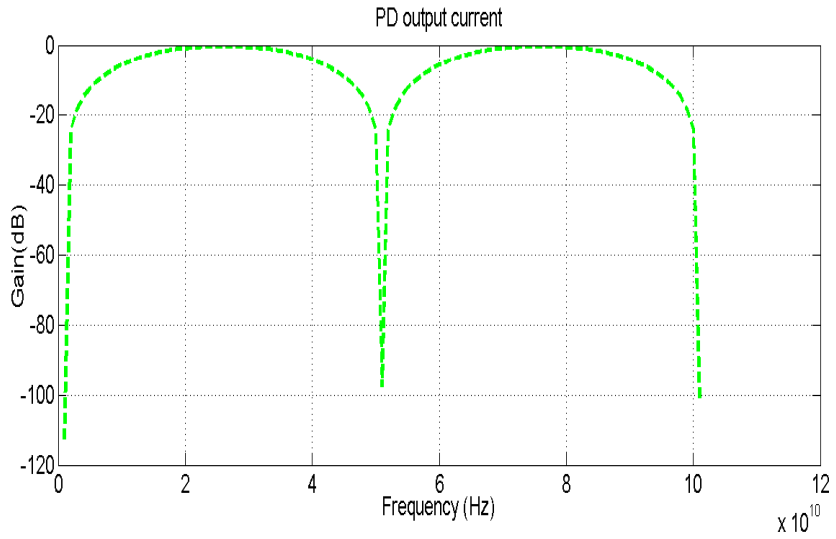

Figure A.29: Output spectrum of photo diode

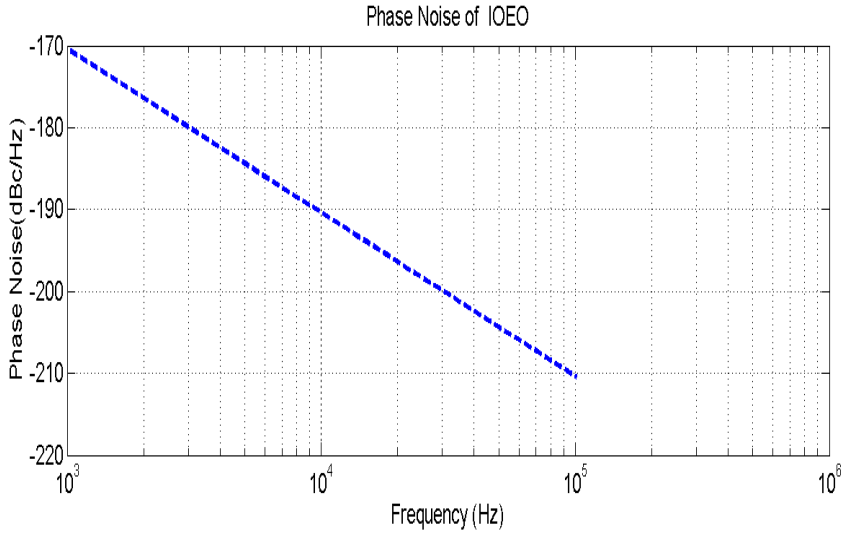

Figure A.30: Phase noise of IOEO using Okamoto model of IOMR (MATLAB result)

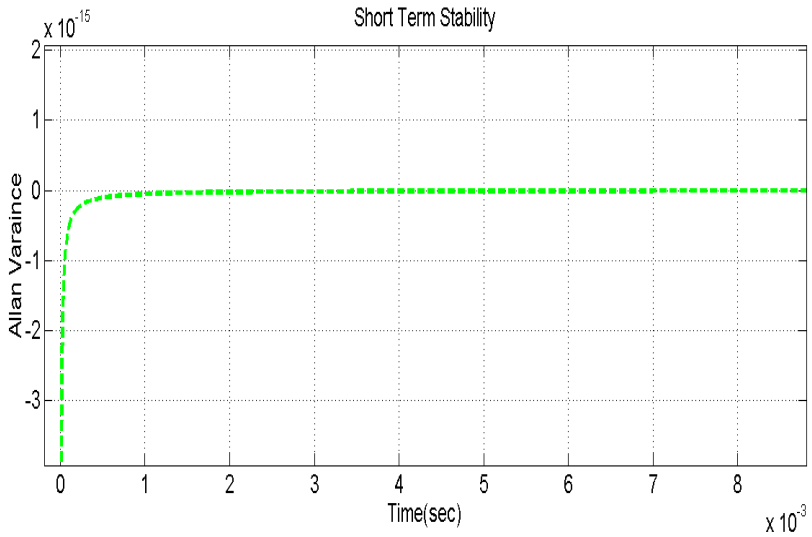

Figure A.31: Short term stability of IOEO using Okamoto model of IOMR (MATLAB result)

A.4 ABCD Matrix Methodology for the Band Pass Filter

The ABCD parameters are also known as transmission matrix parameters. The ABCD parameters are used to cascade the circuit elements. The ABCD parameters for the series and shunt elements of the circuit are defined as follows:

$$\begin{pmatrix} A_{series} & B_{series} \\ C_{series} & D_{series} \end{pmatrix} = \begin{pmatrix} 1 & Z \\ 0 & 1 \end{pmatrix} \tag{A.1}$$

and

$$\begin{pmatrix} A_{shunt} & B_{shunt} \\ C_{shunt} & D_{shunt} \end{pmatrix} = \begin{pmatrix} 1 & 0 \\ \frac{1}{Z} & 1 \end{pmatrix} \tag{A.2}$$

Where, Z is the impedance of the element. The designed BPF shown in Figure 3.22 (refer section 3.3.7) has five elements. The cascading properties of the ABCD parameters have been used to derive the voltage transfer function of the BPF. The BPF as shown in Figure 3.22 has the following elements: Z_A, Z_B, Z_C, Z_D and Z_E. The five elements are defined as: $Z_A = \frac{1}{j\omega 2C_{11}}$, $Z_C = \frac{1}{j\omega 2C_{11}} + \frac{j\omega L_{22}}{2}$, $Z_D = \frac{1}{j\omega C_{22}}$, $Z_B = j\omega L_{11}$ and $Z_E = \frac{j\omega L_{22}}{2}$.

The system ABCD parameters of the Figure 3.22 has been calculated as follows.

$$\begin{pmatrix} A_{BPF} & B_{BPF} \\ C_{BPF} & D_{BPF} \end{pmatrix} = \begin{pmatrix} 1 & Z_A \\ 0 & 1 \end{pmatrix} * \begin{pmatrix} 1 & 0 \\ \frac{1}{Z_B} & 1 \end{pmatrix} * \begin{pmatrix} 1 & Z_c \\ 0 & 1 \end{pmatrix} * \begin{pmatrix} 1 & 0 \\ \frac{1}{Z_D} & 1 \end{pmatrix} * \begin{pmatrix} 1 & Z_E \\ 0 & 1 \end{pmatrix} \tag{A.3}$$

$$\begin{pmatrix} A_{BPF} & B_{BPF} \\ C_{BPF} & D_{BPF} \end{pmatrix} = \begin{pmatrix} 1+\frac{Z_A}{Z_B} & Z_A \\ \frac{1}{Z_B} & 1 \end{pmatrix} * \begin{pmatrix} 1 & Z_c \\ 0 & 1 \end{pmatrix} * \begin{pmatrix} 1 & 0 \\ \frac{1}{Z_D} & 1 \end{pmatrix} * \begin{pmatrix} 1 & Z_E \\ 0 & 1 \end{pmatrix} \tag{A.4}$$

$$\begin{pmatrix} A_{BPF} & B_{BPF} \\ C_{BPF} & D_{BPF} \end{pmatrix} = \begin{pmatrix} 1+\frac{Z_A}{Z_B} & Z_C(1+\frac{Z_A}{Z_B})+Z_A \\ \frac{1}{Z_B} & \frac{Z_C}{Z_B}+11 \end{pmatrix} * \begin{pmatrix} 1 & 0 \\ \frac{1}{Z_D} & 1 \end{pmatrix} * \begin{pmatrix} 1 & Z_E \\ 0 & 1 \end{pmatrix} \tag{A.5}$$

$$\begin{pmatrix} A_{BPF} & B_{BPF} \\ C_{BPF} & D_{BPF} \end{pmatrix} = \begin{pmatrix} 1+\frac{Z_A}{Z_B}+\frac{1}{Z_D}(Z_C+\frac{Z_CZ_A}{Z_B}+Z_A) & Z_C(1+\frac{Z_A}{Z_B})+Z_A \\ \frac{1}{Z_B}+\frac{1}{Z_D}(\frac{Z_C}{Z_B}+1) & \frac{Z_C}{Z_B}+1 \end{pmatrix} * \begin{pmatrix} 1 & Z_E \\ 0 & 1 \end{pmatrix} \tag{A.6}$$

Let $T1 = 1+\frac{Z_A}{Z_B}+\frac{1}{Z_D}(Z_C+\frac{Z_CZ_A}{Z_B}+Z_A)$, $T2 = Z_C(1+\frac{Z_A}{Z_B})+Z_A$,
$T3 = \frac{1}{Z_B}+\frac{1}{Z_D}(\frac{Z_C}{Z_B}+1)$, and $T4 = \frac{Z_C}{Z_B}+1$.
Then the ABCD parameters of the BPF can be rewritten as

$$\begin{pmatrix} A_{BPF} & B_{BPF} \\ C_{BPF} & D_{BPF} \end{pmatrix} = \begin{pmatrix} T1 & Z_E[T1]+T2 \\ T3 & Z_E[T3]+T4 \end{pmatrix} \tag{A.7}$$

From the ABCD parameters of BPF, the $\frac{1}{A_{BPF}}$ is defined as the voltage transfer function of the BPF.

A.5 Beam Steering using the Designed IOEO

This section discusses the beam steering using the designed IOEO. The conditions for the beam steering of 0.5^0, 1^0, 2^0 and 4^0 have been shown in Table A.1. The SMF1, SMF2, SMF3 and SMF4 are the Single Mode Fiber used before each photo diode (refer Figure 6.3) in the designed IOEO. The corresponding time delay required to achieve the beam steering of 0.5^0, 1^0, 2^0 and 4^0 is also listed in Table A.1.

Table A.1: Additional length of SMF required for beam steering with designed IOEO

S.No.	SMF1 (km)	SMF2 (km)	SMF3 (km)	SMF4 (km)	Relative Time Delay (ps)	Beam Steering (Degree)
1	0.005	0.125	0.250	0.375	2	0.5
2	0.005	0.250	0.500	0.750	4	1
3	0.005	0.500	1	1.5	8	2
4	0.005	1	2	3	16	4

The amplitude time response of all the photo diodes for 1^0 phase shift (4 ps time difference) is shown in Figures A.32, A.33, A.34 and A.35 respectively. Figures A.36, A.37 and A.38 depict the expanded view of output of beamformer with 4 antenna elements for the relative time delay of 4 ps, 8 ps and 16 ps respectively.

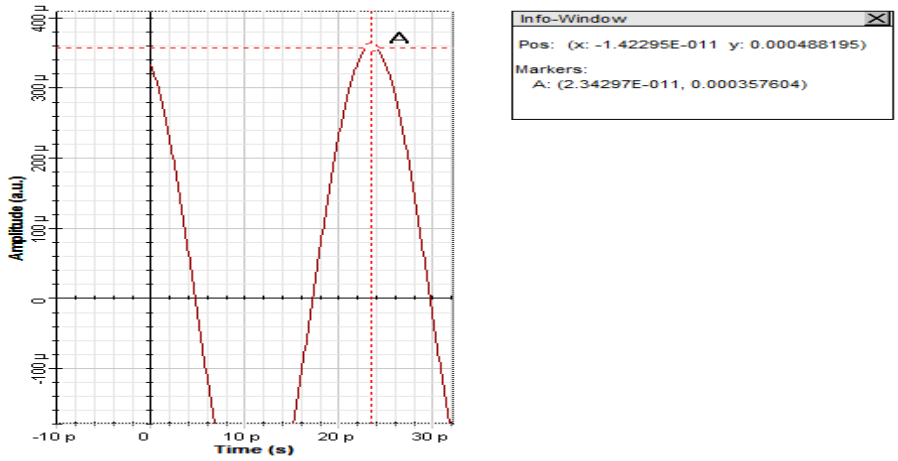

Figure A.32: Amplitude time response of first photo diode using Optisystem version 7.0

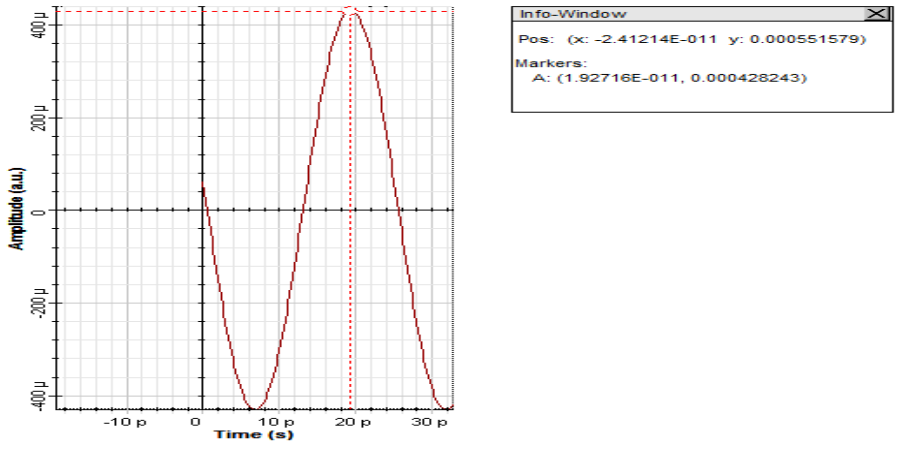

Figure A.33: Amplitude time response of second photo diode using Optisystem version 7.0

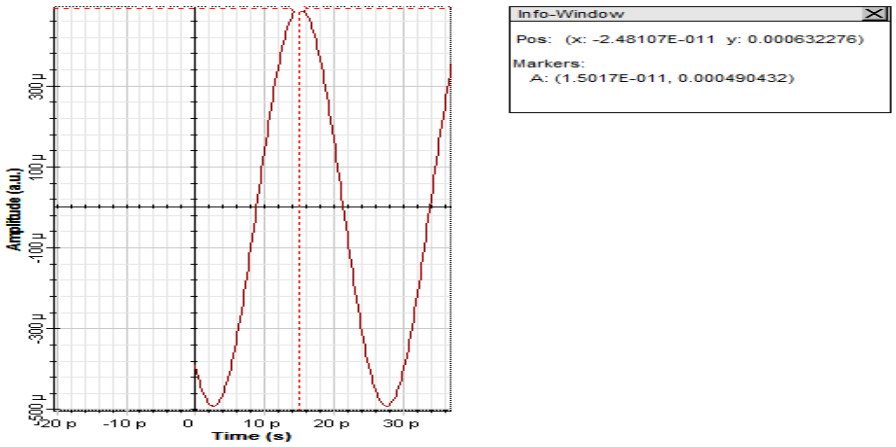

Figure A.34: Amplitude time response of third photo diode using Optisystem version 7.0

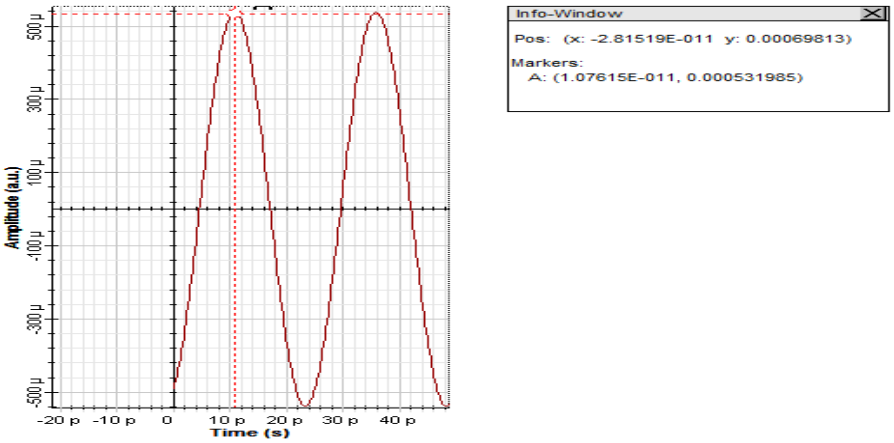

Figure A.35: Amplitude time response of fourth photo diode using Optisystem version 7.0

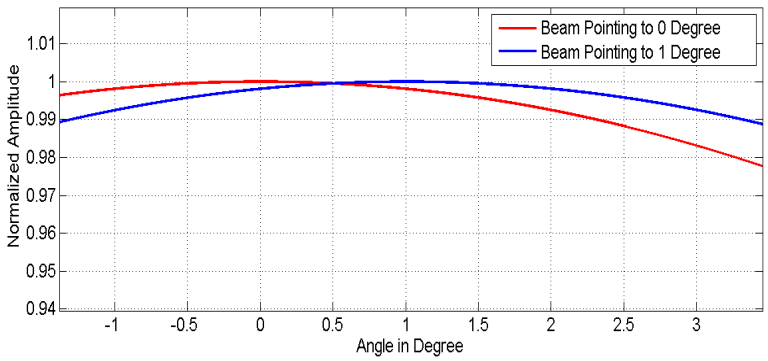

Figure A.36: Expanded view of beam pointing at 1^0 using MATLAB version 7. 12 (R2011a)

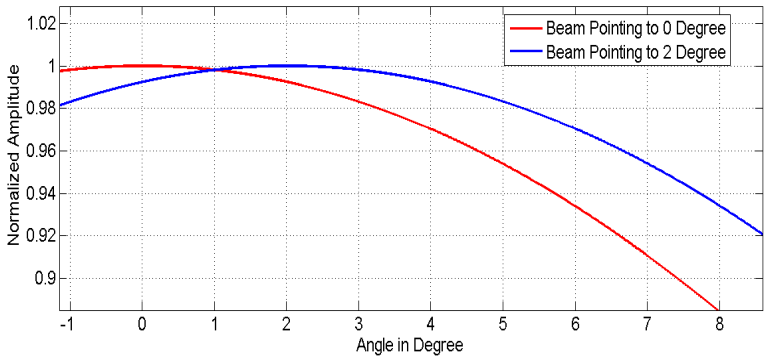

Figure A.37: Expanded view of beam pointing at 2^0 using MATLAB version 7. 12 (R2011a)

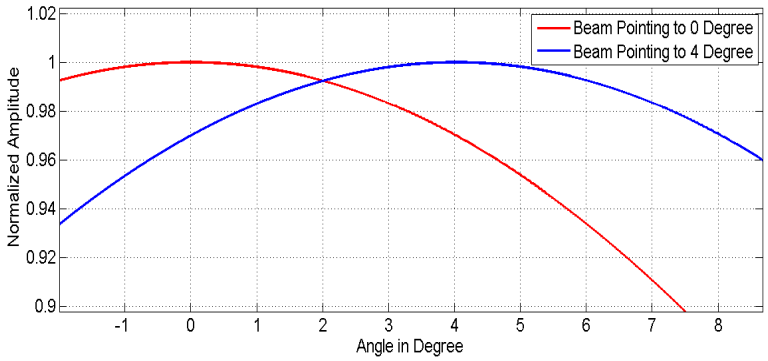

Figure A.38: Expanded view of beam pointing at 4^0 using MATLAB version 7. 12 (R2011a)

A.6 Simulation Model of Band Pass Filter with ADS version 2011.01

The Band Pass Filter as shown in Figure 3.26 has been simulated with ADS version 2011.01 environment. The schematic of the simulated BPF is shown in Figures A.39 and A.40.

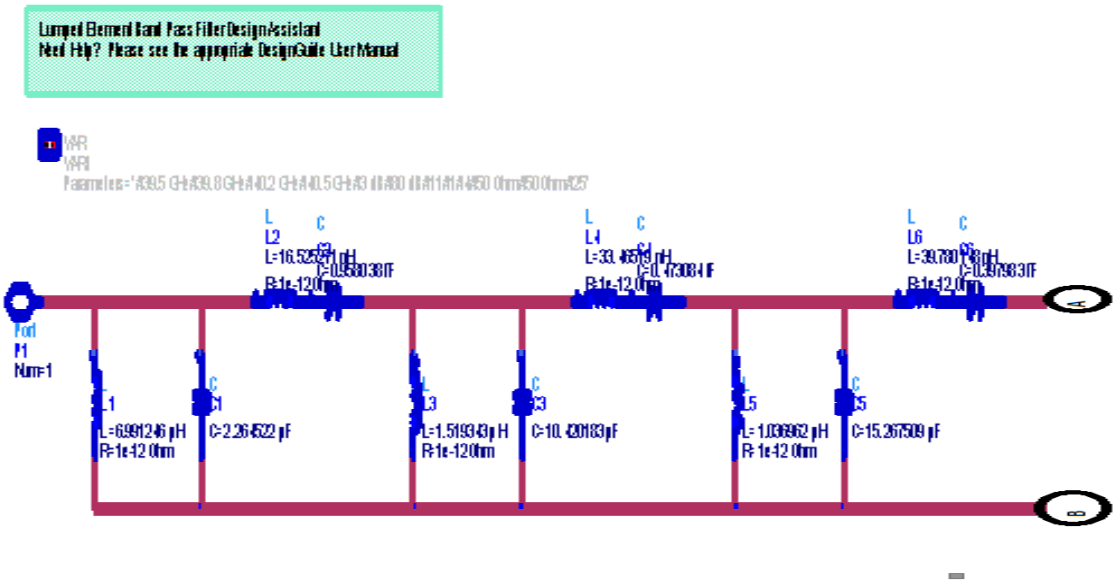

Figure A.39: Schematic of BPF using ADS version 2011.01

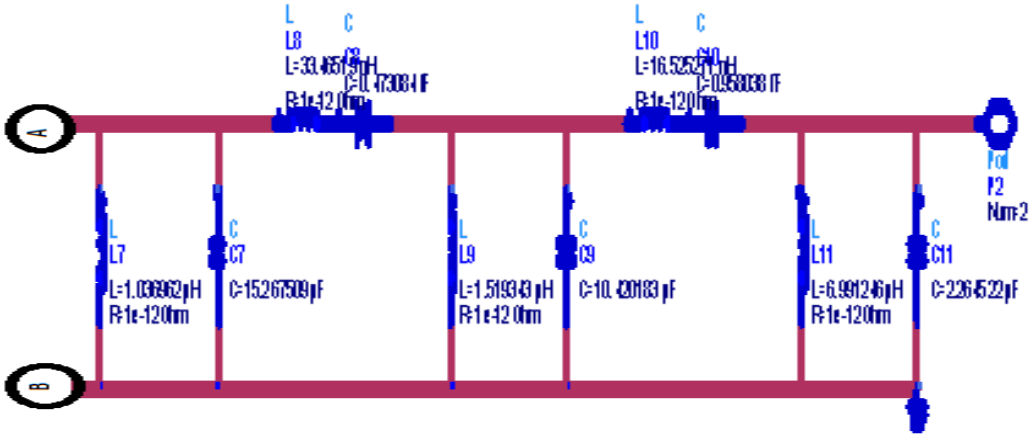

Figure A.40: Schematic of BPF using ADS version 2011.01

A.7 Feasibility of Fabrication of Capacitance and Inductance in BPF

This section discusses the fabrication of the 0.395 fF capacitance and 1.0369 pH inductance of the BPF. The minimum microstrip line length of the existing multilayer PCB is 0.003 inch or 0.0762 mm (Shenzhen Xinchenger Electronic, n.d.). For the dielectric thickness (FR-4 material) of 0.3 mm (Best Technology, n.d.) and the microstrip line width of 0.0762, the effective dielectric constant (ε_{eff}) is found to be 2.841 (Pozar, 2009) using Equation

(A.8).

$$\varepsilon_{eff} = \frac{\varepsilon_r + 1}{2} + \frac{\varepsilon_r - 1}{2} \times \frac{1}{\sqrt{1 + 12\frac{h4}{w4}}} \tag{A.8}$$

Where, ε_r=4.22 (dielectric constant of FR-4 material), $h4$ is the height of the dielectric medium and $w4$ is the width of the conducting transmission line (microstrip line). The least inductance possible with the existing minimum length for the microstrip line is calculated as follows;

$$Z_{in} = Z_0 \tan \frac{2\pi\sqrt{\varepsilon_{eff}}ll}{\lambda} \tag{A.9}$$

Where, Z_{in} is the input impedance, Z_0 is the characteristic impedance, λ is the wavelength, $\sqrt{\varepsilon_{eff}}$ is the effective dielectric constant of the medium and ll is the length of the microstripline.

The Equation (A.9) is written as:

$$2\pi f L_{least} = Z_0 \tan \frac{2\pi\sqrt{\varepsilon_{eff}}ll}{\lambda} \tag{A.10}$$

$$L_{least} = \frac{Z_0}{2\pi f} \tan \frac{2\pi\sqrt{\varepsilon_{eff}}ll}{\lambda} \tag{A.11}$$

Given, λ=7.5 mm at 40 GHz, ε_{eff}=2.841, Z_0=50 ohm and ll=0.0762 mm, one gets

$$L_{least} = \frac{50}{2\pi 40 \times 10^9} \tan \frac{2\pi\sqrt{2.841} \times 0.0762}{7.5} \tag{A.12}$$

The computed value of L_{least} (manufacturable minimum inductance) is 0.3754 pH.

Similarly, the least capacitance possible with the existing minimum length for the microstrip line is calculated as follows;

$$\frac{1}{2\pi f C_{least}} = Z_0 cot \frac{2\pi\sqrt{\varepsilon_{eff}}ll}{\lambda} \tag{A.13}$$

The Equation (A.13) is written as:

$$\frac{1}{C_{least}} = 2\pi f Z_0 cot \frac{2\pi\sqrt{\varepsilon_{eff}}ll}{\lambda} \tag{A.14}$$

Given, λ=7.5 mm at 40 GHz, ε_{eff}=2.841, Z_0=50 ohm and ll=0.0762 mm, one gets

$$\frac{1}{C_{least}} = 2\pi 40 \times 10^9 \times 50 cot \frac{2\pi\sqrt{2.841} \times 0.0762}{7.5} \tag{A.15}$$

The computed value of C_{least} (manufacturable minimum capacitance) is 0.1494 fF.

APPENDIX B

RESEARCH PUBLICATIONS RELATED TO THESIS

B.1 Research publications

Research publication associated with the thesis

- Roy, U. M., Malathi, S., and Kadambi, G. R. (2013) 'Analytical study on the Butt-coupling co-efficient for the Optical Micro-Ring Resonator'. *In Workshop on Recent Advances in Photonics (WRAP)*, p. 1-2, IEEE

Poster presentation associated with the thesis

- Roy, U. M., Malathi, S., Kadambi G. R., and Vershinin Y. (2015) 'Design and Analysis of an Integrated Opto- Electronic Oscillator Based Biosensor'. *International Conference On Optics and Photonics 2015*: held 20-22 February 2015 at University of Calcutta, India

REFERENCES

AMONICS (n.d.) *Standard EDFA*[online] available from<http://www.amonics.com/ amonics/php /en/products-details.php?id=149>[23 August 2017]

Banky, T., Horvath, B., and Berceli, T. (2006) 'Optimum configuration of multiloop optoelectronic oscillators'. *JOSA B*, 23(7), 1371–1380

Best Technology (n.d.)*Extra Thin PCB*[online]available from<http://www.bestpcbs.com /products/ extra-thin-pcb.htm>[08 August 2017]

Binh, L. N. (2008) *Photonic Signal Processing: Techniques and Applications.* London: CRC Press

Burla, M., Khan, M., Zhuang, L., and Roeloffzen, C. (2008) 'Multiwavelength optical beam Forming network with ring resonator-based binary-tree architecture for broadband phased array antenna systems'. *IEEE/LEOS Benelux Symposium*, 99–102

Chang, D., Fetterman, H., Erlig, H., Zhang, H., Oh, M., Zhang, C., and Steier, W. (2002)'39-GHz optoelectronic oscillator using broad-band polymer electrooptic modulator'. *Photonics Technology Letters, IEEE*, 14(2), 191–193

Chembo, Y. K., Volyanskiy, K., Larger, L., Rubiola, E., and Colet, P. (2009) 'Determination of phase noise spectra in optoelectronic microwave oscillators: a Langevin approach'. *Quantum Electronics, IEEE Journal of* , 45(2), 178–186

Chenakin, A. (2009) 'Phase noise reduction in microwave oscillators'. *Microw. J*, 52,124–140

Chou, H.-F., Chiu, Y.-J., and Bowers, J. (2002) '40 GHz optical pulse generation using sinusoidally-driven travelling-wave electroabsorption modulator'. *Electronics Letters*, 38(8), 379–380

Davidson, T., Goldgeier, P., Eisenstein, G., and Orenstein, M. (1999) High spectralpurity CW oscillation and pulse generation in optoelectronic microwave oscillator. *Electronics Letters*, 35(15), 1260–1261

Demir, A. (2002) 'Phase noise and timing jitter in oscillators with colored-noise sources'. *Circuits and Systems I: Fundamental Theory and Applications, IEEE Transactions on*, 49(12), 1782–1791

Desai R. Dr. (2014)*SMBG SELF MONITORING (MEASUREMENT) OF BLOOD GLUCOSE (SMBG)*[online] available from<http://drrajivdesaimd.com/2014/11/01/self-monitoring-measurement-of-bloodglucose-smbg/>[12 August 2017]

Devgan, P. (2013) 'A review of optoelectronic oscillators for high speed signal processing applications'. *International Scholarly Research Notices Electronics* Article ID 401969, http://dx.doi.org/10.1155/2013/401969

Devgan, P., Lasri, J., Tang, R., and Kumar, P. (2003) 'Ultra-low-jitter multiwavelength synchronised optical pulse source for C-, L-and U-bands'. *Electronics Letters*, 39(18), 1337–1339

Devgan, P. S., Urick, V. J., McKinney, J. D., and Williams, K. J. (2007). 'A low-jitter master-slave optoelectronic oscillator employing all-photonic gain'. *In Microwave Photonics, 2007 IEEE International Topical Meeting on* (pp. 70–73)

Devgan, P. S., Urick, V. J., and Williams, K. J. (2012) 'Detection of low-power RF signals using a two laser multimode optoelectronic oscillator'. *Photonics Technology Letters, IEEE*, 24(10), 857–859

De Vos, K., Bartolozzi, I., Schacht, E., Bienstman, P., and Baets, R. (2007) 'Silicon-on-Insulator microring resonator for sensitive and label-free biosensing'. *Optics express*, 15(12), 7610–7615

Dorren, H., Hill, M., Liu, Y., Tangdiongga, E., Smit, M., and Khoe, G. (2005) 'Optical signal processing and telecommunication applications'. *In Optical Amplifiers and Their Applications, Technical Digest (CD) (Optical Society of America)*, paper WD1

Duy, N. L., Journet, B., Ledoux-Rak, I., Zyss, J., Nam, L. V. H., and Luc, V. V. (2008)'Opto-Electronic oscillator: applications to sensors'. *In Microwave photonics, 2008. Jointly held with the 2008 asia-pacific microwave photonics conference. mwp/apmp 2008. International topical meeting on* (pp. 131–134)

Edson, W. A. (1960) 'Noise in oscillators'. *Proceedings of the IRE*, 48(8), 1454–1466

Einstein, A. (1905) 'The photoelectric effect'. *Ann. Phys*, 17(132), 4

Enablence (n.d.) *PDCS12T 40 Gb/s InGaAs PHOTODIODE*[online] available from<http://www.enablence.com/media/mediamanager/pdf/30-enablence-datasheet-ocsd-pd-pin1310-1550-pdcs12t-40gbs-ingaas.pdf>[23 August 2017]

Fallahkhair, A. B., Li, K. S., and Murphy, T. E. (2008) 'Vector finite difference modesolver for anisotropic dielectric waveguides'. *Journal of Lightwave Technology*, 26(11), 1423–1431

Farago, P. S. (1961) *An Introduction to Linear Network Analysis.* London: English Universities Press

Fukuchi, K. (2001) '10.92-Tb/s (273 X 40-Gb/s) triple-band/ultra-dense WDM Optical repeatered transmission experiment'. *In Optical Fiber Communication Conference. Optical Society of America,* p. PD24

Ghosh, S. (2005) *Network Theory: Analysis and Synthesis.* New Delhi: Prentice-Hall of India

GLOBALFOUNDRIES (2016) *22 nm FD-SOI Platform*[online] available from<http://www.globalfoundries.com/sites/default/files/brochure/22fdx-product-overview.pdf>[23 August 2017]

Guider, R., Gandolfi, D., Chalyan, T., Pasquardini, L., Samusenko, A., Pucker, G., . . .Pavesi, L. (2015) 'Design and Optimization of SiON Ring Resonator-Based Biosensors for Aflatoxin M1 Detection'. *Sensors*, 15(7), 17300–17312

Gunn, C., Guckenberger, D., Pinguet, T., Gunn, D., Eliyahu, D., Mansoorian, B., . . .Salminen, O. (2007) 'A low phase noise 10 GHz optoelectronic RF oscillator implemented using CMOS photonics'. *In Solid-State Circuits Conference, 2007. ISSCC 2007. Digest of Technical Papers. IEEE International* (pp. 570–622)

Gunn, D., Henderson, M., Ilchenko, V., Kossakovski, D. A., and Morozov, N. (2007, August 21) *Integrated Opto-Electronic Oscillators. Google Patents*. (US Patent 7,260,279)

Guo, W., Xu, F., and Lu, Y.-q. (2012) 'Coupling influence on the refractive index sensitivity of photonic wire ring resonator'. *Optics Communications*, 285(24), 5144–5147

Hajimiri, A., and Lee, T. H. (1998) 'A general theory of phase noise in electrical oscillators'. *Solid-State Circuits, IEEE Journal of* , 33(2), 179–194

Ham, D., Andress, W., and Ricketts, D. (2004) 'Phase noise in oscillators'. *In International Workshop on SiP/SoC Integration of MEMS and Passive Components with RF-ICs, available at http://www. usl. chibau. ac. jp/ken/Symp2004/PDF/1C3. pdf*

Hardy, A., and Streifer, W. (1985) 'Coupled mode theory of parallel waveguides'. *Journal of lightwave technology*, 3(5), 1135–1146

Haus, H., Huang, W.-P., Kawakami, S., and Whitaker, N. (1987) 'Coupled-mode theory Of optical waveguides'. *Lightwave Technology, Journal of* , 5(1), 16–23

Haus, H. A., and Huang, W. (1991a) 'Coupled-mode theory'. *Proceedings of the IEEE*, 79(10), 1505–1518

He, J.-J. (2012) 'Intensity Interrogated Planar Waveguide Biosensors'. *In Information Optoelectronics, Nanofabrication and Testing* (pp. IF3B–1)

Huang,W., and Haus, H. A. (1991b) 'A simple variational approach to optical rib Waveguides'. *Journal of lightwave technology*, 9(1), 56–61

Hunsperger, R. G., Yariv, A., and Lee, A. (1977) 'Parallel end-butt coupling for optical integrated circuits'. *Applied optics*, 16(4), 1026–1032

iXblue (n.d.) *Lithium Niobate Electro Optic Modulator : Intensity Modulators*[online] available from<https://photonics.ixblue.com/product-detail/mxan-ln-40>[08 August 2017]

Jalil, M. A., Amiri, I. S., Teeka, C., Ali, J., and Yupapin, P. (2011) 'All-optical logic XOR/XNOR gate operation using microring and nanoring resonators'. *Global Journal of Physics Express*, 1(1), 15–22

Ji, Y., Yao, X., and Maleki, L. (1999) 'Compact optoelectronic oscillator with ultra-low phase noise performance'. *Electronics Letters*, 35(18), 1554–1555

Jauch (n.d.) *Quartz Crystal Theory*[online] available from<http://www.jauch.de/ downloadfile /5804d138f41b5 c3e35434e616a6a82bd5/quartz crystal theory 2007.pdf>[23 August 2017]

Jiang, L. A., Grein, M. E., Ippen, E. P., McNeilage, C., Searls, J., and Yokoyama, H. (2002) 'Quantum-limited noise performance of a mode-locked laser diode'. *Optics letters*,27(1), 49–51

Keiser, G. (2013) *Optical Fiber Communications.* Chennai: McGraw Hill Education

Khare, R. (2004) *Fiber Optics and Optoelectronics.* New Delhi:Oxford University Press.

Kitching, J., Knappe, S., and Hollberg, L. (2002) 'Miniature vapor-cell atomic-frequency references'. *Applied Physics Letters*, 81(3), 553–555

Kominato, T., Ohmori, Y., Takato, N., Okazaki, H., and Yasu, M. (1992) 'Ring resonators composed of GeO2-doped silica waveguides'. *Lightwave Technology, Journal of*, 10(12), 1781–1788

Kouomou Chembo, Y., Larger, L., Tavernier, H., Bendoula, R., Rubiola, E., and Colet, P. (2007) 'Dynamic instabilities of microwaves generated with optoelectronic oscillators'. *Optics letters*, 32(17), 2571–2573

Lasri, J., Devgan, P., Tang, R., and Kumar, P. (2003) 'Self-starting optoelectronic Oscillator for generating ultra-low-jitter high-rate (10GHz or higher) optical pulses'. *Optics express*, 11(12), 1430–1435

Laughton, M. A., and Say, M. G. (2013) *Electrical Engineers Reference Book.* Elsevier Inc

Lee, K.-H., Kim, J.-Y., and Choi, W.-Y. (2008) 'Injection-locked hybrid optoelectronic oscillators for single-mode oscillation'. *IEEE Photon. Technol. Lett*, 20(19), 1645–1647

Leeson, D. B. (1966) 'A simple model of feedback oscillator noise spectrum'. *Proceedings of the IEEE*, 329–330

Leviton, D. B., and Frey, B. J. (2006) 'Temperature-dependent absolute refractive index measurements of synthetic fused silica'. *In SPIE Astronomical Telescopes + Instrumentation* (pp. 62732K62732K)

Li, C., Chen, F., and Zhang, J. (2015) 'A tunable optoelectronic oscillator based on single sideband modulation and stimulated Brillouin scattering'. *In Computational Intelligence and Virtual Environments for Measurement Systems and Applications (CIVEMSA), 2015 IEEE International Conference on* (pp. 1–3)

Liu, B., Shakouri, A., and Bowers, J. E. (2001) 'Passive microring-resonator-coupled lasers'. *Applied physics letters*, 79(22), 3561–3563

Liu, X., Pan, W., Zou, X., Luo, B., Yan, L., and Lu, B. (2012) 'A reconfigurable Opto-electronic oscillator based on cascaded coherence-controllable recirculating delay lines'. *Optics express*, 20(12), 13296–13301

Liu, Y., Chang, T., and Craig, A. E. (2005) 'Coupled mode theory for modeling microring resonators'. *Optical Engineering*, 44(8), 084601–084601

Liu, Y., Hering, P., and Scully, M. (1992) 'An integrated optical sensor for measuring glucose concentration'. *Applied Physics B*, 54(1), 18–23

Lu, D., Pan, B., Chen, H., and Zhao, L. (2015) 'Frequency-tunable optoelectronic oscillator using a dual-mode amplified feedback laser as an electrically controlled active microwave photonic filter'. *Optics letters*, 40(18), 4340–4343

Mal, P., Patel, P. D., and Beyette, F. R. (2009) 'Design and demonstration of a fully integrated multi-technology FPGA: a reconfigurable architecture for photonic and other multi-technology applications'. *IEEE Transactions on Circuits and Systems I:Regular papers*, 56(6), 1182–1191

Malathi, S., Mangal, N., Samad, S. A., Honnungar, R. V., and Srinivas, T. (2011) 'SOI strip waveguide microring resonator for homogeneous biosensing'. *In SPIE Optical Engineering+ Applications* (pp. 81290B–81290B)

Maleki, L., Seidel, D., Ilchenko, V., Eliyahu, D., Savchenkov, A., and Matsko, A. (2015,March 10) *Tunable Opto-Electronic Oscillator having Optical Resonator Filter Operating at Selected Modulation Sideband*. Google Patents. (US Patent 8,976,822)

Marcuse, D. (1971) 'The coupling of degenerate modes in two parallel dielectric waveguides'. *Bell System Technical Journal*, 50(6), 1791–1816

Matsko, A., Maleki, L., Savchenkov, A., and Ilchenko, V. (2003) 'Whispering gallery mode based optoelectronic microwave oscillator'. *Journal of modern optics*, 50(15-17), 2523–2542

Matsko, A. B., and Ilchenko, V. S. (2006) Optical resonators with whispering gallery modes I: basics. *IEEE J. Sel. Top. Quantum Electron*, 12(3)

McManamon, P. (2009) 'Conformal EO aperture array based lasers systems'. *In Aerospace & electronics conference (naecon), proceedings of the IEEE 2009 national* (pp. 1–80)

McNeill, J. A. (1997) 'Jitter in ring oscillators'. *Solid-State Circuits, IEEE Journal of*, 32(6), 870–879

Meijerink, A., Roeloffzen, C., Zhuang, L., Marpaung, D., Heideman, R., Borreman, A., and van Etten, W. (2007) 'Optical beam forming for phased-array antennas'. *Fotonica magazine* 31(4), 5–9

Merrer, P.-H., Llopis, O., and Cibiel, G. (2008). 'Laser stabilization on a fiber ring Resonator and application to RF filtering'. *IEEE Photonics Technology Letters*, 20(16), 1399–1401

Miller, P. (2007) 'K_a-Band the future of satellite communication?'. *TELE-satellite & Broadband*, 1(9), 12–14

Millman, J., and Halkias, C. C. (1972)*Integrated Electronics: Analog and Digital Circuits and Systems.* Mcgraw-Hill (Tx)

Nguyen, L. D., Nakatani, K., and Journet, B. (2010) 'Refractive index measurement by using an optoelectronic oscillator'. *Photonics Technology Letters, IEEE*, 22(12), 857–859

Odyniec, M. (1999) 'Oscillator stability analysis'. *Microwave Journal*, 42(6), 6

OEwaves (n.d.) *Advanced Opto Electronic Oscillator*[online] available from<https://www.oewaves.cohttp://www.oewaves.com/ advanced-oeo-sp-1171610647>[23 August 2017]

Ohuchi, W., Chujo, W., Fujino, Y., and Koyamada, Y. (2007) '40 GHz phase shift experiments of WDM-based optically controlled transmitting array antenna'. *In Proc. 2007 International Symposium on Antenna and Propagation, ISAP2007*, 4B31 (pp. 1266–1269)

Okamoto, K. (2010) *Fundamentals of Optical Waveguides.* Academic press

Ozdur, I., Akbulut, M., Hoghooghi, N., Mandridis, D., Piracha, M. U., and Delfyett, P. J.(2010) 'Optoelectronic loop design with 1000 finesse Fabry-Perot etalon'. *Optics letters*, 35(6), 799–801

Pan, S., and Yao, J. (2009) 'A frequency-doubling optoelectronic oscillator using a polarization modulator'. *Photonics Technology Letters, IEEE*, 21(13), 929–931

Pan, S., and Yao, J. (2010) 'Wideband and frequency-tunable microwave generation Using an optoelectronic oscillator incorporating a FabryPerot laser diode with External optical injection'. *Optics letters*, 35(11), 1911–1913

Perez Serna, E., Thombre, S., Valkama, M., Lohan, S., Syrjala, V., Detratti, M. and Nurmi, J. (2010) 'Local oscillator phase noise effects on GNSS code tracking'. *InsideGNSS*

Pham, T. T., Ledoux-Rak, I., Journet, B., and Vu, V. Y. (2015) 'A new technique to monitor the long-term stability of an optoelectronic oscillator'. *In Photonics Prague* 2014 (pp. 94500C–94500C)

Photonics Research Laboratory (n.d.) *WGMODES*[online] available from <https://www.photonics.umd.edu/software/wgmodes/>[06 July 2017]

Pierce, J., and Tien, P. K. (1954) 'Coupling of modes in helixes'. *Proceedings of the IRE*,42(9), 1389–1396

Pollock, C. R., and Lipson, M. (2003) *Integrated Photonics.* Springer

Pozar, D. M. (2009) *Microwave Engineering.* USA: John Wiley & Sons

Quan, H., and Guo, Z. (2005) 'Simulation of whispering-gallery-mode resonance shifts for optical miniature biosensors'. *Journal of Quantitative Spectroscopy and Radiative Transfer*, 93(1), 231–243

Quan, H., Guo, Z., Xu, L., and Pau, S. (2005) 'Design, fabrication, and characterization of whispering-gallery mode miniature sensors'. *In Optics East* (pp. 373–381)

Rabus, D. G. (2002) *Realization of optical filters using ring resonators with integrated semiconductor optical amplifiers in GaInAsP/InP.* Unpublished doctoral dissertation. Berlin: Technische Universitt

Rao, M., Chen, Q., Shi, H., and Varghese, T. (2006) 'Spatial-angular compounding for elastography using beam steering on linear array transducers'. *Medical physics*,33(3), 618–626

Raytheon RF Components (2002) *LNA Low Noise Amplifier MMIC*[online]available from<https://https://www.digchip.com/datasheets/parts/datasheet/395/RMLA31400.php>[23 August 2017]

Reed, G. T., and Knights, A. P. (2004) *Silicon Photonics: An Introduction.* John Wiley & Sons

Renk, K. F. (2012) 'FabryPerot Resonator'. *In Basics of laser physics* (pp. 43–54). Springer

Righini, G., Dumeige, Y., Feron, P., Ferrari, M., Nunzi Conti, G., Ristic, D., and Soria, S. (2011) 'Whispering gallery mode microresonators: fundamentals and applications'. *Rivista del Nuovo Cimento*, 34(7), 435

Romisch, S., Kitching, J., Ferr'e-Pikal, E., Hollberg, L., and Walls, F. L. (2000) 'Performance evaluation of an optoelectronic oscillator'. *Ultrasonics, Ferroelectrics and Frequency Control, IEEE Transactions on*, 47(5), 1159–1165

Rouger, N., Chrostowski, L., and Vafaei, R. (2010) 'Temperature effects on silicon- Oninsulator (SOI) racetrack resonators: A coupled analytic and 2-D finite difference approach'. *Journal of Lightwave Technology*, 28(9), 1380–1391

Rubiola, E. (2008) *Phase Noise and Frequency Stability in Oscillators.* New York: Cambridge University Press

Sadiku, M. N. O. (2009) *Principles of Electromagnetics.* New Delhi: Oxford University Press

Sakamoto, T., Kawanishi, T., and Izutsu, M. (2006) 'Optoelectronic oscillator using a LiNbO3 phase modulator for self-oscillating frequency comb generation'. *Optics letters*, 31(6), 811–813

Sakamoto, T., Kawanishi, T., and Izutsu, M. (2007) 'Optoelectronic oscillator employing reciprocating optical modulator for millimetre-wave generation'. *Electronics Letters*, 43(19), 1031–1033

Saleh, K., Merrer, P.-H., Llopis, O., and Cibiel, G. (2012) 'Optoelectronic oscillator based on fiber ring resonator: overall system optimization and phase noise reduction'. *In IEEE International Frequency Control Symposium (IFCS 2012)* (p. 6p)

Salik, E., Yu, N., and Maleki, L. (2007) 'An ultralow phase noise coupled optoelectronic oscillator'. *Photonics Technology Letters, IEEE*, 19(6), 444–446

Salik, E., Yu, N., Tu, M., and Maleki, L. (2004) 'EDFA-based coupled Opto-Electronic oscillator and its phase noise'.*In Optical Fiber Communication Conference* (p. FB6)

Sauvage, G. (1977) 'Phase noise in oscillators: A mathematical analysis of Leesons model'. *IEEE Trans. Instrum. Meas*, 26(4), 408–410

Savchenkov, A., Ilchenko, V., Byrd, J., Liang, W., Eliyahu, D., Matsko, A., . . . Maleki, L.(2010) 'Whispering-gallery mode based Opto-Electronic oscillators'. *In Frequency Control Symposium (FCS), 2010 IEEE International* (pp. 554–557)

Schweinsberg, A., Hocde, S., Lepeshkin, N. N., Boyd, R. W., Chase, C., and Fajardo, J.E.(2007) 'An environmental sensor based on an integrated optical whispering gallery mode disk resonator'. *Sensors and Actuators B: Chemical*, 123(2), 727–732

Shenzhen Xinchenger Electronic (n.d.)*PCBAC Printed Circuit Board Assembly Capabilities*[online] available from<http://www.fr4-pcb.com/pcbassembly-capabilities>[23 August 2017]

Shin, M., Devgan, P. S., Grigoryan, V. S., Kumar, P., Chung, Y.-D., and Kim, J. (2006)'Low phase-noise 40 GHz optical pulses from a self-starting electroabsorption modulator-based optoelectronic oscillator'. *In Optical Fiber Communication Conference* (p. OFB1)

Shin, M., and Kumar, P. (2007a) 'Millimeter-wave generation via frequency quadrupling in an optically-injected optoelectronic oscillator'. *In Optical Fiber Communication Conference* (p. OWN7)

Shin, M., and Kumar, P. (2007b) 'Optical microwave frequency up-conversion via a Frequency-doubling optoelectronic oscillator'. *Photonics Technology Letters, IEEE*,19(21), 1726–1728

Shin, M., and Kumar, P. (2012) 'Frequency up-conversion of optical microwaves for Multichannel optical microwave system on a WDM network'. *Optical Fiber Technology*, 18(4), 242–246

Snyder, A.W. (1972) 'Coupled-mode theory for optical fibers'. *JOSA*, 62(11), 1267–1277.

Steglich, P., Villringer, C., Pulwer, S., Heinrich, F., Bauer, J., Dietzel, B., . . . Schrader, S. (2017) 'Hybrid-Waveguide Ring Resonator for Biochemical Sensing'. *IEEE Sensors Journal*, 17, 4781–47901

Strekalov, D., Aveline, D., Yu, N., Thompson, R., Matsko, A. B., and Maleki, L. (2003) 'Stabilizing an optoelectronic microwave oscillator with photonic filters'. *Journal of lightwave technology*, 21(12), 3052–3061

Sun, Y., and Fan, X. (2011) 'Optical ring resonators for biochemical and chemical sensing'. *Analytical and bioanalytical chemistry*, 399(1), 205–211

Tsuchida, H. (2009) 'Simultaneous prescaled clock recovery and serial-to-parallel Conversion of data signals using a polarization modulator-based optoelectronic oscillator'. *Lightwave Technology, Journal of*, 27(17), 3777–3782

Van Dijk, F., Enard, A., Buet, X., Lelarge, F., and Duan, G.-H. (2008) 'Phase noise Reduction of a quantum dash mode-locked laser in a millimeter-wave coupled Opto-Electronic oscillator'. *Journal of Lightwave Technology*, 26(15), 2789–2794

Vidal, B., Mengual, T., and Mart, J. (2012) 'Fast Optical Beamforming Architectures for Satellite-Based Applications'. *Advances in Optical Technologies*, 2012

Volyanskiy, K., Chembo, Y. K., Larger, L., and Rubiola, E. (2010) 'Contribution of laser frequency and power fluctuations to the microwave phase noise of optoelectronic oscillators'. *Lightwave Technology, Journal of*, 28(18), 2730–2735

Wang, G., Tokumitsu, T., Hanawa, I., Sato, K., and Kobayashi, M. (2002) 'Analysis of high speed PIN photodiode S-parameters by a novel small-signal equivalent circuit model'. *IEEE microwave and wireless components letters*, 12(10), 378–380

X-FAB (n.d.) *0.18μm Process Family*[online] available from<http://www.xfab.com/fileadmin/X-FAB/Download Center/Technology/Datasheet/XT018 Datasheet.pdf>[8 December 2017]

Xie, X., Zhang, C., Sun, T., Guo, P., Zhu, X., Zhu, L., . . . Chen, Z. (2013) 'Wideband tunable optoelectronic oscillator based on a phase modulator and a tunable optical filter'. *Optics letters*, 38(5), 655–657

Xu, Q., and Lipson, M. (2007) 'All-optical logic based on silicon micro-ring resonators'. *Optics Express*, 15(3), 924–929

Yang, B., Jin, X., Chi, H., Zhang, X., Zheng, S., Zou, S., . . . Koonen, T. (2012) 'Optically tunable frequency-doubling brillouin optoelectronic oscillator with carrier phaseshifted double sideband modulation'. *Photonics Technology Letters, IEEE*, 24(12), 1051–1053

Yao, X., Maleki, L., Wu, C., Davis, L., and Forouhar, S. (1998) 'Recent Results With Coupled Opto-Electronic Oscillators'. *Telecommunications and Mission Operations Progress Report*, 135, 1

Yao, X. S. (1997) 'High-quality microwave signal generation by use of Brillouin scattering in optical fibers'. *Optics letters*, 22(17), 1329–1331.

Yao, X. S., Davis, L., and Maleki, L. (2000) 'Coupled optoelectronic oscillators for generating both RF signal and optical pulses'. *Journal of Lightwave Technology*, 18(1), 73

Yao, X. S., and Maleki, L. (1995) 'A novel photonic oscillator'. *TDA Progress Report*,42–122

Yao, X. S., and Maleki, L. (1996a) 'Converting light into spectrally pure microwave oscillation'. *Optics Letters*, 21(7), 483–485

Yao, X. S., and Maleki, L. (1996b) 'Optoelectronic microwave oscillator'. *JOSA B*, 13(8), 1725–1735

Yao, X. S., and Maleki, L. (1997) 'Dual microwave and optical oscillator'. *Optics Letters*, 22(24), 1867–1869

Yao, X. S., and Maleki, L. (2000) 'Multiloop optoelectronic oscillator'. *Quantum Electronics, IEEE Journal of*, 36(1), 79–84

Yariv, A. (1973) 'Coupled-mode theory for guided-wave optics'. *Quantum Electronics, IEEE Journal of*, 9(9), 919–933

Yu, N., Salik, E., and Maleki, L. (2005) 'Ultralow-noise mode-locked laser with coupled optoelectronic oscillator configuration'. *Optics letters*, 30(10), 1231–1233

Zhang, S., Chen, H., and Fu, H. (2015) 'Fiber-optic temperature sensor using an opto-electronic oscillator'. *In Optical Communications and Networks (ICOCN), 2015 14th International Conference on* (pp. 1–3)

Zhou, W., and Blasche, G. (2005) 'Injection-locked dual Opto-Electronic oscillator with ultra-low phase noise and ultra-low spurious level'. *IEEE Transactions on microwave theory and techniques*, 53(3), 929–933

Zhou, W., Okusaga, O., Nelson, C., Howe, D., and Carter, G. (2008) '10 GHz dual loop Opto-Electronic oscillator without RF-amplifiers'. *In Integrated Optoelectronic Devices* 2008 (pp. 68970Z–68970Z)

Zhu, D., Pan, S., Cai, S., and Ben, D. (2012) 'High-performance photonic microwave downconverter based on a frequency-doubling optoelectronic oscillator'. *Lightwave Technology, Journal of*, 30(18), 3036–3042